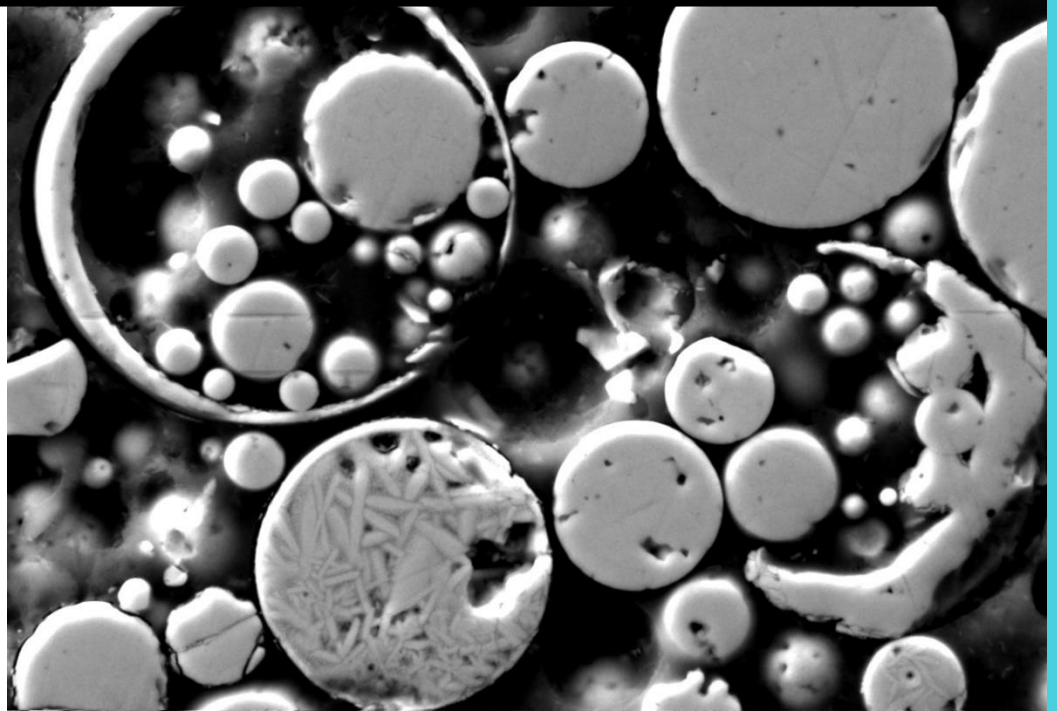


Processing and Properties of Advanced Ceramics and Glass



**WORKSHOP
PROCEEDINGS**

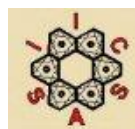
Vrátna –Belá

November 8 – 10, 2017

ORGANIZING INSTITUTIONS:

Vitrum Laugaricio

Glass Centre of Competence, the joint research laboratory of:
Alexander Dubček University of Trenčín, Institute of Inorganic Chemistry of the Slovak
Academy of Sciences and Faculty of Chemical and Food Technology of the Slovak
University of Technology in Bratislava



Slovak Silicate Scientific-Technological Society



SCIENTIFIC BOARD:

Prof. RNDr. Ján Dusza, DrSc.

Prof. Ing. Dušan Galusek, DrSc.

Prof. RNDr. Pavol Šajgalík, DrSc.

ORGANIZING COMMITTEE:

Ing. Dagmar Galusková, PhD.

Anna Jurová

Mgr. Vanda Mokráňová

Andrea Stropková, M.B.A.

ISBN 978-80-8075-786-1

EAN 9788080757861

This conference is part of a project that has received funding from the **European Union's Horizon 2020 research and innovation programme under grant agreement N°739566**



FunGlass
centre for functional and
surface functionalized glass

CONTENTS

| | |
|--|-----|
| PREPARATION AND PROPERTIES OF SiC-Y ₂ O ₃ -Sc ₂ O ₃ COMPOSITES WITH GRAPHENE / O. Hanzel | 3 |
| ELECTRICALLY CONDUCTIVE COMPOSITES BASED ON SiC / R. Bystrický..... | 10 |
| EFFECT OF TEMPERATURE ON BEHAVIOUR OF SiOC LONG FIBRE REINFORCED COMPOSITES / Z. Chlup..... | 18 |
| INFLUENCE OF PROCESSING PARAMETERS ON THE PHASE COMPOSITION, STRUCTURAL AND MECHANICAL PROPERTIES OF ALUMINOSILICATE CERAMICS / M. Orlovská | 24 |
| PREPARATION AND CHARACTERIZATION OF YB ₄ -SiC CERAMICS / Z. Kováčová | 32 |
| POWDER TRANSPORT USING SEQUENTIALLY PULSED COPLANAR BARRIER DISCHARGE / J. Ráhel'..... | 41 |
| PREPARATION AND CHARACTERIZATION OF CERAMICS AND GLASSCERAMICS MATERIALS WITH EUTECTIC MICROSTRUCTURES IN Al ₂ O ₃ -Y ₂ O ₃ SYSTEM / J. Valúchová..... | 48 |
| PRODUCTION OF HOLLOW GLASS MICROSPHERES FROM WASTE GLASSES BY FLAME SYNTHESIS WITH Na ₂ SO ₄ BLOWING AGENT / J. Kraxner..... | 56 |
| PREPARATION OF Bi-DOPED GEHLENITE GLASS MICROSPHERES BY SOLID STATE REACTION AND FLAME SYNTHESIS / M. Majerová | 62 |
| Eu ³⁺ /Eu ²⁺ DOPED YTTRIUM ALUMINATE GLASS AND POLYCRYSTALLINE PHOSPHORS EXCITED BY UV LIGHT AS POTENTIAL CANDIDATES FOR pc-WLED / K. Haladejová | 73 |
| WILLEMITE BASED PHOTO LUMINESCENT MATERIALS. GRAIN MORPHOLOGY AND FLORESCENT SPECTRA BY USING DIFFERENT ACTIVATORS OF LUMINESCENCE / P. Švančárek | 84 |
| YTTRIA NANOPOWDERS PREPARED BY PRECIPITATION METHOD FOR TRANSPARENT YTTRIA CERAMICS / Nibu P G..... | 93 |
| APPLICATION OF THz SPECTROSCOPY FOR CHARACTERISATION OF CERAMIC AND SILICATE MATERIALS / M. Janek..... | 100 |
| LA-ICP-MS IN THE CHEMICAL ANALYSIS OF GLASS, CERAMIC AND MINERAL MATERIALS / P. Chrást | 108 |
| DETERMINATION OF LITHIUM IN GLASS CERAMIC MATERIALS USING ATOMIC SPECTROMETRY / H. Kaňková..... | 125 |

| | |
|---|-----|
| CORROSION OF ZIRCONIA – BASED DENTAL CERAMICS / A. Nowicka..... | 132 |
| THE INFLUENCE OF GLYCINE ON THE PROPERTIES OF SOLS AND XEROGELS IN THE SiO ₂ SYSTEM STABILIZED BY Na ⁺ IONS / P. Balážová..... | 141 |
| THE EFFECT OF THE HEAT TREATMENT ON THE PROPERTIES OF SURFACE OF INORGANIC-ORGANIC LAYERS / M. Čierniková..... | 149 |
| PREPARATION AND CHARACTERIZATION OF PRECURSOR DERIVED CERAMIC COATINGS WITH GLASS FILLER PARTICLES ON STEEL SUBSTRATE / I. Petříková | 157 |

PRÍPRAVA A VLASTNOSTI SiC-Y₂O₃-Sc₂O₃ KOMPOZITOV S PRÍDAVKOM GRAFÉNU

PREPARATION AND PROPERTIES OF SiC-Y₂O₃-Sc₂O₃ COMPOSITES WITH GRAPHENE

O. Hanzel¹, Z. Lenčoš¹, Y.W. Kim², P. Šajgalík¹

¹*Institute of Inorganic Chemistry, Slovak Academy of Sciences, Dúbravská cesta 9, 845 36
Bratislava, Slovak Republic*

²*Functional Ceramics Laboratory, Department of Materials Science and Engineering,
University of Seoul, Seoul 02504, Republic of Korea*

ABSTRACT

Dense silicon carbide/graphene nanoplatelets (GNPs) and silicon carbide/graphene oxide (GO) with yttrium oxide and scandium oxide as a sintering additives were prepared by rapid hot pressing (RHP). Sintering of composites was performed in nitrogen atmosphere at 2000°C for 30 min under uniaxial pressure of 50 MPa. After sintering samples were annealed in gas pressure sintering (GPS) furnace at 1800°C for 6 h under 30 MPa of pressure in a nitrogen atmosphere. The aim of the present contribution was to investigate the influence of the GNPs and GO additions, orientations of the graphene layers and effect of annealing on electrical and thermal properties of such prepared composites.

Keywords: silicon carbide, graphene, rapid hot press, functional properties

INTRODUCTION

Silicon carbide (SiC) is an important structural material due to its excellent thermal conductivity, wear resistance, oxidation resistance, and high-temperature mechanical properties [1–7]. Tailoring of electrical and thermal conductivity of structural ceramics is important for many applications, for example, static charge dissipation devices, manufacturing components by electro-discharge machining, heat exchangers and electronic substrates. From this point of view incorporation of graphene into ceramic matrix is very promising due to its extraordinary

electrical and thermal conductivity [8-11]. Polycrystalline SiC ceramics exhibits a wide range of thermal conductivity values from 30 W/m.K to 270 W/m.K. It depends on many factors like specific chemistry of sintering additives, microstructure and post-heat treatment conditions. For example, hot-pressed SiC sintered with BeO yielded a thermal conductivity of 270 W/m.K [12]. A SiC ceramic sintered with Al₂O₃-Y₂O₃ had a conductivity of 55–90 W/m.K. [13,14]. There are several strategies for improvement of thermal conductivity of SiC ceramics: (1) decrease in lattice oxygen from SiC grains by using Y₂O₃ and Sc₂O₃ as a sintering additives, (2) the use of sintering additives comprising cations insoluble in SiC such as the replacement of the Al compound by sintering additives with no or low solubility in SiC, (3) a decrease in grain boundary segregation, which induces grain boundary scattering [15], (4) annealing of sintered sample in order to increase grain size and also to anneal defects in structure of graphene incorporated in ceramic matrix.

EXPERIMENTAL

For preparation of composite powders we used either commercially available GNPs (thickness < 4 nm, Cheap Tubes Inc., USA) or we synthesized GO in lab.

SiC/GNPs composite powders with different content of graphene nanoplatelets (1, 5 and 10 wt. %) were prepared. First, appropriate amount of GNPs were mixed in isopropanol and ultrasonicated 60 min by strong ultrasound probe (Sonopuls HD 3200, Bandelin electronic GmbH, Germany). After that 98.632 wt. % SiC, 0.849 wt. % Y₂O₃ and 0.519 wt. % Sc₂O₃ were mixed in isopropanol, added to suspension with graphene nanoplatelets and stirred on magnetic stirrer for 3 h followed by 10 min. ultrasonication by ultrasound probe. Isopropanol was removed from suspension by vacuum rotary evaporator. Resulting composite powders were dried at 80°C over night and then sieved through 71 µm microscreen.

SiC/GO composite powders with 1 wt. % of graphene oxide were prepared. First, appropriate amount of GO were mixed in distilled water and ultrasonicated 60 min by strong ultrasound probe (Sonopuls HD 3200, Bandelin electronic GmbH, Germany). After that 98.632 wt. % SiC, 0.849 wt. % Y₂O₃ and 0.519 wt. % Sc₂O₃ were mixed in isopropanol, added to suspension with graphene nanoplatelets and stirred on magnetic stirrer for 3 h followed by 10 min. ultrasonication by ultrasound probe. Suspension was then sprayed into the liquid nitrogen a subsequently frozen powder was placed in freeze dryer in order to remove water by sublimation. Resulting composite powders were dried at 80°C over night and then sieved through a 71 µm microscreen.

In case of reference powder (NS327) without any addition of graphene, all components were ball milled together in isopropanol with SiC balls for 24 h. Isopropanol was removed from suspension by vacuum rotary evaporator. Resulting reference powder were dried at 80°C overnight and then sieved through 71 µm microscreen.

Composite and reference powders were placed in graphite die and surrounded by graphite paper (foil) in order to prevent direct contact between powder compact and graphite die and sintered in rapid hot press (DSP 507, Dr. Fritsch GmbH., Germany) at 2000°C with holding time of 30 min, uniaxial pressure 50 MPa under nitrogen atmosphere and with heating rates 100°C/min. In detail sintering regime is described below (Fig. 1). From each composition three samples were made in order to get materials for testing of electrical and thermal conductivity and studying influence of graphene layers orientations and effect of annealing on properties of such prepared materials. Final dimensions of prepared samples were 20 mm in diameter and thickness approximately 3-4 mm and approximately 10 mm in case of thick samples.

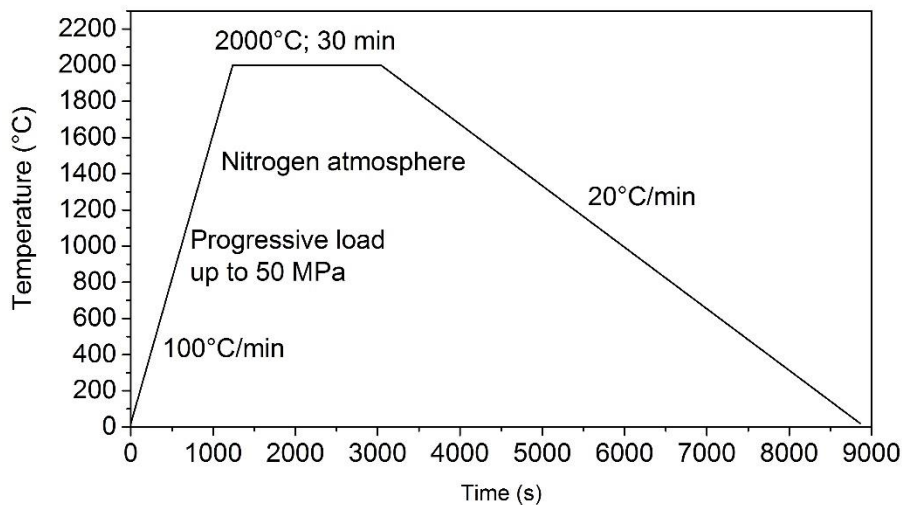


Fig. 1. Schema of sintering regime for rapid hot press

After sintering some samples were annealed in gas pressure sintering (GPS) furnace at 1800°C for 6 h under 30 MPa of pressure in a nitrogen atmosphere.

Densities of prepared composites and also after annealing were measured by Archimedes method using mercury as the immersion medium.

Thermal diffusivity measurements were done using Laser flash analyser Linseis LFA 1000 in direction parallel and perpendicular to pressing axis and also before and after annealing. To

evaluate thermal diffusivity sample 10 x 10 mm and thickness approximately 2 - 3 mm were cut and plane parallel grinded. Data were averaged for each measuring temperature over at least three measurements.

Electrical conductivity was measured by four point probe method in direction parallel and perpendicular to pressing axis and also before and after annealing.

RESULTS

Relative density of prepared composites slightly decrease with increasing content of graphene. However almost fully dense composites were prepared by RHP even at high loading of graphene, in case of sample with 10 wt. % relative density was around 97 % (Fig. 2).

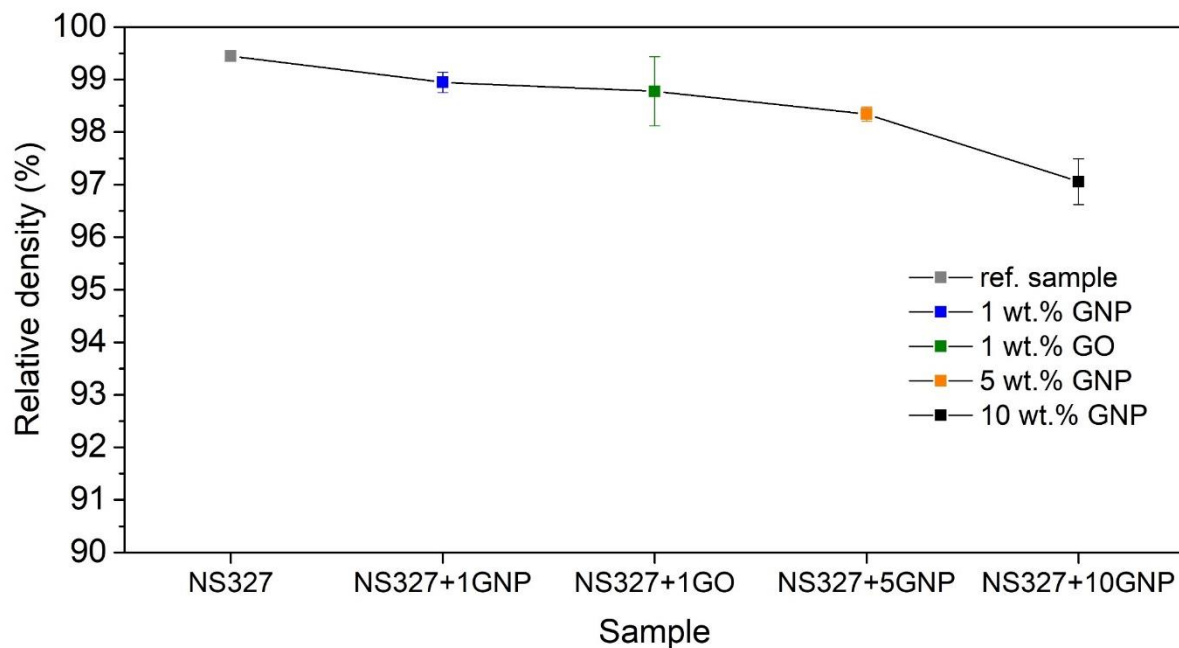


Fig. 2. Relative densities of reference sample and composites with graphene nanoplatelets and graphene oxide.

After sintering, part of prepared samples were annealed at 1800 °C for 6 h in nitrogen overpressure of 30 MPa. Purpose of this step were incorporation of nitrogen atoms into the structure of composites, annealing of structural defects of graphene layers and increase of grains size. XRD was used for verification of some possible new phases after annealing. Temperature of annealing and overpressure of nitrogen was chosen in order to prevent formation of Si_3N_4 .

XRD results confirmed that after annealing no new phases was formed and graphene was retained in structure of composites after annealing (Fig. 3).

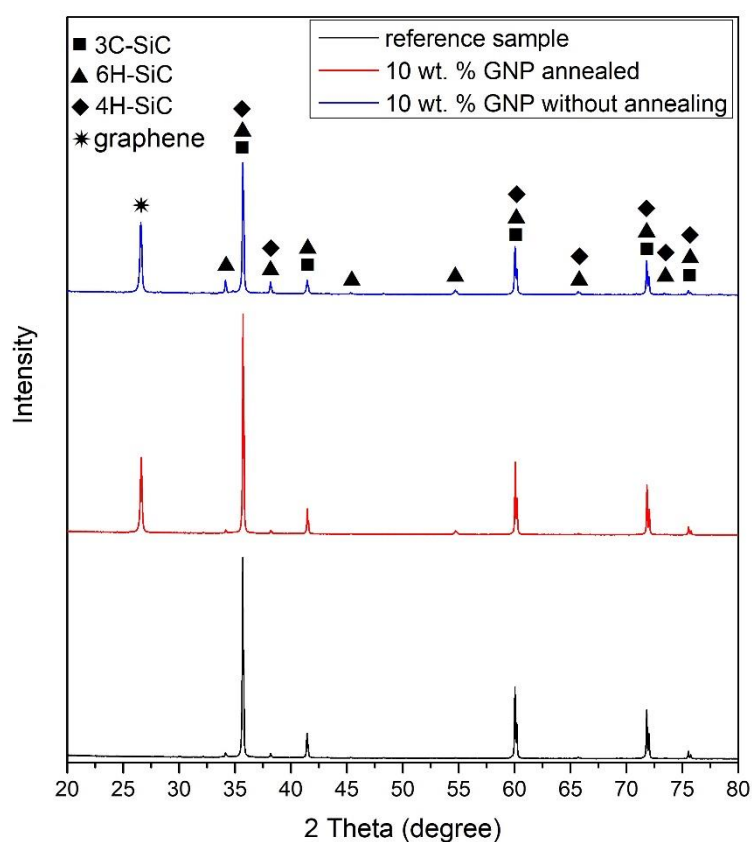


Fig 3. XRD of reference sample, composite with 10 wt. % of GNP before and after annealing

CONCLUSION

SiC-Y₂O₃-Sc₂O₃ composites with addition of either GNPs or GO were successfully prepared. Almost fully dense composites were prepared by RHP even at high loading of GNPs (RD were higher than 97 %). After sintering, part of samples was annealed at 1800°C for 6 h in nitrogen overpressure of 30 MPa. After annealing no new phases was detected and GNPs were also preserved in composites. In future we will study effect of amount and type of used graphene, orientation of graphene layers, and effect of annealing on functional properties (especially of thermal conductivity) of SiC-graphene composites.

ACKNOWLEDGMENT

This work is the result of the project Competence center for new materials, advanced technologies and energy ITMS 26240220073, supported by the Research and Development Operational Program funded by the European Regional Development Fund. This work was financially supported by the Slovak Grant Agency VEGA Project No. 2/0065/14, APVV-15-0469 and ERA-NET project GRACE.

REFERENCES

- [1] Kleebe, H. J. SiC and Si₃N₄ materials with improved fracture resistance, J. Eur. Ceram. Soc., 10 (1992) 151–159.
- [2] Sciti, D., Bellosi, A. Effects of additives on densification, microstructure and properties of liquid-phase sintered silicon carbide, J. Mater. Sci., 35 (2000) 3849–3855.
- [3] Biswas, K., Rixecker, G., Aldinger, F. Improved high temperature properties of SiC-ceramics sintered with Lu₂O₃-containing additives, J. Eur. Ceram. Soc., 23 (2003) 1099–1104.
- [4] Strecker, K., Hoffmann, M. J. Effect of AlN-content on the microstructure and fracture toughness of hot-pressed and heat-treated LPS-SiC ceramics, J. Eur. Ceram. Soc., 25 (2005) 801–807.
- [5] Balog, M., Šajgalík, P., Hnatko, M., Lenčič, Z., Monteverde, F., Keckes, J., Huang, J.L. Nano-versus macro-hardness of liquid phase sintered SiC, J. Eur. Ceram. Soc., 25 (2005) 529–534.
- [6] Kaur, S., Riedel, R., Ionescu, E. Pressureless fabrication of dense monolithic SiC ceramics from a polycarbosilane, J. Eur. Ceram. Soc., 34 (2014) 3571–3578.
- [7] Kim, K. J., Lim, K. Y., Kim, Y. W. Electrical and thermal properties of SiC ceramics sintered with yttria and nitrides, J. Am. Ceram. Soc., 97 (2014) 2943–2949.
- [8] Prasher, R. Graphene spreads the heat. Materials Science, 328 (2010) 185-186.
- [9] Balandin, A. A. Thermal properties of graphene and nanostructured carbon materials. Nature materials, 10 (2011) 569-581.
- [10] Ghosh, S., Calizo, I., Teweldebrhan, D., Pokatilov, E. P., Nika, D. L., Balandin, A. A., Bao, W., Miao, F., Lau, C. N. Extremely high thermal conductivity of graphene: Prospects for thermal management applications in nanoelectronic circuits. Applied Physics Letters, 92 (2008) 151911-1-3.

[11] Chen, J., Jang, C., Xiao, S., Ishigami, M., Fuhre, M. S. Electronic properties and devices: intrinsic and extrinsic performance limits of graphene devices on SiO₂.

Nature Nanotechnology, 3 (2008) 206–209.

[12] Ogihara, S., Maeda, K., Yakeda, Y., Nakamura, K. Effect of impurity and carrier concentrations on electrical resistivity and thermal conductivity of SiC ceramics containing BeO, J. Am. Ceram. Soc., 68 (1985) C16–C18.

[13] Liu, D. M., Lin, B. W. Thermal conductivity in hot-pressed silicon carbide, Ceram. Int., 22 (1996) 407–414.

[14] Volz, E., Roosen, A., Hartung, W., Winnacker, A. Electrical and thermal conductivity of liquid phase sintered SiC, J. Eur. Ceram. Soc., 21 (2001) 2089–2093.

[15] Kim, Y. W., Lim, K. Y., Seo, W. S. Microstructure and thermal conductivity of silicon carbide with Yttria and Scandia. J. Am. Ceram. Soc., 97 (2014) 923-928.

ELEKTRICKY VODIVÉ KOMPOZITY NA BÁZE SiC

ELECTRICALLY CONDUCTIVE COMPOSITES BASED ON SiC

R. Bystrický¹, J. Sedláček¹, P. Šajgalík¹

¹*Ústav anorganickej chémie, Slovenská akadémia vied, Dúbravská cesta 9, 841 04 Bratislava*

ABSTRACT

In this work silicon carbide based composites were prepared by hot-press and rapid hot-press method. 20, 30, 40 and 50 mass% of Ti and NbC were used as sintering additives. Their molar ratio was kept at 1:1.8 (Ti:NbC). Samples were sintered by hot-press method by two step sintering to avoid the squeezing out the melted titanium above 1668 °C. Composites were sintered at 1650 °C for 3 h and subsequently at 1850 °C for 1 h under mechanical pressure of 30 MPa in Ar atmosphere. Rapid hot-pressed samples were sintered at 1850 °C for 30 min at 30 MPa mechanical pressure in Ar. SiC50TiNbC-HP phase showed the electrical conductivity of 240 S·mm⁻¹, Higher Vickers hardness was achieved on rapid hot-pressed samples, nearly 20.5 GPa. Highest indentation toughness (8.8 MPa·m^{1/2}) was achieved in the sample with 40% of Ti-NbC phase. XRD pattern confirmed the formation of (Ti, Nb)C solid solution in the SiC matrix.

Keywords: silicon carbide, niobium carbide, electrical conductivity, hot-pressing, rapid hot-pressing

INTRODUCTION

Electroceramics are advanced ceramic materials that are used in a wide variety of electrical, optical and magnetic applications. They can find the applications also in energy storage/conversion systems, as high temperature filters, catalyst supports or acoustic metamaterials, in nuclear fusion reactors and in high temperature thermomechanical applications. Conductive ceramics such as silicon carbide are useful as heating elements in furnaces up to 1500 °C in air. Most of the ceramics have high negative temperature coefficients of resistivity and therefore are developed as temperature indicators. Electroceramics with low dielectric constants are made into substrates for integrated circuits, whereas those with high dielectric constants are used in capacitors. Electroceramics with good magnetic properties are suitable for transformer cores, whereas those that exhibit piezoelectricity find applications in transducers for microphones, and so on. [1]

The development of structural electrically conductive ceramic is not simple, namely conductive ceramic materials are usually brittle and do not sinter well, and on the other side, engineering ceramic materials are insulators. A promising approach is a combination of insulating engineering ceramics with electrically conductive phases.

In recent years carbon structures, such as carbon nanotubes (CNTs) or graphene nanoplatelets (GNPs), are incorporated into the ceramic matrix. The aim is enhance of the electrical conductivity and improve the mechanical properties, respectively. Authors were successful by increasing of electrical conductivity of the composites but on the other hand the resulting mechanical properties are contradictory. [1, 2, 3, 4, 5, 6]

Another good candidate for using as secondary phase in ceramics is niobium carbide due to its high stability, high hardness and high wear resistance. Moreover, in combination with Ti helps to densify the SiC ceramics and can significantly increase the electrical conductivity of resulted material. [1]. Moreover, Ti forms TiC at high temperatures, which is another phase with high stability high hardness and high wear resistance.

In this work, we focused on densification of SiC composites with various amounts of Ti-NbC phase by hot-press and rapid hot-press method. Influence of Ti-NbC amount and densification method on the electrical properties and mechanical properties of final composite was investigated.

EXPERIMENTAL PART

The commercially available powders of β -SiC (HSC-059, Superior Graphite, USA), Ti (TOHO Titanium Co., Japan) and NbC (Japan New Metals Co., Japan) were used for the starting mixtures preparation. The SiC-based composites were prepared by the addition of the various amount of electrically conductive Ti-NbC phase what is a mixture of Ti and NbC in a molar ratio 1:1.8 (Ti:NbC). The chemical composition of starting mixtures are briefly listed in Tab. 1.

Tab. 1. Chemical composition of starting mixtures

| Sample | W [mass%] | | |
|------------|-----------|------|------|
| | SiC | Ti | NbC |
| SiC20TiNbC | 80 | 7.2 | 12.8 |
| SiC30TiNbC | 70 | 10.8 | 19.2 |
| SiC40TiNbC | 60 | 14.4 | 25.6 |

| Sample | W [mass%] | | |
|------------|-----------|------|------|
| | SiC | Ti | NbC |
| SiC50TiNbC | 50 | 18.0 | 32.0 |

The powder mixtures were homogenized in planetary mill in water with WC balls at 150 rpm for 1 h. The homogenized suspensions were freeze dried. Hot pressed samples were prepared in two steps: at 1650 °C for 3 h and at 1850 °C for 1 h under mechanical pressure of 30 MPa in Ar atmosphere. Rapid hot-pressed samples were prepared at 1850°C for 15 min under mechanical pressure 30 MPa in Ar atmosphere. The heating rate for hot-press and rapid hot-press were 15 °C/min and 100 °C/min, respectively.

Reference sample without any additives was prepared by hot-press at 1850 °C. Detailed sintering process was described in Ref. 1.

The densities of the samples were measured by Archimedes method in mercury. The theoretical densities were calculated according to the rule of mixtures. The crystalline phases present in the ground samples were identified using X-ray diffraction (XRD) (Panalytical Empyrean, Netherlands, Cu K α radiation).

The electrical conductivity measurement was performed by Van der Pauw method.

The microstructures were observed by scanning electron microscopy (EVO 40HV, Karl Zeiss, Germany). For this purpose the sintered samples were cut and polished.

RESULTS

Tab. 2 shows the densities of sintered samples. Samples made by hot press with addition of 40 and 50 mass % of Ti-NbC phase (SiC40TiNbC-HP, SiC50TiNbC-HP) have densities near theoretical density. Sample SiC30TiNbC-HP has density only 91.7 % of theoretical density. Sample SiC20TiNbC-HP has density only 80% of theoretical density even though powder mixture was prepared by freeze granulation.

Samples made by rapid hot-press with addition of 20 - 40 mass% of Ti-NbC phase (SiC20TiNbC-RHP, SiC30TiNbC-RHP, SiC40TiNbC-RHP) are fully dense.

Tab. 2 The density and relative density of samples after sintering at 1850 °C

| Sample | HP | | Rapid HP | |
|------------------|------------------------------|--------|------------------------------|--------|
| | ρ [g·cm ⁻³] | TD [%] | ρ [g·cm ⁻³] | TD [%] |
| SiC20TiNbC gran. | – | – | 3.53 | 98.8 |
| SiC30TiNbC | 3.44 | 91.7 | 3.74 | 99.7 |
| SiC40TiNbC | 3.86 | 97.2 | 3.96 | 100 |
| SiC50TiNbC | 4.14 | 98.3 | – | – |

Fig. 1 shows the XRD patterns of prepared composites.

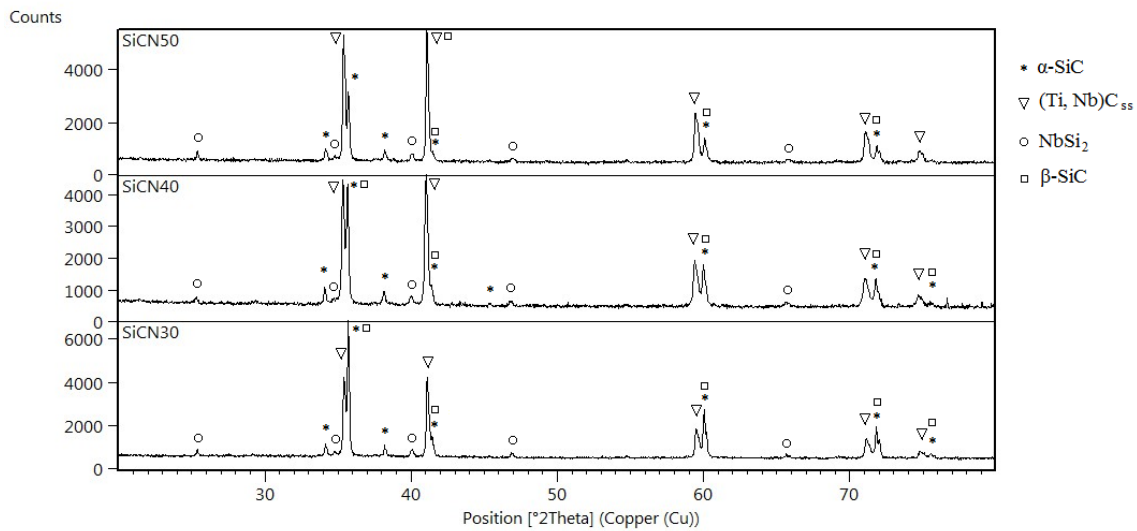
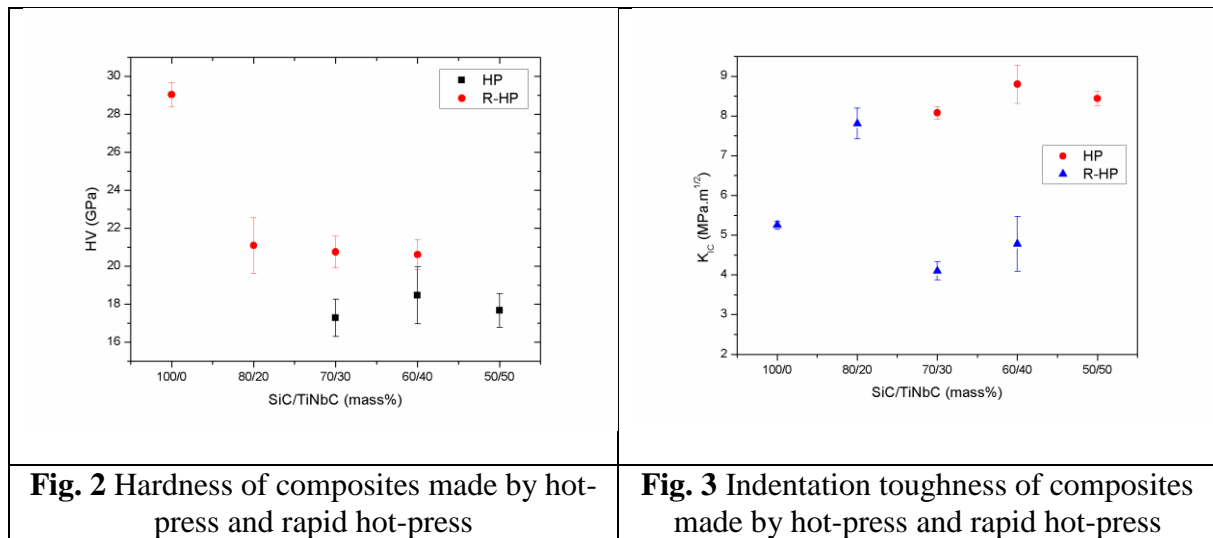


Fig. 1 Comparison of XRD patterns of sintered samples

XRD patterns of samples SiC30TiNbC-HP, SiC40TiNbC-HP, SiC50TiNbC-HP (Fig. 1) showed that the samples contain β -SiC (ICDD 03-065-0360) and α -SiC (ICDD 01-073-1663) as a result of $\beta \rightarrow \alpha$ transformation, also (Ti, Nb) C_{ss} (ICDD 03-065-7915) and NbSi₂ (ICDD 03-065-3551) as secondary phases. Presence of higher content of solid solution encourages phase transformation of SiC matrix.

Samples SiC20TiNbC-RHP, SiC30TiNbC-RHP, SiC40TiNbC-RHP does not contain NbSi₂ phase. It is due to the much shorter sintering regime as at hot-pressed samples and Nb from NbC cannot diffuse into the SiC grain and form NbSi₂ phase.

Fig. 2 shows the hardness of samples made by hot-press and rapid hot-press.



The hardness of samples made by rapid hot-press method is decreasing with higher amount of (Ti, Nb)C_{ss} phase but all values are higher than the values of samples made by hot-press. The lowest hardness in the SiCN30 sample is connected to the higher porosity which is approximately 8%. Comparing to the reference SiC without any additives, hardness of the samples are lower.

Fig. 3 shows the indentation toughness of samples made by hot-press and rapid hot-press. Indentation toughness of hot pressed samples is higher than in the case of rapid hot-pressed samples. The indentation toughness of rapid hot-pressed samples is lower than in reference sample except of SiC20TiNbC-RHP sample where the indentation toughness is about 7,8 MPa.m^{1/2}.

Fig. 4 shows the electrical conductivity of samples made by hot-press and rapid hot-press.

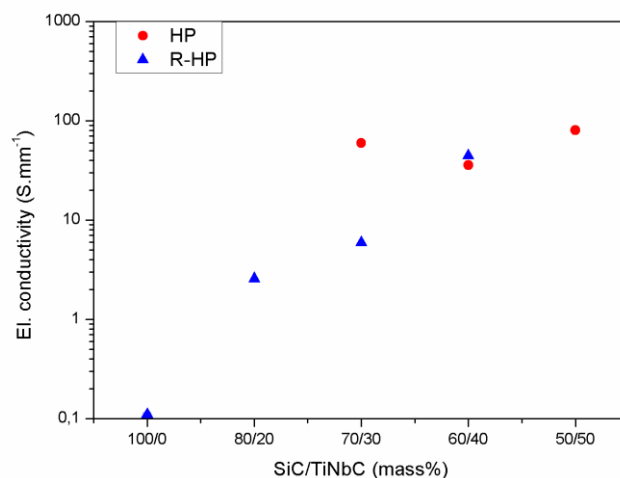


Fig. 4 Electrical conductivity of composites made by hot-press and rapid hot-press

As it can be seen the electrical conductivity of the hot-pressed samples are up to 3 orders of magnitude higher than in reference sample and varied from 19.15 to 240 S·mm⁻¹. Comparing to other composites, SiC50TiNbC-HP sample has 2 orders of magnitude higher value than other published composites with high electrical conductivity [10-15]. The electrical conductivity of rapid hot-pressed samples is increasing with increasing amount of (Ti, Nb)C_{ss}. Comparing to values of hot-pressed samples the electrical conductivity of SiC30TiNbC-RHP is lower while the SiC40TiNbC-RHP has higher electrical conductivity than the sample with the same addition of Ti-NbC made by hot-press.

Fig. 5 shows the microstructure SiC40TiNbC made by hot-press and by rapid hot-press

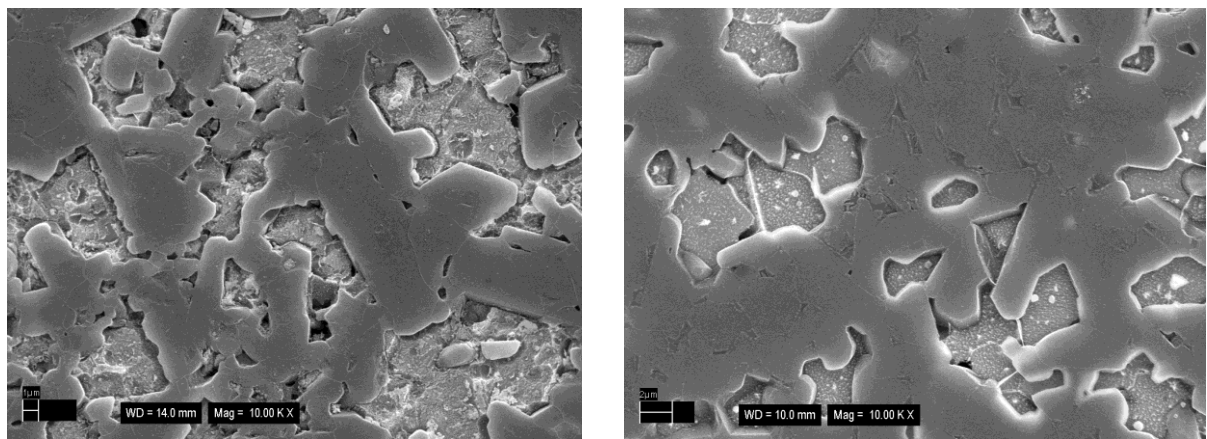


Fig. 5 Microstructure of SiC40TiNbC made by hot-press (left) and by rapid hot-press (right)

The microstructures of both samples reveal dark grains that correspond to SiC whereas the overetched phase is (Ti, Nb)C_{ss}. On the grain boundary there is a thin layer of phase with higher amount of Si, O (as SiO₂ which is an oxidation result of SiC starting powder), Al (as impurity in SiC starting powder) and Ti. The average grain size of hot pressed sample is 3.154 ± 0.48 μm, while the average grain size of rapid hot-pressed sample is 1.65 ± 0.35 μm. This difference of grain size between samples made by different method can explain the discrepancy of mechanical properties. It is also well known that the hardness of sintered ceramics increases and fracture toughness decreases with decreasing grain size.

CONCLUSIONS

Electrically conductive SiC composites were prepared by using NbC and Ti as sintering additives. Composites were sintered at 1650 °C for 3 h and subsequently at 1850 °C for 1 h under mechanical pressure of 30 MPa in Ar atmosphere.

The addition of Ti-NbC phase into the SiC matrix led to decreasing of hardness comparing to reference SiC. Hardness values of rapid hot-pressed samples are higher than values of hot-pressed samples. On the other hand, addition of Ti-NbC phase increases the indentation toughness of composites comparing to reference SiC without any additives, except SiC30TiNbC-RHP and SiC40TiNbC-RHP. The presence of Ti-NbC phase significantly increased the electrical conductivity of SiC composites. The highest electrical conductivity $240 \text{ S}\cdot\text{mm}^{-1}$ was reached in the SiC50TiNbC-HP composite.

SiC composites with electrically conductive Ti-NbC phase are promising materials in fields of industry where ceramics with high electrical conductivity are needed.

ACKNOWLEDGEMENT

This work is the result of the project Competence center for new materials, advanced technologies and energy ITMS 26240220073, supported by the Research and Development Operational Program funded by the European Regional Development Fund. This work was financially supported by the Slovak Grant Agency VEGA Project No. 2/0065/14, APVV-15-0469 and ERA-NET project GRACE.

REFERENCES

- [1] Bharadwaj, S.R., Varma, S., Wani, B.N.: 16 – Electroceramics for Fuel Cells, Batteries and Sensors, Functional Materials, Preparation, Processing and Applications (2012), 639–674
- [2] Michálek, M., Sedláček, J., Parchoviansky, M., Micháľková, M., Galusek, G.: Mechanical properties and electrical conductivity of alumina/MWCNT and alumina/zirconia/MWCNT composites, *Ceramics International*, Volume 40 (2014) 1289-1295
- [3] Hanzel, O., Sedláček, J., Šajgalík, P.: New approach for distribution of carbon nanotubes in alumina matrix, *Journal of the European Ceramic Society* 34 (2014) 1845–1851
- [4] Kovalčíková, A., Balázs, Cs., Dusza, J., Tapasztó, O.: Mechanical properties and electrical conductivity in a carbon nanotube reinforced silicon nitride composite, *Ceramics International* 38 (2012) 527–533
- [5] Balázs, Cs., Fényi, B., Hegman, N., Kovér, Zs., Wéber, F., Vértesy, Z., Kónya, Z., Kiricsi, I., Biró, L. P., Arató, P.: Development of CNT/Si₃N₄ composites with improved mechanical and electrical properties, *Composites: Part B* 37 (2006) 418–424

- [6] Lee, K., Mo, C. B., Park, S. B., Hong, S. H.: Mechanical and Electrical Properties of Multiwalled CNT-Alumina Nanocomposites Prepared by a Sequential Two-Step Processing of Ultrasonic Spray Pyrolysis and Spark Plasma Sintering, *J. Am. Ceram. Soc.*, 94 (2011) 3774–3779
- [7] Yamamoto, G., Omori, M., Hashida T., Kimura H.: A novel structure for carbon nanotube reinforced alumina composites with improved mechanical properties, *Nanotechnology*, 19 (2008) 315708-315713
- [8] Frajkorová, F., Lenčěš, Z., Šajgalík, P.: Electrically Conductive Silicon Carbide without Oxide Sintering Additives, *J. Kor. Ceram. Soc.*, 49 (2012) 342~346
- [9] Šajgalík P, Sedláček J, Lenčěš Z, Dusza J, Lin HT: Additive-free hot-pressed silicon carbide ceramics-A material with exceptional mechanical properties, *J. Eur. Ceram. Soc.*, 36 (2016) 1333-1341
- [10] Kim, Y.W., Kim, K.J., Kim, H.C., Cho, N.H., Lim, K.Y. Electrodischarge-machinable silicon carbide ceramics sintered with yttrium nitrate. *J. Am. Ceram. Soc.*, 94 (2011) 991–993.
- [11] Román-Manso, B., Domingues, E., Figueiredo, F. M., Belmonte, m., Miranzo, P. Enhanced electrical conductivity of silicon carbide ceramics by addition of graphene nanoplatelets, *J. Eur. Ceram. Soc.*, 35 (2015) 2723-2731
- [12] Lim, K.Y., Kim, Y.W., Kim, K.J., Yu, J.H. Effect of in situ-synthesized nano-size SiC addition on density and electrical resistivity of liquid-phase sintered silicon carbide ceramics, *J. Ceram. Soc. Jpn.*, 119 (2011) 965–967.
- [13] Zhan, G.D., Mitomo, M., Xie, R.J., Mukherjee, A.K. Thermal and electrical properties in plasma-activation-sintered silicon carbide with rare-earth-oxide additives, *J. Am. Ceram. Soc.*, 84 (2001) 2448–2450.
- [14] Can, A., McLachlan, D.S., Sauti, G., Herrmann, M. Relationships between microstructure and electrical properties of liquid-phase sintered silicon carbide materials using impedance spectroscopy. *J. Eur. Ceram. Soc.*, 27 (2007) 1361–1363.
- [15] Hanzel, O., Sedláček, J., Šajgalík, P. New approach for distribution of carbon nanotubes in alumina matrix, *J. Eur. Ceram. Soc.*, 34 (2014) 1845-1851

EFFECT OF TEMPERATURE ON BEHAVIOUR OF SiOC LONG FIBRE REINFORCED COMPOSITES

Z. Chlup¹, M. Černý², A. Strachota³, H. Hadraba¹, M. Halasová⁴

¹ CEITEC IPM, Institute of Physics of Materials AS CR, v.v.i., Brno, Czech Republic

² Institute of Rock Structure and Mechanics AS CR, v.v.i., Prague, Czech Republic

³ Institute of Macromolecular Chemistry AS CR, v.v.i., Prague, Czech Republic

⁴ Institute of Physics of Materials AS CR, v.v.i., Brno, Czech Republic

ABSTRAKT

Composites utilising long fibres as reinforcement are the most effective from the toughening effect point of view. A brittle matrix using brittle fibres as reinforcement was investigated in this case. The polysiloxane resin was used in this composite as matrix precursor and continuous basalt fibres as reinforcement. The pyrolysis process conducted at 650°C under nitrogen atmosphere turn the polymeric precursor to the so-called hybrid matrix consisting of not fully transformed SiOC glass containing polymeric species. The pyrolysis temperature of 650°C was found to be optimal for the mechanical properties of the composite and the fracture toughness was determined on the level of 20 MPa.m^{1/2}. The main aim of this paper is to describe changes in mechanical properties during long-term ageing in an air atmosphere of this composite with the metastable matrix. It was found that with increasing temperature of the ageing the composite behaviour tends to be brittle. This observation is supported by microstructural and fractographic analysis. The degradation of basalt fibres was not observed therefore whole embrittlement process is ascribed to the changes in the hybrid matrix.

Keywords: Composite, Fracture, SiOC, Basalt Fibre, Ageing

INTRODUCTION

Composites reinforced with ceramic fibres are basically used with two different types of matrix: i) polymeric matrix where incorporated fibres enhance mostly stiffness and strength and these composites are predetermined for room temperature applications, and ii) ceramic matrix where

fibres acts as toughening component through various toughening mechanisms and such composites are usually targeted for high-temperature applications. There obviously exists a gap in the temperature range where polymeric matrix composites are not able to serve and ceramic-based ones are too expensive for these applications [1, 2]. The partially pyrolysed polysiloxane based matrix reinforced by basalt fibres are composites with the ability to fill the temperature range between room temperature up to 650°C [3-5]. They may possess an excellent strength attacking level of 1 GPa and the fracture toughness on the level of 20 MPa·m^{1/2} as was reported recently [6]. The aim of this contribution is to describe changes in the mechanical behaviour as well as in the microstructure after application long-term exposition in a harsh oxidative atmosphere of these hybrid composites.

EXPERIMENTAL

Unidirectional long fibre reinforced composites under the investigation from commercially available methylsiloxane (MS) resin Lukosil M130 (Lučební závody Kolín, Czech Republic) reinforced with basalt fibres (Kamenny Vek, Russia) were prepared by the partial pyrolysis at 650°C under nitrogen atmosphere. These composites were in form of bars with nominal dimensions 3 × 4 × 150 mm consequently aged at 300°C, 400°C and 500°C for 1000 h under air atmosphere. After ageing, the specimens were prepared and tested at room temperature. Elastic properties were monitored using an impulse excitation technique using a RFDA (IMCE NV, Genk, Belgium). Flexural strength values were obtained by loading in three-point bending configuration with a span of 40 mm on a universal testing system Instron 8862 (Norwood, USA) with a crosshead speed 0.5 mm/min. The fracture toughness was determined on CNB specimens where chevron notch was cut by an ultra-thin diamond blade using a precise saw Isomet 5000 (Buehler, USA). The same testing system was used as in case of flexural strength tests only the crosshead speed was 100 µm/min and span of 16 mm. The microstructural and fractographic analyses were conducted using an electron scanning microscope Lyra 3 XMU (Tescan, Czech Republic).

RESULTS

The long-term ageing of composites results in their expected degradation due to microstructural changes in the hybrid matrix where underwent only partial polymer to ceramic transformation. Due to the fact of partial pyrolysis, some micro-regions are behaving like SiOC glass and others like polymer. The optimal mixture of these regions provides the composite with its unique mechanical behaviour, i.e. high toughness and strength. The typical properties of as received

material are summarised in **Table 1**. An oxidative atmosphere at elevated temperatures led to the degradation of polymeric chains, oxidising of silica and carbon, some species in the form of gasses, usually carbon oxides resulting in weight losses and microstructural changes. The weight losses were -0.73 % for the highest ageing temperature of 500°C/1000 h as is shown in **Table 1**.

Table 1 Summarisation of results obtained on the hybrid composites in as received state and after various temperatures of ageing. Average values with the standard deviation in brackets.

| Material state Properties | As rec | Ageing temperature for 1000 h | | |
|--|----------------|-------------------------------|---------------|--------------|
| | | 300°C | 400°C | 500°C |
| Weight loses (%) | - | -0.074 | -0.44 | -0.73 |
| Density (g·cm ⁻³) | 2.16 (0.088) | 2.15 (0.012) | 2.17 (0.017) | 2.14 (0.015) |
| Elastic modulus - flexural (GPa) | 62.9 (0.96) | 56.9 (1.22) | 59.37 (0.97) | 57.7 (0.51) |
| Elastic modulus - longitudinal (GPa) | 63.9 (0.40) | 62.7 (0.64) | 63.9 (0.41) | 64.3 (0.38) |
| Flexural strength (MPa) | 793.8 (124.99) | 400.7 (17.94) | 150.3 (26.01) | 96.2 (13.51) |
| Fracture toughness (MPa·m ^{1/2}) | 13.2 (0.65) | 10.7 (1.10) | 4.9 (0.39) | 2.3 (0.19) |

Elastic properties are not severely changed by the application of ageing rather are dependent on the final density of the given specimen. Even though the longitudinal waves (i.e. direction along the fibre axis) show less change than flexural vibration mode which is more sensitive to the specimen surface quality and its homogeneity. The overall changes are under 10 %.

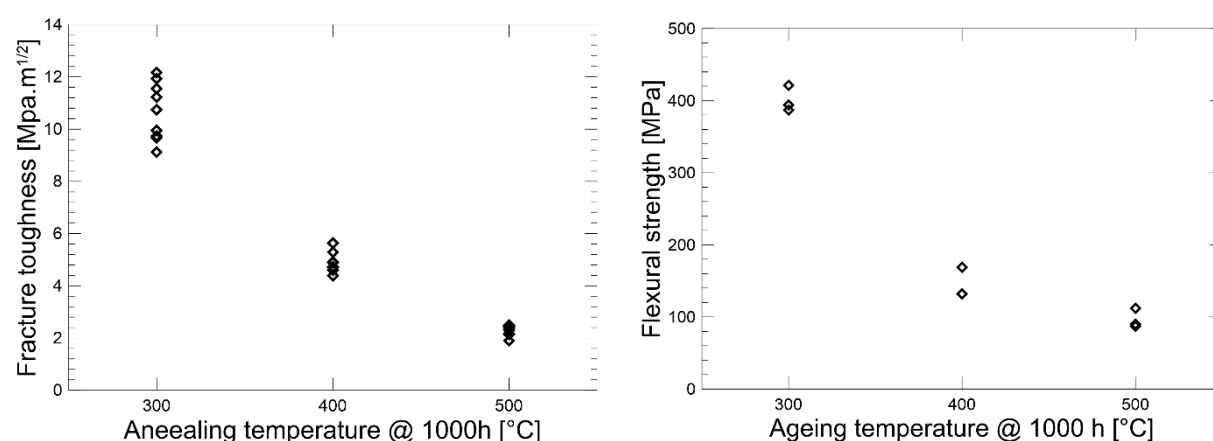


Fig. 1 Dependence of the flexural strength (left) and the fracture toughness both on the ageing temperature.

Contrary to the elastic properties the flexural strength and the fracture toughness are affected severally by the ageing. The effect of ageing temperature on the mechanical properties of individual specimens is plotted in **Fig. 1**. When the as-received composite material is compared with the material exposed to the ageing temperature of 300°C, one can observe 50 % drop in the strength which is accompanied by 20 % drop in the fracture toughness values. Further increase of the ageing temperature led to the decrease of the flexural strength to the level of 100 MPa and the fracture toughness to 2.3 MPa·m^{1/2}.

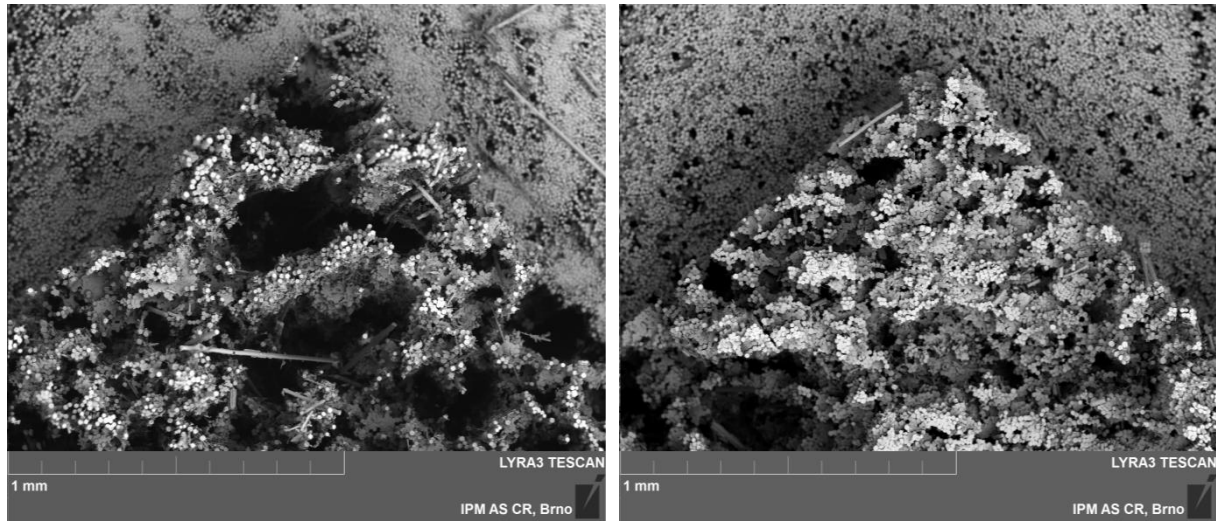


Fig. 2 Fracture surfaces in the vicinity of chevron notch for ageing temperature 400°C (left) and 500°C (right) after fracture toughness tests.

The drop of the strength and fracture toughness can be explained by microstructural changes ongoing in the composite matrix mainly. The typical fracture surfaces of the composite after ageing temperature 400°C and 500°C are shown in **Fig. 2**. The overview reveals differences in the fracture mechanisms acting during loading. It is obvious that fracture surface of the specimen exposed to 400°C has significantly more active fibre pull-out mechanism, therefore, the final fracture surface is more fragmented and consumption of the fracture energy is higher. It is necessary to note that the fracture surface of the specimen aged at 300°C was not possible to observe because the further loading led to the fibre delamination but not fracture, and the specimen still stays in one piece. The detailed view of the fracture surfaces in **Fig. 3** illustrates well the fracture mechanism changes where the higher ageing temperature led to the increase of interfacial bonding between the fibres and the matrix, resulting in the fracture of neighbouring fibres in a monolithic-like fracture (i.e. fracture in the same plane without the fibre matrix delamination necessary for activation of the pull-out toughening mechanism). However, even in this case, a catastrophic sudden fracture was not observed which can be the

advantage of such material having similar fracture toughness after long-term ageing in the air atmosphere as commonly used structural ceramics.

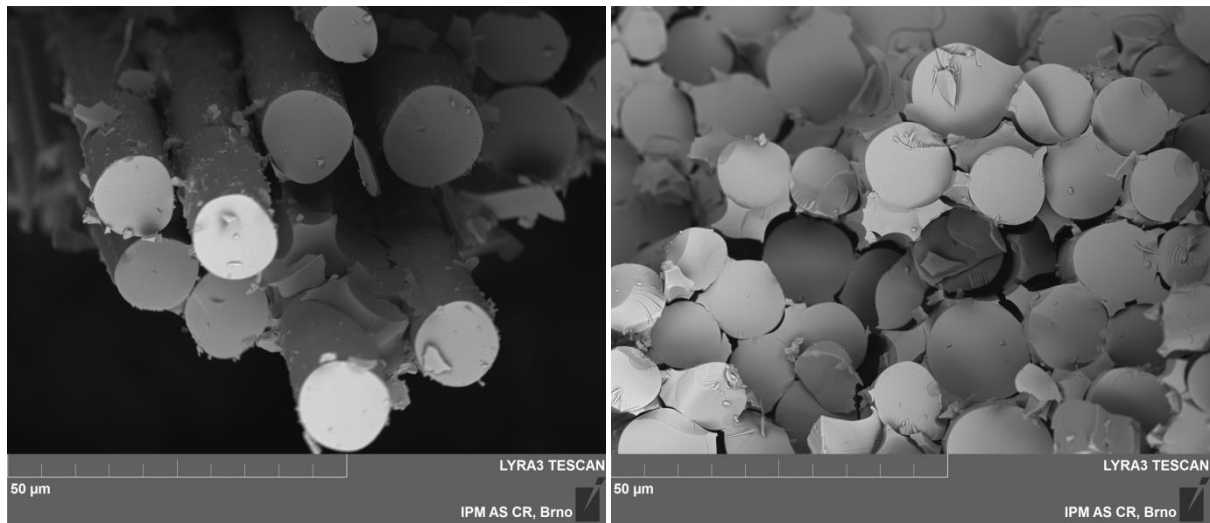


Fig. 3 Detail view of the fracture surfaces for specimens aged at temperature 400°C (left) and 500°C (right) for 1000 h after fracture toughness tests.

CONCLUSION

The presented results show the effect of degradation processes taking place in the polysiloxane-based partially pyrolysed composite matrix with an increasing ageing temperature. The flexural strength decreased to 50 % of the initial strength when aged at 300°C/1000 h and approximately to 100 MPa for the highest ageing temperatures applied. Accordingly, the fracture toughness exhibits the same decreasing trend what corresponds well with the presumption that no larger defects are formed during ageing than those formed during processing. The drop in the fracture toughness and the flexural strength, respectively, can be ascribed to the matrix shrinkage causing clamping of the fibres in some parts and additionally to the chemical bonding by the formation of silicon-oxygen bonds of either matrix with fibres or between neighbouring fibres being in contact. Both undergoing processes inhibited activation and effectiveness of expected toughening mechanisms observed in the as-received composite material. In spite of the described composite degradation shown at ageing at 500°C for 1000 h, the composite can possess reliable properties suitable for expected applications in fire protection systems or other mechanically low loaded parts resistant in given temperature range.

ACKNOWLEDGMENT

This work was financially supported by the Czech Science Foundation under the project (GAP 17-12546S) and by the Ministry of Education, Youth and Sports of the Czech Republic under the project CEITEC 2020 (LQ1601).

REFERENCES

- [1] K.K. Chawla, Composite Materials: Science and Engineering, Springer2012.
- [2] I.M. Low, Ceramic Matrix Composites: Microstructure, Properties and Applications, Woodhead Pub. and Maney Pub.2006.
- [3] V. Fiore, T. Scalici, G. Di Bella, A. Valenza, A review on basalt fibre and its composites, Composites Part B: Engineering 74(Supplement C) (2015) 74-94.
- [4] E.J. Siqueira, I.V.P. Yoshida, L.C. Pardini, M.A. Schiavon, Preparation and characterization of ceramic composites derived from rice husk ash and polysiloxane, Ceramics International 35(1) (2009) 213-220.
- [5] M. Černý, Z. Chlup, A. Strachota, M. Halasová, Š. Rýglová, J. Schweigstillová, J. Svítlová, M. Havelcová, Changes in structure and in mechanical properties during the pyrolysis conversion of crosslinked polymethylsiloxane and polymethylphenylsiloxane resins to silicon oxycarbide glass, Ceramics International (0) (2015) In Press (Doi:10.1016/j.ceramint.2015.01.034).
- [6] M. Cerny, P. Glogar, Z. Sucharda, Z. Chlup, J. Kotek, Partially pyrolyzed composites with basalt fibres - Mechanical properties at laboratory and elevated temperatures, Composites Part a-Applied Science and Manufacturing 40(10) (2009) 1650-1659.

**SLEDOVANIE VPLYVU VÝROBNÝCH PARAMETROV NA FÁZOVÉ ZLOŽENIE,
ŠTRUKTÚRNE A MECHANICKÉ VLASTNOSTI HLINITOKREMIČITEJ
KERAMIKY**

**INFLUENCE OF PROCESSING PARAMETERS ON THE PHASE COMPOSITION,
STRUCTURAL AND MECHANICAL PROPERTIES OF ALUMINOSILICATE
CERAMICS**

M. Orlovská¹, P. Veteška¹, Z. Hajdúchová¹, Ľ. Bača¹

¹Oddelenie anorganických materiálov,

Ústav anorganickej chémie, technológie a materiálov,

FCHPT STU, Radlinského 9, 812 37 Bratislava

ABSTRACT

A commercial ceramic body based on a mixture of aluminosilicate raw materials was investigated in order to optimize processing parameters leading to the improvement of final properties of ceramic products. In the second step an addition of Al₂O₃ powder in the amount of 1, 3, 5, 10 and 20 wt. % on the phase composition, open porosity and bending strength was studied. The green bodies of the ceramic samples were prepared from the wet granulate by cold pressing. After that, green bodies were dried and sintered in laboratory furnace and in conventional tunnel kiln. Results showed that bulk density of ceramic samples increased with the compacting pressure as well as with the sintering temperature up to 1450°C. However, applied pressure had almost no effect on bulk density at the temperature of 1550 °C. In the case of ceramic samples sintered at 1275°C in tunnel kiln, the highest values of the bending strength were observed for samples with the 3 and 10 wt. % addition of aluminium oxide. X-ray diffraction analysis showed that with the increasing amount of Al₂O₃ the intensity of mullite as well as corundum phase increases.

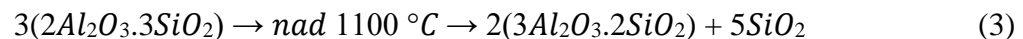
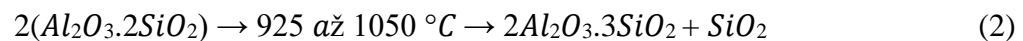
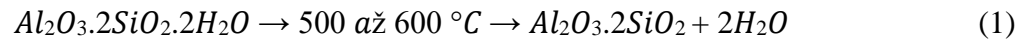
Keywords: ceramics, aluminium oxide, aluminosilicate, alumina Al₂O₃, strength

INTRODUCTION

For the production of traditional ceramics mainly natural raw materials are utilized, whereas technical ceramics use a mixture of natural and synthetic materials or only synthetic raw

materials. Synthetic precursors allow maintaining constant properties and their adjustment, while the main advantage of natural raw materials is their price [1-4].

In aluminosilicate ceramics the carrier of the main mechanical strength at normal as well as at elevated temperatures is mullite ($3Al_2O_3 \cdot 2SiO_2$). Mullite originates from high temperature reactions between silicon oxide and aluminium oxide. Its excellent high temperature properties (improved thermal shock and thermal stress) are attributed to the low thermal expansion, good strength and interlocking grain structure [5]. The largest use of mullite is the steel industry, where refractoriness, high creep resistance and thermal shock resistance are important. The natural raw materials for mullite are easily obtainable for reasonable price. One of the widely used aluminosilicates natural raw material for mullite based ceramics is kaolin which undergoes several reactions during thermal treatment. In accordance to the Equations 1 – 3, a dehydration of kaolinite to metakaolinite occurs in the first step. Afterwards the intermediate product with defect spinel structure accrues which is then transformed in mullite and cristobalite and/or amorphous phase [6, 7]. The presence of impurities can lower the melting point of the glassy phase, promoting the development of whisker shaped grains of mullite [8].



The amount of SiO_2 in kaolin is much higher than needed for the preparation of mullite ceramics, therefore pure mullite ceramics cannot be fabricated without additional source of aluminium. In the literature several studies can be found, where the alumina [9, 10], aluminium hydroxide [11] or gibbsite [12] was used as the aluminium source. For example, Santos et al. [12] studied thermal phase sequences in gibbsite/kaolinite clay between the temperatures 1000 – 1550°C. They found that content of mullite increases with the temperature, while corundum phase increases only till 1300°C. It was suggested that above this temperature, there is an interaction between multiple high temperature phases.

In the present work, porous mullite ceramics were fabricated from the commercial ceramic body based on a mixture of aluminosilicate raw materials. The effect of processing parameters and alumina addition on the bulk density, apparent porosity, phase composition and mechanical properties was investigated.

EXPERIMENTAL

Green bodies were prepared from commercial aluminosilicate ceramic body and in the second part of the work aluminium oxide was mixed with above mentioned ceramic mass in amount 1, 3, 5, 10, 20 wt. %. Samples were cold pressed, dried and sintered in laboratory furnace and conventional tunnel kiln. Samples without addition of alumina were pressed at 3, 5 and 7 MPa and sintered at temperatures of 1250, 1350, 1450 and 1550 °C in laboratory furnace with holding time of 1 hour. Samples prepared with the addition of alumina were sintered only in tunnel furnace at temperature 1275°C and the shifting time was 45 minutes. The basic properties such as bulk density and apparent porosity of sintered samples were measured according to Archimedes and ISO 5017:2013, respectively. The 3-point bending strength of prisms (120 x 10 x 10 mm) was measured on the Instron electromechanical materials testing system Series 4465 as an average of 10 measurements. The microstructure was characterized by scanning electron microscope HITACHI SU3500 equipped with SE and BSE detectors. The phase composition was investigated by using of X-ray diffraction (STOE Theta-Theta, Germany, Co K α radiation, in the 2 θ range of 10–70°)

RESULTS AND DISCUSSION

The bulk density of the mullite-based ceramics as a function of the applied pressure during cold pressing and sintering temperature is shown in Fig. 1.

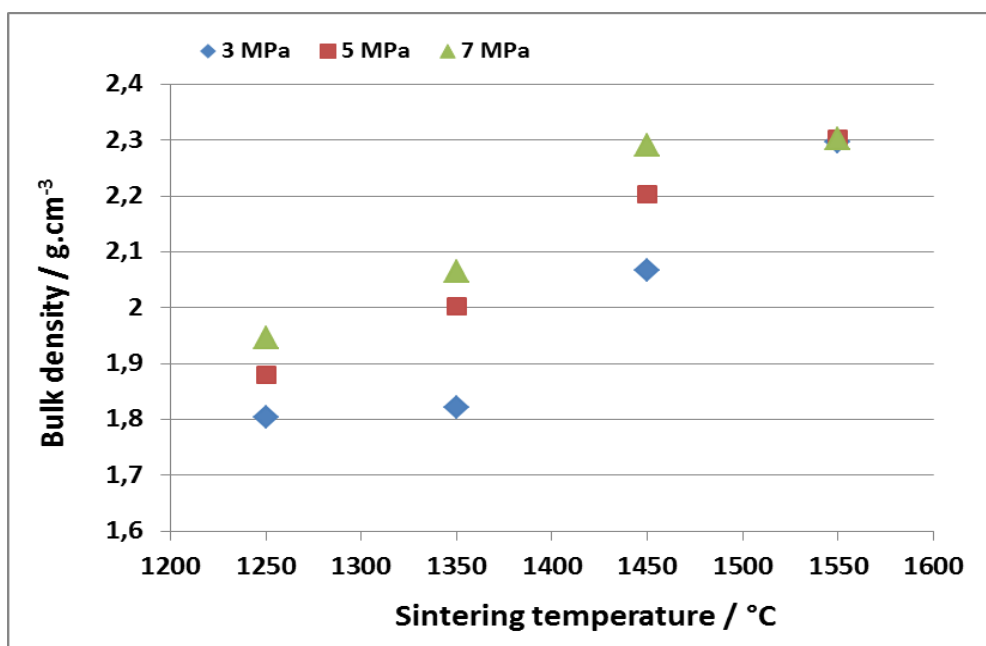


Fig. 1 The bulk density of clay-derived ceramics as a function of applied compacting pressure and sintering temperature

The final density of prepared ceramic samples cannot be calculated solely from theoretical density of mullite as can be seen in Fig. 2, where the XRD patterns show variability in the phase composition as well as in their quantity.

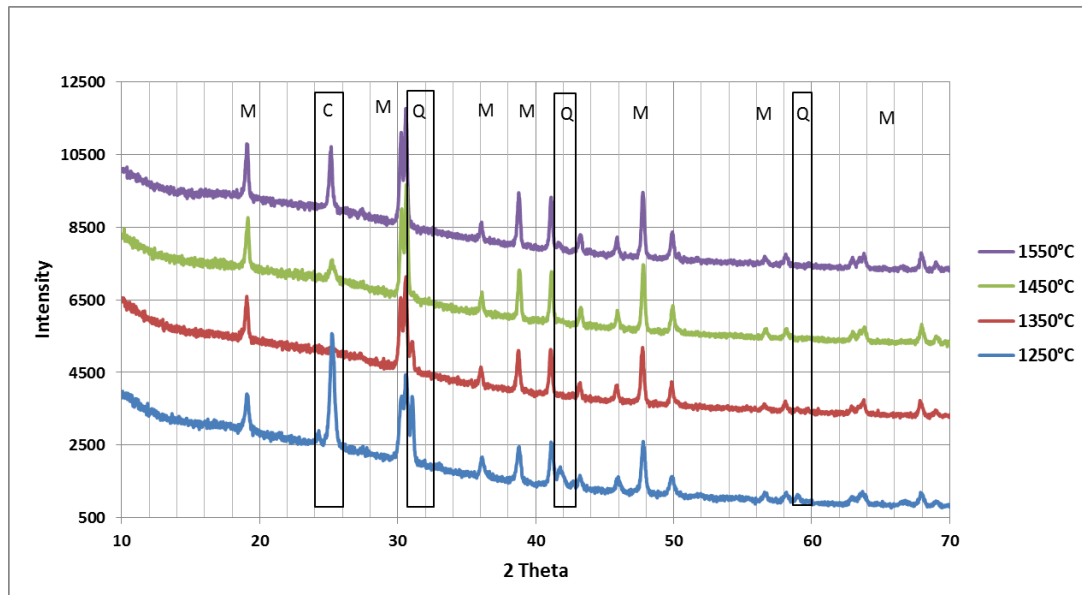


Fig. 2 XRD patterns of the porous clay-derived ceramics prepared at various temperatures; M – mullite, C-cristobalite, Q-quartz

Prepared samples were sintered at various temperatures for 1h and as expected the mullite phase increased with the temperature. The cristobalite together with the mullite and quartz were dominant phases at 1250 °C. At 1350 °C the intensity of quartz phase decreased while cristobalite phase completely disappeared. The rise of temperature to 1450 °C led to the reappearance of cristobalite phase with further increase of intensity at 1550 °C. This sequence in phase composition would indicate the transient dissolution of crystalline SiO₂ and formation of glassy phase. These observations are in agreement with the works of Lee et al. [14] or Rezaie et al. [15]. It is worth noting that mullite observed in vitreous systems is likely to be far from equilibrium especially in the presence of other impurities contained in the clay. It is believed that there is a spread of mullite compositions in vitreous systems across the 2:1 to 3:2 range, in vitreous systems with the exact composition being dependent to large extent on the local liquid phase composition, particularly the availability of Al₂O₃ [16].

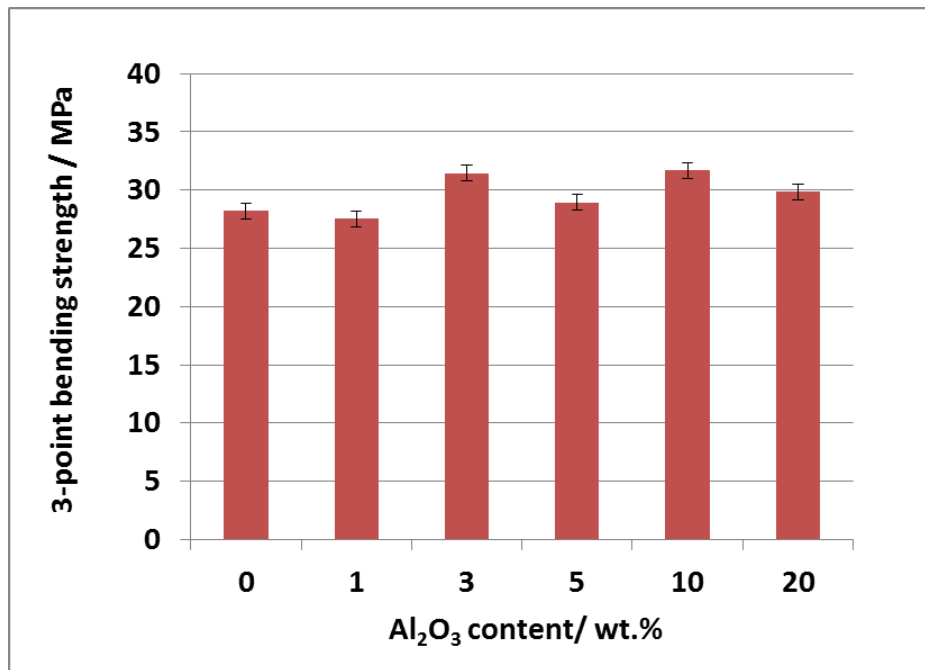


Fig. 3 Three-point bending strength of clay-derived ceramics as function of alumina amount

In the next part of the study the influence of Al₂O₃ amount on the three-point bending strength and microstructure was investigated. It is seen from Fig.3 that average strength of clay-derived samples sintered at 1275 °C in tunnel kiln tends to be higher for samples containing three and more wt. % of Al₂O₃. Average strength of samples with content of alumina higher than 3 wt. % reached values above 30 MPa although with some irregularities. However, the strength of ceramic samples is a statistical quantity with a relative wide scatter due to the low fracture toughness and significant influence of even small pre-existing defects. More pronounced it can be seen in porous samples e.g. in our samples with 5 wt. % of alumina doping the average strength was 28.9 MPa compared to samples with 3 and 10 wt. % of Al₂O₃, where the strength values reached 31.5 and 31.7 MPa, respectively. X-ray diffraction patterns and results of absorptivity tests (not shown here) revealed that the intensity of corundum peaks as well as apparent porosity increases with the alumina doping especially for 5 wt. % and higher. The microstructure analysis of the sample with 5 wt. % of alumina doping is shown in the Fig. 4. The micrograph shows the mullite and partly cristobalite clusters crystallized from glassy-like matrix formed during the firing of clay derived ceramic.

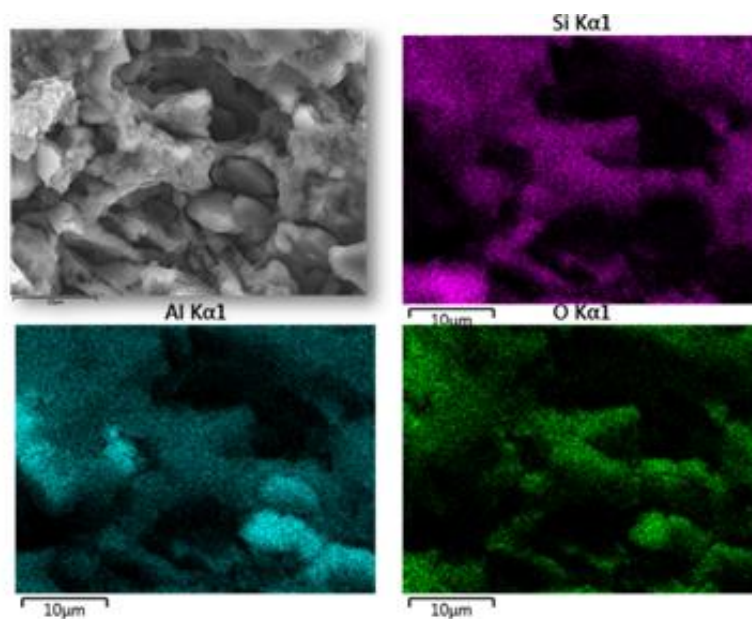


Fig. 4 Mullite and cristobalite clusters of the sample prepared with 5 wt. % of alumina

At the same time clearly visible grains located in a matrix were detected. These grains were characterized by EDX analysis and contained only Al and O elements which indicate the presence of corundum. Matrix was mostly formed by aluminium, silicium and oxygen which belong mainly to mullite phase.

CONCLUSION

In this study a commercial aluminosilicate ceramic material was investigated in order to optimize processing parameters. Results showed that bulk density of ceramic samples increased with the compacting pressure as well as with the sintering temperature up to 1450°C. However, applied pressure had almost no effect on bulk density at the temperature of 1550 °C.

For samples with increasing amount of alumina sintered at 1275°C in tunnel kiln, the highest values of the bending strength were observed for samples with the 3 wt. % and 10 wt. % addition of aluminium oxide. The apparent porosity increases with the alumina content in the samples and the change being more pronounced at alumina levels above 5 wt. %.

Based on these results, the most effective way to enhance the mechanical properties of the studied system is the addition of 3 wt. % of aluminium oxide – the material maintains reasonable low porosity and yields acceptable levels of bending strength.

ACKNOWLEDGMENT

The financial support of this work by the project VEGA 1/0906/17 is gratefully acknowledged.

REFERENCES

- [1] Pokluda, J. et al., *Mechanické vlastnosti a struktura pevných látek*, PC-DIR spol. s.r.o., Brno (1994), ISBN 80-214-0575-9.
- [2] Hlaváč, J., *Základy technologie silikátů*, 2.vydanie, Praha (1988).
- [3] Pánek, Z. et al., *Konštrukčná keramika*, Bratislava (1992).
- [4] *Keramické materiály* [online]. [cit. 2016-08-28]. Dostupné na internete <http://www.ceramtec.cz/ceramic-materials/>.
- [5] H. Schneider et al., Structure and properties of mullite - a review, *J. Eur. Ceram. Soc.* 28 (2) (2008) 329–344.
- [6] Staroň, J., Tomšů, F., *Žiaruvzdorné materiály*, Banská Bystrica (2000).
- [7] Chen, Y. et al., Phase transformation and growth of mullite in kaolin ceramics, *Journal of the European Ceramic Society* 24, (2004), 2389 – 2397.
- [8] B. M. Kim et al., Mullite whiskers derived from kaolin, *Ceram. Int.* 35 (2009) 579–583.
- [9] Y. F. Chen et al., Effects of Al₂O₃ addition on the phases, flow characteristics and morphology of the porous kaolin ceramics, *Mater. Sci. Eng. A373* (1) (2004) 221–228.
- [10] Y. F. Chen et al., Kinetics of secondary mullite formation in kaolin-Al₂O₃ ceramics, *Scr. Mater.* 51 (2004) 231–235.
- [11] G. Chen et al., Direct preparation of macroporous mullite supports for membranes by in situ reaction sintering, *J. Membr. Sci.* 318 (2008) 38–44.
- [12] Santos, H. de S. et al., Thermal phase sequences in gibbsite/kaolinite clay: electron microscopy studies, *Ceramics International* 31 (2005) 1077-1084.
- [13] J.F. Shackelford and R.H. Doremus (eds.), *Ceramic and Glass Materials: 27 Structure, Properties and Processing*. © Springer (2008), p.28

- [14] W. E. Lee et al., Solid–liquid interactions: the key to microstructural evolution in ceramics, *J. Eur. Ceram. Soc.* 28 (7) (2008) 1517–1525.
- [15] H. Rezaie et al., Mullite evolution in ceramics derived from kaolinite, kaolinite with added α -alumina and sol–gel precursors, *Br. Ceram. Trans.*, 96 (5) (1997), pp. 181-187.
- [16] W.E. Lee et al., Mullite formation in clays and clay-derived vitreous ceramics, *J. Eur. Ceram. Soc.*, 28 (2008), pp. 465-471.

PRÍPRAVA A VLASTNOSTI YB₄-SiC KERAMIKY

PREPARATION AND CHARACTERIZATION OF YB₄-SiC CERAMICS

Z. Kováčová^{1,2}, Ľ. Bača¹, E. Neubauer², M. Kitzmantel²

¹ *Institute of Inorganic Chemistry, Technology and Materials, Faculty of Chemical and Food Technology, Slovak University of Technology, Radlinského 9, 812 37 Bratislava*

² *RHP-Technology GmbH, Forschungs- und Technologiezentrum, A-2444 Seibersdorf, Austria*

ABSTRACT

Pure yttrium tetraboride (YB₄) was successfully synthesized using combined boron carbide/carbothermal reduction method at 1500 °C for 4 hours in vacuum. Obtained YB₄ powder was used for preparation of composites with 20, 30 and 40 wt% of SiC. YB₄ and YB₄-SiC composites were densified using hot-pressing technique and subjected to oxidation tests up to 1650 °C. Weight changes after oxidation were measured and the thickness of formed oxide layer was evaluated by scanning electron microscopy. X-ray phase analysis was used to identify the phase composition of samples after oxidation. Mechanical properties such as hardness, fracture toughness and elastic modulus at room temperature were evaluated.

Keywords: YB₄, YB₄-SiC composites, oxidation

INTRODUCTION

Borides of rare earth (RE) metals are interesting high-temperature materials with curious chemical and structural properties. In spite of this, detailed studies of RE-B systems are rare and there has been very little research into the potential of rare earth metal borides for use as materials for ultra high temperature applications. Many fundamental and potentially useful

properties have not been widely explored. However, they are suitable candidates for application in some extreme environments [1-3].

According to literature [1] an oxidation of YB_4 can be described as two-step process assuming the following reactions:



Y_2O_3 and B_2O_3 formed during oxidation of YB_4 (1) can interact and form YBO_3 and B_2O_3 as described by reaction (2). Despite of relatively low melting point of YBO_3 (1650 °C) and liquidus temperature (1373 °C) of YBO_3 - B_2O_3 from reaction (2) it is believed that YB_4 has great application potential, especially with combination with other additives (mainly non-oxide ceramics) [1].

It has been shown that addition of SiC to ZrB_2 ceramics resulted in significant improvement of sinterability, oxidation resistance and mechanical properties [4]. An exposure of ZrB_2 -SiC composite to an oxidizing environment at elevated temperatures results in formation of layered structure with protective borosilicate glassy layer on the surface.

Regarding several beneficial effects SiC was logical choice to serve as additive to YB_4 in order to study its oxidation behaviour and potential improvement of thermal and mechanical properties.

The present study is focused on the preparation and characterization of YB_4 and YB_4 -SiC composites. Oxidation behaviour of hot-pressed materials was tested up to 1650 °C. Selected mechanical properties of YB_4 and YB_4 -SiC composites were investigated.

EXPERIMENTAL

Commercially available Y_2O_3 (<2 μm, ABCR), B_4C (<4,8 μm, ABCR) and C (<4 μm, Imerys Graphite & Carbon) were used as starting materials.

The YB₄ powder was synthesized via combined boron carbide/carbothermal reduction method according to following reaction:



Powder mixtures were homogenized on rolls in cyclohexane using zirconia balls, dried in evaporator and cold-pressed into discs. Discs were positioned in graphite crucibles coated with BN. The synthesis was performed in gas pressure furnace (FCT, 8307, FPW) in vacuum at 1500 °C. After synthesis, discs were milled in agate mortar into powder and consequently analysed by XRD (Stoe Theta-Theta with Cok α radiation) and SEM (JEOL 6061, FEG – JEOL 7600F).

Commercially available SiC (<0.65 μm , ABCR) was used for the preparation of YB₄-SiC composites. Prepared YB₄ was mixed with 20 wt% (YB₄-20SiC), 30 wt% (YB₄-30SiC) and 40 wt% (YB₄-40SiC) of SiC. Powder mixtures were processed as mentioned before.

Discs with 50 mm diameter were directly hot-pressed (DSP518, Dr. Fritsch Sondermaschinen GmbH, Germany) at 1900 °C for 30 min under vacuum and 30 MPa of applied pressure using graphite die with BN coating. The sintered samples were grinded and then the bulk densities were measured using the Archimedes method in distilled water. Small cylinders with diameter 10 mm were cut out from the hot-pressed discs by electrical discharge machining (EDM) and exposed to oxidation.

Oxidation tests were carried out in a furnace at temperatures 1100°C, 1300°C, 1400 °C, 1500°C and 1650°C for 60 min in stagnant air. The phase compositions of samples were analysed by XRD. The specimen surfaces and microstructure were observed using light microscope (Leica DMI5000 M). Cross-sections of oxidized samples were embedded in polymer matrix, grinded and polished. Oxidation resistance was evaluated according to the mass changes and layer thickness after oxidation.

QNESS Q10 M was used for measuring of Vickers's hardness and also for calculation of fracture toughness values. Young's modulus of materials was determined using ultrasound system Olympus 38DL Plus.

RESULTS AND DISCUSSION

Synthesis of YB₄

The XRD analysis pattern from the combined boron carbide/carbothermal reduction is presented in Fig. 1. Results show that the pure YB₄ was successfully synthesized at selected conditions by combined boron carbide/carbothermal reduction method.

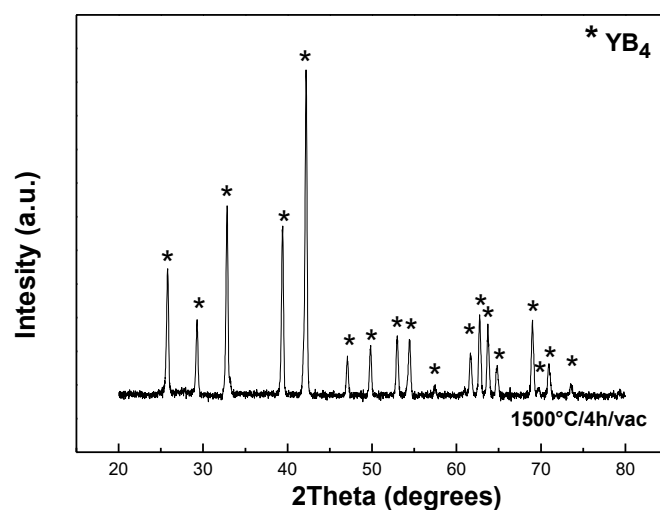


Fig. 1. XRD patterns of powders synthesized according to reaction (3) at 1500 °C for 4 hours in vacuum

Detailed microstructural analysis of as synthesized powder, Fig. 2, revealed equiaxed grains with narrow size distribution around 1-5 μm .

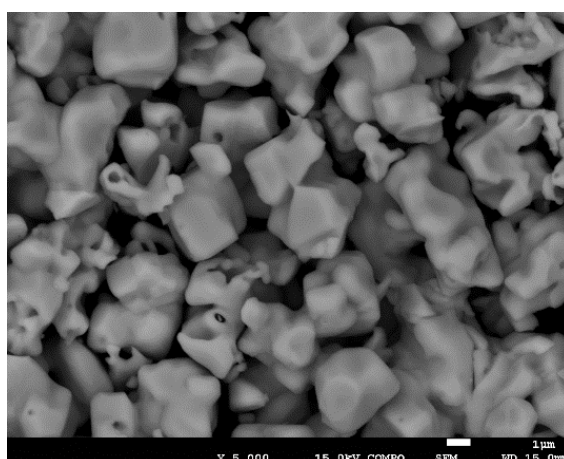


Fig. 2. SEM images of powder synthesized according to reaction (3) at 1500 °C for 4 hours in vacuum

Preparation and characterization of YB₄ and YB₄-SiC composites

Rapid hot-pressing technique was used for densification of YB₄ and YB₄-SiC composites at the same conditions (1900°C/30min/30MPa). All compositions, densities as well as obtained mechanical properties of prepared samples are summarised in Table 1.

| Material | YB ₄ | YB ₄ -20SiC | YB ₄ -30SiC | YB ₄ -40SiC |
|--|-----------------|------------------------|------------------------|------------------------|
| Relative density (%) | 96.3 | 99.6 | 99.8 | 99.3 |
| Vickers hardness HV1 (GPa) | 13.82 ± 0.32 | 17.84 ± 0.13 | 20.09 ± 0.11 | 21.20 ± 0.38 |
| Fracture toughness K _{1c} (MPa.m ^{1/2}) | 3.40 ± 0.24 | 3.46 ± 0.22 | 3.64 ± 0.24 | 4.00 ± 0.25 |
| Young's modulus (GPa) | 343 | 369 | 383 | 388 |

Table 1. Summary of properties of prepared samples hot-pressed at 1900°C/30min/30MPa

Addition of SiC resulted in improved densification of YB₄-SiC composites (>99%) in comparison to the monolithic YB₄ (96.3%). SEM images of YB₄-SiC composites show homogenous distribution of SiC grains (dark) in YB₄ matrix (bright) (Fig. 3). The SiC grains are segregated on the grain boundaries with no evidence of other phases or impurities

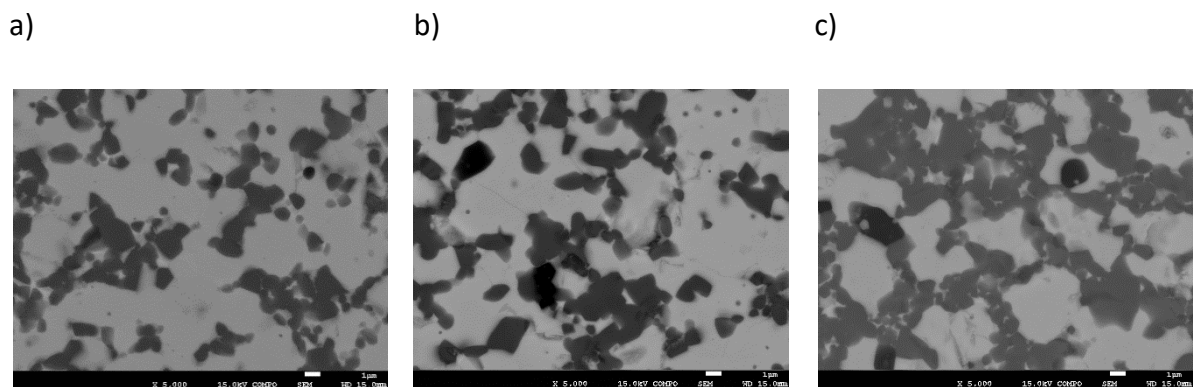


Fig. 3. Microstructure of samples after densification: a) YB₄-20SiC, b) YB₄-30SiC and c) YB₄-40SiC

Vickers hardness of YB₄-SiC composites increases with the increasing amount of SiC though the hardness of pure YB₄ seems to be very low in comparison to the literature data [1, 6]. However, also values of YB₄ hardness reported in the literature differ greatly. Calculated hardness of pure YB₄ was supposed to be 17,04 GPa by Fu et al. [6] whereas experimental value reached 27.40 GPa using 1 kg load [1]. Compared to these values, measured value of YB₄ hardness (13.82 GPa) is significantly lower probably as a consequence of lower density (96.3%). On the other hand, Young's modulus is consistent with calculated value (342 GPa [6]) despite of lower relative density. Indentation fracture toughness of bulk YB₄ reached 3.40 MPa.m^{1/2} and as the content of SiC increased also K_{IC} values were improved. (see Table 1).

Oxidation of YB₄ and YB₄-SiC composites

The effect of oxidation temperature on the specific mass change of tested samples is presented in Fig. 4. Results show that specific weight change was low and slightly negative up to 1300 °C and increased more rapidly above 1400 °C. Increasing SiC content resulted in decreasing specific weight change, especially at higher oxidation temperatures (1500 °C and 1650 °C).

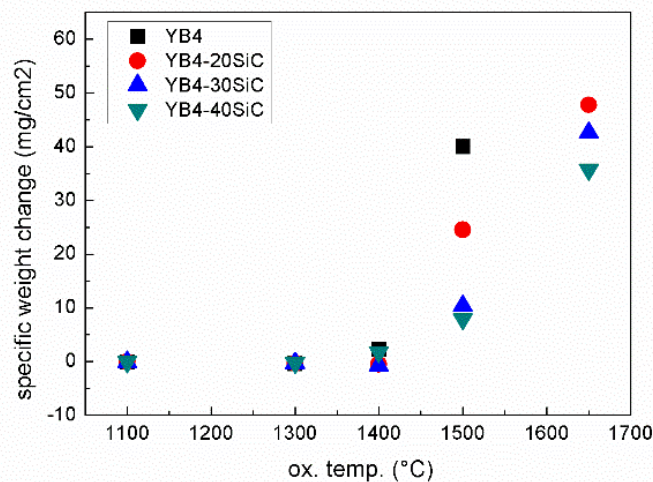


Fig. 4. Mass change vs. oxidation temperature of tested samples

a)



b)

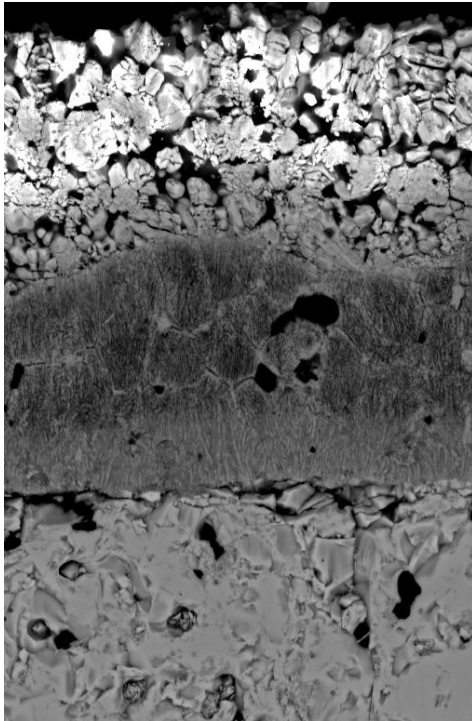


Fig.5. YB₄ sample after oxidation at 1400 °C for 1 hour: a) before spallation, b) after spallation

a) Samples after oxidation were covered by white layer on the surface. However, this layer was not stable and materials have undergone spallations (during preparing of cross-sections – cutting), especially in case of monolithic YB₄ (Fig. 5). Hence direct comparison of thickness of oxidized layers was not possible for evaluation of oxidation resistance of YB₄ and YB₄-

SiC composites at temperatures higher as 1300 °C. Fig. 6 shows cross-sections of YB₄ and YB₄-40SiC samples after oxidation at 1300 °C. Thickness of oxidized layer was 45.1 μm for YB₄ and a little less for YB₄-40SiC, 37.3 μm. The examination of cross-sectioned surface of YB₄-40SiC samples showed that the thickness of layer rapidly increased with oxidation temperature (from 11.5 μm at 1100 C to 810 μm at 1650 °C).

a)



b)

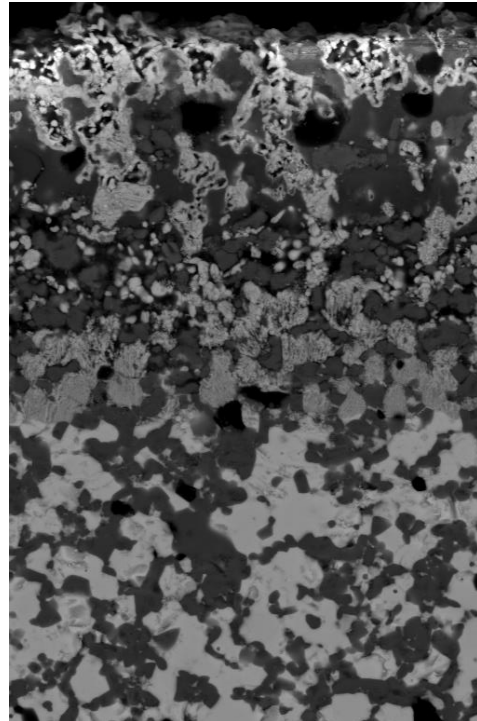


Fig. 6. Cross-sections of a) YB₄ and b) YB₄-40SiC oxidized at 1300 °C for 1 hour

The only crystalline oxidation product of YB_4 identified by XRD was found the YBO_3 (after all oxidation temperatures). Oxidation of YB_4 -SiC led to the formation of several products including YBO_3 , $Y_2Si_2O_7$ and SiO_2 . $Y_2Si_2O_7$ is also reported as refractory phase with strong effect on thermal and mechanical properties [7]. Formation of such phase could have an interesting influence on oxidation behaviour and further investigation is needed.

CONCLUSION

The yttrium tetraboride powder with grain size around 1-2 μm was successfully synthesized by combined boron carbide/carbothermal reduction method without by-products.

Addition of SiC into YB_4 resulted in nearly full densification of YB_4 -SiC composites. Moreover, measured mechanical properties (hardness, fracture toughness and Young's modulus) were superior in comparison to monolithic YB_4 ceramics.

Increasing content of SiC resulted in improvement of oxidation resistance at elevated oxidation temperatures in terms of specific weight change. Oxidation of YB_4 led to the formation of ablative YBO_3 layer on the surface. Due to these spallations the direct comparison of thickness of oxidized layers of the samples was not possible for evaluation of oxidation resistance.

REFERENCES

- [1] Zaykoski, J. A., Opeka, M. M., Smith, L. H., Talmy, I. G. Synthesis and characterization of YB_4 Ceramics, *J. Am. Ceram. Soc.*, 2011, p. 4059-4065.5.
- [2] Li, J., Peng, A., He, Y., Yuan, H., Guo, Q., She, Q., Zhang, L. Synthesis of Pure YB_4 Powder via the Reaction of Y_2O_3 with B_4C , *J. Am. Ceram. Soc.*, 2012, p. 2127-2129.
- [3] Guo, Q., Xiang, H., Sun, X., Wang, X., Zhou, Y. Preparation of porous YB_4 ceramics using a combination of in-situ borothermal reaction and high temperature partial sintering, *J. Eur. Ceram. Soc.*, 2015, p. 3411-3418.
- [4] Eakins, E., Jayaseelan, D.D., Lee, W.E. Toward oxidation-resistant ZrB_2 -SiC ultra-high temperature ceramics, *Metall. Mater. Trans.*, 42A (2011), p. 878-887.
- [5] Matkovich, V. I. Boron and Refractory Borides, Second edition, Springer - Verlag, 1977, ISBN 978-3-642-66622-3.

- [6] Fu, Y.-Y., Li, Y.-W., Hunag, H.-M. Elastic and dynamical properties of YB₄: First-principles study, *Chin. Phys. Lett.*, 31 (2014), 116201.
- [7] Gmelin Handbook of Inorganic and Organometallic Chemistry, 8th Edition, Springer – Verlag, ISBN 0-387-93604-1.
- [8] Sun, Z., Zhou, Y., Wang, J., Li, M. Thermal Properties and Thermal Shock Resistance of γ -Y₂Si₂O₇, *J. Am. Ceram. Soc.*, 91 (2008), p. 3623-3629.

TRANSPORT PRÁŠKOV POMOCOUCI SEKVENČNE BUDENÉHO KOPLANÁRNEHO BARIÉROVÉHO VÝBOJA

POWDER TRANSPORT USING SEQUENTIALLY PULSED COPLANAR BARRIER DISCHARGE

J. Ráhel', M. Zemánek, M. Ilčíková, R. Zischka

¹*Masaryk University, Department of Physical Electronics, Kotlářská 2, 611 37 Brno*

ABSTRACT

Practical implementation of atmospheric pressure non-thermal plasma activation of fine powder materials requires proper management of its transport through the active plasma zone. We present a new method for the powder transport, which takes advantage from the natural tendency of powders to concentrate outside the microfilament plasma channel. Two new HV electrodes designs were devised and consequently tested. To execute sequential powering, a dedicated rotating switch has been constructed. The paper is focused on technical aspects of the method and outlines the roadmap to its future development.

Keywords: powders, transport, coplanar DBD

INTRODUCTION

Our recent findings on positive effect of atmospheric pressure DBD (dielectric barrier discharge) plasma pre-treatment for the output of fine ceramic powders processing [1,2] and stability of their water dispersions gave rise to new set of practical problems associated with the controlled transport of treated powders through the active plasma zone. Effective plasma treatment requires rather long 10-60 sec contact of powders with the discharge plasma (residence time). This forces us to use only a gentle air flow to carry the treated powders through the active plasma zone. Unfortunately, during the plasma treatment, powder particles are electrically charged, and attracted to the discharge electrode. Almost always the attractive force outgrows the tangential force of the weak air flow. Powder particles become stuck to the surface of electrode, from where they have to be removed mechanically. The layer of adhering powder has a detrimental effect of formation of DBD plasma microchannels. It represents the path of

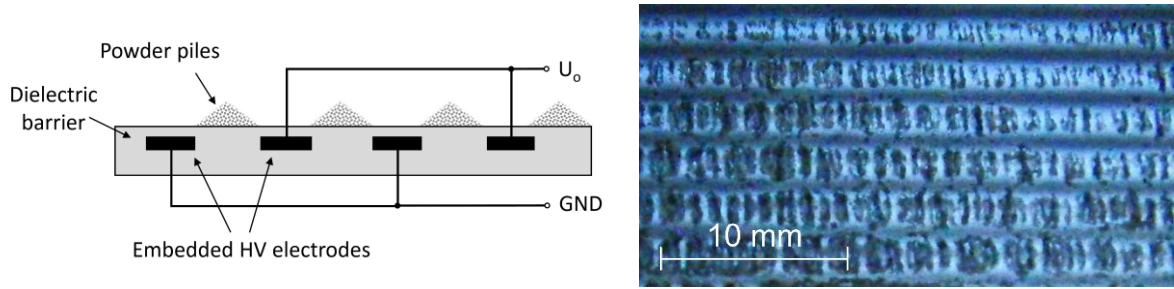


Fig. 1. Schematic cross-section and actual view (Al_2O_3 powder) documenting the piling effect.

higher electrical resistivity, therefore DBD microchannels are starting to form outside the area occupied by piles of adhered powder. The contact of powders with discharge plasma is ceased.

An intriguing phenomenon associated with the use of coplanar geometry type of DBD is that powder piles are formed preferentially in the area above the inter-electrode space. The effect is illustrated in Fig. 1. We suppose that the ‘piling effect’ can be explained by the interplay of at least four distinct factors: (1) specific shape of coplanar DBD plasma microchannels; (2) creation of stationary vertex by plasma microchannels induced ionic wind from opposite directions; (3) ponderomotive force attracting the charged particles to the highest electric field gradient situated above the electrode edges; and (4) piezoelectric vibrations of HV powered DBD electrode dielectrics. The relative importance of the listed factors has not been studied in detail yet. But we expect that their relative importance corresponds well to the respective number of the listing above.

Despite the lack of deeper understanding of the actual mechanism, the piling effect seems to be a general phenomenon. It was observed on all types of tested inorganic and organic powder materials e.g. Al_2O_3 , TiO_2 , SiO_2 , $\text{Na}_2\text{O}_{13}\text{Ti}_6$ or paint pigments. Based on this, we have decided to employ the effect for inducing lateral drift of piled powders along the surface of dielectric electrode. We have extended the number of HV power electrodes and started to sequentially energize only a given electrode pair. By doing so, plasma was incited only at a specific place of discharge area, causing powders to pile up at the corresponding location. By switching to another electrode pair, the place of powder piling should be moved. At optimized conditions, the repetitive shift of piling area should be sufficient to introduce a native unidirectional drift of treated powder material.

EXPERIMENTAL

Two distinct designs of coplanar multiple electrodes were tested. The first one (Fig. 2a) consisted of 3 distinct electrodes interlaced in the pattern of 1-2-3-1-2-3-. We termed this system as ‘3-phase electrode’. The second system (Fig. 2b,c) had the common ground (GND) placed between each of the HV powered electrodes. The electrode pattern can be described as 1-GND-2- GND-3-GND-1- etc. We termed this system as ‘4-phase electrode’

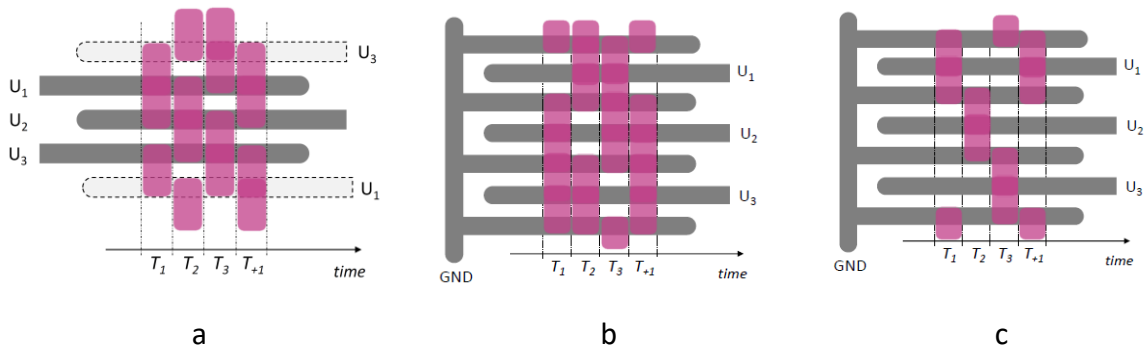


Fig. 2 Schematic of tested electrode designs and electrode energizing pattern.

Discharge plasma between the neighboring electrode pair is incited when, and only when, one of the electrode is connected to HV side of power supply, and the other is grounded. Hence, to achieve a traveling plasma wave in the 3-phase electrode of Fig 2a, we had to sequentially ground one of the electrodes U_1 , U_2 , U_3 , while keeping the rest connected to the HV (or vice versa). Resulting sequence of areas covered by the discharge plasma (pink color) is schematically shown in Fig. 2a.

Sequential grounding was realized by the rotating switch presented in Fig.3. The switch’s stator had three mechanical contacts with the same polar distance from the rotation axis. Along the rotor circumference two electrically non-interconnected metallic pads were mounted. The first pad was connected to the HV output of power supply (Lifetech, 20 kHz, 15 kV_{rms}), the second was grounded. Actual position and size of metallic pads was chosen so that the rotation would cause periodical grounding of respective stator contact, while interconnecting (shortcutting) the two remaining contacts.

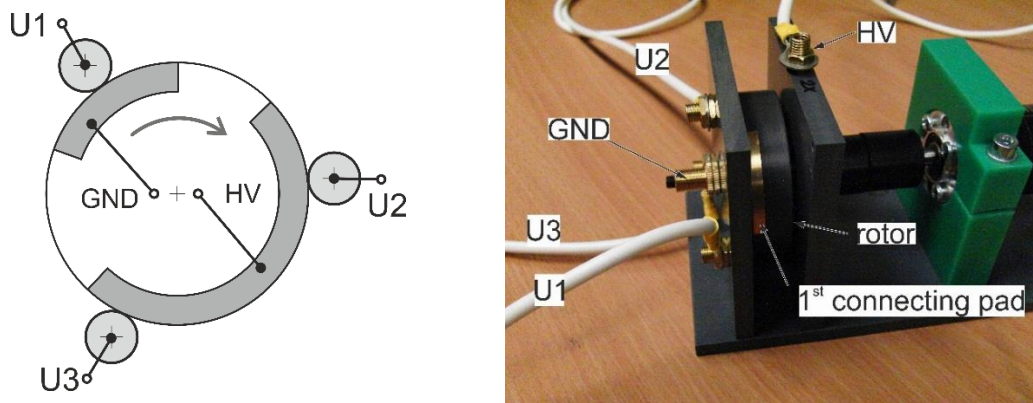


Fig. 3. Schematic wiring and actual view of the rotating switch.

Disconnecting the electrical contact while at the high voltage potential would inevitably cause the arc breakdown and HV power supply malfunction. Therefore, HV voltage had to be always reduced before the rotating switch made its turn off event. The angular position of stator was monitored by the photodiode sensor, which controlled the driving circuit of power supply. Reduction of applied voltage was achieved by switching off the driving frequency. Electrical measurements confirmed that the resulting dumped oscillation in the discharge system was sufficiently fast to provide the required reduction of HV amplitude.

Replacing the rotating switch by a suitable electronic equivalent would allow substantially higher switching frequency and hence the powder transport speed. Unfortunately, the design of 3-phase electrode (Fig. 2a) is difficult to implement electronically, owing to the undesired backward induction to the primary side of HV transformers when the high voltage outputs U_1 , U_2 , U_3 are permanently connected to the discharge electrodes. The 4-phase electrode system, with one additional permanently powered electrode, was used to solve the backward induction problem. Two possible powering patterns were tested, using the same rotating switch of Fig. 3. First pattern was based on alternative grounding of only electrode, while keeping the rest on the high potential (see Fig. 2b). This should form a thin propagating belt without any plasma present. The second pattern (see Fig. 2c) corresponded to the inverse situation. Only one of the electrode was connected to the HV, while the remaining two were grounded (i.e. had the same potential as the additional GND electrode). Technically, the second pattern powering was achieved by flipping over the polarity of metallic pads at the rotor circumference (see Fig. 3). The second powering pattern formed a thin belt of propagating plasma.

RESULTS

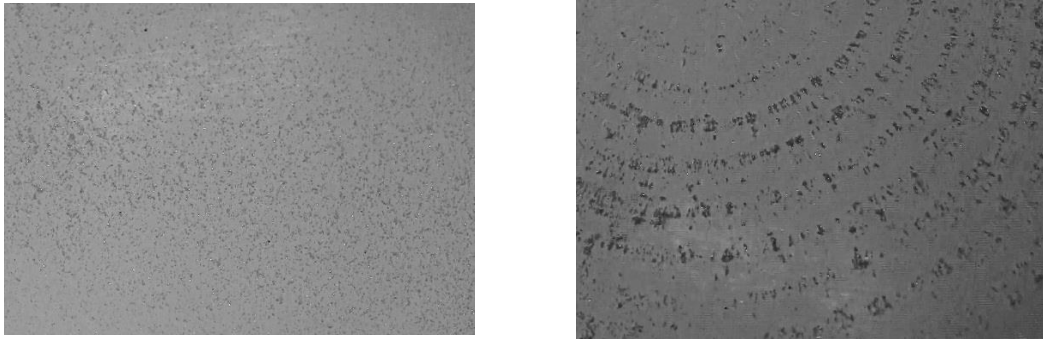


Fig. 4. Initial state of uniformly dispersed glass beads, and the formation of their traveling fronts.

The presence of transport effect will be illustrated by the transport of glass microbeads (ballotini) of 100-200 μm average diameter. The experimental set-up corresponding to Fig. 2a revealed clear traveling wave effect, shown by the snapshots in Fig. 4. A narrow microbeads pile was formed at the outer edge plasma formed region, which upon switching to another electrode pair changed rapidly its position to the new freshly formed region. It was found experimentally, that two conditions had to be met in order to observe strong particles drift. First, the density of dispersed particles has to be less than some critical value. If not, too massive particles pile is formed, which would prevent further discharge formation. The transport effect would be ceased. Second, the frequency of rotation switch has to be adjusted to some resonant one. Experiments with different particles sizes revealed, that the light particles (such as fine ceramic powders) require higher driving frequency. This is due to their higher acceleration obtained by the given plasma impulse. As the result, the ceasing plasma by extensive piling occurs in much shorter times. Faster switching unit is therefore needed to transport fine powders. Before attempting to construct a faster switching circuit we have decided to verify, whether the 4-phase electrode design (required for the fast switching) is able to provide the adequate powder movement, and what powering pattern would offer better results.

The outcome of performed experiment was that the configuration of Fig. 2c is better suited for the glass microbeads transport. The configuration of Fig. 2b created a moving piles of powder medium. These however did not manifest a unidirectional drift. Instead they oscillated around the stable central position. Our analysis suggested, that it is due to the imperfect (non-symmetric) generation of plasma from the opposite edges of the same electrode strip, caused by the spiral electrode geometry which we had adopted (Fig. 5). Still, the oscillating behavior

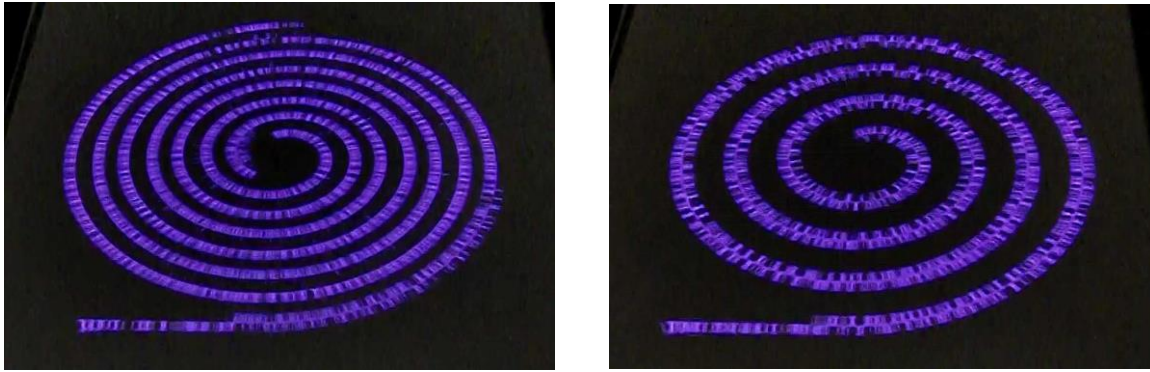


Fig.5. Discharge appearance for energizing pattern of Fig. 2b (left) and Fig.2c (right).

of the powders can be beneficial for better mixing of particles with the active species generated by the plasma treatment.

CONCLUSION

Sequentially pulsed coplanar DBD is able to provide a considerable unidirectional drift to plasma treated powders. Two important constraints were identified: (1) only a thin powder layer can be manipulated; (2) driving frequency has to be matched to the mass of transported powders. The 3-phase electrode system exhibited the strongest transport properties for the tested material. However, its up-scaling to higher speeds is a challenging HV engineering task. Alternative 4-phase system simplifies the design requirements on multiphase HV power supply, while offering still a reasonably strong powder transport. In the tested spiral electrode system sequential powering of just one from all three HV electrodes appears to deliver better results.

ACKNOWLEDGMENT

This work was funded by the Technology Agency of Czech Republic, project no. TACR TE02000011, Czech Science Foundation project no. 17-05620S. The work was supported by project LO1411 (NPU I) funded by the Ministry of Education, Youth and Sports of Czech Republic.

REFERENCES

- [1] Szalay, Z., Bodišová, K., Pálková, H., Švančárek, P., Ďurina, P., Ráhel', J., Zahoranová, A., Galusek, D. Atmospheric pressure air plasma treated alumina powder for ceramic sintering, *Ceramics International*, 40 (8 PART B), (2014), pp. 12737-12743.
- [2] Morávek, T., Ambrico, P. F., Ambrico, M., Schiavulli, L., Ráhel' J. Parametric study of plasma-mediated thermoluminescence produced by Al₂O₃ sub-micron powders. *J. Phys. D: Appl. Phys.*, 50(41), 2017, pp. 415306-41531.

**PRÍPRAVA A CHARAKTERIZÁCIA KERAMICKÝCH A SKLOKERAMICKÝCH
MATERIÁLOV S EUTEKTICKOU MIKROŠTRUKTÚROU V SYSTÉME $\text{Al}_2\text{O}_3\text{-Y}_2\text{O}_3$**

**PREPARATION AND CHARACTERIZATION OF CERAMICS AND
GLASSCERAMICS MATERIALS WITH EUTECTIC MICROSTRUCTURES IN
 $\text{Al}_2\text{O}_3\text{-Y}_2\text{O}_3$ SYSTEM**

J. Valúchová¹, A. Prnová¹, M. Parchovianský¹, R. Klement¹, P. Švančárek¹, Ľ. Hric²,
D. Galusek¹

¹*Vitrum Laugaricio – Joint Glass Center of the IIC SAS, TnU AD, and FCHPT STU,
Študentská 2, SK-911 50 Trenčín, Slovak Republic*

²*Institute of Inorganic Chemistry, Slovak Academy of Sciences, Dúbravská cesta 9,
845 36 Bratislava, Slovak Republic*

ABSTRACT

The glass microspheres with eutectic composition were prepared by combination of modified sol-gel Pechini method and flame synthesis. The prepared glass microspheres were characterized by OM, SEM, X-ray powder diffraction analysis and DSC. Hot-press sintering method at different conditions was used for preparation of bulk ceramic materials. The sintered samples were characterized by SEM, X-ray powder diffraction. The density of prepared bodies was measured using Archimedes method in mercury. Finally, the Vickers hardness and fracture toughness was measured. The highest value of Vickers hardness 18.0 ± 0.7 GPa and fracture toughness 4.9 ± 0.3 MPa.m^{1/2} was achieved for the sample sintered for 30 min at 1600°C, under the pressure of 80 MPa. Very fine-grained microstructures consisting of mutually percolating submicron $\alpha\text{-Al}_2\text{O}_3$ and $\text{Y}_3\text{Al}_5\text{O}_{12}$ grains (“eutectic” microstructure) were observed in the samples sintered at temperatures $\geq 1550^\circ\text{C}$. Preliminary results indicate the possibility of preparation of ceramics materials with very fine (submicron) microstructure by hot-press sintering of glass microspheres.

INTRODUCTION

Rare earth aluminate-based materials with eutectic microstructures represent an interesting approach to ceramics with important mechanical properties (hardness, fracture strength/toughness), thermal stability and creep resistance at elevated temperatures [1]. These properties are attributed to strong eutectic interfaces between present phases and designate these materials for various aerospace (jet aircraft engines) and industrial (high efficiency power generation gas turbines components) applications [2]. Also, the high temperature characteristics of melt-grown eutectic ceramics are linked to the unique microstructures of entangled single crystal phases [3]. A number of works have been published and several groups of eutectic compositions in the systems $\text{Al}_2\text{O}_3\text{-Y}_2\text{O}_3$ and $\text{Al}_2\text{O}_3\text{-Y}_2\text{O}_3\text{-ZrO}_2$ were prepared by using directional solidification methods (e.g. Bridgman method [4], laser floating zone technique [5], laser zone remelting [6], micro pulling down technique [7]) in the form of rods and fibers. However, these methods are time and energy consuming and difficult to fabricate large and complex parts. In order to solving these problems, preparation of eutectic ceramic by indirect methods, using conventional sintering, hot-press or spark plasma sintering (high temperatures and high pressures are required) were described. An alternative route is represented by controlled crystallization of eutectic glasses with eutectic composition [8-11]. The combination of precipitation method and flame synthesis was used for preparation of glass microspheres with eutectic composition in system $\text{Al}_2\text{O}_3\text{-Y}_2\text{O}_3$ in our previous work [12]. The prepared materials were subsequently HP (hot press) sintered at different temperatures and different holding times. IR transparent ceramics and glass ceramics with fine two phase microstructure with Al_2O_3 and YAG phases percolating at submicrometre level and with hardness exceeding 15 GPa resulted from the experiments. In this work, the yttrium-aluminate glass microspheres with eutectic compositions were prepared by combination of sol-gel Pechini [13] method and flame synthesis to achieve a better compositional homogeneity of glass microspheres and improved mechanical properties of final bulk ceramic materials. The prepared glass microspheres were HP sintered at different temperatures, pressures and times. The hardness and fracture toughness of prepared ceramics materials was measured and final microstructures were studied by SEM.

EXPERIMENTAL

Precursor powders containing 60 wt.% (76.8 mol.%) Al_2O_3 and 40 wt.% (23.2 mol.%) Y_2O_3 were prepared by modified Pechini [13] sol-gel method. Aluminium nitrate ($\text{Al}(\text{NO}_3)_3 \cdot 9\text{H}_2\text{O}$; 99.9%;Sigma Aldrich, Germany) was dissolved in deionized water and mixed

with yttrium nitrate solution prepared by dissolution of yttrium oxide (Y_2O_3 ; 99.9%, Treibacher Industry, Austria) in diluted nitric acid. An aqueous solution of citric acid and ethylene glycol in the molar ratio 1:1 was then added. The mixture was refluxed at 85 °C for 2 h and then heated to 150 °C to promote polymerization and to evaporate the solvent. Viscosity of the solution increased rapidly with time until aerated resin was formed. Finally, organic compounds were removed by calcination of the reaction product at 800 °C for 6 h in ambient atmosphere. The narrow fraction obtained by sieving the prepared powder through 40 and 25 μm sieves was used as precursor powders for flame synthesis. The precursor powders were fed into methane-oxygen flame where the powder particles melted. The molten droplets were quenched with de-ionised water, collected and separated. Glass microspheres were dried and calcined at 650°C for 1 h to remove any organic residua. HP experiments were carried out in vacuum under various conditions (pressure 30 and 80 MPa, temperatures 1050°C, 1300°C, 1550°C and 1600°C, dwell times 0 - 30 min). The HP conditions of individual experiments are summarized in Tab.1. The microspheres were characterized by optical microscopy and SEM (JEOL 7600F, at accelerating voltage 20kV). Glass transition temperature T_g and the onset of crystallization temperature T_x were determined using DSC analysis in the temperature range 35-1200 °C and with heating rate of 10°C/min (Netzsch STA 449 F1 Jupiter). Nitrogen atmosphere (5.0 purity) and platinum crucibles with the sample weight of $\approx 15\text{mg}$ were used in the DSC experiments. The phase composition of all three systems, i.e. the precursor powders, the microspheres and bulk hot pressed materials was evaluated by X-ray powder diffraction (Panalytical Empyrean, accelerating voltage 45kV, $\text{CuK}\alpha$ radiation with $\lambda=1.5405\text{\AA}$, 2θ range 20-80°). The diffraction data were evaluated using the software High Score Plus (v.3.0.4, PAN Analytical, The Netherlands) with the use of the Crystallographic Open Database (COD_2013). Hardness and fracture toughness of hot pressed specimens was determined by Vickers indentation (WIKI 200, Lapmaster Wolters, IL, USA) on polished cross sections at 10 N and 100 N loads, respectively. Hot pressed specimens were embedded into polymer resin (Simplimet 1000, Buehler), and polished (Ecomet 300, Buehler), and then the microstructure was examined by SEM. Density of bulk materials was measured by Archimedes method in mercury.

RESULTS AND DISCUSSION

The Al_2O_3 - $\text{Y}_3\text{Al}_5\text{O}_{12}$ eutectic composition (76.8 mol.% of Al_2O_3 and 23.2 mol.% of Y_2O_3) was selected for preparation of glass microspheres as starting material for HP (hot-press) sintering. The narrow fraction (25-40 μm) of sol-gel prepared powders was used for flame synthesis of glass microspheres. The prepared particles were spherical, fully remelted and

transparent. The detail examination of prepared microspheres by SEM revealed the presence of amorphous particles with diameters mainly in the intervals 1-5 μm and 5-10 μm and only small fraction of microspheres with larger diameters 10-20 μm . The amorphous nature of prepared system was confirmed by X-ray powder diffraction analysis. In DSC record of prepared microspheres two exothermic effects were observed: both effects were attributed to crystallization of YAG phase, as was in detail described in our previous work [14]. The glass transition temperature $T_g=890^\circ\text{C}$, onset of crystallization peak temperature $T_{x1}=931^\circ\text{C}$, $T_{x2}=996^\circ\text{C}$ maximum of crystallization peak temperature $T_{p1}=942^\circ\text{C}$, $T_{p2}=1007^\circ\text{C}$ and inflection points $T_{c1}=938^\circ\text{C}$ and $T_{c2}=1003^\circ\text{C}$ of both exothermic effects were determined. Based on these results and the results of HP sintering experiments described in our previous work [12], the conditions of hot-press experiments were determined (Tab.1). The densities of sintered bodies were measured by Archimedes method in mercury and relative density was calculated as a ratio of measured densities and a theoretical density of the eutectic system calculated by the rule of mixtures ($4.42\text{ g}\cdot\text{cm}^{-3}$). Relative densities of all prepared samples were in the interval 95-98%, indicating good sintering ability of prepared glass microspheres under the conditions applied during the experiment (Tab.1). The highest relative density 98.1% was obtained in the sample sintered for 20 min at 1550°C , and 30 MPa applied pressure. The sintered bodies were next studied by X-ray powder diffraction analysis. The presence of YAG as majority crystalline phase was observed in all samples. It is in good agreement with the results our previous works [14, 15], in which the crystallization of YAG (yttrium aluminum garnet) phase was observed in the temperature range ($900\text{-}1200^\circ\text{C}$). Other detected crystalline phases were: yttrium aluminum perovskite (YAP), $\theta\text{-Al}_2\text{O}_3$ and $\alpha\text{-Al}_2\text{O}_3$. The YAP phase is an intermediate phase, which presence is associated with formation of YAG phase in sintered samples; similarly the presence of $\theta\text{-Al}_2\text{O}_3$ is related to formation of $\alpha\text{-Al}_2\text{O}_3$ (at temperatures $\geq 1300^\circ\text{C}$ [14]) in the sintered system. The results of Vickers hardness and fracture toughness measurements of the prepared samples were lower in the samples sintered at lower temperatures and shorter times. In these samples also the presence of intermediate phases (YAP, $\theta\text{-Al}_2\text{O}_3$) was observed, which indicates that the applied conditions were inadequate for formation of YAG and $\alpha\text{-Al}_2\text{O}_3$ as pure phases. In contrast, the samples sintered at higher temperatures $\geq 1300^\circ\text{C}$ show higher values of HV (Vickers hardness) (16-18 GPa) and fracture toughness (4.6-4.9 $\text{MPa}\cdot\text{m}^{1/2}$). Also, only pure YAG and $\alpha\text{-Al}_2\text{O}_3$ phases were detected in these samples. In the samples sintered at higher pressure (80 MPa), higher HV values were observed (≈ 18 GPa), which was associated with microstructure refinement, as confirmed by detailed study of

microstructure by SEM. Fine grained microstructure was observed also in the sample sintered at 1600°C, under 30 MPa pressure without isothermal holding time. Only negligible grain growth was observed during the hot pressing experiments, most likely as the result of percolating microstructure with grains of the two phases mutually impeding their growth. The results indicate the possibility of preparation of ceramic materials with very fine eutectics microstructure and interesting mechanical properties by HP sintering of glass microspheres. However, extensive and systematic HP experiments will be necessary to determine appropriate conditions for further improvement of mechanical properties and for preparation of defect-free eutectic microstructures. Fig.1 shows microstructure of the samples sintered at 1600°C under different hot pressing conditions.

Tab.1 List of performed hot-press experiments.

| <i>Temperature</i> | <i>pressure</i> | <i>Holding time</i> | <i>XRD phase analysis</i> | <i>Measured density</i> | <i>relative density</i> | <i>HV</i> | <i>Fracture toughness</i> |
|--------------------|-----------------|---------------------|--|-------------------------|-------------------------|-----------|---------------------------|
| [°C] | [MPa] | [min] | | [g.cm ⁻³] | [%] | [GPa] | [MPa.m ^{1/2}] |
| 1050 | 80 | 0 | YAG, YAP, θ -Al ₂ O ₃ | 4.20 | 94.9 | 11.3±0.7 | n.m. |
| 1300 | 80 | 30 | θ -Al ₂ O ₃ , YAG | 4.32 | 97.6 | 17.4±1.0 | n.m. |
| 1550 | 30 | 0 | YAG, α -Al ₂ O ₃ | 4.33 | 97.9 | 15.9±0.4 | n.m. |
| 1550 | 30 | 20 | YAG, α -Al ₂ O ₃ | 4.34 | 98.1 | 15.8±0.7 | 4.6±0.2 |
| 1600 | 30 | 0 | YAG, α -Al ₂ O ₃ | 4.29 | 97.1 | 15.1±0.7 | 4.1±0.2 |
| 1600 | 80 | 30 | YAG, α -Al ₂ O ₃ | 4.26 | 96.3 | 18.0±0.7 | 4.9±0.3 |

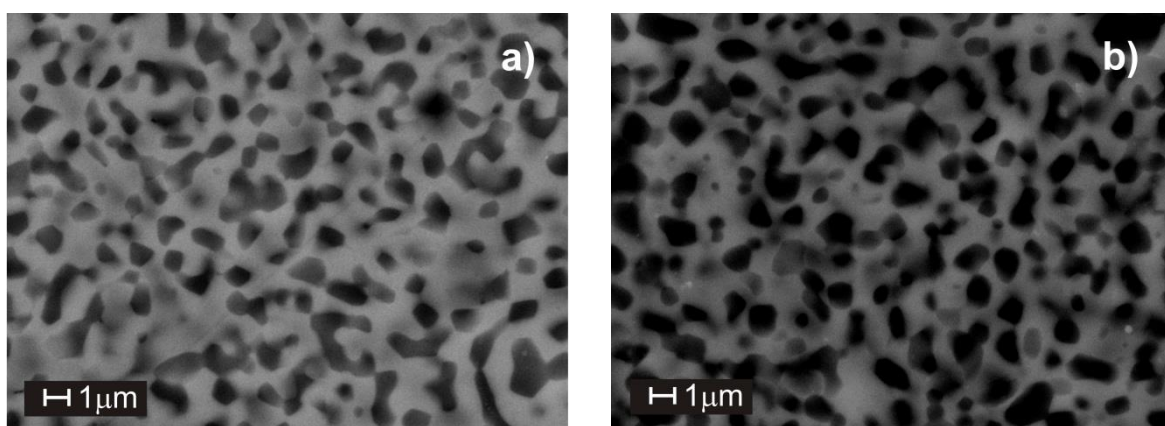


Fig.1 Comparison of microstructures of samples sintered at 1600°C, 80 MPa for 30 min holding time (a), and sample sintered at 1600°C, 30 MPa for without holding time (b)

CONCLUSION

The glass microspheres with eutectic composition were prepared by combination of sol-gel (Pechini) method and flame synthesis. The prepared glass microspheres were hot-press sintered at different conditions. The improvement of mechanical properties was observed with increasing temperature $\geq 1550^{\circ}\text{C}$ and pressure, which can be attributed to formation of pure YAG and $\alpha\text{-Al}_2\text{O}_3$ phases in the samples. Microstructure refinement was observed with application of higher pressure during experiments. The Vickers hardness $\approx 18.0 \pm 0.7$ GPa and fracture toughness 4.9 ± 0.3 $\text{MPa}\cdot\text{m}^{1/2}$ was measured for the sample sintered at 1600°C , at 80 MPa for 30 min. Possibility of preparation of ceramic materials with fine-grained (submicron) microstructure and interesting mechanical properties by hot-press sintering of glass microspheres was confirmed.

ACKNOWLEDGEMENT

The financial support of this work by the project SAS-MOST JRP 2015/6, VEGA 1/0631/14, VEGA 2/0026/17, and APVV 0014-15 is gratefully acknowledged. This publication was created in the frame of the project "Centre of excellence for ceramics, glass, and silicate materials" ITMS code 262 201 20056, based on the Operational Program Research and Development funded from the European Regional Development Fund.

REFERENCES

- [1] Yoshikawa, A., Epelbaum, B.M., Hasegawa, K., Durbin, S.D., Fukuda, T. Microstructure in oxide eutectic fibers grown by a modified micro-pulling-down method, *J.Cryst.Growth.* 205 (1999) 305-316
- [2] Fu, X.S., Fu, L.S., Chen, G.Q., Han, W.B., Zhou, W.L. High temperature deformation of non-directionally solidified $\text{Al}_2\text{O}_3/\text{YAG}/\text{ZrO}_2$ eutectic bulk ceramic, *Ceram. Int.* 43 (2017) 1781-1787
- [3] Waku, Y., Nakagawa, N., Ohtsubo, H., Mitani, A., Shimidzu, K. Fracture and deformation behavior of melt growth composites at very high temperatures, *J. Mater.Sci.*36 (2001) 1585-1594

- [4] U. Buyuk, S. Engin, N. Marasli, Directional solidification of Zn-Al-Cu eutectic alloy by the vertical Bridgman method, *Journal of mining and metallurgy section B-metallurgy*, 51 (2015) 67-72
- [5] Echigoya, J., Takabayashi, Y., Suto, H., Ishigame, M. Structure and crystallography of directionally solidified $\text{Al}_2\text{O}_3\text{-ZrO}_2\text{-Y}_2\text{O}_3$ eutectic by the floating zone-melting method, *Journal of Materials Science Letters*, 5 (1986) 150-152
- [6] Su, H.J., Zhang, J., Ren, Q., Deng, Y.F., Liu, L., Fu, H.Z., Soh, A.K. Laser zone remelting of $\text{Al}_2\text{O}_3/\text{Er}_3\text{Al}_5\text{O}_{12}$ bulk oxide in situ composite thermal emission ceramics: Influence of rapid solidification, *Material Research Bulletin*, 48 (2013) 544-550
- [7] Yoshikawa, A., Epelbaum, B.M., Fukuda, T., Suzuki, K., Waku, Y. Growth of $\text{Al}_2\text{O}_3/\text{Y}_3\text{Al}_5\text{O}_{12}$ eutectic fiber by micro-pulling-down method and its high-temperature strength and thermal stability, *Japanese Journal of Applied Physics*, 38 (1999) L55-L58
- [8] Harada, Y., Uekawa, N., Kojima, T., Koikegawa, K. Fabrication of $\text{Y}_3\text{Al}_5\text{O}_{12}\text{-Al}_2\text{O}_3$ eutectic materials having ultra fine microstructure. *J Eur Ceram Soc.* 28 (2008) 235
- [9] Raj, R., Cologna, M., Francis, JS. Influence of externally imposed and internally generated electrical fields on grain growth, diffusional creep, sintering and related phenomena in Ceramics. *J Am Ceram Soc.* 94 (2011) 1941
- [10] Dianguang, L., Yan, G., Jinling, L., Fangzhong, L., Kai, L., Haijun, S., Yiguang, W., Linan, A., Preparation of $\text{Al}_2\text{O}_3\text{-Y}_3\text{Al}_5\text{O}_{12}\text{-ZrO}_2$ eutectic ceramic by flash sintering. *Scripta Mater.* 14 (2016) 108
- [11] Tarafder, A., Molla, AR., Karmakar, B. Effects of nano-YAG ($\text{Y}_3\text{Al}_5\text{O}_{12}$) crystallisation on the structure and photoluminescence properties of Nd^{3+} - doped $\text{K}_2\text{O-SiO}_2\text{-Y}_2\text{O}_3\text{-Al}_2\text{O}_3$ glasses. *Sol Sci.* 12 (2010) 1756
- [12] Prnová, A., Galusek, D., Hnatko, M., Kozánková, J., Vávra, I. Composites with eutectic microstructure by hot pressing of $\text{Al}_2\text{O}_3\text{-Y}_2\text{O}_3$ glass microspheres, *Ceramics – Silikáty*, 55 (2011) 208-213
- [13] Pechini, M. P., Method of preparing lead and alkaline-earth titanates and niobates and coating method using the same to form a capacitor, U. S. Pat. No. 3 330 697, July 11 (1967)
- [14] Prnová, A., Klement, R., Bodišová, J., Valúchová, J., Galusek, D., Bruneel, E., Driessche, I.V. Thermal behaviour of yttrium aluminate glasses studied by DSC, high temperature X-

ray diffraction, SEM and SEM EDS, J Therm Anal Calorim. (2017) DOI 10.1007/s10973-016-6078-2

- [15] Prnová, A., Plško, A., Valúchová, J., Haladejová, K., Klement, R., Galusek, D. Crystallization kinetics of glass microspheres with YAG (yttrium aluminium garnet) composition. Journal of Thermal Analysis and Calorimetry (2017) DOI: 10.1007/s10973-017-6690-9

PRODUCTION OF HOLLOW GLASS MICROSPHERES FROM WASTE GLASSES BY FLAME SYNTHESIS WITH Na₂SO₄ BLOWING AGENT

J. Kraxner, J. Chovanec, D. Galusek

*Vitrum Laugaricio, Joint Glass Centre of the IIC SAS, TnU AD and FCHFT STU, Trenčín,
911 50, Slovak Republic*

jozef.kraxner@tnuni.sk

ABSTRACT

Hollow glass microspheres (HGMs) are a unique class of materials with number of various applications. The use of HGMs has expanded in last years for their excellent properties. The combination of heat resistance, lightweight and favorable mechanical properties offered by these new materials opens up application in aviation transport and the automotive industry. This paper illustrates the possibility of using recycled glass to obtain hollow glass microspheres with Na₂SO₄ blowing agent. HGMs were prepared from soda lime glasses (automotive glasses) by flame spheroidization process in oxygen-methane (O₂/CH₄) flame. The morphology of the hollow glass microspheres was examined by scanning electron microscopy (SEM) and the composition of the waste glass powders and glass precursor (glass powders with blowing agent) were determined using SEM-EDS. The influence of feed rate of glass precursor on formation of hollow glass microspheres was investigated. The various feed flow rate of automotive glass precursor (particle size 40-63 μm) into the flame yielded different weight fraction (wt.%) conversion to HGMs. In the case of feed rate of 2.3 g/min the conversion to HGMs was 26 wt.% and for the feed rate of 0.5 g/min was up to 48 wt.%.

Keywords: Waste glass, Recycling, Hollow glass microspheres, Blowing agent, Flame spheroidization

INTRODUCTION

Hollow glass microspheres are a low cost but high performance material with a number of various applications. HGMs are desirable in many industries for use as fillers for various organic and inorganic matrices, or can find applications in the medical field, for fabrication of lightweight composite materials, buoyancy materials [1], thermal insulation materials and for gas storage [2, 3]. Reducing the weight of thermoplastics parts has been a high priority objective in various industries such as transportation, aerospace, handheld electronics, and sports and leisure. Automotive plastics have been extensively used for years to replace metal parts and cut

weight to improve Corporate Average Fuel Economy (CAFE) levels, compared to those of generation ago. HGMs are currently used in a variety lightweight automotive applications [4]. Hollow glass microspheres are commercially made in several ways. In one method, HGMs are produced from glass powder obtained by grinding glass cullet, mixed with or contains as part of the composition a blowing agent (e.g., sodium sulfate, sodium selenite, urea), which decomposes at the high-temperature in gas-air flame. As the temperature is quickly raised, the blowing agent decomposes and the resulting gas expands from inside, thus forming HGMs. The HGMs are then quenched with a water spray, carried with the quench water, and collected by flotation. The important primary formation parameters include the powder feed rate, air-to-gas ratio, flame velocity and the length of the flame. The percentage of the blowing agent required is very low, often 0.5-2 % is preferred, depending on the blowing ability [5].

The aim of this present work is to verify the possibilities of flame synthesis for preparation of HGMs with Na_2SO_4 blowing agent from ordinary glass waste from automotive industry (e.g. windshields) with the objective to reuse the automotive waste glass as fillers for composite polymeric materials. .

EXPERIMENTAL

Broken automotive glass from the laboratory was crushed to particle size 0-40 μm . The automotive glass powder mixed with the blowing agent, Na_2SO_4 solution in water (3.2 wt.% of SO_3) has been stirred at room temperature for one hour. The glass precursor (glass powder with blowing agent) was dried in the oven at 80°C. At first, the glass precursor powder was melted in Pt-10%Rh crucible in laboratory furnace with superkanthal heating elements at 1000°C for 5 hours in ambient atmosphere; the heating rate was 10°C/min. Then the melting temperature increased up to 1500°C, using heating rate 15°C/min. The homogeneity was ensured by repeated hand mixing of the melt three times every 10 minutes and the glass melt was poured into deionized water and dried. The dried product was ground and sieved to particle size in the range 40-63 μm , dried at 120°C for 12 h and stored in desiccator. This powder was used as the feed glass precursor to prepare HGMs. The precursor powder was fed into an oxygen-methane (O_2/CH_4) torch with a vacuum powder feeder. Three experiments with different settings were carried out to investigate the influence of feed rate of glass precursor on formation of hollow glass microspheres (Exp.1-2.3g/min, Exp.2-0.9/min, Exp.3-0.5g/min), using oxygen carrier gas. The spherical melt particles were formed in high temperature oxy-methane flame

(estimated temperature 2800°C) and then quenched by spraying by deionized water to form hollow glass microspheres (HGMs). The glass microspheres (solid and hollow) were separated from deionized water by microfiltration through a ceramic filter with pore size <0.3 μm. The solid (SGMs) and hollow (HGMs) glass microspheres were separated by floatation method using deionized water. The surface morphology of glass powder precursor and the microspheres were examined by scanning electron microscopy (SEM JEOL 7600F). Approximately 1 mg of glass powder precursor and HGMs were fixed on a conductive carbon tape, coated with Au-Pd to prevent charging and examined by SEM. The microspheres were also embedded in a polymeric resin, polished cross sections were prepared by EcoMet/AutoMet 300 Grinder-Polisher, and after coating with Au-Pd the details on size and morphology of cavities inside the HGM were obtained by SEM.

RESULTS AND DISCUSSION

The chemical composition of the waste automotive glass powder (before melting process) and feed glass precursor with blowing agent (after melting process) are shown in Table 1. After melting process the SO₃ content in the glass was approximately 0.60 ± 0.07 wt.% and the concentration of Na₂O, too, increased from 12.90 ± 0.08 wt.% to 14.77 ± 0.20 wt.%. SEM images of automotive feed glass precursor and product of SGMs a HGMs are shown in Fig.1.

Table 1: Chemical composition of waste automotive glass and feed glass precursor.

| Oxide | SiO ₂ | Al ₂ O ₃ | CaO | MgO | Na ₂ O | K ₂ O | SO ₃ |
|-------------------------------|------------------|--------------------------------|-------------|-------------|-------------------|------------------|-----------------|
| Before melting process (wt.%) | 73.89 ± 0.19 | 0.82 ± 0.24 | 8.08 ± 0.35 | 3.85 ± 0.14 | 12.90 ± 0.08 | 0.46 ± 0.09 | ----- |
| After melting process (wt.%) | 71.21 ± 0.08 | 0.99 ± 0.04 | 7.98 ± 0.19 | 3.68 ± 0.05 | 14.77 ± 0.20 | 0.34 ± 0.06 | 0.60 ± 0.07 |

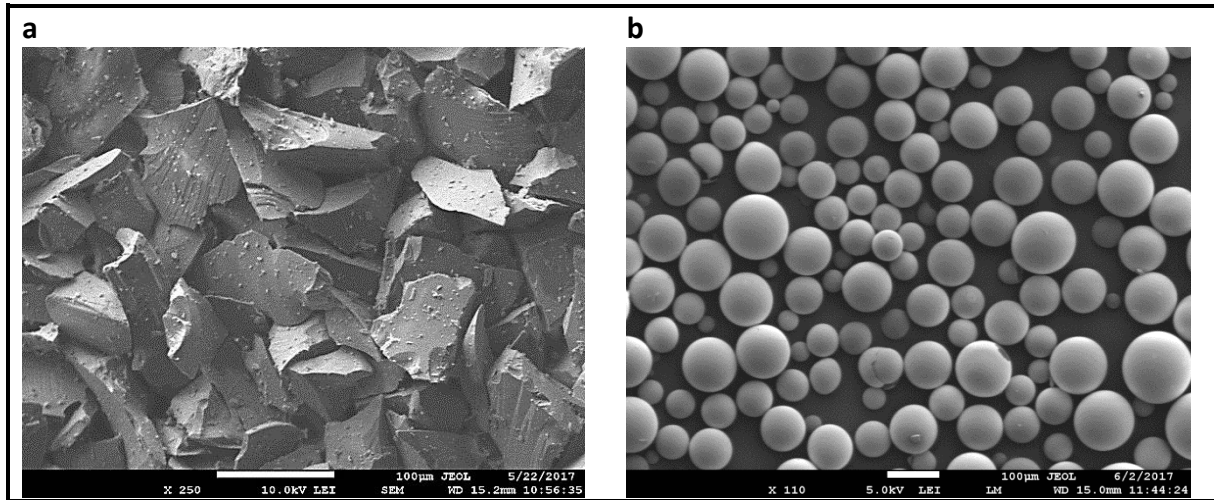


Fig. 1. SEM images of waste glass powder in the range 40-63 μm (a), product of SGMs and HGMs (b).

The influence of feed rate of precursor powders into the flame on formation of hollow glass microspheres (conversion rate to HGMs) is shown in Fig. 2. The feed particle size in the range 40-63 μm and feed flow rate 2.3 g/min was found to give ~ 26% (by weight) of HGMs (Exp.1), 0.9g/min feed rate yielded ~ 42% (Exp.2) and 0.5g/min gave ~ 48% (Exp.3) conversion to hollow glass microspheres. Conversion to HGMs increased when the feed rate was decreased from 2.3 to 0.5g/min. SEM images of the HGMs after separation in deionized water for all experiments (Exp.1, Exp.2 and Exp.3) are shown in Fig. 3.

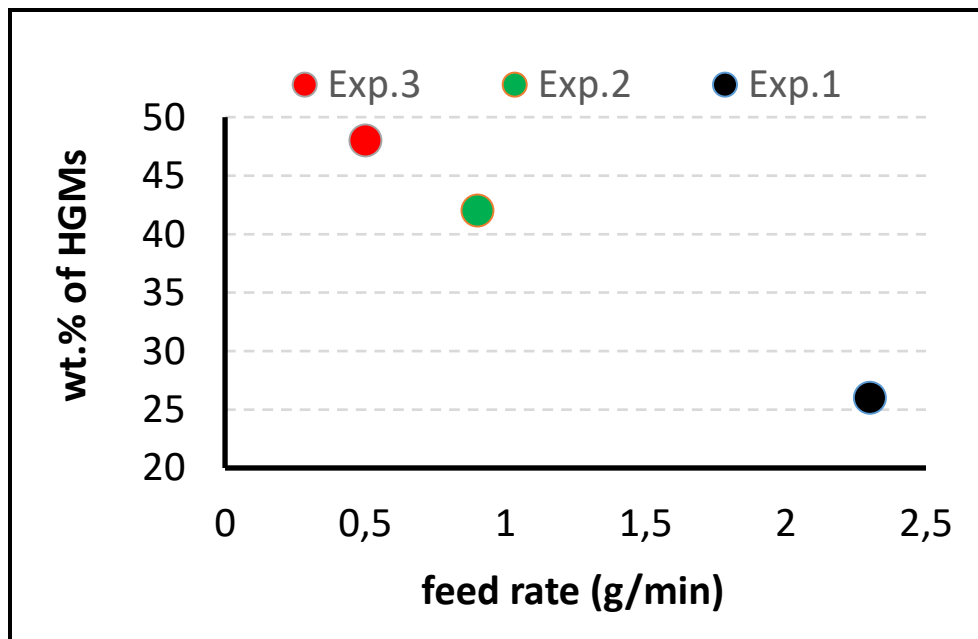


Fig. 2. Feed rate into the flame of precursors on formation to hollow glass microspheres (conversion to HGMs).

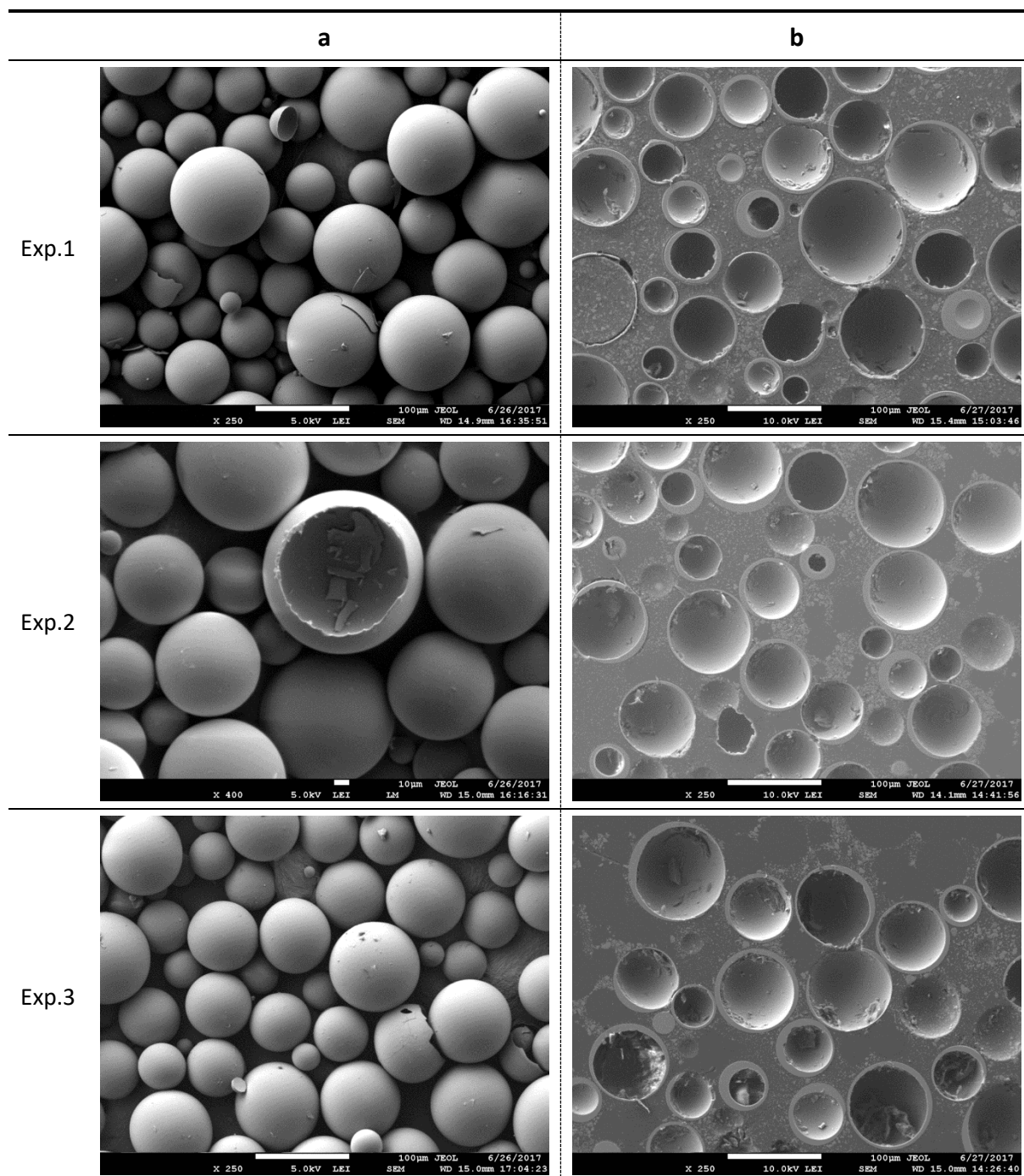


Fig. 3 SEM images of HGMs (a) and cross section of HGMs (b) from experiments (Exp.1, Exp.2, Exp.3).

CONCLUSION

Hollow glass microspheres were successfully prepared from automotive glass frit by flame spraying method in oxygen-methane (O_2/CH_4) flame using sodium sulfate as the blowing agent. During melting of glass powder mixed with blowing agent the sulfate (SO_3) dissolved in

automotive glasses in the amount of approximately 0.60 ± 0.07 wt.%. The conversion to HGMs depends on the feed rate of glass precursors into the flame. By reducing flow rate from 2.3 to 0.5g/min the formation of hollow glass microspheres increased from 26 to 48 wt.%.

ACKNOWLEDGMENT

The financial support by the APVV 0014-15 is gratefully acknowledged. This publication was created in the frame of the project "FUNGLASS" based on the 8th European Framework programme for Research and Innovation HORIZON 2020. This publication was created in the frame of the project "Centre of excellence for ceramics, glass, and silicate materials" ITMS code 262 201 20056, based on the Operational Program Research and Development funded from the European Regional Development Fund.

REFERENCES

- [1] Sue Ren, Anran Guo, et al.: Preparation and characteristic of a temperature resistance buoyancy material through a gelcasting process. *Chemical Engineering Journal* 288 (2016).
- [2] Sridhar Dalai, Pragya Shrivastava, S. Vijayalakshmi, Pratibha Sharma, Adsorption of nitrogen and hydrogen on hollow glass microspheres (HGMs), *Energy Environ. Eng. J.* 1 (2) (2012).
- [3] Hu Yan, Riguo Mei, Zhenguo An, Jingjie Zhang, Silicon rubber/hollow glass microspheres composites: influence of broken hollow glass microsphere on mechanical and thermal insulation property, *Compos. Sci. Technol.* 79 (2013).
- [4] Stephen E Amos, Baris Yalcin, *Hollow Glass Microspheres for Plastics, Elastomers and Adhesives Compounds*. Elsevier 2015.
- [5] Srinidhar Dalai, et al.: Preparation and characterization of hollow glass microspheres (HGMs) for hydrogen storage using urea as a blowing agent. *Microelectronic Engineering* 126 (2014).

**PRÍPRAVA GEHLENITOVÝVH BI DOPOVANÝCH SKLENÝCH
MIKROGULÔČOK REAKCIOU V TUHEJ FÁZE A PLAMEŇOVOU SYNTÉZOU**

**PREPARATION OF Bi-DOPED GEHLENITE GLASS MICROSPHERES BY SOLID
STATE REACTION AND FLAME SYNTHESIS**

M. Majerová¹, R. Klement², A. Prnová², J. Kraxner², D. Galusek²

¹ *Ústav merania, Slovenská akadémia vied, Dúbravská cesta 9, 842 19 Bratislava,*

² *Vitrum Laugaricio, Centrum kompetencie skla, Spoločné pracovisko ÚACh SAV, TnU AD
a FChPT STU, Študentská 2, 911 50 Trenčín*

ABSTRACT

The gehlenite glass microspheres, doped with different concentration of Bi³⁺ ions (0.5, 1, 3 mol. %) were prepared by combination of solid state reaction followed by flame synthesis. The prepared glass microspheres were characterized from the point of view of surface morphology, phase composition, thermal and photoluminescence (PL) properties by optical and SEM microscopy, X-ray diffraction (XRD), differential scanning calorimetry (DSC) and PL spectroscopy. Optical microscopy revealed fully re-melted, spherical and transparent particles. The closer inspection of glass microspheres surface and cross-section morphology by SEM microscopy confirmed smooth surface without any indication of crystal phase embedded in glass matrix and thus amorphous character of prepared glass microspheres. This was further verified by X-ray diffraction, where only broad amorphous background was observed in XRD patterns of all prepared samples. The basic thermal characteristics of prepared glasses, i.e. T_g (glass transition temperature), T_x (onset of crystallization peak temperature), T_f (temperature of the inflection point of the crystallization peak) and T_p (maximum of crystallization peak temperature) were estimated from the DSC records. The PL emission properties of prepared glasses and crystalline analogues (glass crystallized at 1000 °C for 10 h) were studied in the visible and NIR spectral range. When excited at 300 nm, the glasses as well as their crystalline analogues exhibit broad emission in the visible spectral range from 350 to 650 nm centered at about 410-450 nm, corresponding to Bi³⁺ luminescence centres. The emission intensity of crystalline samples were found to be at least 30 times higher than emission of the glass analogues. In addition, the weak emission band was observed around 775 nm under 300 nm excitation. This band is due to the presence of a minor amount of Bi²⁺ species in prepared

samples. In the NIR spectral range, the broad band emission was observed in the spectral range of 1200-1600 nm with the maxima at 1350 nm. The chemistry of Bi and its oxidation state equilibrium in glasses and crystalline matrices is discussed in detail.

Keywords: Gehlenite, Flame synthesis, Glass microspheres, PL properties, Bi³⁺-doped glasses

INTRODUCTION

Since the nineties, the melilite compounds have been intensively studied due to their interesting electrochemical- [1], magnetic- [2, 3], luminescence- [4, 5] and structural-properties [6]. Rare-earth ions doped melilite-type materials representing by gehlenite (Ca₂Al₂SiO₇) have been intensively investigated over the past few decades. For example, gehlenite doped with Nd³⁺ ions is a good candidate for diode pumped laser, with a broad absorption around 806 nm [7]. Ca₂Al₂SiO₇:Eu³⁺, Tb³⁺ as a potential candidate for phosphor converted light-emitting diodes was reported by Yang et al. [8]. Bernardo et al. compared amorphous gehlenite-based Eu³⁺-doped phosphor materials with polycrystalline phosphors of the same composition [9]. It was determined that amorphous phosphor materials contain much more homogenous dopant (or activator), because they have no grain boundaries to accumulate the dopants.

Recently, the optical properties of Bi doped oxide glasses have been intensively investigated [10, 11]. These glasses have some interesting properties, such as simple coloring [12], third order optical non-linearity [13], luminescence in the ultraviolet-visible (UV-VIS) and near-infrared (NIR) spectral range [14, 15].

Bi ion can exist in materials with different valence state, such as 0, +1, +2, +3 and +5. The UV-VIS emissions have been attributed to electronic transition of Bi³⁺ and Bi²⁺. Materials containing Bi³⁺ ions are presented as potential phosphor for display devices, and different magneto-optic devices. Bi²⁺-doped materials are promising novel red phosphors for white light emitting diodes. The origin of NIR emission is still controversial [10].

In this work, we investigated the luminescence properties of Bi₂O₃-doped gehlenite glass microspheres which have been prepared by solid state reaction and flame synthesis, and the influence of crystallization on intensity and wavelength of emitted light in visible and near infra-red spectral range.

EXPERIMENTAL

Powder precursors for flame synthesis were prepared by solid state reaction, from high-purity SiO₂ (p.a., Polske odczynniki chemiczne, Gliwice), Al₂O₃ (p.a., Centralchem, Bratislava), Bi₂O₃ (99,9 %, STREM Chemicals, USA) and CaCO₃ (p.a., Centralchem, Bratislava). The compositions of prepared systems are summarized in the Table 1. At first, suitable amounts of the starting powders were weighed and homogenized in an agate mill in isopropyl alcohol for 4 hours. After drying under infra-red lamp the powders were calcined in a two-step process at 1000°C for 4 hours in air. In the next step the calcined powders were annealed at 1300°C for 4 hours in Pt crucible.

Glass microspheres were prepared from powder precursors by flame synthesis. The powders were fed into CH₄-O₂ flame with the estimated temperature of about 2200°C. The molten particles were quenched by spraying them with distilled water (to achieve a sufficient cooling rate to avoid crystallization), separated and dried. To eliminate any residue from flame synthesis, the glass microspheres were calcined at 650 °C in air for 4 hours.

Primary information on the morphology of prepared microspheres was obtained by optical microscopy (Nikon ECLIPSE ME 600) in transmitted light at 10-50x magnification. More detailed examination of prepared glass microspheres was carried out by scanning electron microscopy (FEG SEM JEOL 7600F) at accelerating voltage 20 kV. The microspheres were fixed on an aluminum sample holder using conductive adhesive graphite tape and sputtered with gold (Carl Zeiss SC 7620 sputter coater) to prevent charging. For the SEM examination of polished cross section of glass microspheres, the microspheres were embedded into polymeric resin (Simplimet 1000, Buehler), carefully polished to prepare cross sections (Ecomet 300, Buehler) and sputtered with carbon to prevent charging.

The differential scanning calorimetry measurements were carried out in the temperature range (30 °C - 1200 °C) with the use of Netzsch STA 449 F1 Jupiter analyser. Nitrogen atmosphere (5.0 purity), heating rate (10 °C/min) and platinum crucibles with the sample mass ≈ 15 mg were used in the DSC experiments.

Phase composition of prepared precursor powders and glass microspheres were studied by X-ray diffraction (Pananalytical Empyrean, CuK α radiation, at ambient temperature in the 2θ range of 10-80°). The software High Score Plus (v. 3.0.4, Pananalytical, The Netherlands) was used to evaluate diffraction data with the use of the COD database. The photoluminescence

spectra were recorded by Fluorolog FL3-21 spectrometer (Horiba Jobin Yvon) using Xe (450W) arc lamp as an excitation source.

The influence of crystallinity on luminescence properties of prepared and crystallized samples was studied and isothermal crystallization experiments at 1000°C for 10 h under ambient atmosphere were performed.

RESULTS

Preliminary inspection of prepared glasses using optical microscopy revealed that the glass microspheres were of spherical shape with diameter up to 25 μm (Fig. 1a). The microspheres were transparent in the visible wavelength region. More detailed examination of prepared micro beads was carried out by scanning electron microscopy. Representative SEM micrographs of microspheres are shown in Fig. 1b, c, d. Amorphous nature of glass microspheres was indicated by their smooth surfaces. SEM micrograph of polished cross section confirmed amorphous character of prepared glass microspheres.

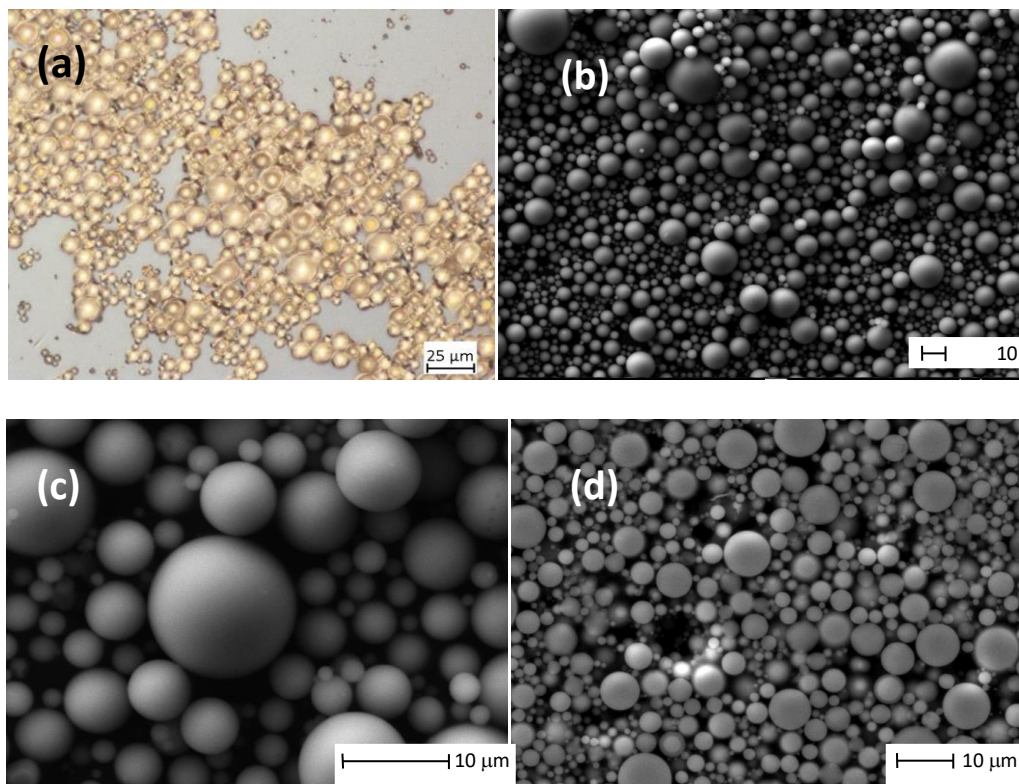


Fig. 1. The results of OM and SEM examination of GBi0.5 sample. Optical micrograph (a), SEM image glass microspheres (b), SEM image detail (c), SEM micrograph of a polished cross section (d)

The phase composition of prepared glass microspheres was identified using XRD, as shown in the inset in Fig. 2. The absence of any crystalline phases and presence of broad amorphous shoulder (in 2θ range 24° - 36°) in XRD patterns confirmed amorphous nature of the prepared microspheres. The XRD patterns of crystallized microspheres (Fig. 2) revealed polycrystalline nature of samples with the presence of gehlenite as a pure phase (01-074-1607 COD) in case of GBi3 and GBi1. In case of GBi0.5, traces of calcium aluminate CaAl_2O_4 (00-034-0440 COD) were also detected.

DSC study of glass microspheres revealed marked differences in thermal behavior of prepared systems. The DSC records of GBi0.5 and GBi1.0 samples contained one narrow exothermic peak centered at $T_p = 996^\circ\text{C}$ and 976°C , respectively. On the contrary, the DSC curve of GBi3.0 sample contained two broad exothermic peaks centered at 884°C and 972°C . The basic thermal characteristics of prepared glasses are summarized in Table 1. In addition, the inflection points of crystallization peaks (T_{f1} , T_{f2}) were determined (the first derivatives of the DSC curves). Observed exothermic effects can be attributed to crystallization processes (based on comparison with reference [16]). The authors reported formation of crystalline gehlenite in the temperature region between 800°C and 1000°C . From comparison of DSC analysis results with XRD patterns of crystallized microspheres, we can conclude that in GBi1.0 and GBi3.0 samples, $\text{Ca}_2\text{Al}_2\text{SiO}_7$ – gehlenite crystallized as the only phase. In case of GBi0.5, XRD analysis indicated presence of another phase, calcium aluminium oxide (CaAl_2O_4). Also, with increasing content of Bi in the samples, a decrease of the onset of crystallization temperature (T_x) and the maxima of the crystallization effects (T_p) (Fig.3) was observed which indicated higher crystallization ability of the GBi3 sample.

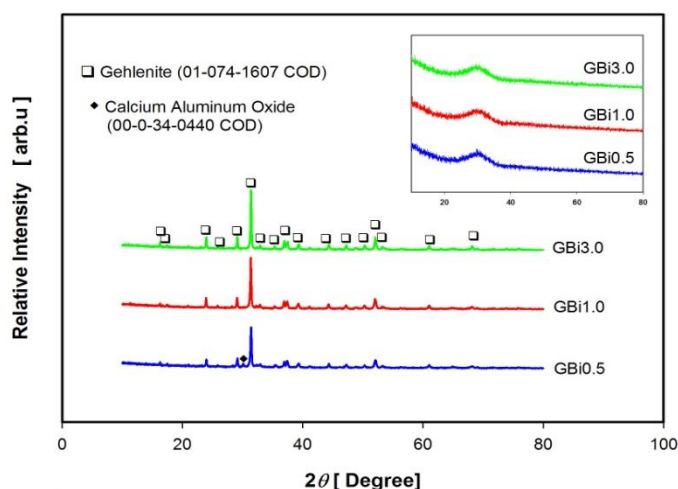


Fig. 2. XRD patterns of crystallized microspheres. The inset shows XRD patterns of Bi doped gehlenite glassy particles after flame synthesis.

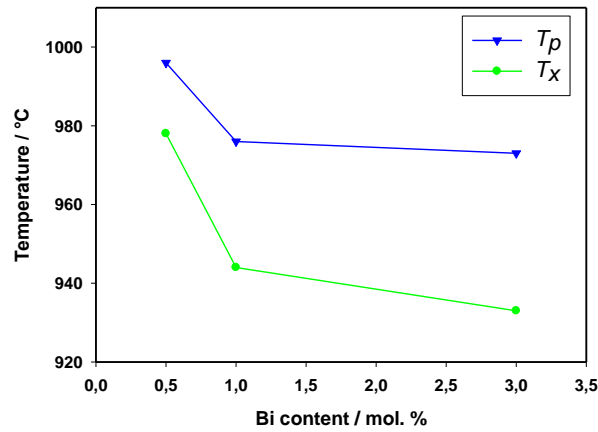


Fig. 3. Decrease of the onset of crystallization peak temperature (T_x) and maxima of the crystallization effects (T_p) with increasing content of Bi in the samples

Tab.1. Composition and basic properties of prepared samples, (T_g - glass transition temperature, T_x - onset of crystallization peak temperature, T_f - temperatures of the inflection points of the crystallization peaks, T_p - maximum of crystallization peak temperature)

| Sample | Mol. % | | | | XRD quality | T_g /°C | T_x /°C | T_{f1} /°C | T_{f2} /°C | T_p /°C |
|--------|--------|--------------------------------|------------------|--------------------------------|-------------|-----------|------------|--------------|--------------|------------|
| | CaO | Al ₂ O ₃ | SiO ₂ | Bi ₂ O ₃ | | | | | | |
| GBi0.5 | 49.76 | 24.88 | 24.88 | 0.5 | amorphous | 838 | 978 | 989 | 1003 | 996 |
| GBi1.0 | 49.5 | 24.75 | 24.75 | 1.0 | amorphous | 728 | 944 | 962 | 990 | 976 |
| GBi3.0 | 48.5 | 24.25 | 24.25 | 3.0 | amorphous | 807 | 862 933 | 872 966 | 890 995 | 884 973 |

The PL emission properties of prepared glasses and crystalline analogues (glass crystallized at 1000 °C for 10 h) were studied in the visible and NIR spectral range. The excitation (PLE) and emission (PL) spectra of prepared samples are shown in Fig.4. Due to the very low PL emission intensity of glasses compared to the polycrystalline samples, the discussion is mainly focused on PL properties of polycrystalline samples.

The Bi³⁺ ion has 6s² electron configuration and thus the ground state is ¹S₀, and 6s6p configuration in the excited state, which gives rise to the triplet levels ³P₀, ³P₁, ³P₂ and singlet state ¹P₁, in order of increasing energy. According to the dipole selection rules, excitations

usually occur from the 1S_0 ground state to the 3P_1 and 3P_1 states [17]. The excitation spectra ($\lambda_{\text{mon}} = 410$ nm) exhibit broad absorption band centered at about 300 nm, corresponding to $^1S_0 \rightarrow ^1P_1$ transition of Bi^{3+} , that is slightly red shifted as the concentration of Bi^{3+} ions increases (from 293 to 303 nm); see Fig. 4a. When excited at 300 nm, the glasses as well as their crystalline analogues exhibit broad emission band in the visible spectral range from 350 to 650 nm centered at about 410–450 nm, corresponding to $^3P_1 \rightarrow ^1S_0$ transition within the Bi^{3+} luminescence centers. Similar broad band emission was observed by Li et al. [18] in charge non-compensated and alkali ion charge compensated Bi^{3+} doped gehlenite, obtained by solid state reaction. The emission intensity of crystalline samples is high and was found to be at least 30 times higher than emission of the glass samples. The PL intensity increases with increasing Bi^{3+} concentration. However, for sample with 3 % of Bi^{3+} the intensity is lowered thus indicating that concentration quenching may operate at this doping level.

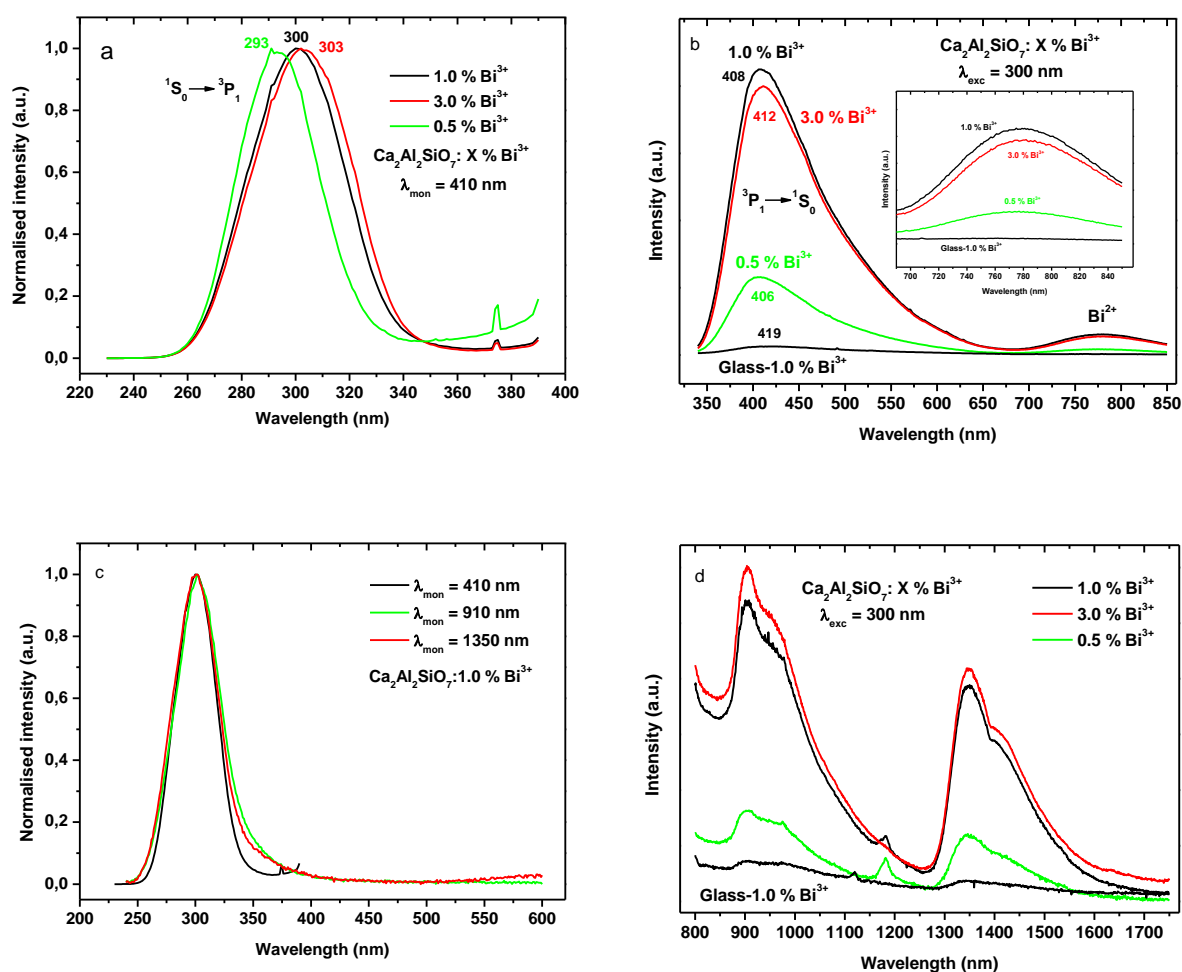


Fig. 4. The photoluminescence excitation - PLE (a, c) and emission - PL spectra (b, d) of Bi^{3+} -doped crystallized microspheres

In addition, the weak emission band was observed around 775 nm under 300 nm light excitation. This band is due to the presence of Bi^{2+} species in prepared samples. The electronic configuration of Bi^{2+} is $6s^26p^1$ with $^2P_{1/2}$ ground state and $^2P_{3/2}$ as the first excited state. This excited state can be further separated by crystal field splitting into two sublevels $^2P_{3/2}(1)$ and $^2P_{3/2}(2)$, in order of increasing energy. In fact, the transition $^2P_{3/2}(1) \rightarrow ^2P_{1/2}$ is responsible for emission that is usually observed in the orange-red spectral range (emission maxima 600-700 nm) [19]. The shift of this emission found in our Bi-doped samples to the deep red spectral range indicates the strong crystal field splitting of the $^2P_{3/2}$ states.

In the NIR spectral region, two broad band emissions were observed in the spectral range of 850-1200 and 1600-1600 nm with the maxima at 905 and 1350 nm, respectively (Fig.4 c,d). The first emission is superposed on the deep red emission originating from $^2P_{3/2}(1) \rightarrow ^2P_{1/2}$ transition of Bi^{2+} ions. The concentration dependence of NIR emission intensity follows the same order as described above for visible range emission. The origin of these NIR emissions is still the matter of dispute, however, many authors ascribe this transition to the lower oxidation state of the bismuth, such as Bi^+ , Bi^0 or cluster ions [20]. Thus it is reasonable to expect that the observed NIR emissions originate from Bi^+ ions incorporated in the gehlenite crystal host.

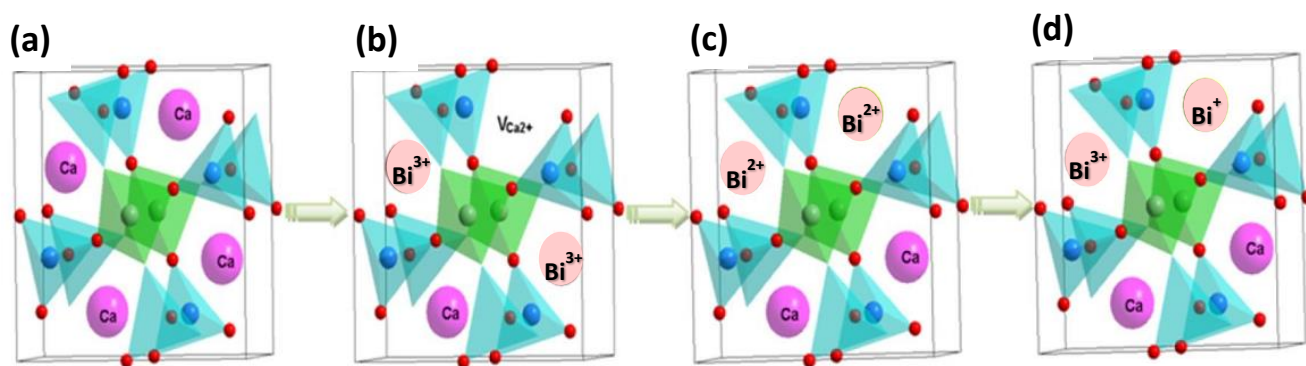


Fig. 5. (a) The $\text{Ca}_2\text{Al}_2\text{SiO}_7$ host structure; (b) the incorporation of the Bi^{3+} ions; (c, d) the incorporation of the Bi^{2+} ions; the incorporation of the Bi^{3+} and Bi^+ ions into the host structure for charge compensation [18].

The structure of gehlenite ($\text{Ca}_2\text{Al}_2\text{SiO}_7$) is schematically depicted in Fig.5a. The Ca atoms are closely surrounded by $(\text{Al}/\text{Si})\text{O}_7$ and AlO_4 polyhedra creating a porous structure. Ca^{2+} in the tetragonal $\text{Ca}_2\text{Al}_2\text{SiO}_7$ is coordinated with eight O^{2-} atoms, forming a distorted polyhedron. When Bi^{3+} is doped into $\text{Ca}_2\text{Al}_2\text{SiO}_7$, it tends to substitute for calcium rather than aluminium or silicon sites as a result of matched ionic size [note: for Bi^{3+} with coordination number (CN)

of 8, $R_{\text{Bi}^{3+}, \text{CN}=8} = 1.17 \text{ \AA}$; and $R_{\text{Ca}^{2+}, \text{CN}=8} = 1.12 \text{ \AA}$; $R_{\text{Al}^{3+}, \text{CN}=4} = 0.39 \text{ \AA}$; $R_{\text{Si}^{4+}, \text{CN}=4} = 0.26 \text{ \AA}$]. There is however the charge imbalance between Bi^{3+} and Ca^{2+} ions. In general, the charge imbalance is induced by creation of internal defect, for instance, negatively charged Ca^{2+} vacancies or positively charged O^{2-} vacancies. These internal structural defects often lead to quenching of luminescence due to the energy transfer from luminescence centers to defects. The Fig. 5b demonstrates such situation, when 3Ca^{2+} ions have been replaced by 2Bi^{3+} ions, resulting in a Ca^{2+} vacancy: $3\text{Ca}^{2+} = 2\text{Bi}^{3+} + \text{V}_{\text{Ca}^{2+}}$. In order to compensate the charge defect, the M^+ ion (e.g. alkali ions Li^+ , Na^+ , K^+) should be introduced as the charge compensation or the Bi^{3+} ions should change its oxidation state to Bi^{2+} and/or Bi^+ (Fig. 5c,d). This is most likely the case in samples studied in this work, as documented by PL emissions originating from three different bismuth sites, Bi^{3+} , Bi^{2+} and Bi^+ , respectively. All three bismuth oxidation states were also observed in PL spectra of the prepared glass samples, however with much lower emission intensity.

CONCLUSION

Three Bi-doped gehlenite precursor powders with different concentration of Bi^{3+} ions (0.5, 1, 3 mol. %) were prepared by a standard solid-state reaction method. X-ray amorphous glass microspheres, with diameters up to 25 μm and transparent in visible light, were then prepared from the precursor powders by flame synthesis. The addition of various amount of Bi has significant effect on the thermal properties of prepared glass microspheres:

1. the onset of crystallization temperature of gehlenite glasses decreases with increasing content of Bi in the samples,
2. apart from the GBi0.5 glass where traces of CaAl_2O_4 were observed, formation of gehlenite as the only crystalline phase was detected in other two compositions,
3. unlike the two compositions with lower Bi contents (0.5 and 1 %) where only one exothermic effect was observed, two exothermic maxima were found on the DSC curve of the GeBi3.0 glass. This behavior, and its relation to structural function of Bi in glass matrix, requires further investigation.

The PL emission properties of prepared glasses and their crystalline analogues (glass crystallized at 1000 $^\circ\text{C}$ for 10 h) were studied in the visible and NIR spectral range. The emission intensity of crystalline samples was found to be at least 30 times higher than emission of the glass analogues. The three types of PL emissions in different spectral regions (visible,

deep red and NIR range) revealed the simultaneous presence of bismuth ions in three oxidation states Bi^{3+} , Bi^{2+} and Bi^{+} , with the last two oxidation states stabilizing the host structure and compensating charge imbalance between the Bi^{3+} and Ca^{2+} ions. This structural arrangement favors replacement of Ca^{2+} in the crystal host and hence, strong luminescence emission from Bi^{3+} .

ACKNOWLEDGMENT

The financial support of this work by the project SAS-MOST JRP 2015/6, VEGA 1/0631/14, and VEGA 2/0026/17 is gratefully acknowledged. This publication was created in the frame of the project "Centre of excellence for ceramics, glass, and silicate materials" ITMS code 262 201 20056, based on the Operational Program Research and Development funded from the European Regional Development Fund.

REFERENCES

- [1] Park, H.J., Kim, T.-G., Kwak, C., Lee, S., Lee, K.H., $\text{Sr}_2(\text{Mg}_{1-x}\text{Ga}_x)\text{Ge}_2\text{O}_{7+0.5x}$: Melilite-type oxygen ionic conductor associated with fivefold coordinated germanium and gallium, *J. Power Sources* 275 (2015) 884-887
- [2] Nöller, R., Knoll, H., Magnetic properties of calcium-silicates (diopside and gehlenite) doped with iron (III), *Solid State Communications* Vol. 47, No. 4 (1983) 237-239
- [3] M. Majerova, A. Dvurecenskij, A. Cigan, M. Skratek, A. Prnova, J. Kraxner, D. Galusek, Magnetic properties of synthetic gehlenite glass microspheres, *Acta Physica Polonica A* 131 (2017) 699-701
- [4] Shi, Y., Zhu, G., Mikami, M., Shimomura, Y., Wang, Y., Color-tunable $\text{LaCaAl}_3\text{O}_7:\text{Ce}^{3+}$, Tb^{3+} phosphors for UV light- emitting diodes, *Materials Research Bulletin*, 48 (2013) 114-117
- [5] Shih, S.J., Lin, Y.Ch., Lin, S.H., Veteska, P., Galusek, D., Tuan, W.H., Preparation and characterization of Eu-doped gehlenite glassy using spray pyrolysis, *Ceramics International* 42 (2016) 11324-11329
- [6] Yahia, H.M., Essehli, R., Belharouak, I., Gaudin, E., Crystal structure and magnetic properties of $\text{K}_2\text{CoV}_2\text{O}_7$, *Materials Research Bulletin*, 71 (2015) 7-10
- [7] Viana, B., Lejus, A.M., Saber, D., Duxin, N., Vivien, D., Optical properties and energy transfer among Nd^{3+} in $\text{Nd}:\text{Ca}_2\text{Al}_2\text{SiO}_7$ crystals for diode pumped lasers, *Optical Materials* 3 (1994) 307-316
- [8] P. Yang, X. Yu, H. Yu, T. Jiang, X. Xu, Z. Yang, D. Zhou, Z. Song, Y. Yang, Z. Zhao, J. Qiu, $\text{Ca}_2\text{Al}_2\text{SiO}_7:\text{Bi}^{3+}$, Eu^{3+} , Tb^{3+} : A potential single-phased tunable-color-emitting phosphor, *Journal of Luminiscence* 135 (2013) 206-210
- [9] E. Bernardo, L. Fiocco, A. Prnova, R. Klement, D. Galusek, Gehlenite: Eu^{3+} phosphors from a silicone resin and nano-sized fillers, *Optical Materials* 36 (2014) 1243-1249

- [10] Liu, J.F., Luminescence properties of bismuth-doped SrO-B₂O₃ glasses with multiple valences state, *Optik* 126 (2015) 4115-4118
- [11] Peng, M., Wondraczek, L., Bi²⁺-doped strontium borates for white-light-emitting diodes, *Optics Letters*, 34 (2009) 2885-2887
- [12] Weyl, W.A., *Coloured glasses*, fifth ed. Society of Glass Technology, Sheffield, 1999
- [13] Lin, G., Tan, D., Luo, F., Chen, D., Zhao, Q., Qiu, J., Linear and nonlinear optical properties of glasses doped with Bi nanoparticles, *Journal of Non-Crystalline Solids*, 357 (2011) 2312-2315
- [14] Xu, W., Peng, M., Ma, Z., Dong, G., Qiu, J., A new study on bismuth doped oxide glasses, *Optics Express*, 20 (2012) 15692-15702
- [15] Dianov, E.M., Nature of Bi-related near IR active centers in glasses: state of the art and first reliable results, *Laser, Physics Letters*, 12 (2015) 095106 (6pp)
- [16] Teixeira, V.C., Montes, P.J.R., Valerio, M.E.G., Structural and optical characterization of Ca₂Al₂SiO₇:Ce³⁺, Mn²⁺ nanoparticles produced via a hybrid route, *Optical Materials* 36 (2014) 1580-1590
- [17] Yousif A., Jafer R. M., Som S., Duvenhage M. M., Coetsee E., Swart H. C., Ultra-broadband luminescent from a Bi doped CaO matrix, *RSC Adv.*, 5 (2015) 54115-54122.
- [18] Li M., Wang L., Ran W., Liu Q., Ren Ch., Jiang H., Shi J., Broadly Tuning emission from Ca₂Al₂SiO₇:Bi phosphor based on crystal field modulation around Bi ions, *New J. Chem.*, 40 (2016) 9579-9585.
- [19] Peng M., Wondraczek L., Orange-to-Red emission from Bi²⁺ and alkaline earth codoped strontium borate phosphors for white light emitting diodes, *J. Am. Ceram. Soc.*, 93 (2010) 1437-1442.
- [20] Peng M., Dong G., Wondraczek L., Zhang L. Zhang N., Qiu J., Discussion on the origin of NIR emission from Bi-doped materials, *J. Non.-Cryst. Solids*, 357 (2011) 2241-2245.

Eu³⁺/Eu²⁺ DOPOVANÉ YTRIUM HLINITANOVÉ SKLÁ A POLYKRYŠTALICKÉ FOSFORY EXCITOVANÉ UV SVETLOM AKO POTENCIÁLNY KANDIDÁTI PRE pc-WLED

Eu³⁺/Eu²⁺ DOPED YTTRIUM ALUMINATE GLASS AND POLYCRYSTALLINE PHOSPHORS EXCITED BY UV LIGHT AS POTENTIAL CANDIDATES FOR pc-WLED

K. Haladejová¹, R. Klement¹, A. Prnová¹, J. Kraxner¹, D. Galusek¹

¹ *Vitrum Laugaricio – Joint Glass Centre of the IIC SAS, TnU AD and FChPT STU, Študentská 2, SK-91150 Trenčín, Slovakia*

ABSTRACT

The Eu³⁺ doped glass in the Y₂O₃-Al₂O₃ system with eutectic composition (76.86 mol. % (60 wt. %) Al₂O₃ and 23.13 mol. % (40 wt. %) Y₂O₃, corresponding to ~50 mol. % of YAG and ~50 mol. % of Al₂O₃) were prepared by flame-spraying synthesis in the form of glass microspheres from precursor powder synthesized by sol-gel method. The doping level ranges from 0.5 to 2.0 at. % of Eu³⁺. The prepared glass microspheres were found to be almost XRD amorphous. The DSC analysis revealed the two exothermic effects corresponding to crystallization of glass at characteristic temperatures. The origin of the two crystallization peaks examined by high temperature XRD (HT XRD) revealed the crystallization of YAG phase (Y₃Al₅O₁₂) up to 1200 °C. The both exothermic effects thus unusually correspond to YAG phase crystallization; the first peak mainly to nucleation and partial crystallization of YAG phase, the second peak to crystal growth of YAG phase. The polycrystalline phosphors were prepared from glass by controlled crystallization at selected time-temperature regime. The photoluminescence (PL) properties of glass and polycrystalline phosphors were studied in detail. In as prepared glass, the both oxidation states of europium, Eu³⁺ and Eu²⁺, were found to coexist in glass matrix. The emission spectra of Eu³⁺ glasses under UV excitation at 393 nm exhibit intensive red emission in the spectral range of 570-720 nm, while Eu²⁺ containing glass (excited at 345 nm) emit the light in broad spectral range from 400-700 nm with the emission maximum at ~520 nm. The PL properties of Eu³⁺/Eu²⁺-doped glass and corresponding polycrystalline phosphors were compared. The prepared phosphors belongs to the family of good candidates for pc-WLED under UV light excitation.

Keywords: photoluminescence, YAG, phosphor, glass, Eu^{3+} , Eu^{2+} , aluminate glass

INTRODUCTION

The spectroscopic properties of phosphors result from the energy diagram of the doping ion (rare earth – RE, transition metal – TM, or others), which is affected by crystal field [1]. Indeed, in certain cases (e.g. Ce^{3+} , Eu^{2+} etc.), the energy levels of particular photoluminescence centre can be effectively tuned by the crystal field strength of a host matrix thus producing the emissions from blue to red spectral range. Luminescent materials are widely applied today and the major applications are in emissive displays and fluorescent lamps [2]. In addition, some X-ray detection systems are based on luminescent materials as well. However, the major trend in recent years is the development of phosphors for applications as new white-light sources based in light-emitting diodes (LEDs), known as solid-state lighting (SSL) systems [1-3].

The yttrium aluminium garnet $\text{Y}_3\text{Al}_5\text{O}_{12}$ (YAG) have been used as a host material for lasers and phosphors for their excellent luminescent properties, remarkable chemical stability at high temperatures, pronounced corrosion resistance, good mechanical properties, and excellent structural compatibility [4,5]. Recently, YAG doped with a small amount of luminescent ions such as Eu, Ce and Tb became widely used as a solid-state optical material in the illumination and display field. For instance, cerium-activated YAG is suitable for converting the blue light into a very broad yellow emission and is used in a white light-emitting diode [6, 7]; furthermore, ytterbium-activated YAG is of interest for diode-pumped solid-state lasers [8] whereas terbium- and europium-activated YAGs are promising green and red phosphors for plasma display panels [9]. However, there is also a great interest in fabrication of transparent YAG ceramics [10-12].

Various methods have been utilized to synthesize YAG-based phosphors. Nevertheless, it is difficult to obtain Eu^{2+} -doped YAG phosphor through conventional methods, such as synthesis under reduction atmosphere, because Eu^{3+} is very difficult to reduce to Eu^{2+} ion in the YAG crystal lattice. On the other hand, the frequently used Eu_2O_3 is very stable and cannot be reduced to Eu^{2+} at low temperatures [13,14].

In this work, we report the preparation of $\text{Eu}^{3+}/\text{Eu}^{2+}$ -doped $\text{Y}_2\text{O}_3\text{-Al}_2\text{O}_3$ glass by combination of the sol-gel method based precursor synthesis and flame spraying technique. The glass and corresponding polycrystalline glass-ceramics were characterized and their thermal, structural, and photoluminescence properties were studied in detail.

EXPERIMENTAL

The yttrium aluminate glass microspheres with composition of Y40A60 doped at different Eu^{3+} concentration level have been prepared from precursor powders by flame spraying technique. Precursor powders were synthesised via sol-gel process employing citric acid as complexing and ethylene glycol as polymerizing agents [15]. Yttrium oxide and europium oxide were individually dissolved in diluted nitric acid. Analytical-grade aluminium nitrate was dissolved in deionized water. The ratio of ethylene glycol to citric acid used in present work was 1:1. Stoichiometric amount of above solutions were mixed and the final solution was initially heated at 85°C in air and continuously stirred for 2 hours, until the solution turned to yellowish sol. Then the sol was heated at 80°C and stirred continually to get sticky gel. The gel was rapidly heated to 120°C and auto-combustion process took place yielding a yellowish fluffy precursor. The precursor was calcined in a resistant heat furnace at 1000°C for 4h in air to remove all organic residue. Finally, the white precursor powders were obtained. The as prepared precursor powders were fed into methane-oxygen flame to melt the particles. The molten glass droplets were quenched with de-ionised water and glass microspheres were collected and separated by rapid filtration. The reduction/oxidation of the glass samples ($\text{Eu}^{3+} \rightarrow \text{Eu}^{2+}$ / vice versa) were carried out in $\text{N}_2:\text{H}_2$ (10 vol. % H_2)/ O_2 atmosphere at $750^\circ\text{C}/24\text{h}$, respectively. The polycrystalline samples were prepared in two steps: first, the glasses were reduced/oxidised in $\text{N}_2:\text{H}_2$ (10 vol. % H_2)/ O_2 atmosphere at $750^\circ\text{C}/24\text{h}$, and than crystallised at $1050^\circ\text{C}/24\text{h}$ in the same atmosphere.

The morphology of prepared glass microspheres was examined by optical (Nicon Eclipse LV100ND) and SEM microscopy (JEOL JSM-7600 F/EDS/EBDS). The composition of the prepared glass was determined using EDS analysis on the polished microspheres cross-section surface; the powder was embedded into a polymeric resin, polished and sputtered by carbon. The glassy character of the prepared glass microspheres and phase composition of polycrystalline samples were confirmed by XRD analysis using the Panalytical Empyrean X-ray powder diffractometer (XRD) with $\text{CuK}\alpha$ -radiation, at ambient temperature in the 2θ range of 10 - 80° . The phase evolution during the glass crystallization process in the temperature range of 600 - 1500°C was studied on the same diffractometer using a high temperature cell Anton Paar HTK16. The thermal properties of prepared glass and their crystallization process were examined using differential scanning calorimetry (DSC) on simultaneous thermal analyser Netzch STA 449 F1 Jupiter (TG/DTA/DSC) at the heating rate of $10^\circ\text{C}/\text{min}$ in the temperature range from 25°C to 1300°C . The photoluminescence steady state (PL) spectra were recorded at

RT on the Fluorolog (FL3-21, Horiba) spectrometer equipped with a 450W xenon lamp as an excitation source. The decay curves were recorded either on phosphorescence module (for Eu^{3+}) or using the TCSPC technique (Time Correlated Single Photon Counting, for Eu^{2+}) on the same spectrometer. The pulsed Xe-lamp or pulsed laser diodes were used as an excitation source.

RESULTS

The composition of the prepared glass was derived from the eutectic composition in the pseudobinary system $\text{Al}_2\text{O}_3\text{-Y}_3\text{Al}_5\text{O}_{12}$ – 60 wt% (76,8 mol%) Al_2O_3 and 40 wt% (23,2 mol%) Y_2O_3 . The glass was doped with small amount of Eu^{3+} ions at the concentration level of 0.5 to 2 at. %. The composition of all prepared aluminate glass is summarized in Table 1.

The obtained glass microspheres were first examined by optical microscopy and SEM (Fig. 1) that revealed spherical particles with diameter ranging from a few to several tens of microns. Closer inspection by SEM shows regular features at the surface of very small portion of microspheres indicating that some of them were at least partially crystalline. The composition of prepared glass determined by SEM-EDS was found to be very close to the theoretical composition (Tab. 1). The SEM-EDS element mapping revealed the homogeneous distribution of Eu^{3+} ions in the samples.

Tab. 1: Composition of prepared glass microbeads.

| SAMPLE | Theoretical composition | | | SAMPLE | EDX determined composition | | |
|------------------|-------------------------|-------------------------|-------------------------|------------------|----------------------------|-------------------------|-------------------------|
| | Y_2O_3 | Al_2O_3 | Eu_2O_3 | | Y_2O_3 | Al_2O_3 | Eu_2O_3 |
| A6Y4Eu0,5 | 76,836 | 22,887 | 0,250 | A6Y4Eu0,5 | 77,2±1,2 | 22,6±0,8 | 0,3±0,1 |
| A6Y4Eu1,0 | 76,836 | 22,637 | 0,500 | A6Y4Eu1,0 | 76,5±1,7 | 22,9±0,8 | 0,5±0,1 |
| A6Y4Eu1,5 | 76,836 | 22,387 | 0,750 | A6Y4Eu1,5 | 76,4±1,1 | 22,8±0,6 | 0,8±0,1 |
| A6Y4Eu2,0 | 76,836 | 22,137 | 1,000 | A6Y4Eu2,0 | 76,4±1,1 | 22,5±0,7 | 1,1±0,1 |

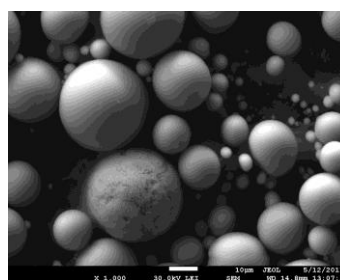
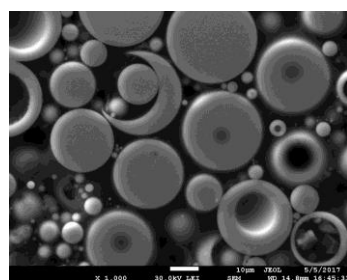


Fig.1: The SEM images of A6Y4Eu1,5 glass microspheres.

The prepared glass microspheres were found to be almost XRD amorphous within detection limit (not shown). When glass microspheres were crystallised at 1050°C/24h, the diffraction patterns of all crystallized samples indicate the presence of only one phase identified as Y₃Al₅O₁₂ (YAG) phase (JCPDS file 33-0040). No other crystalline phases could be detected. The glass thermal properties were examined by DSC analysis. The DSC records of the glass microbeads are shown in Fig. 2. They exhibit two exothermic effects corresponding to crystallization of glass at characteristic temperatures; peak 1: $T_{x1} \sim 920$ °C (onset), $T_{p1} \sim 935$ °C (peak), peak 2: $T_{x2} \sim 990$ °C and $T_{p2} \sim 1000$ °C, respectively. The glass transition temperature (T_g) was found to be in the range 882–902 °C (880 onset, 883 maximum, 902 endset of endothermic effect). It should be noted, that while the first peak temperature is almost the same for all studied samples with different composition, there is a slight temperature shift observed for the second peak. The origin of the two crystallization peaks (exothermic effect) was studied by high temperature XRD (HT XRD) that surprisingly revealed the crystallization of only YAG phase (Y₃Al₅O₁₂) up to the temperature of 1200 °C. The crystallization of α -Al₂O₃ phase was observed at temperatures above 1300 °C. The both exothermic effects in DSC traces thus unusually correspond to YAG phase crystallization; the most probably, the first peak mainly to nucleation and partial crystallization of YAG phase, the second peak to crystal growth of YAG phase.

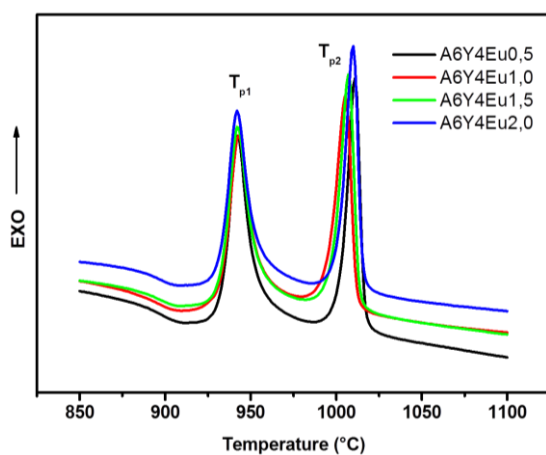


Fig.1: DSC curves obtained from as-prepared glass microspheres.

The emission spectra of as prepared Eu³⁺-doped glass microspheres are presented in Fig. 3a; the samples were excited at 393 nm. The emission bands are relatively broad which indicates that the Eu³⁺ luminescence centres are embedded in the glass or disordered host matrix. The emission lines show the characteristic orange-red peaks of Eu³⁺, corresponding to the intra-configurational parity-forbidden 4f-4f transitions from the excited ⁵D₀ level to the ⁷F_J

($J = 0, 1, 2, 3$ and 4) levels of $4f^6$ configuration. However, an anomaly was observed in the intensity vs. concentration of Eu^{3+} ions in the glass matrix. The emission intensity is almost the same for samples containing 1.0 and 1.5 at. % of Eu^{3+} and then again increases for sample with 2.0 at. % of Eu^{3+} . In case when no concentration quenching operates in studied samples the emission intensity should gradually increase with increasing Eu^{3+} concentration. If the concentration quenching operates, the emission intensity should reach the maximum at specific Eu^{3+} concentration and then decrease with increasing concentration of PL active ions. Moreover, closer inspection of emission spectra at lower wavelength region (400-550 nm) revealed low intense broad emission not associated with Eu^{3+} ions. When the glass was excited by 345 nm excitation light, the very broad emission in range from 400 to 750 nm was observed which is superposed with Eu^{3+} orange-red emission (Fig. 3b). The very broad emission can be assigned to the allowed $4f^65d^1 \rightarrow 4f^7$ transition of Eu^{2+} ions. This leads to the conclusion that there is an equilibrium between Eu^{3+} and Eu^{2+} ions in the as prepared glass microspheres. To suppress the Eu^{2+} oxidation state in europium doped samples, the glass was treated in oxidation atmosphere (O_2) at temperature sufficiently below T_g (at 750°C for 24h) not to promote the glass crystallization. The PL spectra shows similar features as spectra of not treated samples, broader bands typical for Eu^{3+} ions in disordered hosts, however, the emission intensity gradually increases from Eu^{3+} concentration 0.5 at. % up to 2.0 at. %. Therefore, no concentration quenching operates in that Eu^{3+} concentration range of yttrium aluminate glass. The decay curves for the O_2 treated glass samples were recorded under 393 nm excitation while monitoring emission at 613 nm. The decay curves were well fitted with single-exponential decay function with the lifetime of 1.55 ms for all Eu^{3+} concentrations, further indicating that no concentration quenching affect the lifetime of red emission. The polycrystalline phosphors were prepared from the glass by controlled crystallization at $1050^\circ\text{C}/24\text{h}$ in O_2 atmosphere. The PL emission spectra of polycrystalline phosphors (Fig. 3c) are significantly different than those originating from glass samples. The emission lines are very narrow indicating that Eu^{3+} ions are effectively embedded into the YAG crystal host; the Eu^{3+} ions substitute Y^{3+} ions in the YAG crystal lattice. Moreover, the alteration of the emission intensities of $^5\text{D}_0 \rightarrow ^7\text{F}_1$ (induced electric-dipole allowed transition) and $^5\text{D}_0 \rightarrow ^7\text{F}_2$ (induced magnetic-dipole allowed transition) transitions was observed when going from disordered (glass) to ordered (crystal lattice) environment around the Eu^{3+} ions. It is well known, that the local environment around Eu^{3+} does not affect $^5\text{D}_0 \rightarrow ^7\text{F}_1$ PL (independent of local environment), but the probability of $^5\text{D}_0 \rightarrow ^7\text{F}_2$ relaxation strongly depends on ligand symmetry (structural symmetry of the

coordination polyhedra). Thus, the PL integrated intensity ratio of both transitions R ($R = I(^5D_0 \rightarrow ^7F_2)/I(^5D_0 \rightarrow ^7F_1)$), so called asymmetry ratio, can be used as a measure to evaluate the ligand symmetry of the Eu^{3+} sites. In general, a low value of R represents a high ligand symmetry and a low bond covalency of Eu^{3+} sites. The R value for the glass samples was found to be ~ 4.5 , which indicates that Eu^{3+} ions occupy highly non-centrosymmetric sites in the glass. For the polycrystalline samples with $\text{YAG}:\text{Eu}^{3+}$ phase, the R values around 0.6 suggest that Eu^{3+} ions are located in much more symmetric and less covalent coordination environment.

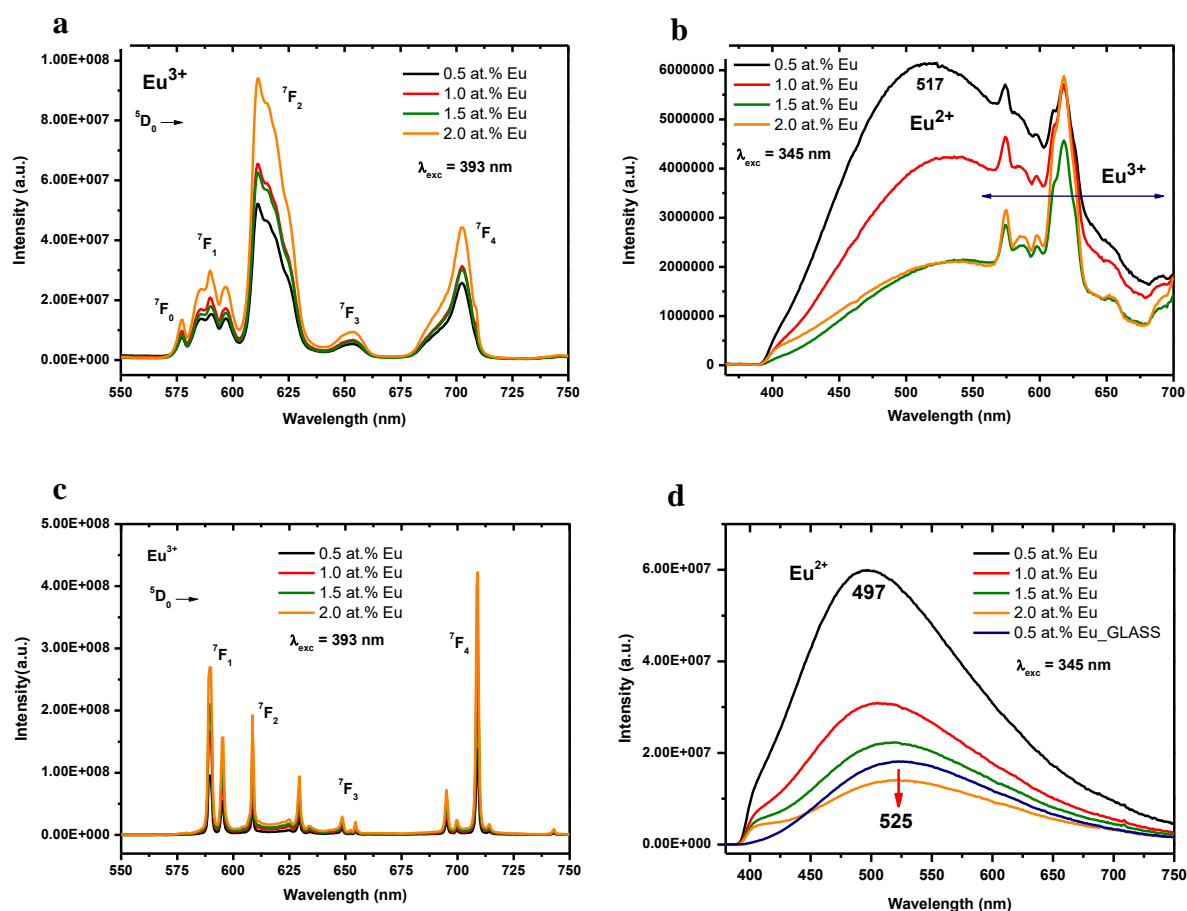


Fig. 2: (a,b) Emission spectra of as-prepared $\text{A6Y4}:\text{Eu}^{3+}/\text{Eu}^{2+}$ glass microspheres. (c) Glass microspheres treated in O_2 atmosphere at $750^\circ\text{C}/24\text{h}$ and crystallised at $1050^\circ\text{C}/24\text{h}$. (d) Glass microspheres treated in $\text{H}_2:\text{N}_2$ (10 v/v % H_2) atmosphere at $750^\circ\text{C}/24\text{h}$ and crystallised at $1050^\circ\text{C}/24\text{h}$

The PL intensity increases with increasing Eu^{3+} concentration similar as for the glass analogues treated in O_2 atmosphere, and no concentration quenching was observed. The decay curves (at excitation 393 nm and 590 nm emission monitoring) were fitted with single-exponential decay function with the lifetime of 3.73 ms for all Eu^{3+} doped samples. These values are somewhat higher than those found for glass samples.

In order to convert the Eu^{3+} ions to Eu^{2+} ions, the glass samples were reduced in the $\text{N}_2:\text{H}_2$ (10 vol. % H_2) atmosphere at $750\text{ }^\circ\text{C}$ for 24h. The polycrystalline samples were prepared from reduced glass ($750\text{ }^\circ\text{C}/24\text{h}$) by crystallization in reduction atmosphere at temperature $1050\text{ }^\circ\text{C}$ and time 24h. However, it should be noted, that even after a long time, the reduction $\text{Eu}^{3+}\rightarrow\text{Eu}^{2+}$ was not complete due to the high stability of the Eu^{3+} ions in the glass and YAG phase, respectively. The emission spectra of the glass and polycrystalline samples are unusually broad with emission ranging from 400 to 750 nm (Fig. 3d). The FWHM (Full Width at Half Maximum) was found to be 170 nm (5885 cm^{-1}) which is one of the highest values reported so far. This broad emission originates from allowed $4f^65d^1 \rightarrow 4f^7$ transition of Eu^{2+} . The maximum emission intensity was observed for the concentration 0.5 at. % of Eu, and with increasing concentration the emission intensity significantly decreases. The same trend was found for polycrystalline samples, but emission intensity was several times (3x for 0.5 at. % Eu) higher than observed for glass analogues at the same Eu concentration. Moreover, after crystallization the emission maximum is significantly blue shifted compared to glass. The luminescence decay obeys two-exponential law with lifetimes decreasing with increasing Eu concentration in the prepared samples (Fig. 4). This decrease is most likely due to the defects that are created in the glass during the reduction and in crystal host as Eu^{2+} ions substitutes Y^{3+} (charge imbalance) in the crystal lattice; energy transfer from Eu^{2+} to defects.

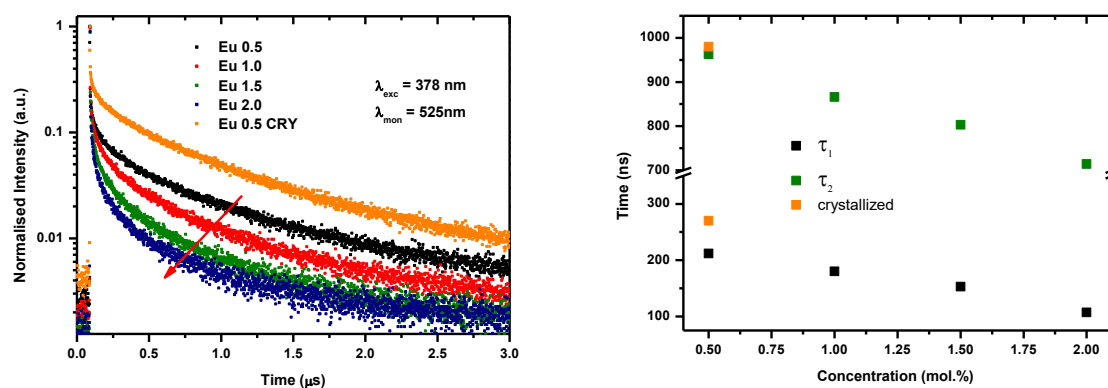


Fig. 4: The decay curves for reduced Eu-doped glass (left) and decay time vs. Eu concentration (right).

To evaluate the material performance on color luminescent emission, CIE chromaticity coordinates were evaluated adopting the standard procedures [16]. In general, the color of any light source can be represented as an (x, y) coordinate in the color space. The chromatic coordinates (x, y) were calculated as follows [17]: $x = X/(X+Y+Z)$ and $y = Y/(X+Y+Z)$ where X ,

X , Y , and Z are defined as $X = \int \bar{x}(\lambda)s(\lambda)d\lambda$; $Y = \int \bar{y}(\lambda)s(\lambda)d\lambda$; $Z = \int \bar{z}(\lambda)s(\lambda)d\lambda$; $\bar{x}(\lambda)$, $\bar{y}(\lambda)$, $\bar{z}(\lambda)$ are CIE x , y and z color matching functions, respectively and $s(\lambda)$ is the spectrum (spectral power distribution) of a light source. The (x, y) values for studied samples were calculated from corrected PL emission spectra under excitation at 345 and 393 nm and selected values are summarised in Fig 5. The values of (x, y) coordinates of samples oxidised in O_2 atmosphere were found to be (0.647, 0.353) for glass and (0.620, 0.379) for polycrystalline analogue at 393 nm excitation and are very close to the “Red” line. These values are comparable with the commercial red phosphors like $Y_2O_3:Eu^{3+}$ (0.645, 0.347) and $Y_2O_2S:Eu^{3+}$ (0.647, 0.343). On the other hand, the reduced samples with 0.5 at. % of Eu emit almost white light under 345 nm excitation; for glass, the emission with greenish hue was observed, while polycrystalline analogue emits almost cold white light.

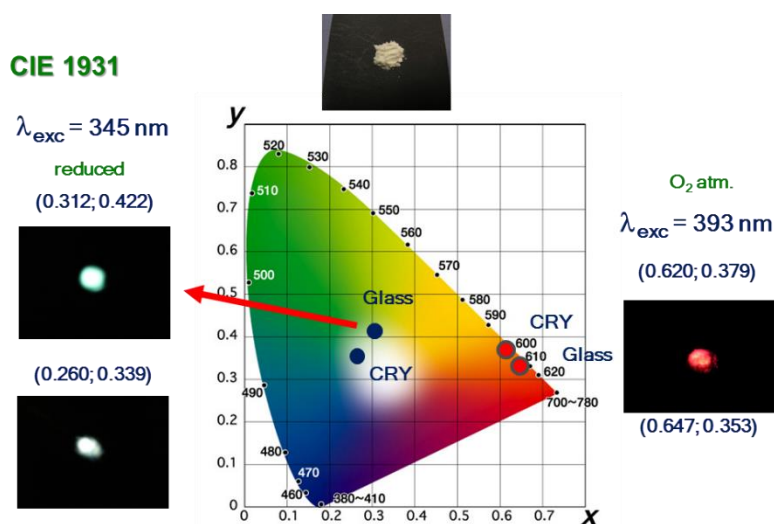


Fig. 5: The CIE 1931 color coordinates of emitted light from samples under UV excitation. The photographs represent the sample in daylight and either reduced or oxidised samples irradiated by UV light 345 and 393 nm, respectively.

CONCLUSION

The Y40A60 phosphors with the coexistence of Eu^{3+} and Eu^{2+} ions have been successfully prepared by flame-spraying technique. The thermal properties were studied by DSC technique and characteristic temperatures have been estimated for two exothermic effects observed in DSC traces. These exothermic effects unusually correspond to YAG phase crystallization. The luminescence spectra of the Eu^{3+} doped glass and crystallized glass show red emission under NUV excitation. The Eu^{3+} decay time values of glass/polycrystalline phosphors were 1,55 and 3,73 ms, respectively. No concentration quenching was observed. Broad emission band in spectral range 400-750 nm with FWHM 170 nm and CIE (0.260, 0.339) –close to white light–

corresponds to Eu^{2+} in glass/polycrystalline materials. Emission intensity/lifetime decreases with increasing Eu^{2+} concentration due to the energy transfer from Eu^{2+} to defects. The prepared materials are very promising candidates for pc-WLED applications.

ACKNOWLEDGMENT

The financial support of this work by the projects SAS-NSC JRP 2015/16 and VEGA 1/0631/14, is gratefully acknowledged. This publication was created in the frame of the project "Centre of excellence for ceramics, glass, and silicate materials" ITMS code 262 201 20056, based on the Operational Program Research and Development funded from the European Regional Development Fund.

REFERENCES

- [1] Ye, S. Xiao, Y.X. Ma, Y.Y. Zhang, QY. Mater. Sci. Eng. R. 71(2010) 1-34.
- [2] Ronda, C.R. Jüstel, T. Nikol, H. J. Alloys. Compd. (1988)669-76275-277.
- [3] Lin, C.C. Liu, R.S. J. Phys. Chem. Lett. 2 (2011) 1268-77.
- [4] Nyen, Y.T. Lu, T.H. Bandi, V.R. Chen, I.G. Microstructure and photoluminescence characterizations of $\text{Y}_3\text{Al}_5\text{O}_{12}:\text{Ce}$ phosphor ceramics sintered with silica, J. Am. Soc. (2012) 1378-82.
- [5] Li, j. Chen, Q. Feng, G.Y. Wu, W.J. Xiao, D.Q. Zhu, J.G. Optical properties of the polycrystalline transparent Nd:YAG ceramics prepared by two-steps sintering, Ceram. Intern. 38 (2012) 649-52.
- [6] Nien, Y.T., Chen, K.M. Chen, G. J. Am. Ceram. Soc. 93 (2010) 1688.
- [7] Yang, H. Zhu, G. Zhang, C. Li, F. Xu, H. Yu, A. J. Am. Ceram. Soc. 95 (2012) 49.
- [8] Rumpel, A. Voss, M. Moeller, M. Habel, F. Moormann, C. Schacht, M. Graf, T. Ahmed, M.A. Optic. Lett.. 37 (2012) 41188.
- [9] Sharma, P.K. Dutta, R.K. Pandey, A.C. J. Nanopart. Res. 14 (2012) 731
- [10] Hreniak, D. Fedyk, R. Bednarkiewicz, A. Streck, W. Lojkowski, W. Opt. Mater. 29 (2007) 1244.
- [11] Lukowiak, A. Wiglusz, R.J. Maczka, M. Gluchowski P. Streck, W. Chem. Phys. Lett. 494 (2010) 279.
- [12] Ikesue, A. Aung, Y.L. J. Am. Ceram. Soc. 89 (2006) 1936.
- [13] Yu, X. Xu, X.H. Yang, P.H. Jiao, Q. Yang, Z.W. Song, Z.G. Qiu, J.B. Optical properties of Eu-activated calcium aluminosilicates synthesized in different atmospheres, Opt. Mater. 34 (2012) 931-4.
- [14] Piao, X.Q. Machida, K. Horikwa, T. Yun, B.G. Acetate reduction synthesis of $\text{Sr}_2\text{Si}_5\text{N}_8:\text{Eu}^{2+}$ phosphor and its luminescence properties, J. Lumin. 130 (2010) 8-12.

- [15] Prnová, A. Bodišová, K. Klement, R. Migát, M. Veteška, P. Škrátek, M. Bruneel, E. Van Driessche, J. Galusek, D. Preparation and characterization of $\text{Yb}_2\text{O}_3\text{-Al}_2\text{O}_3$ glasses by the Pechini sol gel method combined with flame synthesis, *Ceram. Int.* 40 (2013) 6179–6184.
- [16] Publication CIE no 17.4. International Lighting Vocabulary, Central Bureau of the Commission Internationale de L'Eclairage, Vienna, Austria, 1987.
- [17] G.B. Stringfellow, M.G. Craford, High Brightness Light Emitting Diodes, *Semiconductors and Semimetals*, vol. 48, Academic Press, 1997, p. 247.

WILLEMITE BASED PHOTO LUMINESCENT MATERIALS. GRAIN MORPHOLOGY AND FLORESCENT SPECTRA BY USING DIFFERENT ACTIVATORS OF LUMINESCENCE

Peter Švančárek, Robert Klement, Dušan Galusek

Vitrum Laugaricio – Joint Glass Centre of the IIC SAS, TnU AD and FChPT STU, Trenčín, Slovakia

e-mail: peter.svancarek@tnuni.sk

ABSTRACT

Orange - red light emitting $\text{Zn}_2\text{SiO}_4:\text{Eu}^{3+}$ phosphors have been synthesized from a mixture of ZnO , SiO_2 and Eu_2O_3 powders as the reagents by solid-state reaction in ambient atmosphere at $1300\text{ }^\circ\text{C}$ (2 h isothermal heating),. Eu^{3+} ion was selected as an efficient activator emitting in orange-red wavelength range. Orange emission at the wavelengths between 587-597 nm is allowed by ${}^5\text{D}_0 \rightarrow {}^7\text{F}_1$ transition. Orange to red emission at the wavelengths between 610-623 nm and a relatively strong red emission at 690-705 nm is allowed by the ${}^5\text{D}_0 \rightarrow {}^7\text{F}_2$ and ${}^5\text{D}_0 \rightarrow {}^7\text{F}_4$ transitions, respectively. Because Eu^{3+} is trivalent cation, it is not interchangeable with divalent Zn^{2+} cations easily. Therefore, various doping concentrations of Li^+ cations ranging from 0 to 5 at% were added for charge compensation, and the influence of Li^+ addition on grain morphology, spectral characteristics and fluorescent properties of Eu^{3+} -doped willemite was studied. The addition of Li^+ cations leads to thickening of willemite region at the surface of SiO_2 grains as well as better incorporation of Eu^{3+} cations into the willemite host matrix. Spectroscopically, the doping by Li^+ cations results in more intensive luminescence caused by higher fraction of optically active Eu^{3+} cations built in the willemite matrix, and emergence of a wide band centered at around 760 nm which most likely originates from structural defects.

Keywords: *willemite, Eu^{3+} , Li^+ , orange-red luminescence, charge compensation,*

INTRODUCTION

Willemite (Zinc Silicate) is one of the best known fluorescent minerals in nature and in the past it was used as a source of zinc. Because of natural occurrence and similar ionic radii, the Mn^{2+} is often found to replace Zn^{2+} cations in the crystal lattice. When subjected to ultraviolet (254 nm) irradiation, the alpha willemite emits bright green light due to manganese impurities in its crystal lattice. Its chemical and thermal stability is often a reason why this compound is

often selected as a phosphor of choice. X-ray, UV light or electron radiation are used as energy carriers to charge willemite crystal lattice, and Mn^{2+} ions, which are incorporated into the lattice as a substitute for small fraction of Zn^{2+} ions.

In this work we focused on preparation of Eu^{3+} doped willemite. Because industry demands highly efficient and easily obtainable phosphors, solid state synthesis was selected as a preparation route due to its simplicity. The main problem encountered during the synthesis was insufficient fraction of Eu^{3+} ions built into the crystal lattice of willemite. The cause is twofold:

1. The crystal ionic radius of Eu^{3+} is much larger than that of Zn^{2+} (108.7 pm for Eu^{3+} vs 88 pm for Zn^{2+}) which inherently leads to deformation of crystal lattice [1].
2. The presence of three-valent cations (Eu^{3+}) which replace Zn^{2+} cations leads to creation of vacancies in the willemite crystal lattice.

While there is no way to change ionic radius, the vacancies may be filled by other ions to compensate the charge imbalance. For charge compensation, the monovalent cations such as Li^+ , Na^+ and K^+ are most often used. [2]. Conveniently, the lithium cation has ionic radius close to the ionic radius of Zn^{2+} .

The luminescence spectra of Eu^{3+} doped willemite is much more complex than Eu^{2+} doped willemite [3] and Stark splitting in the strong crystal field is often observed when the symmetry at Eu^{3+} ion site is low. Transitions from base $^5D_0 \rightarrow ^7F_x$ ($x=0, 1, 2, 3, 4\dots$) allows luminescence from orange (for $x=0, 1, 2$) to red (for $x=3, 4\dots$) part of spectra. [4].

In this paper we report on the effect of Eu^{3+} concentration as well as the effect of co-doping by various concentrations of Li^+ to observe effects of Eu^{3+}/Li^+ molar ratio on luminescence intensity in orange-red emitting $Zn_2SiO_4:Eu^{3+}$ phosphors under UV light excitation. The phosphors were prepared by solid-state reaction in the ambient atmosphere with the ZnO/SiO_2 molar ratio equal to 1. The Eu^{3+} and Li^+ concentrations were varied in the lower concentration region (0 to 5%).

EXPERIMENTAL

The SiO_2 , ZnO , Li_2CO_3 and Eu_2O_3 of analytical grade or higher purity were weighed to obtain mixtures of powders with compositions corresponding to $Zn_{x-y-z}Eu_yLi_zSiO_3$ (**Table 1**).

| | ZnO | SiO ₂ | Eu ₂ O ₃ | Li ₂ O |
|-----------------|------|------------------|--------------------------------|-------------------|
| W 0.03Li | 0.97 | 1 | 0 | 0.015 |
| W 0.03Eu | 0.97 | 1 | 0.015 | 0 |
| W 0.03Eu 0.03Li | 0.94 | 1 | 0.015 | 0.015 |

| | | | | |
|--|-------|---|---------|---------|
| W 0.01Eu 0.01Li | 0.98 | 1 | 0.005 | 0.005 |
| W 0.005Eu 0.005Li | 0.99 | 1 | 0.0025 | 0.0025 |
| W 0.0025Eu 0.0025Li | 0.995 | 1 | 0.00125 | 0.00125 |
| W 0.005Eu 0.01Li | 0.985 | 1 | 0.0025 | 0.005 |
| W 0.005Eu 0.02Li | 0.975 | 1 | 0.0025 | 0.01 |
| W 0.005Eu 0.03Li | 0.965 | 1 | 0.0025 | 0.015 |
| W 0.005Eu 0.05Li | 0.945 | 1 | 0.0025 | 0.025 |
| Table 1. Molar compositions of Eu ³⁺ doped willemite phosphors | | | | |

Fine powders were prepared by ball milling and homogenization of powder mixtures in vibratory mill for 30 minutes. Obtained mixture of fine powders was calcined for 2 h at 1300 °C in air. For the SEM/EDX analysis (JEOL JSM-7600 Thermal FE SEM) powders were cast into phenolic conductive resin and polished by diamond polishing disc. The phase composition was determined using powder X-ray diffraction (PANalytical Empyrean Series 2 X-ray diffractometer). Both emission (PL) and excitation (PLE) fluorescence spectra were measured by Fluorolog 3 (FL3-21, Horiba) fluorescence spectrometer in front-face mode. The Xe-lamp (450 W) was used as an excitation source. All emission spectra, measured at RT, were corrected for spectrometer and excitation lamp response.

RESULTS AND DISCUSSION

SEM has shown significant differences in morphology of the calcined powder products. Lithium free samples contained grains with sizable dark core (SiO₂) and lighter shell (willemite). In addition there were grains of unreacted Eu₂O₃ (**Fig 1.A.**). However, addition of lithium changed the situation. Not only the willemite shell expanded in volume, but willemite was present also in the SiO₂ cores (**Fig. 1. B and C. vs A.**). This suggests the Li⁺ ions promoted the diffusion of Zn²⁺ and other ions into the interior of SiO₂ powder particles. SEM-EDX mapping and point analysis revealed that distribution of Eu³⁺ in europium doped samples was not uniform; the aggregates containing relatively high concentration of Eu³⁺ were studied in all studied specimens (up to 15 at. %: note the volume of analyzed material is given by the diameter of the electron beam and the depth of its penetration. It therefore includes also surrounding material into the analysis, efficiently decreasing the measured values. The real concentrations of Eu in Eu-rich regions is probably much higher). High dissimilarity in crystal ionic radii between Zn²⁺ and Eu³⁺ as well as the difference of charges of these cations are considered being the reason for compositional inhomogeneities in the synthesized material.

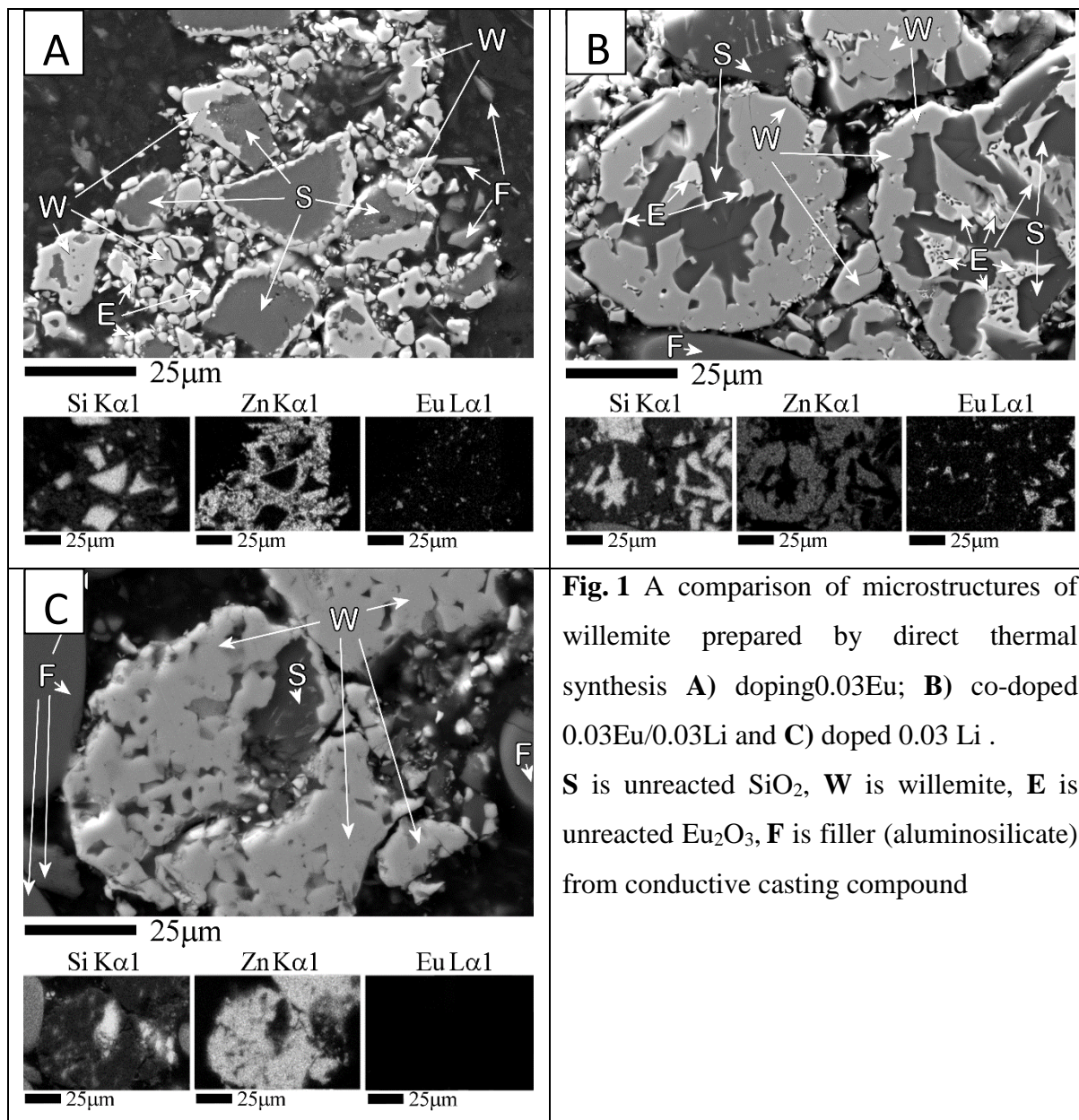


Fig. 1 A comparison of microstructures of willemite prepared by direct thermal synthesis **A)** doping 0.03Eu; **B)** co-doped 0.03Eu/0.03Li and **C)** doped 0.03 Li. **S** is unreacted SiO₂, **W** is willemite, **E** is unreacted Eu₂O₃, **F** is filler (aluminosilicate) from conductive casting compound

The X-ray powder diffraction patterns of all four studied systems showed the presence of willemite (Zn₂SiO₄) as a major crystalline phase, together with traces of unreacted SiO₂ (cristobalite). Small amount of detected cristobalite suggests that the majority of SiO₂ remains in amorphous state. The XRD patterns corresponding to Li⁺ undoped and co-doped analogues are almost identical and no lithium containing phases were identified.

The photoluminescence emission and excitation spectra are shown in **Fig. 2** and **Fig. 3**. It is common knowledge that $^5D_0 \rightarrow ^7F_{0,1}$ transition is directed by selection rules for intermediate magnetic-dipole coupling $\Delta J = 0, \pm 1$, and the $^5D_0 \rightarrow ^7F_{2,4,6}$ are allowed electric-dipole transitions. Generally, when the Eu³⁺ ion occupies the crystallographic site with inversion symmetry, its magnetic-dipole transition $^5D_0 \rightarrow ^7F_1$ orange emission dominates in the emission spectrum, while the electric-dipole transitions $^5D_0 \rightarrow ^7F_{2,4}$ red emission is dominant if the Eu³⁺

ion is located at an non-inversion center. Based on such general presumptions, Eu^{3+} ions most likely occupy both inversion and non-inversion lattice sites in the studied systems. Very well resolved splitting of ${}^5\text{D}_0 \rightarrow {}^7\text{F}_{1,2}$ transitions to three and five lines is observed due to the Stark splitting in the strong crystal field which also indicates that the symmetry at Eu^{3+} ion site is low.

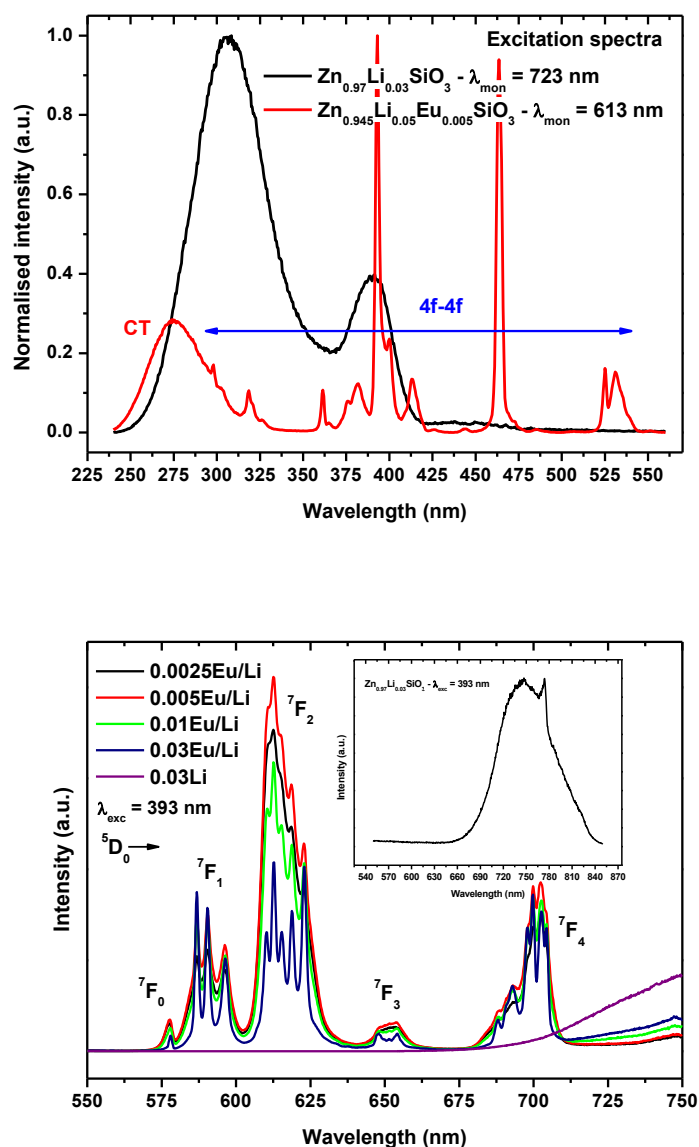


Fig. 2: The representative excitation (upper) and emission spectra (lower) of the Eu^{3+} -doped willemite equimolarly charge compensated by Li^+ ions. Inset: Li^+ -doped willemite matrix.

The doping of RE ions into the Zn_2SiO_4 matrix is very difficult due to two reasons: (1) the ionic radius of RE^{3+} ions (e.g. $\text{Eu}^{3+} \sim 100$ pm) are much larger than that of Zn^{2+} ions (~ 74 pm), and

(2) substitution creates a charge imbalance, as RE^{3+} ions substitute the Zn^{2+} sites in the willemite host matrix. The charge compensation from local defect sites results in the lattice deformation, which is not desired, and the created defects may affect the luminescence properties to some extent. It is therefore much more convenient to provide a charge compensating material for the formation of a stable compound. The alkali metals, like Li, Na, K, are the most suitable candidates in this respect. In order to reduce the number of defects, Li^+ ions were added into the $Zn_2SiO_4:Eu^{3+}$ as charge compensator. Two Zn^{2+} ions are replaced by a Eu^{3+} ion and a Li^+ ion in the Zn_2SiO_4 lattice.

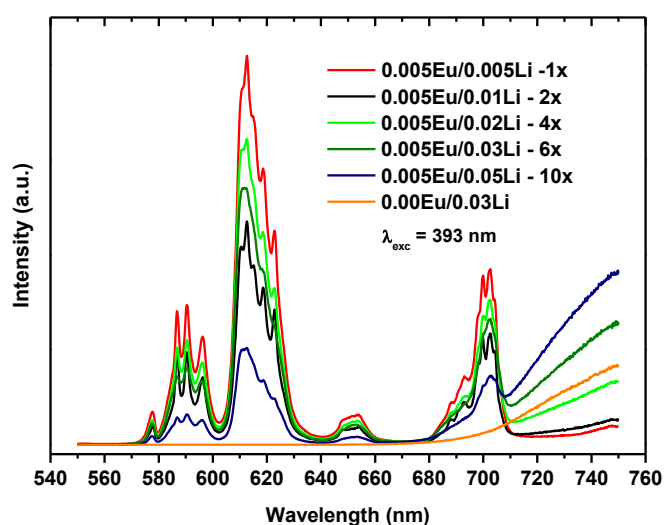
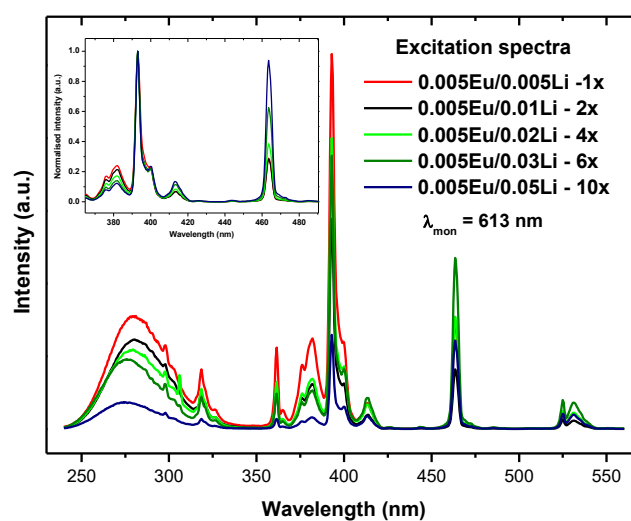


Fig. 3: The excitation (upper) and emission spectra (lower) of the Eu^{3+} -doped willemite, charge compensated by different amount of Li^+ ions. The inset represents the normalized intensity excitation spectra.

The PL properties were studied in two types of samples. First, the effect of dopant concentration on the luminescence was investigated (samples equimolarly charge compensated by Li^+ ions). Then the sample with highest emission intensity was selected and the effect of $\text{Eu}^{3+}/\text{Li}^+$ ratio was studied to reveal how this ratio affects the luminescence properties of prepared samples. The representative excitation (PLE) spectrum of the Eu^{3+} doped willemite samples is shown in the Fig. 2. The PLE spectra of all samples were monitored at 613 nm and recorded in the spectral range from 230-560 nm. The PLE spectra exhibits the features typical for Eu^{3+} ions, i.e. the broad band and several sharp peaks between 320-600 nm. The broad band absorption centered at 274 nm is associated with charge transfer transition in the $\text{Eu}^{3+}-\text{O}^{2-}$ species and sharp lines are assigned to the intra-configurational 4f-4f transitions of the Eu^{3+} ion with the highest intensity absorption at 393 nm corresponding to ${}^7\text{F}_0 \rightarrow {}^5\text{L}_6$ transition.

The photoluminescence emission (PL) spectra of Eu^{3+} doped willemite at different concentration levels are shown in Fig. 2. The PL spectra of studied samples exhibit five major emission bands attributed to 4f-4f transitions of the Eu^{3+} ions originating from ${}^5\text{D}_0 \rightarrow {}^7\text{F}_J$ levels ($J = 0, 1, 2, 3, 4$). The transitions corresponding to ${}^7\text{F}_1$ and ${}^7\text{F}_2$ levels are clearly separated into three and five lines due to the crystal field splitting (Stark splitting). In addition, one can observe the increase of background intensity that is clearly observed over the 710 nm in the measured spectra of all studied samples. The emission spectra measured in extended spectral range up to 850 nm (NIR range) revealed the broad emission band with the maximum intensity at about 760 nm (spectra not shown); the intensity of this band increases with increasing Li^+ concentration. To clarify the origin of this emission, the Eu^{3+} -free sample was prepared with the $\text{Zn}_{0.97}\text{Li}_{0.03}\text{SiO}_3$ composition. It should be noted however, that no NIR emission was observed in the Li^+ free ZnSiO_3 composition. The excitation and emission spectra are shown in the inset in Fig. 2. The PLE spectrum exhibits two absorption broad bands centered at 306 and 390 nm, respectively, and the band with lower intensity effectively overlaps with the Eu^{3+} absorption at 393 nm (${}^7\text{F}_0 \rightarrow {}^5\text{L}_6$ transition). When excited at 393 nm, the un-doped sample shows broad emission in the spectral range from 660 to 850 nm with the band maximum emission intensity at ~ 750 nm. This type of emission was also observed in Zn_2SiO_4 , $\text{SiO}_2/\text{Zn}_2\text{SiO}_4$ and $\text{ZnO}/\text{Zn}_2\text{SiO}_4/\text{SiO}_2$ composites [5, - 7], and attributed to the energy transfer

from Zn_2SiO_4 to NBOHs (non-bonding oxygen) interface defects. These defects are certainly induced in higher extent by Li^+ co-doping and play a key role for luminescence phenomena.

The PL intensity originating from Eu^{3+} luminescence centers increases up to 0.005Eu/Li sample, than gradually decreases with increasing content of Eu^{3+} and Li^+ ions in the samples, which is most likely due to concentration quenching and /or energy transfer to the structural defects in the host lattice. The effect of $\text{Eu}^{3+}/\text{Li}^+$ ratio on emission intensity of studied samples is documented in Fig. 3. As the $\text{Eu}^{3+}/\text{Li}^+$ ratio increases the PL intensity due to the luminescence of Eu^{3+} centers decreases, while the NIR emission intensity at 760 nm increases. The highest Eu^{3+} PL intensity was found for $\text{Eu}^{3+}/\text{Li}^+$ ratio equal to 1 (predominantly charge compensation effect). This clearly indicates that number of structural defects in the Zn_2SiO_4 host increases. Their higher concentration thus finally results in significant reduction of Eu^{3+} PL emission intensity as a consequence of luminescence quenching by Li^+ induced structural defects in the Zn_2SiO_4 crystal host.

CONCLUSIONS

The positive effect of Li^+ co-doping on PL emission Eu^{3+} centers was observed. Increase of intensity in $\text{Eu}^{3+}/\text{Li}^+$ doped systems, compared to system without Li^+ co-doping can be explained by the charge compensation effect. The formation of vacancies is not favorable for the emission PL activator (Eu^{3+}) because of the energy transfer from activator to vacancy is more efficient, and hence a certain amount of vacancies will negatively affect the photoluminescence intensity. On the other hand, the Li^+ co-doping may induce the formation of structural defects in the Zn_2SiO_4 host lattice, which is documented by the luminescence of NBOHs interface defects in NIR spectral range (600-850 nm with band maximum at 760 nm). As the $\text{Eu}^{3+}/\text{Li}^+$ ratio increases the PL intensity due to the luminescence of Eu^{3+} centers decreases, while the NIR emission intensity at 760 nm increases. The highest Eu^{3+} PL intensity was found for $\text{Eu}^{3+}/\text{Li}^+$ ratio equal to 1 (predominantly charge compensation effect). The higher concentration of defect sites thus finally results in significant reduction of Eu^{3+} PL emission intensity as a consequence of luminescence quenching by Li^+ induced structural defects in the Zn_2SiO_4 crystal host.

ACKNOWLEDGEMENTS

The financial support of this work by the projects SAS-NSC JRP 2012/14 and VEGA 1/0631/14, is gratefully acknowledged. This publication was created in the frame of the project "Centre of excellence for ceramics, glass, and silicate materials" ITMS code 262 201 20056, based on the Operational Program Research and Development funded from the European Regional Development Fund.

REFERENCES

- [1] R. D. Shannon, Revised Effective Ionic Radii and Systematic Studies of Interatomic Distances in Halides and Chalcogenides, *Acta Cryst.* (1976). A32, 751.
- [2] E. Cavalli, A. Belletti, E. Zannoni: Luminescence of Fe-doped Willemite Single Crystals, *Journal of Solid State Chemistry*, 117 (1995), 16-20.
- [3] D. Ehrt, Photoluminescence in glasses and glass ceramics, *IOP Conf. Series: Materials Science and Engineering* 2 (2009) 012001
- [4] K. Binnemans: Interpretation of europium(III) spectra, *Coordination Chemistry Reviews* 295 (2015) 1–45.
- [5] J. El Ghoul, K. Omri, A. Alyamani, C. Barthou, L. El Mir, Synthesis and luminescence of $\text{SiO}_2/\text{Zn}_2\text{SiO}_4$ and $\text{SiO}_2/\text{Zn}_2\text{SiO}_4:\text{Mn}$ composite with sol-gel methods, *J. Lumin.* 138 (2013) 218.
- [6] L. El Mir, A. Amlouk, C. Barthou, S. Alaya, Synthesis and luminescence properties of $\text{ZnO}/\text{Zn}_2\text{SiO}_4/\text{SiO}_2$ composite based on nanosized zinc oxide-confined silica aerogels, *Physica B* 388 (2007) 412 – 417.
- [7] K. Omri, L. El Mir, Effect of manganese concentration on photoluminescence properties of $\text{Zn}_2\text{SiO}_4:\text{Mn}$ nanophosphor material, *Superlattices and Microstructures* 70 (2014) 24–32.

YTTRIA NANOPOWDERS PREPARED BY PRECIPITATION METHOD FOR TRANSPARENT YTTRIA CERAMICS

Nibu P G, Dušan Galusek

Centre for Functional and Surface Functionalized Glass

Alexander Dubcek University of Trencin

Slovak Republic

ABSTRACT

Transparent ceramics are attractive optical materials that offer many advantages over single crystals, including greater shape control, higher homogeneity of the dopant, and faster and lower cost fabrication methods. Transparent polycrystalline ceramic can be used as replacement of glass and single crystals in production of solid state lasers. Successful preparation of transparent polycrystalline ceramics requires high purity nanopowders with good sinterability and deagglomerated particles. Such nanopowders are then shaped into green bodies with high relative density (usually more than 55%). Among transparent ceramic materials yttria ceramics has been developed for applications in e.g. solid state lasers. Y_2O_3 transparent ceramics are also very efficient NIR-visible up-converters, and can be used as materials for X-ray scintillator applications. Our results report on preparation of Y_2O_3 nanopowders by precipitation method using ammonium hydroxide as precipitation agent. The influence of precipitation agent and concentration of reactants, morphology, particle size and degree of agglomeration was evaluated. Partly agglomerated powders with the primary size of Y_2O_3 nanoparticles ~200 nm with cubic crystal structure were prepared. The optimum concentration of ammonia precipitation agent was found to be 0.5N. Ultrasonic deagglomeration of the powder was most efficient if the pH value was adjusted to 11 through addition of NH_4OH solution.

Keywords: Y_2O_3 , Transparent ceramics

INTRODUCTION

Recently, the development of polycrystalline laser materials has been accelerated due to the fabrication technology of transparent ceramics [1-2]. In the field of optics, transparency is the physical property of materials allowing light pass through it without being scattered [3]. Transparent polycrystalline ceramic (TPC) materials have attracted a significant attention as

candidates for various applications, including laser gain media in solid state lasers, [4] electro-optical devices and scintillators [5]. Yttria (Y_2O_3) is widely known as a promising optical material owing to its broad range transparency, high melting temperature ($2430^\circ C$), outstanding refractoriness and excellent chemical stability [6]. Therefore, polycrystalline transparent yttria ceramics have been exploited as perfect candidate to replace single crystals. Over past few decades, transparent yttria ceramics have been shown to possess great potential in various applications, including transparent windows, missile domes, bulb envelopes and laser hosts [7]. However, the fabrication of high performance transparent yttria ceramics is not an easy task, as the complete elimination of residual pores is essential in spite of high melting point of yttria. Therefore, high sintering temperatures, suitable additives and specific sintering techniques must be applied in order to accelerate the densification of yttria. Successful preparation of transparent polycrystalline ceramics also requires high purity nanopowders with good sinterability and deagglomerated particles. In this work preparation of Ce-doped Y_2O_3 nanopowders by precipitation method using ammonium hydroxide as precipitation agent is reported and discussed [8-9].

MATERIALS AND EXPERIMENTAL DETAILS

The aqueous nitrate solution of Y^{3+} was prepared by dissolving yttria powders (99.99 %,) in diluted nitric acid (HNO_3) and deionized water under stirring and heating, then diluted into 0.1 M with deionized water. The solution of Ce^{3+} was prepared by dissolving cerium nitrate (99.99 %,) in deionized water then diluted into 0.1M with deionized water. The solution was dripped into a 0.5 M ammonium solution, under continuous rapid stirring, ensuring there was sufficiently high excess of ammonia to eliminate any pH fluctuations throughout the process. The solution was added with the use of peristaltic pump at 5.0 ml/min, completing the reaction in 24 h. The mixed solution turned to an opaque white slurry. After 12 h aging the slurry was vacuum filtered through filter paper and the resulting white precipitate washed with distilled water. The washed precipitate was dried overnight in air at $100^\circ C$. The dried precipitate was crushed and ground in an agate mortar and pestle, and calcined in air for 3 h at $700^\circ C$ (heating rate $10^\circ C/min$). Ultrasonication was then used to de-agglomerate the nanopowder, using calculated amounts of Y_2O_3 powder and ammonium solution to adjust the pH value of the suspension. After sonication particle size and particle size distribution were determined as a function of pH and sonication time using particle size analyser (Brookhaven 90Plus BI-Zeta).

CHARACTERIZATION OF POWDERS

Crystallization temperatures of the pre-calcined powders were determined by differential scanning calorimetry combined with and thermogravimetry (Netzsch STA 449 F1 Jupiter TG / DTA / DSC). Powder X-ray diffraction (XRD) patterns were acquired using powder X-ray diffractometer (Panalytical Empyrean DY1098). Particle size distributions and particle morphologies were determined through scanning electron microscope (JEOL JSM-7600 F / EDS / WDS / EBSD).

RESULTS

Figure 1 shows the DTA/TGA data for the precipitated hydroxide precursor. A large endothermic peak from room temperature until approximately 600°C is observed coupled with significant mass loss. The TGA signal shows two inflection points at approximately 350°C and 550°C indicating two modes of de-hydroxylation, one attributed to the desorption of water from the surface of the hydroxide nanoparticles and another one due to hydroxide decomposition/crystallization.

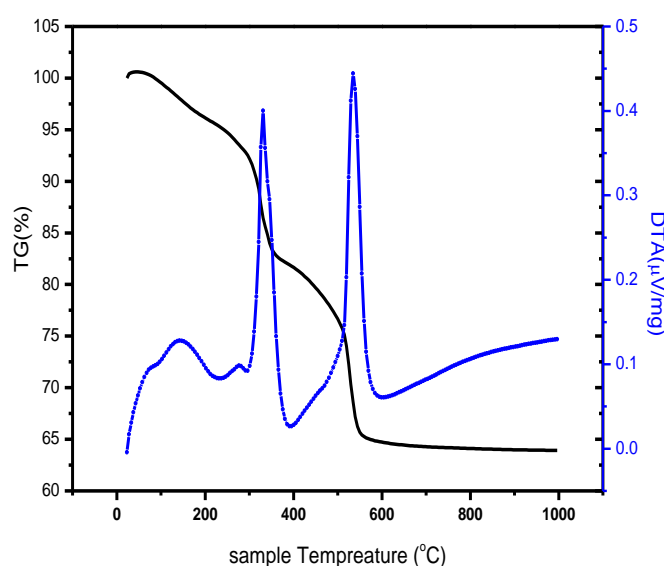


Figure 1 DTA/TGA data for the precipitated hydroxide precursor.

Figure 2 shows the XRD patterns of Y_2O_3 powder calcined at 700°C. As shown in the figure, the pure cubic Y_2O_3 phase was obtained with good crystallinity and the primary particle size

of approximately 50nm, as determined from the Scherer equation.

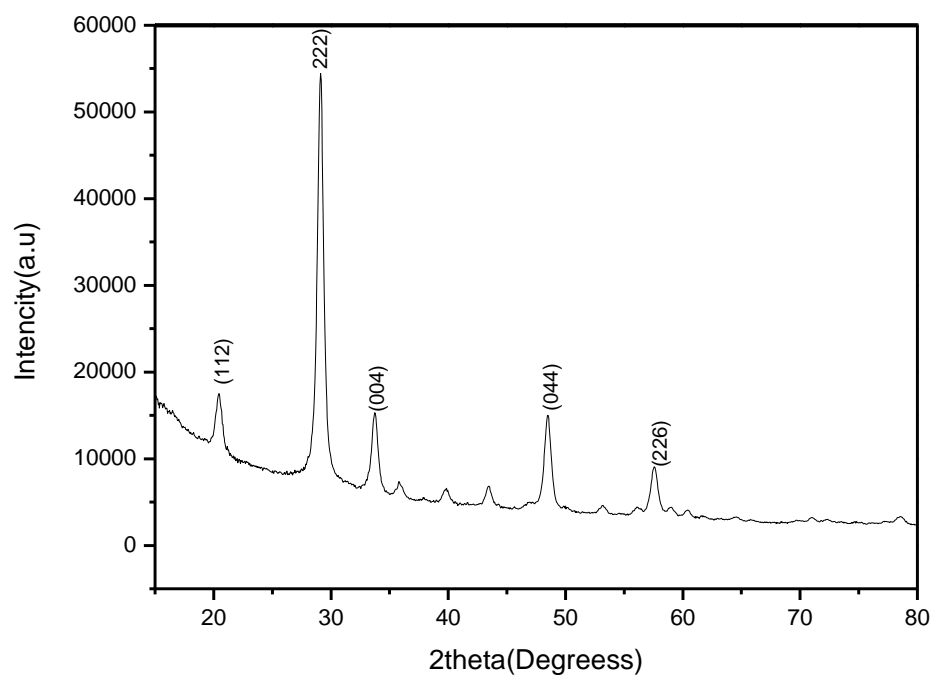


Figure 2 XRD pattern of prepared Y₂O₃ powder calcined at 700 °C.

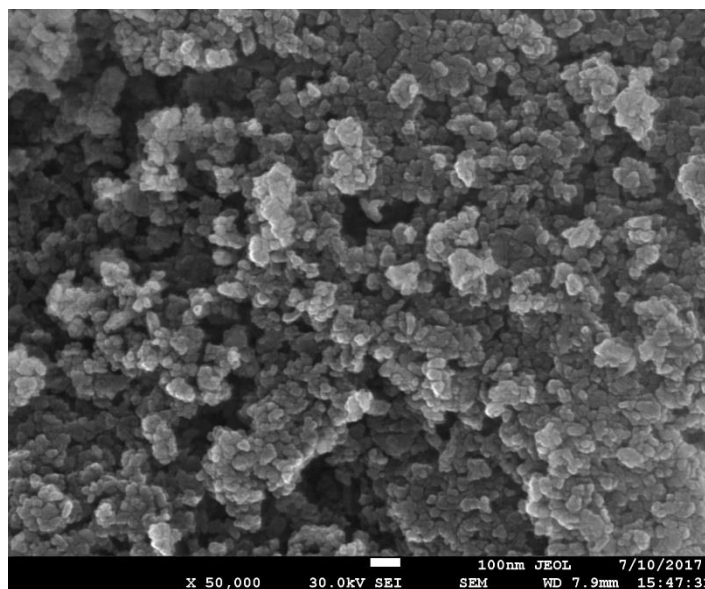


Figure 3 SEM micrograph of the prepared Y₂O₃ powder

Figure 3 shows the SEM micrograph of synthesised Y_2O_3 powder. The powder is partly agglomerated with the primary particle size of approximately 55 nm, which is in good accord with the X-ray diffraction data.

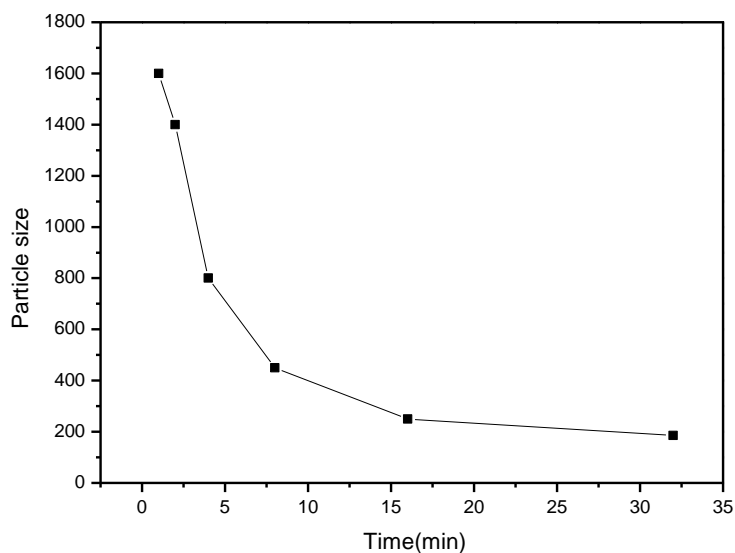


Figure 4 The change of particle size of the Y_2O_3 powder with the sonication time.

Figure 4 summarizes the changes in particle size of yttria powder with the sonication time. Extension of the ultrasonication time results in significant reduction of both the mean size of powder particles, and the width of the particle size distribution, indicating de-agglomeration of the yttria powder. The best results were achieved after 32 minutes sonication time. However, the mean size of 200 nm clearly shows that the powder was not de-agglomerated down to primary particle size, and hard agglomerates with the diameter of about 200 nm are still present.

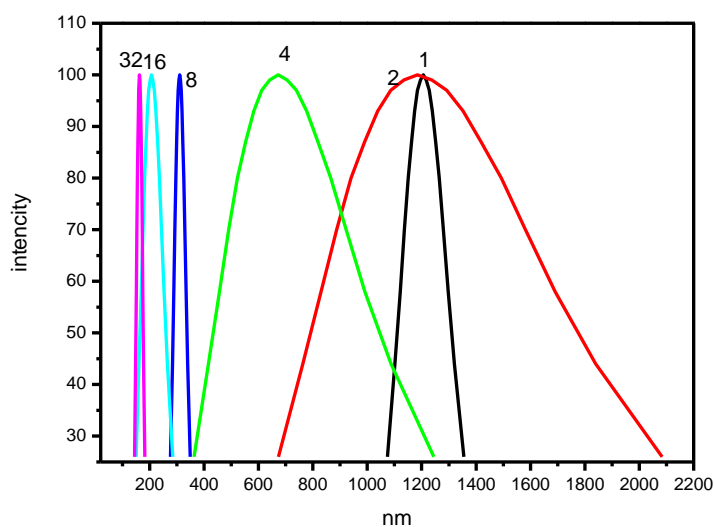


Figure 5 The change of particle size distributions of the Y_2O_3 powder with the sonication time. The numbers at respective curves indicate the time of ultrasonication.

Figure 5 summarizes the changes in particle size distribution of ultrasonically de-agglomerated powder in the aqueous suspension with pH value adjusted to 11 by the addition of NH_4OH solution.

CONCLUSION

Ce-doped Y_2O_3 nanopowder was synthesized via precipitation method. Partly agglomerated powders with the primary size of Y_2O_3 nanoparticles 55 nm and with cubic crystal structure were prepared. The optimum concentration of ammonia precipitation agent was found to be 0.5 N. Ultrasonic deagglomeration of the powder was most efficient if the pH value was adjusted to 11 through addition of NH_4OH solution.

REFERENCES

1. A. Ikesue, et al. *Nat. Photonics* **2** 721-727(2008)
2. B. Song, et al. *J. Mater. Chem.* **3** 21789-21796(2015)
3. S.Fwang, et al. *j.solid state che.* **41** 20-54(2013)
4. Baneshi, et al. *Ceram. Int.* **40** 14177-14184 (2014)
5. J. F. D. Lima, et al., *Opt. Mater.* **35** 56-60 (2012)

6. W. Kim, et al., *J. Appl. Opt.* **54** 210-221(2015)
7. D.Y. Kosyanov, et al., *J. Alloy. Compd.* **686** (2016)
8. Fukobori A, et al. *Applies physics* **107** 73501(2010)
9. J. F. D. Lima, et al., *Opt. Mater.* **35** 56-60 (2012)

VYUŽITIE THz SPEKTROSKOPIE PRI CHARAKTERIZÁCIÍ KERAMICKÝCH A SILIKÁTOVÝCH MATERIÁLOV.

APPLICATION OF THz SPECTROSCOPY FOR CHARACTERISATION OF CERAMIC AND SILICATE MATERIALS

D. Furka¹, S. Furka¹, D. Lorenc^{1,2}, Ľ. Haizer², M. Janek^{1,3*}

¹*Comenius University, Faculty of Natural Sciences, Department of Physical and Theoretical Chemistry, Mlynská dolina, SK-842 15 Bratislava, Slovakia*

²*International Laser Centre, Ilkovicova 3, SK-81219 Bratislava, Slovakia*

³*Slovak University of Technology, Faculty of Chemical and Food Technology, Radlinského 9, SK-812 37 Bratislava, Slovakia*

ABSTRACT

Terahertz-time domain spectroscopy (THz-TDS) is relatively well established experimental technique, which is not yet frequently applied for characterisation of ceramic and glass materials. Its potential for systematic study of ceramics and glass phase is seen in its sensitivity towards dielectric and spectral characterisation of solids. The principle of this technique is based on femto-second laser technology and e.g. low temperature GaAs photo-optical switches, while the THz radiation is detected coherently. The application of this technique depends on availability of modern femto-second lasers working in pulse mode with pulse duration of about 100 fs. The THz-TDS allows achieving the frequency dependence of material characteristics in far infrared region. As an example we present selection of several results of silicon and muscovite-like aluminosilicate systems.

Keywords: Terahertz-time domain spectroscopy, Far-infrared, Dielectric properties, Spectral characteristics, Aluminosilicates

INTRODUCTION

The ceramic and silicate materials are frequently used as insulators and dielectrics not only in the conventional electro-technical applications but also in many special devices such as Geiger-Müller counters, Clystron tubes, microwaves windows, bolometers, coputers, TV

and communication devices requiring high quality of medical, machine and nuclear applications. THz-TDS has found applications in fields such as chemical sensing, material quality checks and tomographic imaging, which can be applicable also in the studies of ceramic and silicate materials used for material forming by the application of 3D printing.[1,2] THz-TDS is able to extract from one sample measurement, including the determination of a background spectrum, the frequency dependence of the complex refractive index ($\tilde{n}_s = n_s - i\kappa_s$) of the investigated material (the real part of the refractive index, n_s , and the absorption index, κ_s , as the imaginary part) and, at the same time, the thickness, l , of the absorbing medium. The absorption of radiation can be expressed by absorption coefficient α_{vz} , which is function of circular frequency, light speed in vacuum c , and wavelength λ by equation: $\alpha_s = 2\omega\kappa_s/c = 4\pi\kappa_s/\lambda$. From the known frequency dependent refractive index and absorption index can be found the material complex dielectric permittivity $\tilde{\epsilon}_s = \epsilon'_s - i\epsilon''_s$, while $\epsilon'_s = n_s^2 - \kappa_s^2$, and $\epsilon''_s = 2n_s\kappa_s$. The real part of dielectric permittivity ϵ'_s characterise material polarisability and propagation of the radiation through material. The imaginary part corresponding to loss factor ϵ''_s , represents the material ability to absorb electromagnetic radiation at given frequency. The amount of energy absorbed by material at given circular frequency ω and intensity of electromagnetic field E can be expressed by equation $P = \omega\epsilon_0\epsilon''_s|E|^2/2$, where ϵ_0 is the dielectric permittivity of vacuum. The main motivation for our study was the fact that dielectric properties of silicate and glass materials can be an important technological factor in the process of their manifold application specification and that THz-TDS offers unique approach to achieve frequency dependent dielectric properties for defined purpose of applicability.

EXPERIMENTAL

The THz-TDS measurements were done on laboratory build equipment with standard configuration based on femto-second laser driven photoconductive emitter combined with detection based on electro-optic or antenna arrangement. The details can be seen elsewhere [3], briefly; typically around 100 fs long laser pulses with central pulse wavelength of ~800 nm are used. The emitter is based on low-T GaAs with surface Au metallic stripes which are biased with 10 V alternating pulses symmetrically modulated at 10 - 20 kHz. The THz polarization is

linear for the photo-optical switches as the electric field on the emitter is directed from one electrode to another.[4] The equipment delay line is used to ensure a time delay between the pump beam arriving on the emitter and probe beam arriving on the detector. This arrangement results in a measurement of the electric-field dependence of the THz pulse directly in the time domain. All measurements is necessary to perform at the air-conditioned temperature of the laboratory equal to $21.0 \pm 1.0^\circ\text{C}$ and in dried atmosphere to suppress the bands arising from water vapor present in the air. The scheme of the THz-TDS equipment is shown in the Figure 1.

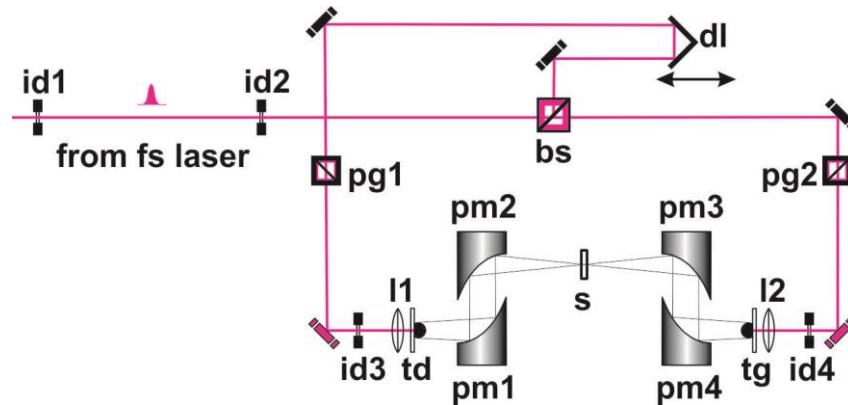


Fig. 1. Schematic representation of terahertz-time domain spectrometer (id – iris diaphragm, bs – beam splitter, dl – delay line, pg – Glan prism, l – lens, td – terahertz detector, tg – terahertz generator, pm – parabolic mirror, s – sample).

The material parameters can be extracted from measurement of sample and reference, which is typically atmosphere used as background. The numerical data calculation include e.g. the fixed-point iteration method used for extraction of the sample complex refractive index $\tilde{n}_s = n_s - i\kappa_s$. From the THz-TDS measurements is calculated the transfer function $H_{measured}(\omega) = E_{sample}(\omega) / E_{reference}(\omega)$, which is used for definition of two-dimensional functions suitable for fixed-point iteration technique.[5] The calculations may include Fabry–Pérot cancellation in the recursive process, when the updated transfer function is used with mapped values of n_s and κ_s . From these values is calculated the material complex dielectric permittivity frequency dependence using the Maxwell equations mentioned above.

RESULTS

Typical THz impulses propagating in dried nitrogen used as a background medium and through a silicon wafer are shown in Figure 2a. The main impulse peak was observed for a dried nitrogen atmosphere at arbitrary position 8.32 ps, with a full width at half maximum for the positive half-cycle at the level of 0.80 ps. For silicon wafer, the impulse position shifted to a higher delay value, and the main impulse peak was observed at 12.52 ps with a full width at half maximum for the positive half-cycle at the level of 0.95 ps. The intensity of positive half-cycle decreased for about 46% for THz pulse which passed the silicon wafer. For perfect plane-parallel orientation of sample interfaces and THz pulse impinging perpendicularly the silicon wafer surface, multiple echo of main impulse peak can be observed (Figure 2a, arrows: 1st, 2nd, 3rd). These are associated with Fabry-Pérot multiple internal reflections.[6]

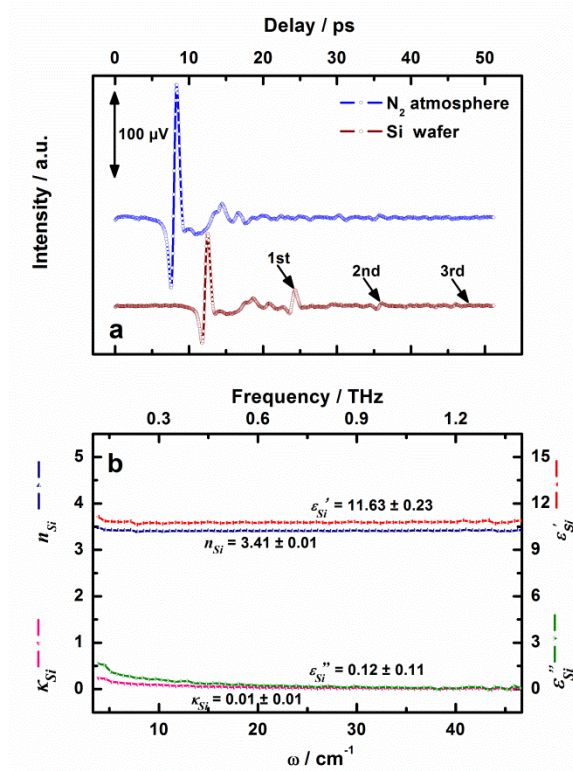


Fig. 2. THz radiation impulses in the nitrogen atmosphere and passing the silicon wafer a) and frequency-dependent – complex refractive index \tilde{n}_{Si} and complex dielectric permittivity $\tilde{\epsilon}_{Si}$ b).

The positions of internal reflections peaks on time-delay scale are related to path length the THz radiation has to travel in silicon and allows also the measurement of sample thickness l . The origin of Fabry-Pérot internal reflections as general case is shown in the Figure 3 and depends also on the ratios of reflection r vs. transmission t coefficient at the interface, hence air

(0) and sample (1) material. It is clear that each echo detected by THz detector originate from the internal reflections, where the propagating wave has to travel double distance d within the sample, which is identical to l , in the case of perpendicular beam incidence. The thickness of Si wafer used for measurement determined using micrometer was $370 \pm 10 \mu\text{m}$ which correspond very well to the value found by THz measurements, hence $368 \mu\text{m}$. Here, we can see that the drop of the intensity for THz positive half-cycle of silicon around 46% can be attributed to the loss arising to the pulse passing the air/sample and sample/air interfaces, despite found zero absorption index of silicon.

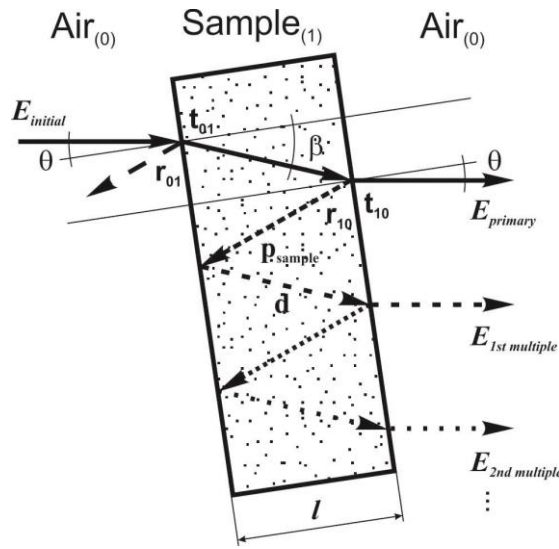


Fig. 3. Scheme of Fabry-Pérot internal reflections origin at the interfaces air (0) sample (1) with transmission coefficients t_{01} , t_{10} and reflection coefficients r_{01} , r_{10} (adapted from [6]).

Using the fixed-point iteration method, the frequency dependent complex refractive index $\tilde{n}_s = n_s - i\kappa_s$ of the silicon was achieved from experimental data Figure 2b. The average value of silicon refractive index at a frequency of ~ 1.0 THz was found $n_{Si} = 3.41 \pm 0.01$ and absorption index of $\kappa_{Si} = 0.01 \pm 0.01$. These values are in a very good agreement with data published by Dai (2004) [7], who determined complex refractive index of silicon: $\tilde{n}_{Si} = 3.417 - i0$. In the previous study Janek et al. (2009) [8] have investigated the effect of chemical composition of various layered mica-like aluminosilicates. Their chemical composition is summarized in the Table 1 (without trace elements and oxygen structural atoms detected). The layered structure of these mica-like aluminosilicates is shown in the Figure 4.

Tab. 1. Chemical composition of selected mica-like aluminosilicates.

| <i>Sample</i> | <i>Atomic percent as determined by EDS.</i> | | | | | |
|---------------|---|-----------|-----------|-----------|-----------|----------|
| | <i>Si</i> | <i>Al</i> | <i>Fe</i> | <i>Mg</i> | <i>Na</i> | <i>K</i> |
| Biotite | 14.6 | 8.1 | 8.0 | 4.6 | 0.1 | 5.1 |
| Phlogopite | 13.3 | 7.1 | 2.0 | 11.2 | 0.5 | 4.6 |
| Vermiculite | 11.4 | 6.4 | 1.1 | 12.9 | n.d. | n.d. |
| Muscovite | 16.4 | 14.4 | 1.3 | 0.5 | 0.5 | 5.2 |

n.d. = not detectable

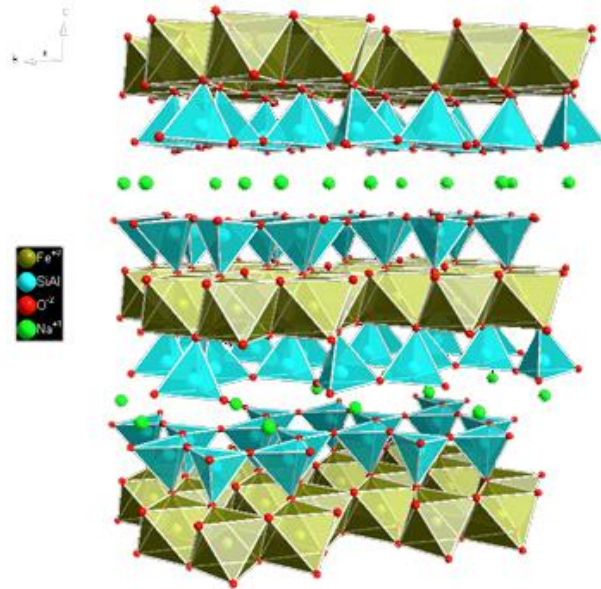


Fig. 4. Structure of layered aluminosilicate with mica-like structure, the real sample layers differ in isomorphous substitutions of Si with Al in tetrahedral networks and Al with Fe or Mg in octahedral network and ratios of exchangeable cations located between the layers e.g. Na, K, Ca or Mg.

The real part of the refraction index found at 1 THz of investigated aluminosilicates was compared with structural iron content. It was found high correlation with reciprocal values of iron content present in the structure of investigated samples (Figure 5). For well developed crystals can be expected change in refractive index due to the change in the size of the unite cell of respective aluminosilicate. It is known that the presences of structural iron affect the height of octahedrons in the single layers, on the other hand, the Wilke et al. (2014) [9] has shown that refraction index of aluminosilicates can be modeled using an effective medium

theory when principle constituents of sample such as SiO_2 and Al_2O_3 (depending on chemical composition as well Fe_2O_3 , MgO) are included in calculation. The calculated index of refraction exhibited good agreement with the measured ones and was in the 5% frame of relative error.

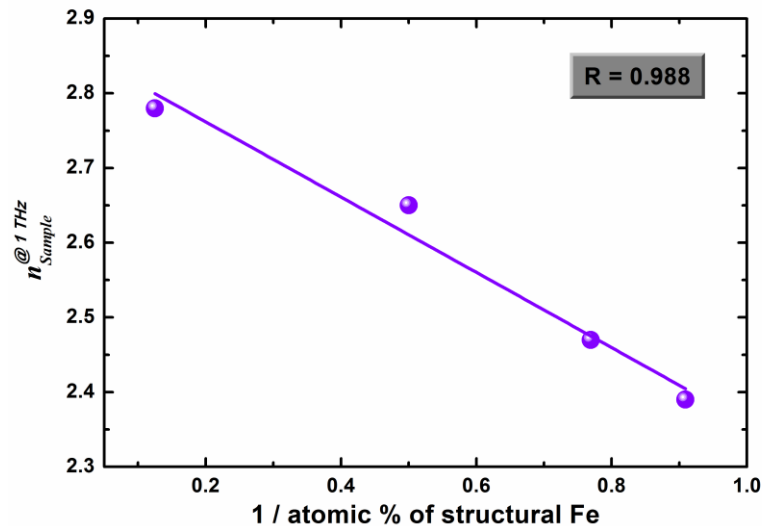


Fig. 5. Correlation of refractive index found for mica-like aluminosilicates with reciprocal values of structural iron content.

CONCLUSION

The optical and dielectric constants frequency dependence of aluminosilicates measured in THz region can be used for silicate material properties determination. The technique has good sensitivity towards principle components e.g. iron content and offers easy approach towards sample characterisation. For well designed species with plan-parallel interface orientations offers this technique the sample thickness measurement from two data set including background and sample measurement. These finding indicate that the aluminosilicate materials are good candidates for their investigation in THz region and this technique in combination with tomography setup can be used as well for close inspection of ceramic parts produced by 3D printing technology.

ACKNOWLEDGMENT

The financial support of the Slovak Grant Agency for Science VEGA grant No. 1/0906/17, the Slovak Research and Development Agency under the contract No. APVV-16-0341, the Grant for PhD students and young UK researchers (UK/163/2017) and NATO grant Emerging Security Challenges Division in the framework of the Science for Peace and Security Programme (SPS984698 "NOTES") are greatly appreciated.

LITERATURE

- [1] Ferguson, B. and Zhang, X.C. Materials for terahertz science and technology. *Nature Materials*, 1 (2002) 26–33.
- [2] Guvendiren M., Molde J., Soares R.M.D., Kohn J. Designing Biomaterials for 3D Printing. *ACS Biomater. Sci. Eng.*, 2(10), (2016) 1679–1693.
- [3] Hoffmann M.C., Fülöp J.A. Intense ultrashort terahertz pulses: generation and applications. *Journal of Physics D: Applied Physics*, IOP Publishing, 44 (8), (2011) pp.83001.
- [4] Reimann K. Table-top sources of ultrashort THz pulses. *Rep. Prog. Phys.* 70 (2007) 1597–1632.
- [5] Withayachumnankul W., Gretel M., Xiaoxia Y., Atakaramians S., Jones I., Lin H., Ung B.S.Y., Balakrishnan J., Ng B.W.-H., Ferguson B., Mickan S., Fischer B.M., Abbott D. *Proc. IEEE* 95 (2007) 1528–1558.
- [6] Dorney, T.D., Baraniuk, R.G., and Mittelman, D.M. Material parameter estimation with terahertz time-domain spectroscopy. *J. Opt. Soc. Am. A*, 18 (2001) 1562–1571.
- [7] Dai, J., Zhang, J., Zhang, W., and Grischkowsky D. Terahertz time-domain spectroscopy characterization of the far-infrared absorption and index of refraction of highresistivity, float-zone silicon. *J. Opt. Soc. Am.*, B7 (2004) 1379–1386.
- [8] Janek M., Bugár I., Lorenc D., Szöcs V., Velič D. and Chorvát D. Terahertz time-domain spectroscopy of selected layered silicates. *Clays Clay Miner.* 57 (2009) 416–424.
- [9] Wilke I., Ramanathan V., LaChance J., Tamalonis A., Aldersley M., Joshi P.C. , Ferris J. Characterization of the terahertz frequency optical constants of montmorillonite. *Appl. Clay Sci.* 87 (2014) 61–65.

LA-ICP-MS IN THE CHEMICAL ANALYSIS OF GLASS, CERAMIC AND MINERAL MATERIALS

Petr Chrást^{1*}, Dagmar Galusková¹, Dušan Galusek

1) *Centre for Functional and Surface Functionalized Glass (FunGlass), Studentská 2, Trenčín*

*) *corresponding author: petr.chrast@tmuni.sk*

ABSTRACT

This paper focuses on the application of laser ablation inductively coupled plasma mass spectrometry (LA-ICP-MS) in material sciences. In the range of atomic spectrochemistry methods this technique became highly demanded due to several reasons: direct elemental analysis of solid samples, shortening the sample preparation time, lowering limits of detection (down to $\mu\text{g kg}^{-1}$), high sensitivity and precision. In addition, the sample consumption is decreased down to μg range.

Complex process of laser ablation is highly matrix-dependent. Material properties such as sample transparency and hardness can affect the coupling of focused laser beam pulse, thus making the analysis difficult if a reference material does not have the same matrix as the analyzed sample.

Samples of glass (SRM NIST 612, 610), ceramics (lithium disilicate, cerium and yttrium doped zirconium oxide ceramics *Ivoclar* and *Longlife*) and geological (synthetic obsidian) materials were analyzed by the means of LA-ICP-MS, using a 213 nm solid-state laser ablation unit (CETAC LSX-213G+) coupled to a quadrupole-based mass spectrometer with a reaction cell (Agilent 7900), and content of major and minor elements was evaluated. Considered matrix effects were quantified in terms of fractionation.

Material differences in terms of hardness and structural composition of said materials was evaluated through the assessment of fractionation index. Ceramic materials exhibited more resistant behavior under laser ablation, resulting in lower ablation rates and thus worse elemental fractionation effects than on silicate materials. This is commented on further in fractionation results.

LA-ICP-MS was used to determine the elemental content (in mg kg^{-1}) of major components and trace elements (considered to be impurities in ceramic samples). The evaluated elemental contents were in accordance with reference values in case of more abundant elements. The content of trace elements (above the limit of detection) was quantified and

compared to reference values, with high precision and trueness, in case the results were not impaired matrix effects.

INTRODUCTION

Inductively coupled plasma mass spectrometry, ICP-MS, is a multi-element analytical method with one of the lowest limits of detection (LOD) from almost all analytical methods, around 0.01 mg kg^{-1} . The connection with ICP ionization source provides stable ion current with almost 100% ionization effectivity, introduced to a mass analyzer. The quadrupole mass analyzer, depicted in Fig. 1. is referred to as mass filter, selecting a discrete mass passing through the system by combining direct current (DC) and radiofrequency (RF) potentials on the quadrupole rods of the mass analyzer. Those ions having a stable oscillation trajectory pass through the filter and reach the detector [1].

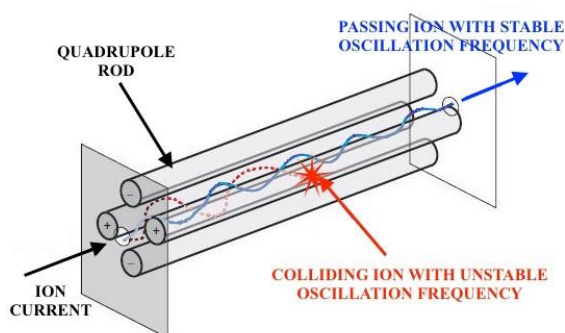


Figure 1 Quadrupole mass filter schematic

A quadrupole filter is, compared to others, a relatively inexpensive analyzer providing reproducible spectra and an appreciable scope of use. Even though it reaches lower resolving powers than other constructions of mass analyzers, its frequent application in ICP-MS systems only confirms its qualities.

All processes involved in LA-ICP-MS, the aerosol formation process, the transport of the aerosol into the ICP, and the conversion of the aerosol into ions within the ICP may potentially alter the stoichiometric composition of the laser-generated aerosol depending on the chemical and physical properties of the elements, contributing to elemental or isotopic fractionation. The composition difference between the examined material and analyzed aerosol is generally referred to as fractionation.

Ceramic matrices, compared to glasses, offer better mechanical properties, which are viable for the subsequent application, but in terms of LA-ICP-MS analysis, the higher material

hardness might go against effective laser ablation sampling, not necessarily in terms of worse sampling behaviour (cracking, thermal affection), but higher laser energy densities required, which produces a significant difference between the reference material (silicate) and the sample (ceramic).

The aim of this work is to verify the usability of this method for a wider range of glass and ceramic materials. Similar LA-ICP-MS applications include ceramic material content characterization [2], but also provenience studies of ancient ceramic samples based on elemental ratios and/or isotopic ratios [3-6].

Samples

For reference, SRM NIST standards were used - silicate glasses with certified content of wide range of elements [7, 8]. The elemental content ranges from tens of mg kg^{-1} for NIST 612 and hundreds of mg kg^{-1} for NIST 610. A synthetic obsidian material was also implemented. The matrix is a silicate (57 %_{m/m} SiO_2) with high content of rare earth elements (in a range of 100 to 300 mg kg^{-1}). Three ceramic materials were further tested: lithium disilicate based dental glass ceramic and two ceramic materials with ZrO_2 matrix, denoted as Ivoclar (Y-doped) and Longlife (Ce-doped). The placement of the samples during the analysis is shown in the figure 2 below.



Figure 2 sample holder with analyzed samples

EXPERIMENTAL

Instrumental setup

The study employed a 213 nm Nd:YAD solid-state laser (CETAC LSX+, USA) with installed Helix II ablation cell.

Table 1 Technical parameters of the laser ablation system

| Parameter | LSX+ |
|-------------------------|--|
| Manufacturer | Teledyne Cetac Technologies |
| Laser type | ND:YAG |
| Wavelength | 213 nm |
| Pulse duration | <4 ns |
| Repetition rate | 1-20 Hz |
| Aperture sizes | 20 sizes giving 3-160 μm circles. 5 sizes 10-150 μm squares (50 μm used) |
| Fluence (max. output) | 35 J cm^{-2} |
| Ablation cell | HelEx II |
| Carrier gas | He |
| Carrier gas flow | 1.00 l min^{-1} |
| Transport tubing length | <1 m |

The ICP-MS mass spectrometer Agilent 7900 is a quadrupole-based mass spectrometer equipped with a He flushed reaction cell (1 ml min^{-1} He).

Table 2 ICP-MS operating parameters

| | |
|------------------------|--|
| ICP-MS | Agilent 7900 |
| rf power | 1150 W |
| Cooling gas flow. Ar | 15.5 l min^{-1} |
| Auxiliary gas flow. Ar | 1.18 l min^{-1} |
| Sample gas flow. Ar | ~550 ml min^{-1} . |
| Resolution | Low (RP <1000) |
| Isotopes measured | 16 ^7Li , ^{23}Na , ^{24}Mg , ^{27}Al , ^{29}Si , ^{44}Ca , ^{47}Ti , ^{88}Sr , ^{89}Y , ^{90}Zr , ^{140}Ce , ^{178}Hf , ^{206}Pb , ^{208}Pb , ^{232}Th , ^{238}U method run: 1.182 s (1 scan) |

Quantification

Elemental content of major, minor and trace elements was calculated using the equation

(1)

$$C_{X \text{ norm.}}^{\text{sample}} = \frac{I_X^{\text{sample}} \cdot c_Y^{\text{sample}}}{I_Y^{\text{sample}}} \cdot \frac{c_X^{\text{standard}}}{c_Y^{\text{norm.}}}, \quad (1)$$

where X is the determined element, Y is the internal reference element/isotope, c denotes content and I denotes the background subtracted intensity. The content of internal reference in the sample is usually measured by an independent analytical approach.

NIST reference and obsidian glasses were used as standards, with reference values used from NIST reference glass certificates [7, 8] and the GeoRem database (<http://georem.mpch-mainz.gwdg.de>). The reference values for the obsidian in-lab reference were evaluated by ICP-MS and EDX.

The internal reference has to be present in the sample homogeneously and in excessive amount, e.g. as the matrix element. As the NIST and obsidian sample matrix is constituted mainly of Si, ^{29}Si was selected for internal reference. ^{90}Zr was selected as the internal reference for the two Zr-based dental ceramic materials.

Standard deviation values are expressed as a value of *corrected sample standard deviation* (2).

$$s = \sqrt{\frac{1}{N-1} \sum_{i=1}^N (x_i^2 - \bar{x})^2} \quad (2)$$

Limits of detection of this method (LOD) were calculated as three times the standard deviation (σ) of background signal, divided by sensitivity. Sensitivity was obtained by dividing the average signal response with subtracted background by elemental content in the sample (3).

$$LOD = \frac{3\sigma}{\text{sensitivity}} \quad (3)$$

The measure of the elemental fractionation is a fractionation index (FI) [9]. It is a ratio of second half of signal intensity to the first half, corrected to an abundant matrix element.

$$FI = \frac{\left(\frac{I_{M_{2/2}}}{I_{N_{2/2}}}\right)}{\left(\frac{I_{M_{1/2}}}{I_{N_{1/2}}}\right)} \quad (4)$$

where I_M is the intensity of the isotope with background subtracted. I_N is the background subtracted intensity of a correction isotope. Indices 1/2 and 2/2 indicate the first and second half of the signal curve.

Under optimal conditions, the sample ablation rate should be same throughout the ablation. Then the signal response is constant and the resulting FI is 1 (Fig. 3, dashed line). But in reality, the ablation pit grows deeper with continuous ablation, resulting in laser beam defocusing and decrease of the fluence. It also changes the size and amount of the ablated particles. With ablation pit recessing, the particles become more difficult to remove from the ablation pit, not mentioning the overall sample surface heating with continuous pulsing and excitation of laser-induced microplasmas, which also contribute to different rate of elemental evaporation. All these factors result in decreased signal intensity of observed element in time, resulting in FI dispersion.

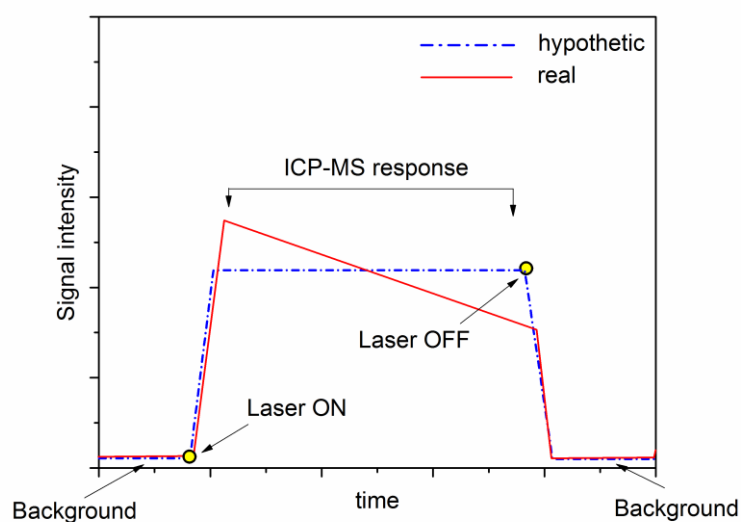


Figure 3 Illustration of fractionation on MS signal

Experimental setup

3 lines with fluence 6.5 J cm^{-2} were ablated with 213 nm laser beam on 2 NIST standards, synthetic obsidian, lithium disilicate and Zr-ceramics. The laser ablation was set up so that the $100 \text{ }\mu\text{m}$ laser beam would scan the sample surface at the speed of $37 \text{ }\mu\text{m s}^{-1}$ to prevent

excessive recession of the ablation crater. Laser pulse frequency was 10 Hz. FI was evaluated and compared to observe the contribution of sample properties and laser ablation mode to the extent of fractionation. Elemental contents were then calculated in NIST612 (verification), synthetic obsidian, lithium disilicate and Zr-ceramics (Y- and Ce- doped).

RESULTS AND DISCUSSION

Fractionation on glass vs. ceramic materials

Figure 4 shows the plotted values of FI for each of the measured isotopes. The more closer the values are to 1, the lesser the extent of fractionation effects is. We can observe lower value variance in the case of glass materials. The SiO₂ matrix in NIST 612 and NIST 610 is well ablated and therefore the size distribution of ablated particles is narrower and shifted towards smaller particles, which are effectively ionized in ICP torch with no further fractionation in the plasma interface (space charge effect). NIST 610 has elemental content of metallic elements (almost the whole periodic system except matrix elements of the silicate matrix) one order higher than NIST 612, and the higher signal intensity resulted in lower standard deviation values.

The black color of the synthetic obsidian sample could contribute to earlier onset of thermal effects on the sample surface, mainly because of the higher absorption in the interaction spot. The more energy is coupled with the surface, the more heat could be generated. Different laser beam interaction with the obsidian material was visually observed compared to the NIST SRM materials, which are lighter in colour (blue tint). However it is not reflected in calculated FI.

The situation significantly changes during the ablation of ceramic samples. Most of the measured isotopes were not detected in abundance (close to LOD), as these materials are manufactured for dental prosthetics and thus their elemental composition is carefully assessed. However, the FI values for the matrix components in lithium disilicate glass ceramic (Al, Li, S) show bigger variance than in the case of glass materials. This phenomenon could be caused by higher hardness of the material, where the sample surface was not easily ablated by the line scan laser ablation and the ablated line exhibited signs of cracking on the edges. To further describe the ablation process on zirconium oxide ceramics, the laser parameters will be optimized to achieve more consistent ablation.

213 nm Nd:YAG laser induced fractionation
 6.2 J cm⁻², 10 Hz, 30 μm beam diameter
 line scan 60 s, 37 μm s⁻¹

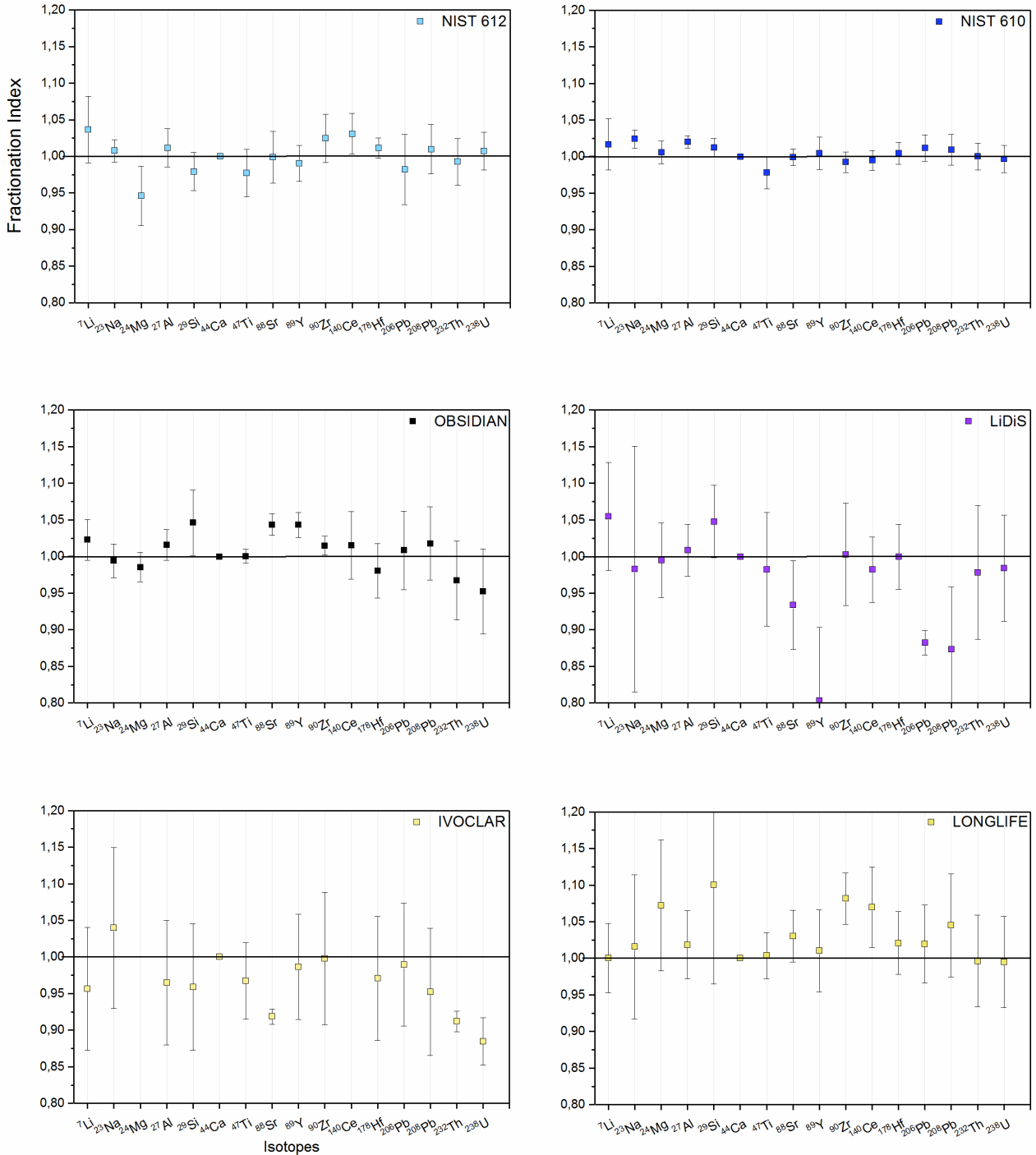


Figure 4 A 213 nm laser induced fractionation of the NIST SRMs, obsidian and zirconia ceramic materials.

Quantification of the elemental content in materials using glass standards

Tables and figures below illustrate the calculated results. The missing values (columns) are due to unavailable reference contents in obsidian standard and ceramic materials.

Table 3 and Figure 5 comprise the quantification results for the NIST 612 glass standard (for verification purposes). Only in the case of using an obsidian standard as a reference, the calculated content differed for several elements (Na, Al, Ca, Ce, Zr, Pb). This difference was not observed if NIST 610 was used as a reference material. Matrix composition and physicochemical properties (high Fe content, black tint) can decrease the trueness of the calculated content – the ablated aerosol does not necessarily correspond to the composition of the bulk material. On top of that, the difference in irradiance or energy density between the standard and the sample must be also taken into consideration.

Table 4 and Figure 6 are related to the quantification of the synthetic obsidian material. Another independent reference value might be needed in order to resolve the disagreement for the values of Ca and Ce.

Comparison of the values displayed in Table 5 and Figure 7 yields similar conclusion: the underestimated content of Na and Ca in lithium disilicate glass ceramic and the overestimation of Ce content (higher for obsidian quantified values) might be caused by matrix indifference.

The Ivoclar ceramic (Y-doped) quantification mismatched only in the case of Al and Y. and the matrix effects might be the cause of decreased trueness.

The surface of Ce-doped Longlife ceramic has been corroded beforehand, which explains the underestimation of Sr content. On the other hand, Sr is present in ceramic Sr-Al phase, so the overestimation of Al content does not correspond well to this conclusion, and more data are required to describe the inconsistency in this case.

Table 8 comprises the calculated LOD (3σ) values.

Table 3 Quantification of the NIST 612 content on NIST 610 and obsidian standard (verification)

| | | NIST 610 | | OBSIDIAN | | reference values |
|---------------------------------------|------------------|----------|-------|----------|-------|------------------|
| Content and SD (% _{m/m}) | | | | | | |
| Element | int. ref. | c | sd | c | sd | c |
| Si | ²⁹ Si | ~ | ~ | ~ | ~ | 34.3 |
| Ca | | 8.504 | 0.079 | 5.258 | 0.049 | 8.5 |
| Na | | 10.52 | 0.14 | 8.75 | 0.11 | 10.6 |
| Content and SD [mg kg ⁻¹] | | | | | | |
| Li | ²⁹ Si | 41.59 | 0.74 | 41.74 | 0.74 | 40.2 |
| Mg | | 65.20 | 1.88 | 65.40 | 1.89 | 68 |
| Al | | 10586.58 | 66.45 | 10090.89 | 63.34 | 10900 |
| Ti | | 40.41 | 0.34 | 40.30 | 0.34 | 44 |
| Sr | | 78.60 | 1.38 | ~ | ~ | 78.4 |
| Y | | 38.56 | 0.88 | 36.06 | 0.82 | 38.3 |
| Zr | | 38.61 | 0.70 | 32.71 | 0.59 | 37.9 |
| Ce | | 38.48 | 0.98 | 49.99 | 1.27 | 38.4 |
| Hf | | 36.23 | 0.94 | ~ | ~ | 36.7 |
| Pb | | 40.56 | 1.48 | 46.61 | 1.70 | 38.57 |
| Th | | 37.08 | 0.98 | ~ | ~ | 37.79 |
| U | | 37.51 | 0.91 | ~ | ~ | 37.38 |

Elemental content in NIST 612 glass
 references - NIST 612, NIST 610, synthetic obsidian
 internal reference element - ²⁹Si

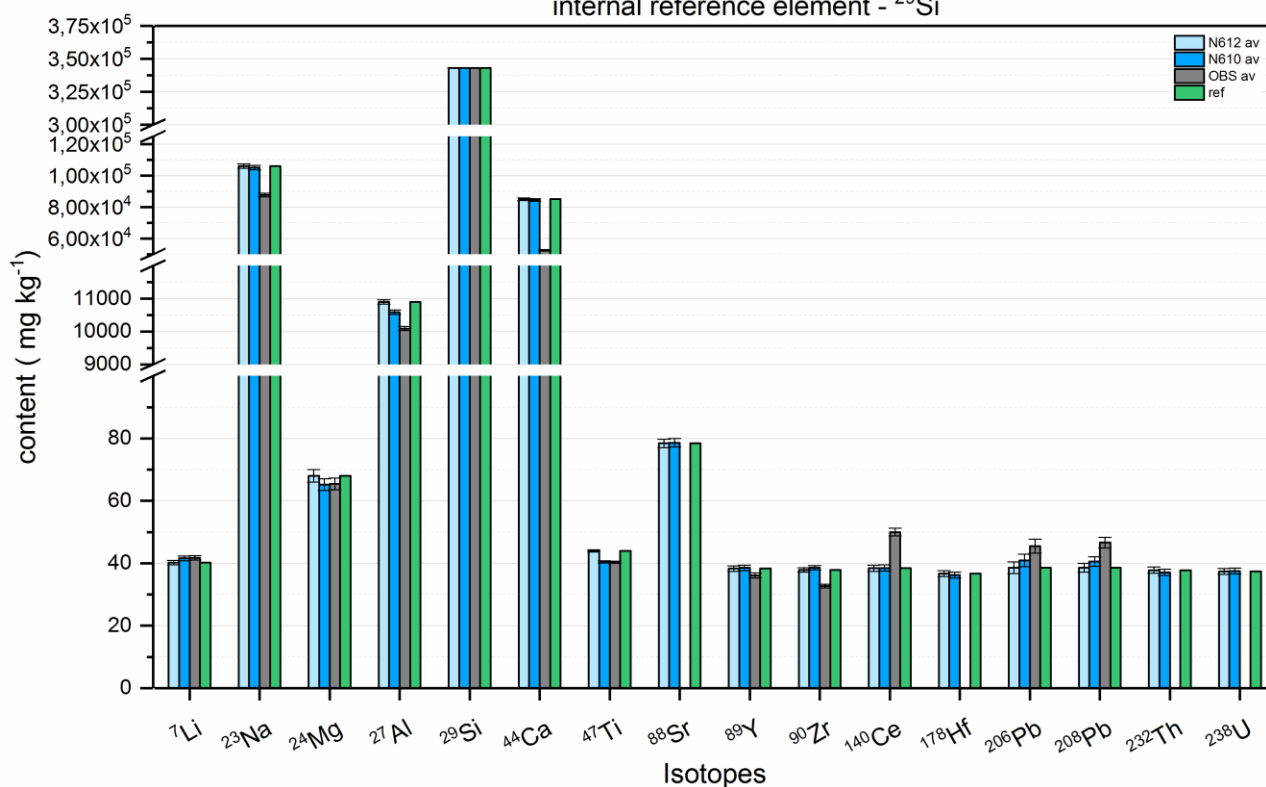


Figure 5 NIST 612 quantification

Table 4 Quantification of the obsidian content on NIST 612 and NIST 610 SRM

| | | NIST 612 | | NIST 610 | | reference values |
|---------------------------------------|------------------|-----------|----------|-----------|----------|------------------|
| Content and SD (% _{m/m}) | | | | | | |
| Element | int. ref. | c | sd | c | sd | c |
| Si | ²⁹ Si | ~ | ~ | ~ | ~ | 26.7 |
| Ca | | 4.80 | 0.10 | 4.76 | 0.11 | 2.96 |
| Na | | 0.681 | 0.031 | 0.675 | 0.031 | 0.561 |
| Content and SD [mg kg ⁻¹] | | | | | | |
| Li | ²⁹ Si | 350.801 | 30.475 | 362.927 | 31.529 | 362.8 |
| Mg | | 13816.592 | 341.483 | 13246.113 | 327.383 | 13273 |
| Al | | 85468.461 | 1381.789 | 83006.545 | 1341.986 | 79065 |
| Ti | | 4942.387 | 112.466 | 4539.364 | 103.295 | 4523 |
| Sr | | 210.163 | 3.179 | 210.680 | 3.187 | ~ |
| Y | | 386.366 | 3.940 | 388.902 | 3.966 | 363.6 |
| Zr | | 214.208 | 2.073 | 218.195 | 2.112 | 184.8 |
| Ce | | 279.185 | 7.640 | 279.755 | 7.656 | 363 |
| Hf | | 5.493 | 0.116 | 5.422 | 0.115 | ~ |
| Pb | | 155.077 | 11.145 | 163.045 | 11.717 | 186.8 |
| Th | | 5.876 | 0.333 | 5.764 | 0.327 | ~ |
| U | | 0.336 | 0.020 | 0.337 | 0.020 | ~ |

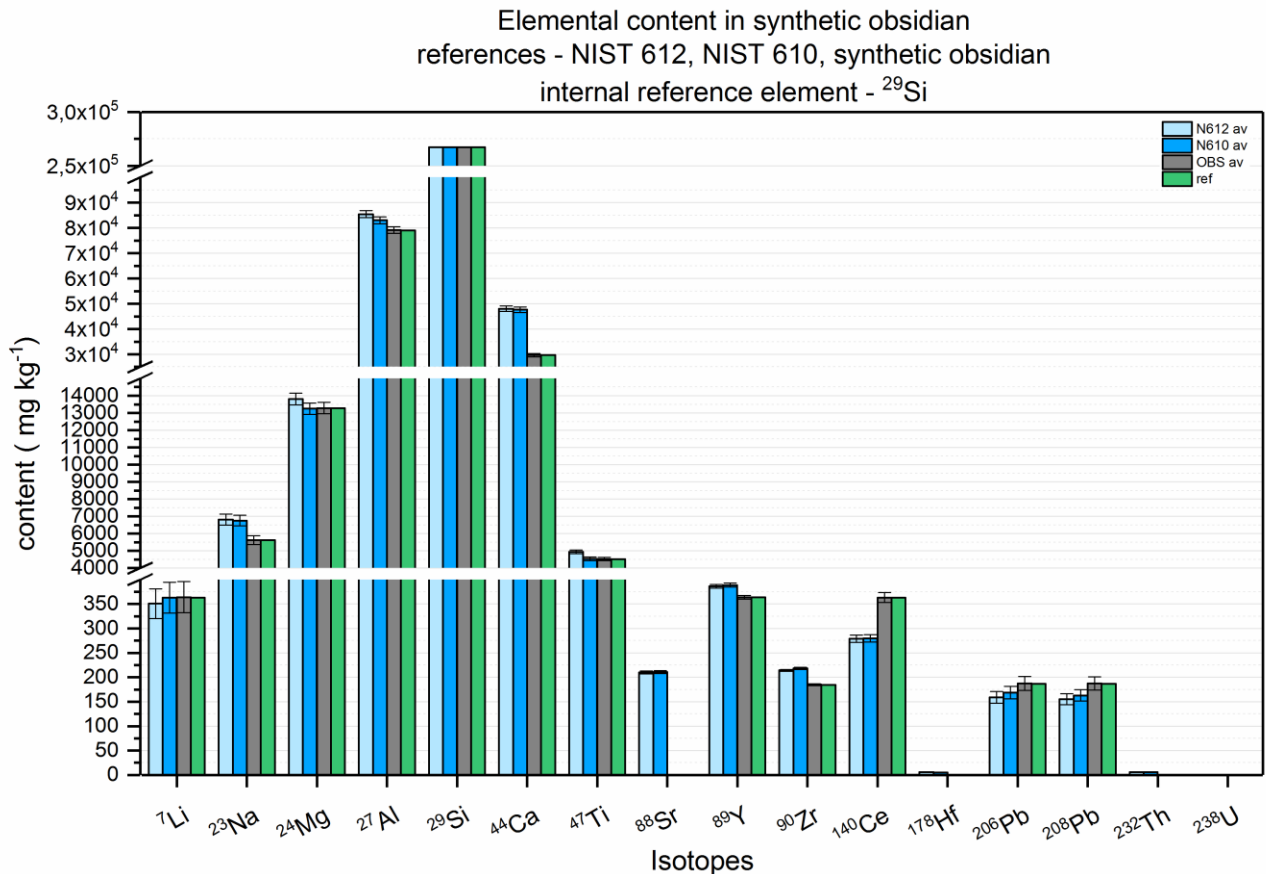


Figure 6 Synthetic obsidian quantification

Table 5 Quantification of the lithium disilicate content on NIST 612, NIST 610 and obsidian standard

| | | NIST 612 | | NIST 610 | | OBSIDIAN | | reference values |
|---------------------------------------|------------------|----------|--------|----------|--------|----------|--------|------------------|
| Element | int. ref. | c | sd | c | c | c | sd | s |
| Li | ²⁹ Si | 6.23 | 0.71 | 6.45 | 0.73 | 6.471 | 0.073 | 6.66 |
| Al | | 1.6987 | 0.0083 | 1.6498 | 0.0081 | 1.5726 | 0.0077 | 1.7888 |
| Si | | ~ | ~ | ~ | ~ | ~ | ~ | 32.88 |
| Content and SD [mg kg ⁻¹] | | | | | | | | |
| Na | ²⁹ Si | 442.25 | 13.63 | 438.53 | 13.51 | 365.11 | 11.25 | 940.61 |
| Mg | | 1396.15 | 15.07 | 1338.50 | 14.45 | 1342.63 | 14.49 | ~ |
| Ca | | 632.19 | 44.24 | 627.67 | 43.92 | 390.86 | 27.35 | 1095.91 |
| Ti | | 133.94 | 4.69 | 123.02 | 4.31 | 122.69 | 4.30 | ~ |
| Sr | | 6.55 | 0.06 | 6.56 | 0.06 | 0.00 | 0.00 | ~ |
| Y | | 13.07 | 0.35 | 13.16 | 0.36 | 12.31 | 0.33 | ~ |
| Zr | | 5485.32 | 63.00 | 5587.41 | 64.18 | 4734.05 | 54.37 | ~ |
| Ce | | 15577.27 | 265.28 | 15609.05 | 265.82 | 20276.78 | 345.32 | 9253.68 |
| Hf | | 119.67 | 0.35 | 118.13 | 0.34 | 0.00 | 0.00 | ~ |
| Pb | | 5.20 | 0.28 | 5.47 | 0.29 | 6.29 | 0.34 | ~ |
| Th | | <LOD | ~ | <LOD | ~ | <LOD | ~ | ~ |
| U | | <LOD | ~ | <LOD | ~ | <LOD | ~ | ~ |

Elemental content in lithium disilicate ceramic references - NIST 612, NIST 610, synthetic obsidian
internal reference element - ²⁹Si

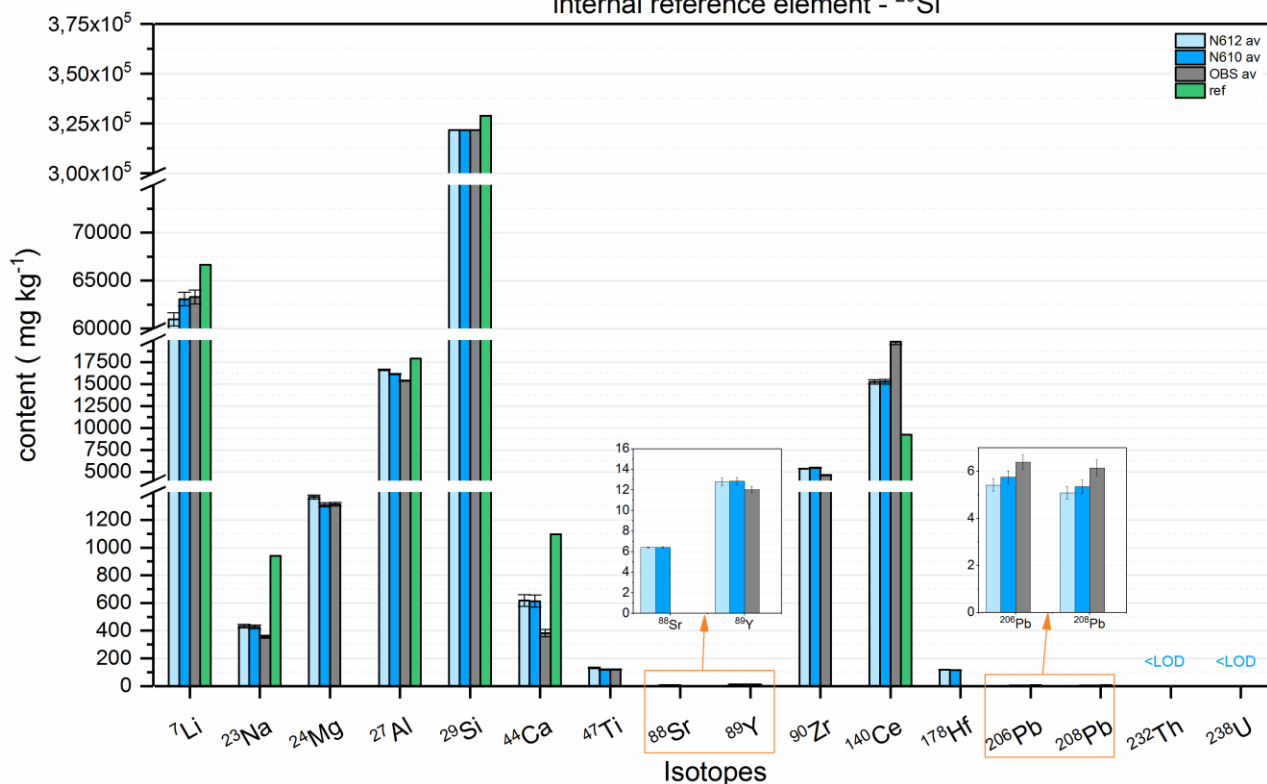


Figure 7 Lithium disilicate quantification

Table 6 Quantification of the Ivoclar Y doped Zr ceramic Ivoclar content on NIST 612, NIST 610 and obsidian standard

| NIST 610 | | NIST 612 | | NIST 610 | | OBSIDIAN | | reference values |
|---------------------------------------|------------------|----------|--------|----------|--------|----------|---------|------------------|
| Element | int. ref. | c | sd | c | c | c | sd | s |
| Y | ⁹⁰ Zr | 4.772 | 0.098 | 4.715 | 0.097 | 5.21 | 0.11 | 4.42 |
| Zr | ~ | ~ | ~ | ~ | ~ | ~ | ~ | 709300 |
| Hf | | 1.673 | 0.030 | 1.62 | 0.029 | ~ | ~ | 1.82 |
| Content and SD [mg kg ⁻¹] | | | | | | | | |
| Na | ⁹⁰ Zr | 65.045 | 2.970 | 63.319 | 2.891 | 62.221 | 2.841 | ~ |
| Mg | | 12.708 | 0.388 | 11.961 | 0.365 | 14.161 | 0.432 | ~ |
| Ca | | 1246.152 | 19.950 | 1188.143 | 19.021 | 1336.657 | 21.399 | 800 |
| Ti | | 330.796 | 70.592 | 324.751 | 69.302 | 383.291 | 81.794 | ~ |
| Sr | | 753.974 | 13.452 | 734.899 | 13.112 | 540.125 | 9.637 | ~ |
| Y | | 2704.078 | 95.868 | 2438.195 | 86.441 | 2869.997 | 101.750 | ~ |
| Zr | | 1.082 | 0.054 | 1.065 | 0.053 | ~ | ~ | ~ |
| Ce | | 0.356 | 0.031 | 0.350 | 0.031 | 0.537 | 0.047 | ~ |
| Pb | | 1.214 | 0.037 | 1.253 | 0.038 | 1.700 | 0.051 | ~ |
| Th | | 0.075 | 0.004 | 0.072 | 0.004 | ~ | ~ | ~ |
| U | | 0.057 | 0.002 | 0.057 | 0.002 | ~ | ~ | ~ |

Elemental content in yttrium doped zirconium oxide ceramic (Ivoclar) references - NIST 612, NIST 610, synthetic obsidian
internal reference element - ⁹⁰Zr

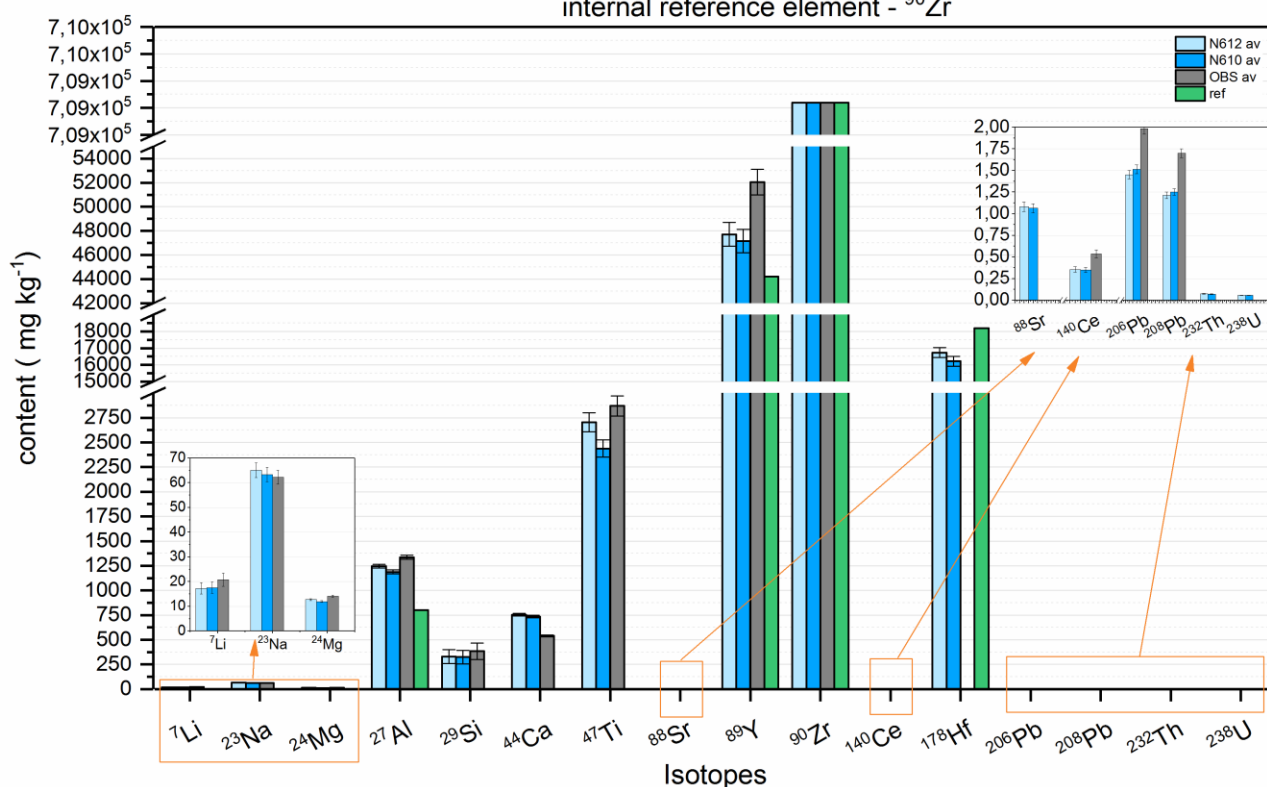


Figure 8 Y doped Zr ceramic Ivoclar quantification

Table 7 quantification of the Ivoclar Ce doped Zr ceramic Longlife content on NIST 612, NIST 610 and obsidian standard

| NIST 610 | | NIST 612 | | NIST 610 | | OBSIDIAN | | reference values |
|---------------------------------------|------------------|-----------|---------|-----------|---------|-----------|---------|------------------|
| Element | int. ref. | c | sd | C | c | c | sd | s |
| Ce | ⁹⁰ Zr | 12.35 | 0.13 | 12.15 | 0.13 | 18.63 | 0.20 | 12.46 |
| Zr | ~ | ~ | ~ | ~ | ~ | ~ | ~ | 64.15 |
| Hf | | 1.5827 | 0.0053 | 1.5338 | 0.0051 | ~ | ~ | ~ |
| Content and SD [mg kg ⁻¹] | | | | | | | | |
| Li | ⁹⁰ Zr | 13.443 | 2.002 | 13.654 | 2.033 | 16.170 | 2.408 | ~ |
| Na | | 34.323 | 1.336 | 33.412 | 1.301 | 32.833 | 1.278 | ~ |
| Mg | | 4.629 | 0.389 | 4.357 | 0.366 | 5.158 | 0.434 | ~ |
| Al | | 54194.394 | 624.746 | 51671.606 | 595.663 | 58130.400 | 670.119 | 14160.000 |
| Si | | 293.476 | 23.042 | 288.114 | 22.621 | 340.049 | 26.699 | ~ |
| Ca | | 1928.441 | 43.760 | 1879.652 | 42.653 | 1381.478 | 31.348 | ~ |
| Ti | | 2474.883 | 8.158 | 2231.537 | 7.356 | 2626.740 | 8.659 | ~ |
| Sr | | 6686.404 | 52.557 | 6580.380 | 51.724 | ~ | ~ | 9290.000 |
| Y | | 73.085 | 0.939 | 72.221 | 0.928 | 79.728 | 1.024 | ~ |
| Pb | | <LOD | ~ | <LOD | ~ | <LOD | ~ | ~ |
| Th | | <LOD | ~ | <LOD | ~ | <LOD | ~ | ~ |
| U | | <LOD | ~ | <LOD | ~ | <LOD | ~ | ~ |

Elemental content in cerium doped zirconium oxide ceramic (Longlife) references - NIST 612, NIST 610, synthetic obsidian internal reference element - ²⁹Si

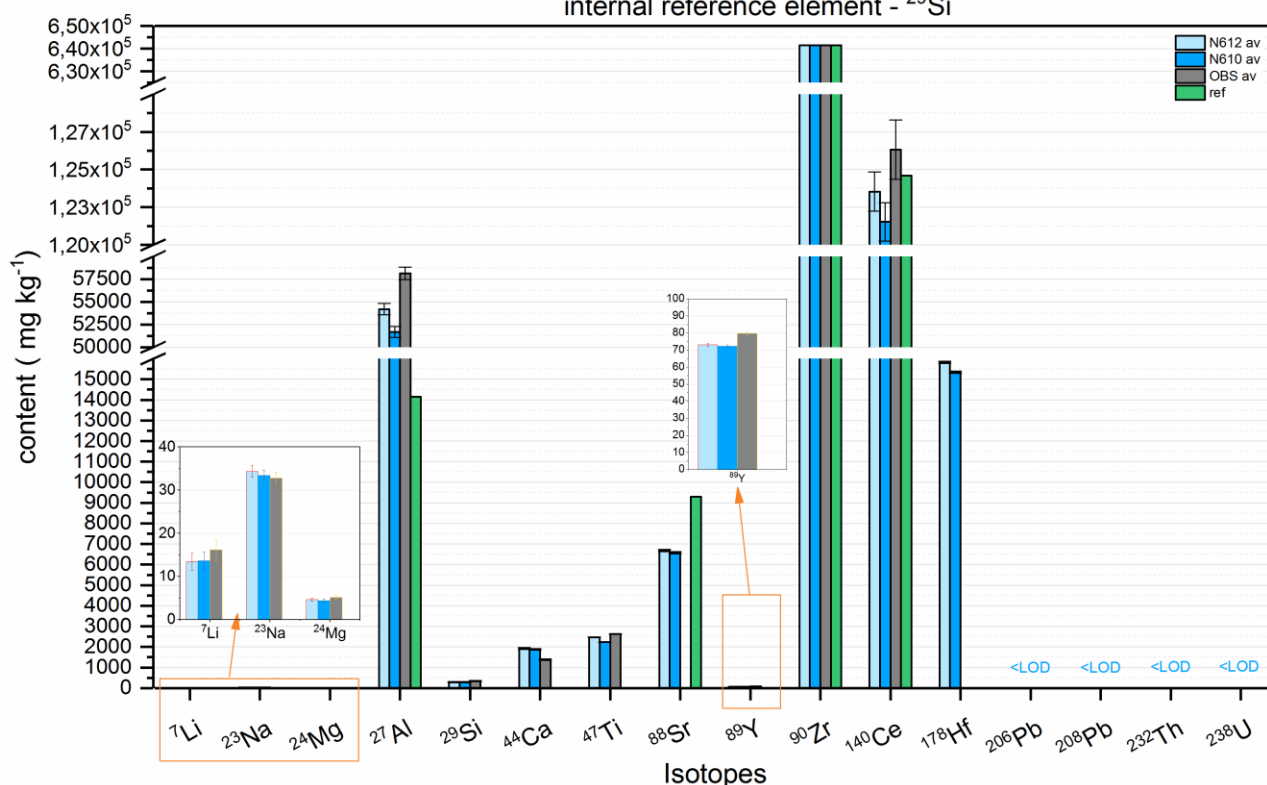


Figure 9 Ce doped Zr ceramic Longlife quantification

Table 8 calculated limits of detection

| | LOD (3σ) mg kg ⁻¹ |
|----|---------------------------------------|
| Li | 8.9 |
| Na | 6.4 |
| Mg | 0.442 |
| Al | 2.1 |
| Si | 953 |
| Ca | 223 |
| Ti | 1.7 |
| Sr | 0.011 |
| Y | 0.0082 |
| Zr | 0.0073 |
| Ce | 0.0033 |
| Hf | 0.019 |
| Pb | 0.028 |
| Th | 0.022 |
| U | 0.0062 |

CONCLUSION

The application of LA-ICP-MS as a microanalytical quantification tool for a range of glass, glass-ceramic and ceramic materials proved itself to provide low limits of detection and results with relatively high precision and trueness. The inconsistencies only show that the matrix matching of a reference material and analyzed sample is a crucial step in the quantification process.

ACKNOWLEDGEMENT

The financial support of this work by the project SAS-MOST JRP 2015/6, VEGA 1/0631/14, VEGA 2/0026/17, and APVV 0014-15 is gratefully acknowledged. This publication was created in the frame of the project "Centre of excellence for ceramics, glass, and silicate materials" ITMS code 262 201 20056, based on the Operational Program Research and Development funded from the European Regional Development Fund.

REFERENCES

- [1] R.E. March, A.W. McMahon, F.A. Londry, R.L. Alfred, J.F.J. Todd, F. Vedel, RESONANCE EXCITATION OF IONS STORED IN A QUADRUPOLE ION TRAP .1. A SIMULATION STUDY, *International Journal of Mass Spectrometry and Ion Processes*, 95 (1989) 119-156.
- [2] M. Ovari, G. Tarsoly, Z. Nemeth, V.G. Mihucz, G. Zaray, Investigation of lanthanum-strontium-cobalt ferrites using laser ablation inductively coupled plasma-mass spectrometry, *Spectrochimica Acta Part B-Atomic Spectroscopy*, 127 (2017) 42-47.
- [3] E.E. Cochrane, T.M. Rieth, Samoan artefact provenance reveals limited artefact transfer within and beyond the archipelago, *Archaeology in Oceania*, 51 (2016) 150-157.
- [4] N. Sharratt, M. Golitko, R. Williams, Pottery production, regional exchange, and state collapse during the Middle Horizon (A. D. 500-1000): LA-ICP-MS analyses of Tiwanaku pottery in the Moquegua Valley, Peru, *Journal of Field Archaeology*, 40 (2015) 397-412.
- [5] D. Gunther, B. Hattendorf, Solid sample analysis using laser ablation inductively coupled plasma mass spectrometry, *Trac-Trends in Analytical Chemistry*, 24 (2005) 255-265.
- [6] D. De Muynck, F. Vanhaecke, Development of a method based on inductively coupled plasma-dynamic reaction cell-mass spectrometry for the simultaneous determination of phosphorus, calcium and strontium in bone and dental tissue, *Spectrochimica Acta Part B-Atomic Spectroscopy*, 64 (2009) 408-415.
- [7] NIST 610 certificate of analysis, <https://www-s.nist.gov/srmors/certificates/610.pdf>, in.
- [8] NIST 612 certificate of analysis; <https://www-s.nist.gov/srmors/certificates/612.pdf>, in.
- [9] R. Machida, T. Nakazawa, N. Furuta, Temporal Changes of Fractionation Index Caused by Changes in the Large Size of Ablated Particles in Laser Ablation-Inductively Coupled Plasma Mass Spectrometry, *Analytical Sciences*, 31 (2015) 345-355.

VYUŽITÍ ATOMOVÉ SPEKTROMETRIE PRO STANOVENÍ OBSAHU LITHIA VE SKLOKERAMICKÝCH MATERIÁLECH

DETERMINATION OF LITHIUM IN GLASS CERAMIC MATERIALS USING ATOMIC SPECTROMETRY

Hana Kaňková, Dagmar Galusková

Centre for Functional and Surface Functionalized Glass

Alexander Dubček University of Trenčín

Corresponding author: hana.kankova@tnuni.sk

ABSTRACT

Inductively coupled plasma optical emission spectrometry (ICP OES) was applied for determination of the chemical composition of following materials: lithium disilicate (LiS₂) glass ceramic and aluminium silicate glass (obsidian, AlSi-Gl). Prior to analysis, the solid material needs to be transferred to aqueous solution. Microwave assisted decomposition in a mixture of mineral acids (aqua regia) was optimised to dissolve LiS₂ and obsidian. Complete digestion process was achieved with the addition of hydrofluoric acid. Complexation with H₃BO₃ or HBF₄ was included in the digestion process in order to remove residues of HF from the solution. Major and minor elements were determined by ICP OES. Traces of metal and rare earth elements in LiS₂ and obsidian were determined by ICP MS. The content of Li₂O in LiS₂ glass-ceramics reached the value of 7 wt%, however using aqua regia as reagent acids was not sufficient for complete dissolution of powder specimen. Including HF into reagent mixture resulted in increase of the content of Li₂O from 7 wt% to 14 wt%. The presented analytical method enables complex determination of oxide composition of the glass-ceramic materials including the oxides, whose determination by other analytical methods is problematic, e.g. Li₂O, B₂O₃ and SiO₂ with the relative standard deviation from 0.3 to 1.5 wt%.

ÚVOD

Stanovení chemického složení materiálů je nevyhnutným předpokladem pro jejich charakterizaci z hlediska mechanických, funkčních a případně i chemických vlastností. Výběr a použití příslušné metody se odvíjí od několika faktorů: citlivost analytické metody, meze

stanovitelnosti prvků, či množství a rozměrů analyzovaného vzorku. Pro analýzu skleněných či keramických vzorků jsou používány především metody rentgenové fluorescenční spektrometrie (RFS), elektronové mikroskopie (SEM EDS/WDS). Méně populární jsou metody optické nebo hmotnostní spektrometrie s iontově vázanou plazmou (ICP-OES, ICP-MS) řazené mezi roztokovou analýzu. Tyto metody jsou časově náročné a vyžadují precizní laboratorní zručnost, navíc vzorek je při přípravě k analýze zcela zničen. Prvně jmenované metody nepatří k „destruktivním“ metodám, avšak jejich použití je limitováno při stanovení lithia a boru. ICP OES a MS umožňují kvantitativní stanovení v širokém koncentračním rozsahu s minimální koncentrací Li a B v řádech 0,01 a 0,1 ppm.

Ideálním způsobem převedení tuhé látky do roztoku je takový způsob rozkladu, kdy se celý vzorek rozpustí za vzniku produktů definovaného složení a dosáhne se tak úplné destrukce vzorku. Tavení pomocí vhodných tavidel (např. boritan lithný, tetraboritan lithný, uhličitán sodný) byl donedávna nejrozšířenější způsob rozkladu vzorků skla. Tímto rozkladným způsobem však ztrácíme možnost stanovení boru či lithia ve vzorcích. V souvislosti s rozšířením instrumentální plazmové spektrometrie došlo k požadavkům na stanovení obsahu sodíku, lithia či boru a odklonu od rozpouštění skleněných materiálů tavením a došlo k nárůstu rozkladů a analýz materiálů pomocí kyseliny fluorovodíkové, která je při analýzách skla a sklářských surovin hlavním rozpouštědlem způsobujícím destrukci silikátových struktur [2].

Rozklad kyselinou fluorovodíkovou obvykle probíhá v přítomnosti silné minerální kyseliny (např. kyselina dusičná). Kyselina fluorovodíková má ovšem silné komplexotvorné vlastnosti, komplexy vytváří s Al, Be, Co, Cr, Fe, Ga, Ge, Hf, In, Mn, Nb, Sb, Ta, Ti, Zr. V některých případech proto může docházet k interferencím, které se mohou projevit snížením koncentrace prvku ve vzorku. Za určitých podmínek tvoří kyselina fluorovodíková stabilní, nerozpustné fluoridy – jedná se o kovy alkalických zemin, Li, Cu, La, Pb, Sc, Y, Zn a prvky vzácných zemin. Kyselina fluorovodíková tvoří rovněž řadu prehavých fluoridů (např. AsF_3 , BF_3 , PF_3 , SeF_6 , SiF_6) z nichž některé mají teplotu varu nižší než 0°C . Pokud má být ve směsi stanoven i křemík, je po ukončení rozkladu ke směsi přidáván nadbytek H_3BO_3 , který váže přebytek HF jako HBF_4 [1 - 3]. Komplexace se rovněž provádí pro ochranu skleněných částí přístroje [4]. Některé zdroje ovšem uvádí, že přídavek kyseliny borité způsobuje při analýze významný „matrix efekt“, což může mít za následek až 20% snížení citlivosti při stanovení Mo, Ni, Pb, Sb, Se, Sn a až 50% při stanovení P [5]. Pro komplexaci HF lze alternativně využít i kyseliny tetrafluoroborité. Některé zdroje kyselinu tetrafluoroboritou používají ve směsi s kyselinou fluorovodíkovou nebo místo ní [5 - 7].

Pro ověření metody rozkladu s využitím minerálních kyselin jsme zvolily komerčně dostupný syntetický dentální sklo-keramický materiál na bázi lithium disilikátu (Li₂S) s obsahem Li na úrovni přibližně 14 hm% a v laboratoři připravené obtížně rozložitelné hlinitokřemičité sklo označované jako AlSi-GI s obsahem Li < 0,50 hm%. Použití různých minerálních kyselin a zařazení různých postupů pro vyvázání zbytkové HF se uskutečnilo s cílem vybrat ekonomicky a časově nejefektivnější způsob přípravy vzorku pro úplnou kvantifikaci složení zkoušených materiálů.

EXPERIMENTÁLNÍ ČÁST

Úplná destrukce vybraných vzorků se uskutečnila ve směsi minerálních kyselin teplem generovaným mikrovlnným zářením. Pro kontrolu mikrovlnného rozkladu a validaci získaných dat byl používán referenční materiál NCS DC 61104 (Eutal-borokřemičité sklo). Vzorky Li₂S, AlSi-GI a referenčního materiálu NCS DC 61104 byly rozdrceny a homogenizovány v achátové misce. K 20 mg vzorku s průměrnou velikostí zrn < 0,025 mm byly ve všech případech přidány 2 ml HNO₃ (65%, ANALPURE, Analytika Ltd.) a 6 ml HCl (47%, SUPRAPURE, Merck) a podle typu rozkladu i ostatní kyseliny (Tabulka 1). Byly provedeny čtyři série rozkladů, při prvním postupu byl rozklad proveden pouze lučavkou královskou (AR – aqua regia), tzn směs HNO₃ a HCl v poměru 1:3. Rozkladné nádoby byly po částečném zreagování reakčních činidel vloženy do rotoru mikrovlnného rozkladného zařízení (SPEEDWAVE 4, Berghof). Teplotní program aplikovaný pro mikrovlnný rozklad zkoumaných materiálů je podrobně uveden v Tabulce 2. Po ukončení rozkladu je obsah nádobky kvantitativně převeden do odměrných baněk demineralizovanou vodou. S každým typem rozkladu byl za stejných podmínek uskutečněn i slepý pokus (*blank*) a rozklad referenčního materiálu pro validaci rozkladné metody a získaných dat.

Tabulka 1: Přehled kyselin přidávaných během jednotlivých rozkladů.

| Postup | HNO ₃ / ml | HCl / ml | HF / ml | Komplexace |
|---|-----------------------|----------|---------|---------------------------------------|
| 1: AR (aqua regia) | 2 | 6 | - | - |
| 2: AR+HF | 2 | 6 | 1 | - |
| 3: AR+HF+H ₃ BO ₃ | 2 | 6 | 1 | H ₃ BO ₃ / 7 ml |
| 4: AR+HF+HBF ₄ | 2 | 6 | 1 | HBF ₄ / 1 ml |

Tabulka 2: Teplotní program mikrovlnného rozkladu.

| Teplota / °C | Ohřev / min | Výdrž / min |
|--------------|-------------|-------------|
| 150 | 10 | 5 |
| 180 | 5 | 10 |
| 210 | 5 | 40 |
| 50 | 1 | 10 |

Prvková analýza získaných čirých roztoků byla provedena na ICP OES (5100 SVDV ICP-OES, Agilent) dvěma způsoby. V prvním případě byly připraveny kalibrační roztoky a ověřovací roztoky ředěním certifikovaných referenčních materiálů (ASTASOL, Analytika Ltd.) s použitím Sc jako vnitřního standardu pro korekci vlivu matrice jednotlivých vzorků. Druhým způsobem stanovení koncentrace je tzv. metoda „*matrix matching*“. V tomto případě nebyly kalibrační a ověřovací roztoky připraveny ve zředěné kyselině dusičné ale pro eliminaci vlivu matrice na stanovení (viskozita měřených vzorků, ovlivnění ionizačních poměrů v plazmě a podobně) byly přidány přímo do matrice – roztoku *blanku*. Podmínky měření jsou uvedeny v Tabulce 3. U většiny prvků byla intenzita zaznamenávána v axiální ose hořáku, radiální pozorování bylo nastaveno pro vápník a lithium. Z důvodů přítomnosti kyseliny fluorovodíkové ve vzorcích byly při měření použity teflonové součásti ICP-OES a speciálně upravený hořák.

Tabulka 3: Podmínky měření na ICP-OES

| | | |
|------------------------|----------------------------------|--|
| <i>RF power: 1,2kW</i> | <i>Průtok Ar: 0,55 l/min</i> | <i>Radiální plasma: pozorovací výška: 9 mm</i> |
| <i>Axiální plasma</i> | <i>Rozprašovač: koncentrický</i> | <i>Mlžná komora: cyklónová</i> |

VÝSLEDKY

V tabulkách 4, 5 a 6 jsou uvedeny hmotnostní procenta jednotlivých oxidů v LiS₂, AlSi-Gl a Eutalu v závislosti na aplikovaných rozkladných kyselinách porovnané s tabelovanými hodnotami (obsah oxidů pro LiS₂ je získaný z [8]). V první části byl efekt matrice vzorků po rozkladech korigován kontinuálním měřením vnitřního standardu (Sc 361 nm) a v druhé části tabulek 4, 5 a 6 jsou hmotnostní procenta spočtena na základě měření koncentrace metodou „*matrix matching*“. Z uvedených tabulek je zřejmé, že rozklad pouhou lučavkou královskou není pro rozklad LiS₂ a AlSi-Gl dostačující. Všechny vzorky po rozkladu lučavkou byly zakalené, z čehož vyplývá, že rozklad nebyl úplný. Přidáním kyseliny fluorovodíkové došlo k úplné destrukci a i u LiS₂ a AlSi-Gl došlo k nárůstu zjišťovaných obsahů kovů. Srovnáním tabelovaných a naměřených hodnot se nepotvrdil očekávaný únik těkavých fluoridů a i hodnoty hmotnostních procent oxidu křemičitého lze oproti očekávání považovat za odpovídající. Získané roztoky byly čiré, nedošlo ani k vysrážení nerozpustného fluoridu vápenatého. Přidáním kyseliny borité či tetrafluoroborité nedošlo k významnému poklesu stanovených hodnot v případě, že byly kalibrační roztoky připraveny ve zředěné kyselině dusičné. Pokud byla kalibrace prováděna přímo v matrici vzorku (prvkové standardy byly přidány do matrice

slepého stanovení) došlo k poklesu stanoveného obsahu P_2O_5 u vzorku LiS2. Vyšší obsah P_2O_5 byl ale pouze u LiS2, proto nelze potvrdit vliv B na stanovení P pomocí ICP-OES.

Obsah P_2O_5 a CeO_2 byl u LiS2 <3 hm%, B_2O_3 , CaO, MgO, MnO_2 a Na_2O byl < 0,5 hm%. U AlSi-Gl byl obsah Fe_2O_3 a K_2O okolo 4 hm%, CeO_2 , MnO_2 , Na_2O , P_2O_5 , < 0,5 hm%. U referenčního skla byl obsah všech stanovovaných oxidů mimo ty uvedené v Tabulce 6, méně než 0,5 hm%.

Tabulka 4: Chemické složení pro LiS2 sklo-keramický materiál uvedené jako hm% v závislosti podle použitých kyselin

| LiS2 | korekce nespektrálních interferencí wt% | | | | | | | |
|------------------------|---|--------|---------|---------|-------------------|--------|---------|---------|
| | vnitřním standardem Sc | | | | "matrix matching" | | | |
| tabelované kyseliny | Al_2O_3 | K_2O | Li_2O | SiO_2 | Al_2O_3 | K_2O | Li_2O | SiO_2 |
| | 4,8 | 4,5 | 14,6 | 72 | 4,8 | 4,5 | 14,6 | 72 |
| AR | 0,56 | 1,41 | 6,38 | 4,33 | x | x | x | x |
| AR+HF | 3,38 | 4,14 | 14,35 | 70,34 | x | x | x | x |
| AR+HF+H3BO3 | 3,32 | 3,85 | 13,66 | 68,96 | 3,24 | 3,84 | 14,76 | 64,28 |
| AR+HF+HBF4 | 3,41 | 3,92 | 14,13 | 72,41 | 3,38 | 3,88 | 15,24 | 66,75 |

(x – nebylo měřeno)

Tabulka 5: Chemické složení pro AlSi-GL uvedené jako hm% v závislosti podle použitých kyselin

| AlSi-GI | korekce nespektrálních interferencí wt% | | | | | | | |
|------------------------|---|------|------|---------|-------------------|------|------|---------|
| | vnitřním standardem Sc | | | | "matrix matching" | | | |
| tabelované kyseliny | Al_2O_3 | CaO | MgO | SiO_2 | Al_2O_3 | CaO | MgO | SiO_2 |
| | 14,94 | 5,81 | 2,2 | 57,18 | 14,94 | 5,81 | 2,2 | 57,18 |
| AR | 2,93 | 1,62 | 0,44 | 4,01 | x | x | x | x |
| AR+HF | 15,54 | 6,85 | 2,39 | 61,16 | x | x | x | x |
| AR+HF+H3BO3 | 16,08 | 7,22 | 2,51 | 61,73 | 15,76 | 7,40 | 2,54 | 57,45 |
| AR+HF+HBF4 | 15,86 | 6,72 | 2,44 | 61,66 | 15,51 | 6,73 | 2,41 | 56,60 |

(x – nebylo měřeno)

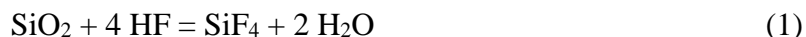
Tabulka 6: Chemické složení pro Eutal-borokřemičité sklo uvedené jako hm% v závislosti podle použitých kyselin

| Eutal | korekce nespektrálních interferencí wt% | | | | | | | | |
|------------------------|---|----------|-------|------|---------|-------------------|-------|------|---------|
| | vnitřním standardem Sc | | | | | "matrix matching" | | | |
| tabelované kyseliny | Al_2O_3 | B_2O_3 | CaO | MgO | SiO_2 | Al_2O_3 | CaO | MgO | SiO_2 |
| | 14,5 | 8,87 | 16,54 | 4,4 | 53,98 | 14,5 | 16,54 | 4,4 | 53,98 |
| AR | 13,56 | 8,63 | 16,42 | 4,33 | 1,32 | x | x | x | x |
| AR+HF | 13,71 | 8,46 | 16,06 | 4,23 | 51,49 | x | x | x | x |
| AR+HF+H3BO3 | 14,30 | - | 16,43 | 4,39 | 52,83 | 13,66 | 16,75 | 4,24 | 49,81 |
| AR+HF+HBF4 | 14,10 | - | 16,23 | 4,39 | 53,61 | 13,69 | 16,36 | 4,27 | 49,40 |

(,,-“, koncentrace B po komplexaci nebyly nevyhodnoceny, x – nebylo měřeno)

DISKUSE

Rozklad silikátových vzorků lučavkou královskou je neúplný, pouze pro kremičitanové sklá s obsahem SiO₂ ~55 hm% byly získány relevantní výsledky a bylo možné kvantitativně stanovit obsahy B (Tabulka 6). Pro materiály s vyšší mírou zesíťování je úplný rozklad tetraedrické silikátové struktury (1) možné dosáhnout minimalizací množství vzorku a přidavkem minimálně 1 ml HF.



Pokud není kyselina boritá v roztoku vyvázaná pomocí kyseliny borité je nevyhnutné pro ICP-OES analýzu použít výrobcem doporučený HF *resistant* dopravní systém. Při analýze vzorků po komplexaci pomocí kyseliny borité nedocházelo k očekávaným významným poklesům intenzity a tak ani poklesům stanovených obsahů oxidů. Výhodou je, že není nutné používat speciální teflonové součásti přístroje, ale dochází k prodloužení doby rozkladu. Nevýhodou však je vnos velkého množství boru a paměťový efekt boru v systému. Z časového a ekonomického hlediska je maskování kyseliny fluorovodíkové možné docílit pomocí HBF₄, která je do reakční směsi přidána ihned na začátku rozkladu a rozklad i komplexace tak probíhá v jednom kroku (Tabulka 1). Přidáním komplexačního činidla (H₃BO₃ či HBF₄) však přicházíme o možnost stanovení obsahu bóru v materiálu.

ZÁVĚRY

Naše výsledky ukazují, že přidání kyseliny fluorovodíkové do reakční směsi mělo za následek významné zvýšení stanovených obsahů jednotlivých oxidů. Stanovené hodnoty tak odpovídají tabelovaným hodnotám. Uvedená metoda umožňuje komplexní stanovení oxidového složení sklokeramických materiálů včetně obsahu Li₂O a B₂O₃ i SiO₂ s relativní odchylkou 0,3 hm%, resp. 1,5 hm% pro SiO₂. V případě použití skleněných součástí při analýze pomocí ICP je z časového a ekonomického hlediska pro maskování kyseliny fluorovodíkové výhodné použít HBF₄.

ACKNOWLEDGMENT

The financial support of this work by funding from the European Union's Horizon 2020 research and innovation programme under grant agreement No 739566 and by the VEGA grant 2/0026/17 is gratefully acknowledged. This publication was created in the frame of the project "Centre of excellence for ceramics, glass, and silicate materials" ITMS code 262 201 20056, based on the Operational Program Research and Development funded from the European Regional Development Fund.

LITERATÚRA

- [1] E.Krakovská, H.M.Kuss: Rozklady v analytickej chémii
- [2] Křest'an V.: Analýza skelných materiálů a surovin pro jejich výrobu
- [3] Greenwood, A. Earnshaw: Chemie prvků
- [4] Application Report: Microwave pressure digestion, Speedwave technology
- [5] Paudin A.M., Smith R.G.: Microwave decomposition of dust, ashes and sediments by ICP-AES. Can.J.Applied Spect.,37, 94-99
- [6] Krachler M., Mohl C., Emons H., Shotyk W.: Influence of digestion procedures on the determination of rare earth elements in peat and plant samples by USN-ICP-MS. J.Anal.At.Spectrom., 2002,17,844-851
- [7] Bock R. in: A Handbook of Decomposition Methods in Analytical Chemistry , Glasgow, 1979, 58-62
- [8] Patent No: US 6455451B1 – Pressable Lithium Disilicate glass ceramics

KORÓZIA DENTÁLNEJ KERAMIKY NA BÁZE OXIDU ZIRKONIČITÉHO

CORROSION OF ZIRCONIA – BASED DENTAL CERAMICS

A. Nowicka, D. Galusková, D. Galusek

*Vitrum Lauguricio – Joint Glass Center of the IIC SAS, TnU AD, and FChFT STU,
Študentská 2, 911 50 Trenčín, Slovakia*

ABSTRACT

This study investigated the effect of corrosion in acidic media and low temperature degradation (LTD) on yttria – stabilized zirconia (Y-TZP) commercial dental ceramics IVOCLAR and DOCERAM, and a Ce-TZP based nano-composite material - LONGLIFE and its effect on ion leaching, phase composition and mechanical properties. Long – term exposure of commercial yttria – stabilized zirconia dental materials to acidic medium resulted in corrosion associated with leaching of yttrium from zirconia ceramics, partial destabilization of tetragonal zirconia, and measurable increase of the content of monoclinic phase at the surface. This, in turn, increased susceptibility of the ceramics to low temperature degradation. Commercial dental ceramics IVOCLAR was the material least resistant to LTD. Based on these results a hypothesis has been formulated that corrosive attack of acidic media from regularly consumed beverages and food combined with poor mouth hygiene, or some health issues associated with excessive production of gastric acid may increase vulnerability of Y-TZP dental ceramics to LTD. However, to draw unambiguous conclusion, longer corrosion experiments are in progress.

Keywords: corrosion, low temperature degradation, dental implants, acetic acid, accelerated aging test

INTRODUCTION

Excellent mechanical properties of zirconia-based materials combined with their superior aesthetics and biocompatibility characteristics have encouraged their application as bioceramics, particularly in the dental field [1]. Ceramics made of zirconium oxide polycrystals stabilized in their tetragonal form by the addition of 3 mol% of yttrium oxide (denoted as 3Y-TZP) is a material of choice in advanced dental applications and dental implantology [2]. However, past research on hip joints made from yttria doped zirconia ceramics revealed that this material was vulnerable to low temperature hydrothermal degradation (LTD) [1, 3], a phenomenon in which, due to the presence of water, the tetragonal – monoclinic phase

transformation is triggered at the ceramic surface. The present work was carried out to study and elucidate the role of corrosion on LTD of zirconia bioceramics that could be used in the dental field but also in other biomedical applications (hip joints, spine prostheses etc.) through determination of long term corrosion behaviour of zirconia bioceramics in-vitro under the conditions simulating those in human body (dental and orthopedic applications) and its effect on LTD.

EXPERIMENTAL

Two commercial zirconia-based dental materials stabilized in their tetragonal form by addition of yttrium (3Y-TZP) – IVOCLAR IPS e.max® ZirCAD and DOCERAM Nacera® were tested. To compare the properties and resistance to LTD, Ce-TZP based nano-composite (denoted as LONGLIFE) developed at INSA Lyon was also used. IVOCLAR, DOCERAM and LONGLIFE ceramics have been corroded at three temperatures (37, 60, 80 °C) in 4 % acetic acid as the corrosion medium for up to 31 days. The samples were exposed to the corrosion medium 3 times for 5 days and 2 times for 8 days. Then the experiments were interrupted for three months and after the break the experiment at 37°C was resumed and proceeded for another 170 days. After each period of time in the corrosion medium the phase composition was determined by X-ray diffraction (Panalytical Empyrean powder diffractometer, CuK α radiation, in the 2 Θ range 25 – 75°). To monitor the amount of leached ions from the materials during the corrosion process chemical analysis of corrosion media was carried out by ICP – OES (Agilent Technologies 5100). Un-corroded materials were subjected also to accelerating aging test (AAT) to check their resistance to LTD. The experiment was carried out in autoclave (Büchi Glas Uster/Limbo II). The samples were exposed to water vapour at an elevated temperature of 134 °C (one hour at 134 °C corresponds to ~ 2 years at 37 °C [1]) for up to 30 h. Before and after the exposure to AAT the content of monoclinic phase was determined, using the method described by Garvie and Nicholson [4]. Furthermore, aging kinetics expressed in terms of the monoclinic phase content change for IVOCLAR samples were fitted by Mehl – Avrami – Johnson (MAJ) law (3), presuming nucleation and grain growth to be the key mechanisms for transformation [4].

$$f_m = 1 - \exp\left(- (bt)^n\right) \quad (1)$$

Where f_m – fraction of tetragonal zirconia that has transformed to monoclinic phase, t – time of exposure to moisture, n – exponent, b – constant

This equation allows prediction of the monoclinic fraction at the surface of aged ceramic for a given time and temperature. At the end of experiments the effect of static corrosion test and AAT on the overall strength of DOCERAM and LONGLIFE samples was carried out, using a biaxial bending test in a ball-on-disk-on three balls arrangement suitable for circular samples. Universal testing machine (INSTRON 8500, Norwood, USA) was used for the measurements. The IVOCLAR was not measured due to unsuitable geometry of tested samples. Three specimens from each material (DOCERAM, LONGLIFE) were tested after static corrosion test, but only one after the AAT due to insufficient amount of available material.

RESULTS

To evaluate the influence of corrosion in 4 % acetic acid on Y^{3+} and Ce^{4+} ions leaching from zirconium dental ceramic and to prove that acidic corrosion of TPZ dental ceramics is associated with leaching of stabilizing ions (Y^{3+} or Ce^{4+}) from zirconia ceramics, the ICP-OES measurements were carried out. The effect of corrosion could be partial destabilization of tetragonal zirconia and an increase of the content of monoclinic phase at the surface. Leaching out of yttrium ions was observed from both tested yttria-stabilized zirconia dental ceramics IVOCLAR and DOCERAM (**Fig. 1**). For IVOCLAR ceramics the concentration of leached ions increased already at 60 °C. However, in the case of DOCERAM ceramics the leaching of yttrium was observed only at the highest temperature (80 °C). The leaching out of cerium ions was observed already at 37°C. Behaviour of the LONGLIFE ceramics was similar to Y-TZP materials and the concentration of Ce^{4+} ions was increasing at higher temperatures. Concentrations of other ions (Al, Sr and Zr), which were leached out of the LONGLIFE ceramics were close to the limit of quantification of the used method. The NL values shown in Fig. 1 represent the amounts of leached elements normalized with respect to the weight fraction of the element in corroded material. The fact that the NL values of other leached elements were close to the detection limits indicate preferential leaching of Ce as the stabilizing agent and higher chemical stability of other phases present in the material.

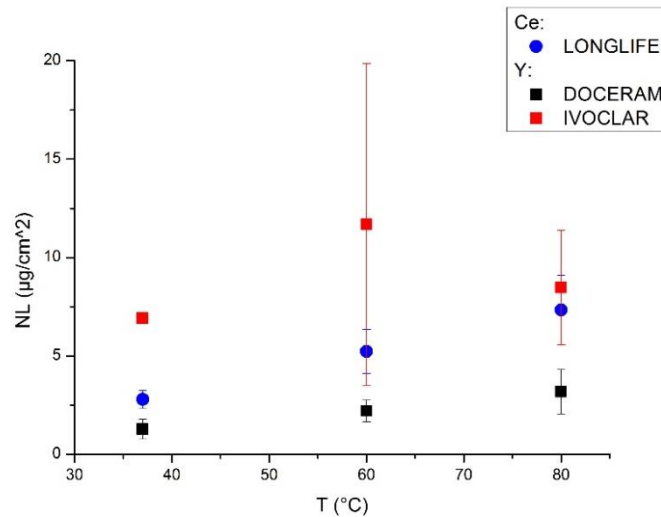


Fig. 1. The amounts of leached Y^{3+} and Ce^{4+} ions from the Y-TZP (IVOCLAR, DOCERAM) and the Ce-TZP (LONGLIFE) ceramic materials after 31 days of exposure to 4 % acetic acid at various temperatures.

After the exposure of IVOCLAR, DOCERAM and LONGLIFE in acidic environment for 31 days at 60°C and 80°C and after 170 days at 37°C the content of monoclinic phase was determined by X-ray powder diffraction measurement (**Fig. 2**). For both materials exposed to acetic acid at 80 °C, their phase development was almost identical until the day 31. At 37 °C for the DOCERAM no measurable increase of the monoclinic phase was detected. At higher temperatures this material was more resistant to LTD than IVOCLAR.

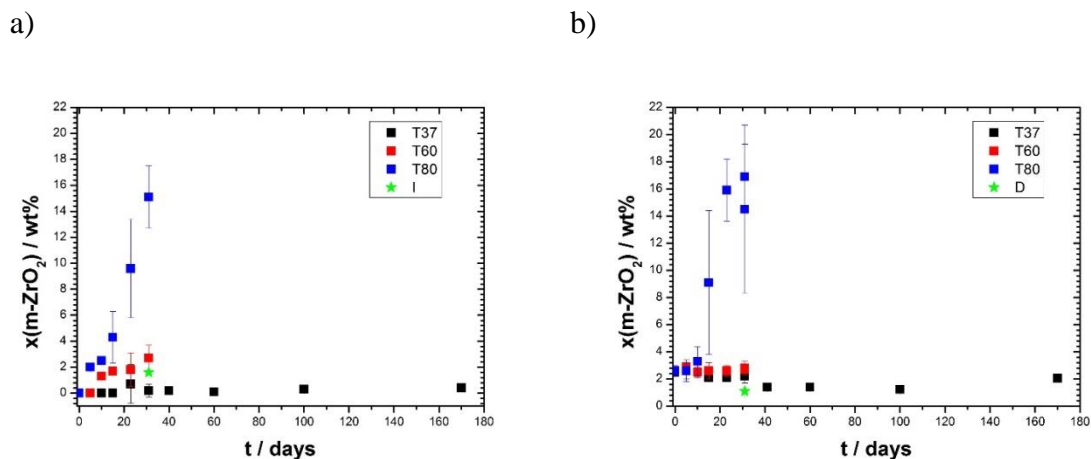


Fig. 2. Time dependence of the content of monoclinic phase in the ceramics exposed to 4 % acetic acid at various temperatures. a) IVOCLAR, b) DOCERAM.

In the LONGLIFE zirconia ceramics (**Fig. 3**) stabilized by the addition of Ce about 2 wt.% of monoclinic phase was detected already after sintering and polishing procedures, but this value did not change after exposure to acidic media after 31 days of the experiment, irrespective of the applied temperature. However, after the three months interruption of the corrosion experiments an abrupt increase in the content of monoclinic phase was observed already after 10 days exposure to corrosion medium at 37°C. The result led to hypothesis that the t-m transformation could occur in the course of storage of the material. To prove this hypothesis the measurements of stored samples of each material corroded for 31 days at 60°C were repeated *prior to* exposure to corrosive medium. The star-shape dot in **Fig. 2a), b)** and in **Fig. 3** represent measured contents of monoclinic phase. While in DOCERAM and IVOCLAR the content of monoclinic phase did not change during storage, a significant increase of m-ZrO₂ content was measured in LONGLIFE.

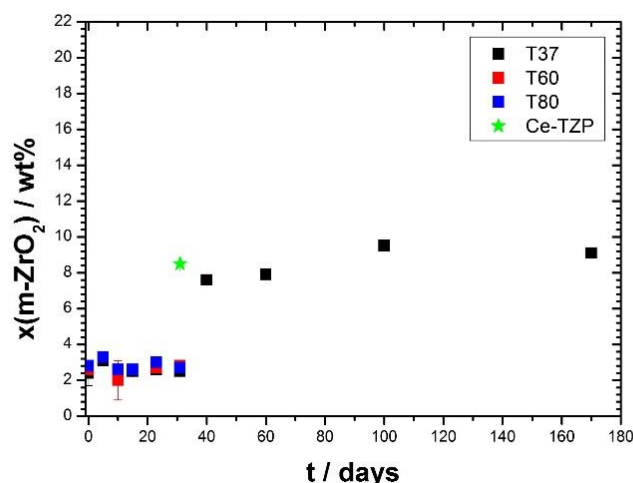


Fig. 3. Time dependence of the content of monoclinic phase in the LONGLIFE ceramics exposed to 4 % acetic acid at various temperatures.

Further changes of the content of monoclinic phase were observed after the accelerating aging test (**Fig. 4**). The content of monoclinic phase in the LONGLIFE ceramics remained constant throughout the whole AAT. DOCERAM ceramics was more resistant to LTD than IVOCLAR, with maximum of 10 wt.% of monoclinic phase after 30 h exposure at 134 °C.

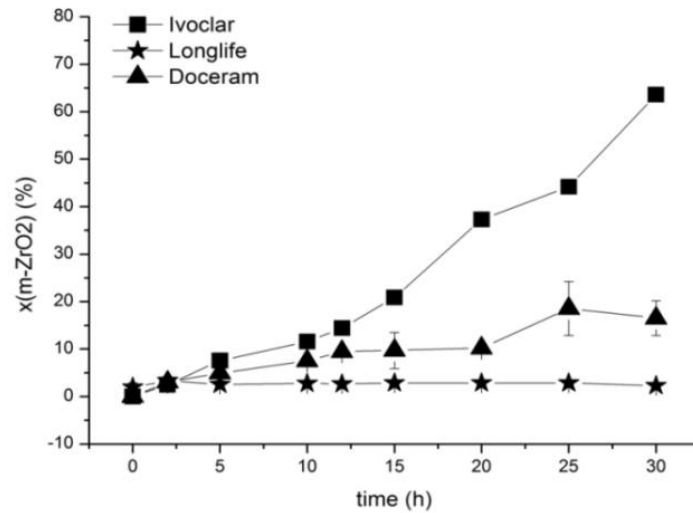


Fig. 4. Content of monoclinic phase after AAT at 134 °C

To verify whether the mechanism of phase transformation during corrosion in acetic acid is different from that of low temperature degradation the MAJ equation was applied for every material. The red solid squares in **Fig 5.** show the time dependence of the content of monoclinic zirconia measured during the AAT at 134 °C for IVOCLAR dental ceramics. Empty symbols represent the estimates of the monoclinic phase contents determined with the use of the Mehl – Avrami- Johnson law for lower temperatures 37, 60 and 80 °C [5], with the use of activation energy determined for the transformation process 80 kJ.mol⁻¹ by Lughì et al. [2]. Solid symbols of other colours (blue, green, black) show the time dependencies of monoclinic phase contents measured by X-ray diffraction after acid corrosion at temperatures from 37 °C to 80 °C.

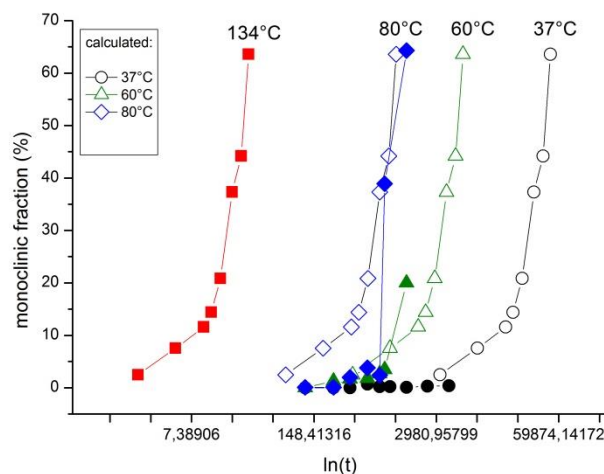


Fig. 5. Relationship between the amount of monoclinic phase and aging time at various temperatures in IVOCLAR: comparison of measured data with the values estimated from the MAJ equation.

The curves calculated with the same value of activation energy of 80 kJ.mol^{-1} determined for LTD, identical to measured phase contents after corrosion tests would indicate identical controlling mechanism(s). After corrosion at $80 \text{ }^\circ\text{C}$ the measured and calculated values were quite different suggesting different mechanism controlling the rate of phase transformation. After initial slow increase of monoclinic phase content an abrupt increase was observed after 23 days, indicating some kind of nucleation process related to zirconia matrix depletion of the stabilizing agent. Markedly higher monoclinic phase content was measured at $60 \text{ }^\circ\text{C}$ then predicted from the MAJ equation after 31 days of the test: however no unambiguous conclusions can be drawn from just one experimental point and longer corrosion experiments will be necessary to confirm the trend. Much longer times of corrosion would be necessary also at $37 \text{ }^\circ\text{C}$ to achieve reasonable overlap between the measured and calculated data.

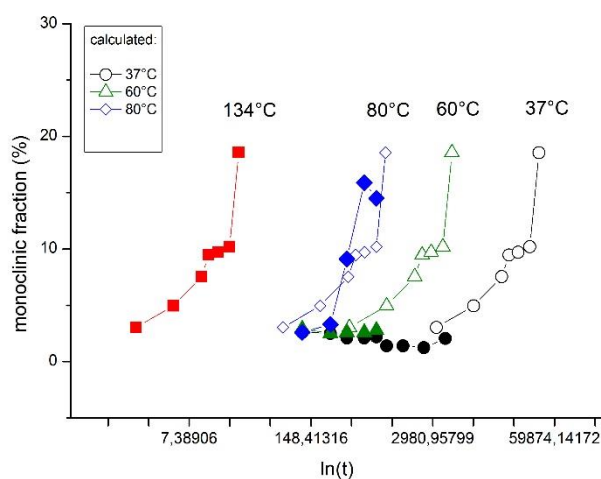


Fig. 6. Relationship between the amount of monoclinic phase and aging time at various temperatures in DOCERAM: comparison of measured data with the values estimated from the MAJ equation.

The same calculations were carried out for DOCERAM (**Fig.6**) and LONGLIFE dental ceramics (**Fig.7**), indicating a different controlling mechanism of corrosion of DOCERAM at $80 \text{ }^\circ\text{C}$, than that responsible for LTD. However, similarly to IVOCLAR, longer corrosion experiments will be necessary at 37 and $60 \text{ }^\circ\text{C}$ to confirm the conclusion. No conclusions could be drawn from the results obtained for LONGLIFE due to very low monoclinic phase contents. The inexplicable increase of $m\text{-ZrO}_2$ content during the 3 months storage also requires further investigation.

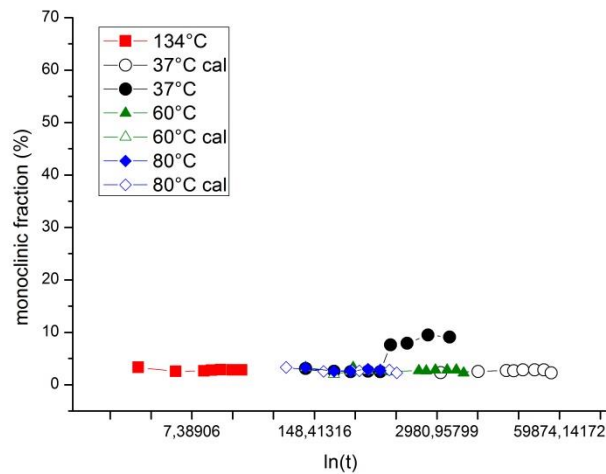


Fig. 7. Relationship between the amount of monoclinic phase and aging time at various temperatures in LONGLIFE: comparison of measured data with the values estimated from the MAJ equation.

The results from biaxial flexural strength (**Fig. 8**) test for DOCERAM and LONGLIFE samples indicated that static corrosion test and AAT had significant effect on the flexural strength for Y-TZP ceramic (DOCERAM). The lowest strength values were measured for DOCERAM samples after AAT, indicating the t-m phase transformation at the surface combined with volume expansion led to micro-cracking and roughening. For the LONGLIFE material the flexural strength remained unaffected, irrespective of the temperature applied during the test. Marginal increase of strength was observed after static corrosion at 60 °C.

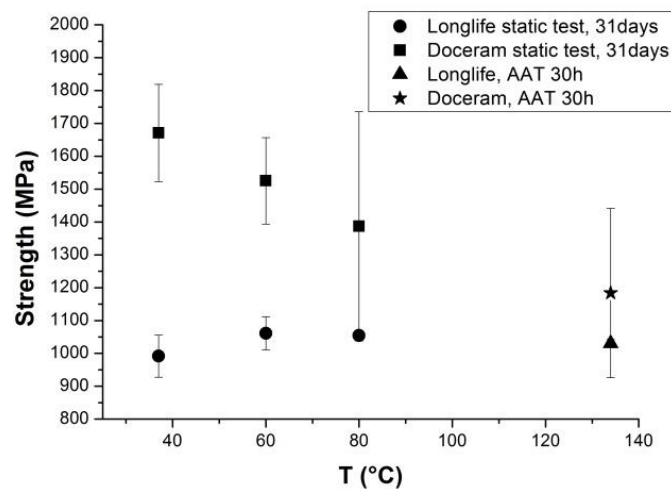


Fig. 8. Biaxial flexural strength test for DOCERAM and LONGLIFE

CONCLUSION

The tested Y-TZP dental ceramics are vulnerable to low temperature hydrothermal degradation (LTD), a phenomenon in which, due to the presence of water, the t–m phase transformation is triggered at the ceramic surface. Acidic corrosion of 3Y-TZP dental ceramics is associated with leaching of yttrium from zirconia ceramics, resulting in partial destabilization of tetragonal zirconia and measurable increase of the content of monoclinic phase at the surface. Preliminary experiments indicate that the corrosion differs by its mechanisms from LTD. However, to draw unambiguous conclusion, longer corrosion experiments will be necessary. Ce-TZP based nano-composite material (LONGLIFE) was the material most resistant both to corrosion and to accelerated aging.

ACKNOWLEDGMENT

Financial support of this work by the JECS Trust grant, contract No 201598, and the grant VEGA 2/0026/17 is gratefully acknowledged. In this work were used the experimental facilities acquired through the project "Centre of excellence for ceramics, glass, and silicate materials" ITMS code 262 201 20056, and the project "Centre for diagnostics and materials quality testing" ITMS code 262 101 20046 based on the Operational Program Research and Development funded from the European Regional Development Fund.

REFERENCES

- [1]Sanon. C., Chevalier J., Douillard T., Cattani-Lorente M., Scherrer S.S., Gremillard L., A new testing protocol for zirconia dental implants. Dent. Mater. 31, 2015, 15–25.
- [2]Lughi V., Sergo V, Low temperature degradation -aging- of zirconia: A critical review of the relevant aspects in dentistry, Dent. Mater. 26, 2010, 807–820.
- [3]Fornabaio M., et. al. Zirconia-based composites for biomedical applications: Role of second phases on composition, microstructure and zirconia transformability. J Eur Ceram Soc. 35, 2015, 4039-4049.
- [4]Garvie RC., Nicholson PS., Phase analysis in zirconia systems. J Am Ceram Soc 55, 1972,303-5.
- [5]Johnson WA, Mehl RF. Reaction kinetics in processes of nucleation and growth. Trans Am Inst Min Metall Pet Eng 135, 1939, 416–41.

VPLYV GLYCÍNU NA VLASTNOSTI SÓLOV A XEROGÉLOV V SYSTÉME SiO₂ STABILIZOVANOM Na⁺ IÓNMI

THE INFLUENCE OF GLYCINE ON THE PROPERTIES OF SOLS AND XEROGELS IN THE SiO₂ SYSTEM STABILIZED BY Na⁺ IONS

P. Balážová¹, M. Čierniková¹, A. Plško¹, J. Pagáčová², I. Papučová²

¹ Alexander Dubček University of Trenčín, Vitrum Laugaricio – Joint Glass Center
of the TnUAD, Študentská 2, 911 50 Trenčín, Slovakia

² Alexander Dubček University of Trenčín, Faculty of Industrial Technologies in Púchov,
I. Krasku 491/30, 020 01 Púchov, Slovakia

ABSTRACT

The work deals with the determination of the influence of glycine on the properties of sols and xerogels prepared in “polymeric silicic acid (PSA) – water (H₂O) – sodium hydroxide (NaOH) – glycine (C₂H₅NO₂)” system. The stabilized sol was prepared by ion exchange, then by addition of NaOH solution and subsequently by refluxing process. From the stabilized sol, the sols with various ratios of $x(\text{C}_2\text{H}_5\text{NO}_2):x(\text{SiO}_2)$ were prepared. The xerogels were prepared by drying of sols at 80 °C. For sols, the size of particle was measured and it was characterized by polydispersity index and volume of particles from total volume of particles. The structure of xerogels were characterized by infrared spectroscopy in the spectral range of 4000 - 400 cm⁻¹. The structure information was supplemented by Raman spectroscopy in range of 1500 - 300 cm⁻¹.

Keywords: colloidal silica, glycine, xerogel, particle size, structure

INTRODUCTION

The interaction of proteins with solid surfaces of materials is not only a fundamental phenomenon but is also key to several important fields, such as biology, medicine, biomaterials, biotechnology, nanotechnology or food processing [1, 2]. In the biomaterials field, protein adsorption is the first step in the integration of an implanted device or materials with tissue. In nanotechnology, protein-surface interactions are pivotal for the assembly of interfacial protein construct, such as sensors, activators and other functional components at the biological or electronic junction [2].

In this work, the simplest protein structural unit and the smallest amino acid – glycine was chosen to interact with the surface of SiO₂ particles [3]. The surface of amorphous silica is covered with silanol groups which can easily form hydrogen bonds. Glycine has two reactive groups able to form hydrogen bonds, the -COOH and the -NH₂ groups [4]. The investigation and understanding the influence of glycine interaction with the surface of SiO₂ particles in sols on their size, as well as changes in the xerogels structure, are closely related to the application options mentioned above.

The SiO₂ xerogels are known for their amorphous structure which consists of [SiO₄] tetrahedra linked together in different ways [5]. The structure of SiO₂ xerogels can be monitored using IR and Raman spectroscopy. Infrared spectra of glycine in the range of 1700 - 1200 cm⁻¹ include the bending vibrations of the -NH₃⁺ groups as well as the wagging, twisting and rocking vibrations of the -CH₂-, -NH₂ and -NH₃⁺ groups. In the Raman spectra in region below 800 cm⁻¹, the vibrations of the -COO⁻ groups and the bending vibrations δ(NCC) can be identified [3]. According the literature, the bands in infrared and Raman spectra of SiO₂ xerogels modified by glycine can be assigned to the vibrations which are summarized in Tab. 1.

Tab. 1. Assignment of bands in the infrared and Raman spectra of SiO₂ xerogels modified by glycine

| Infrared spectra | | | Raman spectra | | |
|--------------------------------|-----------------------------------|-----------|---------------------------------|--|-----------|
| Wavenumber [cm ⁻¹] | Assignment | Reference | Raman shift [cm ⁻¹] | Assignment | Reference |
| 2400 – 3400 | v(NH ₃) | 3 | ~ 1462 | δCH ₂ | 3 |
| ~ 1596 | v _{AS} (COO) | 6 | ~ 1417 | v _s COO | 3 |
| ~ 1505 | δ _S (NH ₃) | 3, 6 | ~ 1331 | ωCH ₂ /t _w CH ₂ | 3 |
| ~ 1444 | δ(CH ₂) | 3 | ~ 1105 and 1120 | ρNH ₃ | 3 |
| ~ 1401 | v _S (COO) | 3, 6 | ~ 1040 | vCN | 3 |
| ~ 1334 | ω(CH ₂) | 3 | ~ 980 | v(Si-OH) | 9 |
| ~ 1080 | v _{AS} (Si-O-Si) | 7 | ~ 899 | vCC | 3 |
| ~ 1034 | v(CN) | 3 | ~ 800 | v _S (Si-O-Si) | 7, 10 |
| ~ 893 | v(CC) | 3 | ~ 703 | δCOO | 3 |
| ~ 698 | δ(COO) | 3 | ~ 608 | ωCOO | 3 |
| ~ 608 | ω(COO) | 3 | ~ 499 | δCCO | 3 |
| ~ 520 | τ(C-N) | 3 | ~ 490 | v _S (Si-O-Si) | 7, 9, 11 |
| ~ 470 | ρ(Si-O-Si) | 7, 8 | ~ 364 | δNCC | 3 |

In the present work, the stabilized SiO₂ sols was prepared from colloidal silica and stabilized by Na⁺ ions. The glycine was used as a particle surface modifier. The influence of the molar ratio $x(\text{C}_2\text{H}_5\text{NO}_2):x(\text{SiO}_2)$ on the particle size in sols as well as the change in the structure of SiO₂ xerogels was studied.

EXPERIMENTAL

In the first step, a larger amount of stabilized SiO₂ sol was prepared. For preparation this sol, the aqueous solution of sodium silicate (Na₂SiO₃) was used (SiO₂ content was 37 wt. %). The solution of sodium silicate was diluted with distilled water until the SiO₂ content was 5 wt. %. The polymeric silicic acid sol was obtained by cation exchange of Na⁺ and H⁺ using ion exchanger Amberlite IR-120. The prepared sol was stabilized by addition of NaOH solution so that the weight ratio of $w(\text{SiO}_2):w(\text{Na}_2\text{O})$ in sols was 150:1 and after that, the sol was refluxed for 3 hours. In the second step, nine sols were prepared from the stabilized sol after 24 hours from its preparation. These sols were prepared by the following way: the required amounts of water as well as the solution of glycine (10 wt. %) were added drop by drop into required amount of stabilized sol during stirring. The obtained mixture was stirred for 30 min. The molar composition of the sols is shown in Tab. 2.

The xerogels were prepared 24 hours after preparation of sols by drying in a thin layer at 80 °C to constant weight. After drying, the xerogels were stored in an environment with RH = 43.2 %. Before FTIR and Raman spectroscopy measurements, the xerogels were crushed on the fraction under 0.315 nm.

The particle size of sols was determined by dynamic light scattering method. Measurements of particle size were carried out using the device Particle size analyzer 90 Plus/BI-MAS. The groups of particles as well as minimum and maximum values of particles size were determined from the distribution of intensity according to diameter of particles. In order to obtain the information about the volume of particles in given group, the distribution of intensity according to diameter of particles were converted by calculation to the distribution of volume according to diameter of particles. From the cumulative curves of intensity according to particles diameter, the polydispersity index was determined for each group of particles [12].

The infrared spectra were measured using reflex mode in the 4 000 - 400 cm⁻¹ region by the device Nicolet iS50 FT-IR, with a resolution 4 cm⁻¹. Raman spectra were measured by the Renishaw inVia Reflex Raman microspectrometer. Spectra were obtained with a monochromator using the 532 nm line of an Argon laser Spectra Physics STABILITE 2017 as an excitation source with a typical power of 2 W. The measurement conditions were following: center at 900 cm⁻¹, 3600 accumulations and exposure time of 10 second.

Tab. 2. Molar composition of sols

| Sample designation | | $x(\text{SiO}_2)$ | $x(\text{C}_2\text{H}_5\text{NO}_2)$ | $x(\text{H}_2\text{O})$ | $x(\text{C}_2\text{H}_5\text{NO}_2):x(\text{SiO}_2)$ |
|--------------------|----------|-------------------|--------------------------------------|-------------------------|--|
| Sol | Xerogel | | | | |
| CB16002S | CB16002X | 0.0061 | 0.0000 | 0.9939 | 0.0000 |
| CB16003S | CB16003X | 0.0061 | 0.0004 | 0.9935 | 0.0667 |
| CB16004S | CB16004X | 0.0061 | 0.0008 | 0.9931 | 0.1334 |
| CB16005S | CB16005X | 0.0061 | 0.0012 | 0.9927 | 0.2001 |
| CB16006S | CB16006X | 0.0061 | 0.0016 | 0.9923 | 0.2668 |
| CB16007S | CB16007X | 0.0061 | 0.0020 | 0.9918 | 0.3335 |
| CB16008S | CB16008X | 0.0061 | 0.0025 | 0.9914 | 0.4002 |
| CB16009S | CB16009X | 0.0061 | 0.0029 | 0.9910 | 0.4669 |
| CB16010S | CB16010X | 0.0061 | 0.0033 | 0.9906 | 0.5336 |

RESULTS AND DISCUSSION

For individual sols, Tab. 3 shows the groups of particles with the values of their minimum and maximum size of particles as well as the values of cumulative volume for given particles from total volume of particles. The particles of the 1st group, with size approximately in the range from 1.0 to 74.1 nm, form dominant group in all sol and the volume of these particles represents 98.1 - 100.0 vol. % from the volume of all particles which are present in sol. In all sol, the particles with the size approximately in the range from 10.0 to 562.3 nm, which form the 2nd group of particles, represent the very small volume from the volume of all particles in sol. The volumes of particles of the 3rd and the 4th groups are negligible and these particles can be attributed to particles of dust and pollution. In the next step, the size of particles was characterized by the polydispersity index (Fig. 1) for particles of the 1st as well as the 2nd group, while the particles of the 3rd and the 4th groups were not considered. Fig. 1 illustrates that the dependences of polydispersity index on the $x(\text{C}_2\text{H}_5\text{NO}_2):x(\text{SiO}_2)$ ratio for the 1st as well as the 2nd group have decreasing tendency.

Tab. 3. The cumulative volume of particles with a given size of particles from the total particles volume

| Sol | Characteristic | Group of particles | | | | | | | |
|----------|----------------|--------------------|------|------|-------|-------|--------|--------|---------|
| | | 1 | 2 | 3 | 4 | 5 | 6 | 7 | 8 |
| CB16002S | Min-Max [nm] | 1.8 | 17.8 | 15.4 | 133.4 | 191.1 | 1154.8 | 3398.2 | 10000.0 |
| | Volume [%] | 0.0 | 99.7 | 99.6 | 100.0 | 100.0 | 100.0 | 100.0 | 100.0 |
| CB16003S | Min-Max [nm] | 2.4 | 31.6 | 20.5 | 562.3 | 103.2 | 3398.2 | 1521.1 | 10000.0 |

| | | | | | | | | | |
|----------|--------------|-----|-------|------|-------|-------|--------|---------|---------|
| | Volume [%] | 0.0 | 99.9 | 99.3 | 100.0 | 100.0 | 100.0 | 100.0 | 100.0 |
| CB16004S | Min-Max [nm] | 3.0 | 74.1 | 14.2 | 348.8 | 83.7 | 1268.0 | 3398.2 | 10000.0 |
| | Volume [%] | 0.0 | 100.0 | 97.3 | 100.0 | 100.0 | 100.0 | 100.0 | 100.0 |
| CB16005S | Min-Max [nm] | 1.3 | 31.6 | 10.0 | 273.8 | 191.1 | 1654.8 | 2371.4 | 10000.0 |
| | Volume [%] | 0.0 | 99.9 | 99.7 | 100.0 | 100.0 | 100.0 | 100.0 | 100.0 |
| CB16006S | Min-Max [nm] | 1.0 | 56.2 | 19.5 | 237.1 | 104.9 | 860.5 | 3398.2 | 10000.0 |
| | Volume [%] | 0.0 | 100.0 | 96.2 | 100.0 | 100.0 | 100.0 | 100.0 | 100.0 |
| CB16007S | Min-Max [nm] | 3.7 | 18.0 | 17.0 | 69.3 | 62.7 | 448.8 | 443.5 | 2031.7 |
| | Volume [%] | 0.0 | 98.1 | 97.4 | 100.0 | 100.0 | 100.0 | 100.0 | 100.0 |
| CB16008S | Min-Max [nm] | 3.0 | 24.4 | 31.7 | 117.2 | 152.2 | 562.9 | 2704.0 | 10000.0 |
| | Volume [%] | 0.0 | 99.4 | 99.7 | 100.0 | 100.0 | 100.0 | 100.0 | 100.0 |
| CB16009S | Min-Max [nm] | 4 | 21.6 | 19.4 | 142.0 | 117.4 | 1681.5 | 7232.86 | 10000.0 |
| | Volume [%] | 0.0 | 98.7 | 98.0 | 100.0 | 100.0 | 100.0 | 100.0 | 100.0 |
| CB16010S | Min-Max [nm] | 3.1 | 15.0 | 22.2 | 103.2 | - | - | - | - |
| | Volume [%] | 0.0 | 99.6 | 99.5 | 100.0 | - | - | - | - |

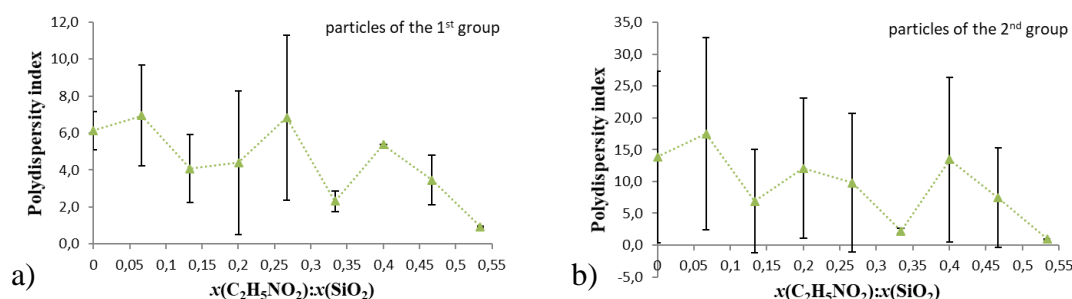


Fig. 1. The dependence of polydispersity index on the ratio of $x(\text{C}_2\text{H}_5\text{NO}_2):x(\text{SiO}_2)$ in sol for a) particles of the 1st group, b) particles of the 2nd group

The infrared spectra of xerogels, prepared from sols with various $x(\text{C}_2\text{H}_5\text{NO}_2):x(\text{SiO}_2)$ ratio as well as the spectrum of glycine in the range of $4000 - 400 \text{ cm}^{-1}$, are shown in Fig. 2. The wavenumbers and assignments of bands in the observed region are the same as it can be seen in Tab. 1.

In term of study of xerogel structure development, the most important region of infrared spectra is the region of $1700 - 1200 \text{ cm}^{-1}$ and it is shown in Fig. 3. It can be seen, that in the infrared spectrum of CB16002X, i.e. sample without glycine, there is no bands in mentioned region. By addition of glycine, the band of asymmetric stretching vibration $\nu_{\text{AS}}(\text{COO})$ is observed near to wavenumber of 1596 cm^{-1} and this band has the wider arm on the side of the higher wavenumber near to 1615 cm^{-1} . Four further bands are also observed. The band occurring at 1505 cm^{-1} corresponds to symmetric bending vibration $\delta_{\text{S}}(\text{NH}_3)$. The band at 1444 cm^{-1} is assigned to bending vibration $\delta(\text{CH}_2)$. The band at 1413 cm^{-1} corresponds to symmetric stretching vibration $\nu_{\text{S}}(\text{COO})$ and the band with a maximum near to 1334 cm^{-1} belongs to wagging vibration $\omega(\text{CH}_2)$. When the ratio of $x(\text{C}_2\text{H}_5\text{NO}_2):x(\text{SiO}_2)$ in sol increases, the increase

of the relative „height“ of the studied bands as well as the changes in the shift of their wavenumber were observed.

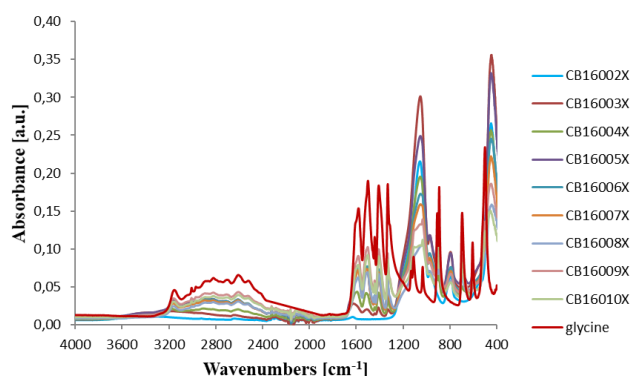


Fig. 2. Infrared spectra of xerogels with various molar ratio of $x(\text{C}_2\text{H}_5\text{NO}_2):x(\text{SiO}_2)$ in sol and spectrum of glycine

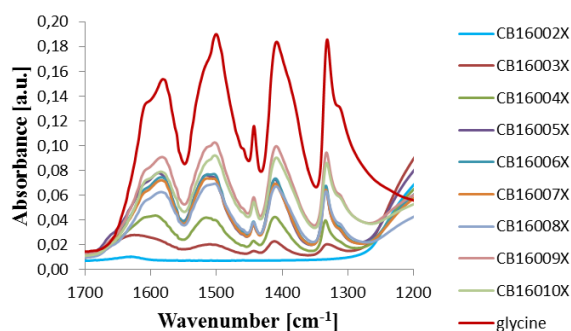


Fig. 3. Infrared spectra of xerogels with various molar ratio of $x(\text{C}_2\text{H}_5\text{NO}_2):x(\text{SiO}_2)$ in sol and spectrum of glycine in range of $1700 - 1200 \text{ cm}^{-1}$

Fig. 4 shows the Raman spectra of xerogels prepared from sols with various $x(\text{C}_2\text{H}_5\text{NO}_2):x(\text{SiO}_2)$ ratio as well as the spectrum of glycine in the range of $1500 - 300 \text{ cm}^{-1}$. The Raman shift and assignments of the individual bands in the mentioned region are the same as it can be seen in Tab. 1. For further analysis, the region of $300 - 700 \text{ cm}^{-1}$ was selected on the basis of reference [3]. Fig. 5 shows the Raman spectra of xerogels prepared from sols with various molar ratio of $x(\text{C}_2\text{H}_5\text{NO}_2):x(\text{SiO}_2)$ in selected region. In the Raman spectrum of sample without glycine, CB16002X, the band of symmetric stretching vibration $\nu_s(\text{Si-O-Si})$ near 490 cm^{-1} is observed. After addition of glycine to sol, the bands at 608 and 703 cm^{-1} are observed in xerogel and they can be attributed to wagging vibration $\omega(\text{COO})$ and bending vibration $\delta(\text{COO})$. In spectra of xerogels with a higher ratio of $x(\text{C}_2\text{H}_5\text{NO}_2):x(\text{SiO}_2)$, the bands around 360 and 499 cm^{-1} are observed and they are associated with bending vibration $\delta(\text{NCC})$

and bending vibration $\delta(\text{CCO})$. The changes in intensity of Raman bands, mentioned above, are observed with increasing $x(\text{C}_2\text{H}_5\text{NO}_2):x(\text{SiO}_2)$ ratio in sol.

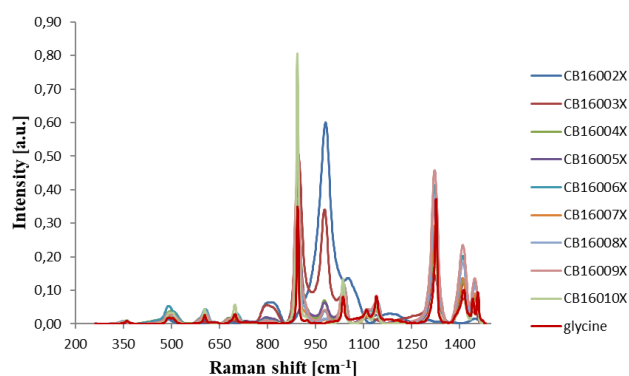


Fig. 4. Raman spectra of xerogels with various molar ratio of $x(\text{C}_2\text{H}_5\text{NO}_2):x(\text{SiO}_2)$ in sol and spectrum of glycine

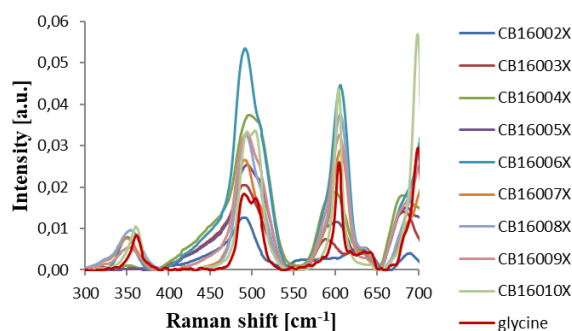


Fig. 5. Raman spectra of xerogels with various molar ratio of $x(\text{C}_2\text{H}_5\text{NO}_2):x(\text{SiO}_2)$ in sol and spectrum of glycine in range of 300 - 700 cm^{-1}

CONCLUSION

In the presented work, the influence of various $x(\text{C}_2\text{H}_5\text{NO}_2):x(\text{SiO}_2)$ molar ratio on the size of particles in sols as well as the change in the structure of prepared xerogels was study. Based on the results, the all prepared sol contains the particles which have the size approximately from 1 to 74 nm and these particles represent the most dominant volume from the volume of all present particles in sol. The index polydispersity has decreasing tendency in dependence on the $x(\text{C}_2\text{H}_5\text{NO}_2):x(\text{SiO}_2)$ molar ratio. The ratio of $x(\text{C}_2\text{H}_5\text{NO}_2):x(\text{SiO}_2)$ has the influence on the position and relative intensity of bands in studied region of infrared and Raman spectra.

ACKNOWLEDGMENT

The work was supported by the „CEDITEK“ project, ITMS 26210120046.

REFERENCES

- [1] Nakanishi, K., Sakiyama, T., Imanura, K. On the adsorption of proteins on solid surfaces a common but very complicated phenomenon, *Journal of Bioscience and Bioengineering*, 91 (2001) 266-244.
- [2] Gray, J. J. The interaction of proteins with solid surfaces, *Current Opinion in Structural Biology*, 14 (2004) 110-115.
- [3] Rosado, M. T., Duarte, M. L. T. S., Fausto, R. Vibrational spectra of acid and alkaline glycine salts, *Vibrational Spectroscopy*, 16 (1998) 35-54.
- [4] Costa, D. et al. Theoretical and experimental study of the adsorption of neutral glycine on silica from the gas phase, *A European Journal of Chemical physics and physical chemistry*, 6 (2005) 1061-1070.
- [5] Mihailova, B. D., Marinov, M. S., Konstantinov, L. L. Infrared absorption spectra of rings of SiO₄ tetrahedra with imposed boundary conditions, *Journal of Non-Crystalline Solids*, 176 (1994) 127-132.
- [6] Kitadai, N., Yokoyama, T., Nakashima, S. ATR-IR spectroscopic study of L-lysine adsorption on amorphous silica, *Journal of Colloid and Interface Science*, 329 (2009) 31-37.
- [7] Fidalgo, A., Ilharco, M. The defect structure of sol-gel-derived silica/polytetrahydrofuran hybrid films by FTIR, *Journal of Non-Crystalline Solids*, 283 (2001) 144-154.
- [8] Innocenzi, P. Infrared spectroscopy of sol-gel derived silica-based films: a spectromicrostructure overview, *Journal of Non-Crystalline Solids*, 316 (2003) 309-319.
- [9] Aguiar, H. et al. Structural study of sol-gel silicate glasses by IR and Raman spectroscopies, *Journal of Non-Crystalline Solids*, 355 (2009) 475-480.
- [10] Handke, M., Jastrzebski, W. Vibrational spectroscopy of the double 4-, 6-membered rings in silicates and siloxanes, *Journal of Molecular Structure*, 744 (2005) 671-675.
- [11] Brinker C. J., Scherer G. W., *Sol-gel Science: The Physics and Chemistry of Sol-Gel Processing*, Academic Press, San Diego, (1990) 909 p. ISBN-13: 9780121349707.
- [12] Dual Scattering Particle Size Analyzer Nano DS, 2013.

VPLYV TEPLoty SPRACOVANIA NA VLASTNOSTI POVRCHU
ANORGANICKO-ORGANICKÝCH VRSTIEV

THE EFFECT OF THE HEAT TREATMENT ON THE PROPERTIES OF SURFACE
OF INORGANIC-ORGANIC LAYERS

M. Čierniková¹, P. Balážová¹, A. Plško¹, J. Pagáčová², I. Papučová²

¹⁾ *Alexander Dubček University of Trenčín, Vitrum Laugaricio – Join Glass Centre
of the TnUAD, Študentská 2, 911 50 Trenčín, Slovakia*

²⁾ *Alexander Dubček University of Trenčín, Faculty of Industrial Technologies in Púchov,
I. Krasku 491/30, 020 01 Púchov, Slovakia*

e-mail: marianna.ciernikova@tnuni.sk

ABSTRACT

The present study deals with the effect of the heat treatment on the properties of surface of inorganic-organic layers prepared in “tetraethoxysilane (TEOS) - triethoxy(octyl)silane (OTES) - distilled water (H₂O) - nitric acid (HNO₃) - isopropyl alcohol (IPA)” system. Inorganic-organic sol was prepared with molar ratios of $x(\text{OTES})/(x(\text{OTES})+x(\text{TEOS})) = 0.3$ and $x(\text{H}_2\text{O})/(x(\text{OTES})+x(\text{TEOS})) = 6$. Inorganic-organic layers were prepared by the dip-coating technique and heat treated at 140, 160, 180, 200 and 220 °C. The morphology, *rms*-roughness, hydrophobicity, surface free energy and its polar and dispersion components were studied on inorganic-organic layers. The prepared inorganic-organic layers were non-uniform and consisted mostly of spherical bumps and depressions of different size and shape. The layers were hydrophobic up to a temperature of 180 °C and above this temperature, the layers became hydrophilic. *Rms*-roughness decreased with increasing temperature of heat treatment except for the layer which were heat treated at 200 °C. Surface free energy and its components slightly increased with increasing temperature of heat treatment. It was found out that the studied properties were significantly affected by the thermal decomposition of octyl groups on the surfaces of inorganic-organic layers which were heat treated at 200 and 220 °C.

Keywords: inorganic-organic layers, morphology, *rms*-roughness, hydrophobic surface, surface free energy

INTRODUCTION

In the last years, the attention is increasingly devoted to preparation of inorganic-organic materials by sol-gel method in the form of transparent thin layers on different substrates due to their high resistance to wear, near-perfect adhesion to the substrate, thermal stability, mechanical strength, high transparency and good processibility [1-3]. These materials are very interesting for a wide variety of application such as protective and self-cleaning thin layers on windows, windscreens, store windows and glass building facades, solar panels, wind turbine blades, optical displays and touch panels, mirrors in the bathroom, etc. [4-8]. The properties of surfaces of these thin layers (morphology, hydrophobicity, *rms*-roughness, surface free energy) play a crucial role in applications mentioned above. In the present work, the sol-gel method was used for preparation of sol using TEOS as inorganic precursor and OTES as modifying organoalkoxysilane. The effect of the heat treatment on the properties of surface of prepared inorganic-organic layers was studied.

EXPERIMENTAL

Inorganic-organic sol with molar ratios of $x(\text{OTES})/(x(\text{OTES})+x(\text{TEOS})) = 0.3$ and $x(\text{H}_2\text{O})/(x(\text{OTES})+x(\text{TEOS})) = 6$ was prepared in the “tetraethoxysilane (TEOS) - triethoxy(octyl)silane (OTES) - distilled water (H₂O) - nitric acid (HNO₃) - isopropyl alcohol (IPA)” system by the sol-gel method. The content of silicon dioxide and nitric acid in sol was constant: $x(\text{OTES})+x(\text{TEOS}) = 0.05$ and $x(\text{HNO}_3) = 0.005$. The inorganic-organic sol was applied by the dip-coating technique on cleaned glassy substrates. The substrates were withdrawn from the sol at a speed of 60 mm min⁻¹. The inorganic-organic layers were heat treated at 140, 160, 180, 200 and 220 °C for 2 hours. The surface of prepared inorganic-organic layers was investigated using the Innova atomic force microscope (Bruker) operating in tapping mode in the air at room temperature. Each layer was measured in five selected places and 2D images (10 × 10 μm) were obtained. The morphology of prepared inorganic-organic layers was observed visually using the program NanoScope Analysis 1.50. *Rms*-roughness (*RMS*) of surfaces was evaluated using the following equations:

$$RMS(N, M) = \sqrt{\frac{1}{NM} \sum_{x=1}^N \sum_{y=1}^M (z(x, y) - \bar{z}(x, y))^2} \quad (1)$$

$$\bar{z}(N, M) = \frac{1}{NM} \sum_{x=1}^N \sum_{y=1}^M z(x, y) \quad (2)$$

where RMS is standard deviation of surface height, N and M are the number of lines and columns corresponding to the raster of the AFM image, z is height in the x, y point in the AFM image (nm) and \bar{z} is the average height of surface inequalities in the AFM image (nm) [9]. The contact angles (θ) of liquids on prepared inorganic-organic layers were determined by the method of sessile drop. Distilled water ($\gamma_l^d = 21.8 \text{ mJ.m}^{-2}$, $\gamma_l^p = 51 \text{ mJ.m}^{-2}$) and diiodomethane ($\gamma_l = \gamma_l^d = 50.8 \text{ mJ.m}^{-2}$) were used as measuring liquids. 12 drops of measuring liquid with a volume of $10 \mu\text{l}$ were placed for each layer. The surface free energy (SFE) and its polar and dispersion components were calculated from the measurement of contact angle using distilled water and diiodomethane by the Owens-Wendt's method on the basis of following equations [10, 11]:

$$\gamma_s = \gamma_s^d + \gamma_s^p \quad (3)$$

$$\gamma_{sl} = \gamma_s + \gamma_l - 2 \left(\sqrt{\gamma_s^d \gamma_l^d} + \sqrt{\gamma_s^p \gamma_l^p} \right) \quad (4)$$

$$\frac{(1+\cos\theta) \cdot \gamma_l}{2\sqrt{\gamma_l^d}} = \sqrt{\gamma_s^p} \sqrt{\frac{\gamma_l^p}{\gamma_l^d}} + \sqrt{\gamma_s^d} \quad (5)$$

where γ_{sl} is SFE on the contact surface between solid and test liquid, γ_s is SFE of solid, γ_l is SFE of liquid, γ_s^d is dispersion component of SFE of solid, γ_s^p is polar component of SFE of solid, γ_l^d is dispersion component of SFE of liquid, γ_l^p is polar component of SFE of liquid and θ is contact angle between tested surface and standard liquid.

RESULTS AND DISCUSSION

The Fig. 1 shows the AFM 2D images of inorganic-organic heat treated layers at 140, 160, 180, 200 and 220 °C. The surfaces of these layers consisted of non-uniformly distributed spherical bumps of different size as well as larger depressions of different size and shape. The surfaces of inorganic-organic layers which were heat treated at 140 °C (Fig. 1a), 160 °C (Fig. 1b) and 180 °C (Fig. 1c) were visually similar, however the spherical bumps reduced their size with increasing temperature of treatment. The increase of the heat treatment temperature up to 200 °C led to a formation of elongated bumps non-uniformly distributed on the surface (Fig. 1d). The inorganic-organic heat treated layer at 220 °C (Fig. 1e) consisted mostly of small depressions with almost circle circumference and small non-uniformly distributed spherical bumps. The changes in morphology of inorganic-organic heat treated layers at 200 and 220 °C can be assignment to the thermal decomposition of octyl groups on the surface.

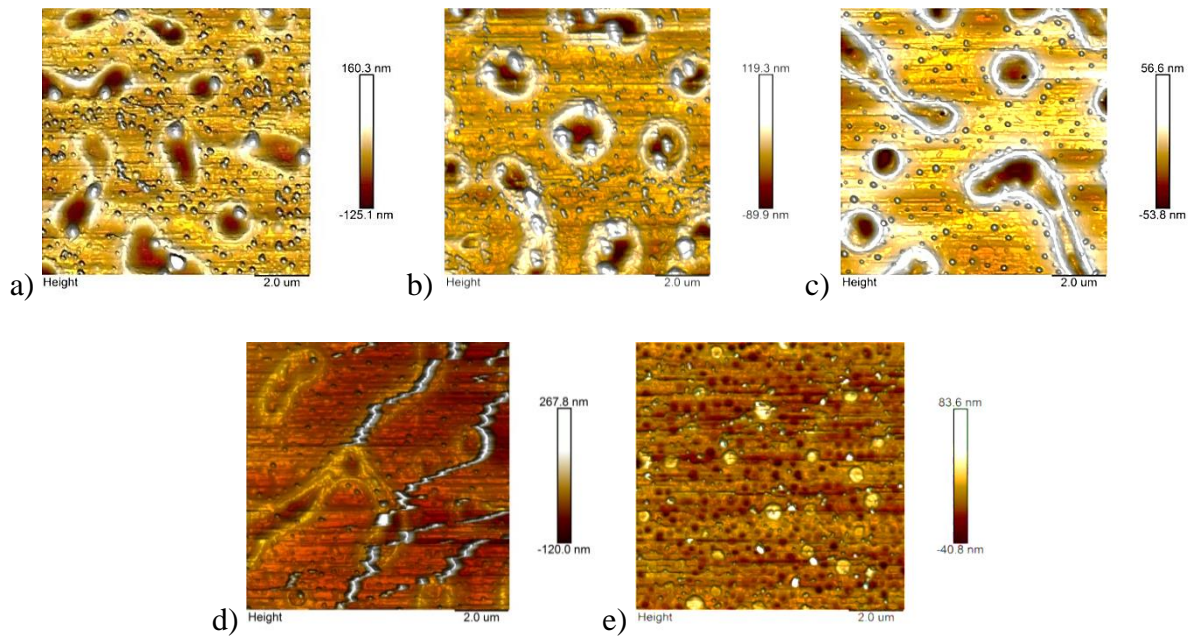


Fig. 1: AFM 2D images of inorganic-organic heat treated layers at: a) 140 °C, b) 160 °C, c) 180 °C, d) 200 °C, e) 220 °C

The Fig. 2 shows the dependence of *rms*-roughness of inorganic-organic layers on the heat treatment. The *rms*-roughness of prepared inorganic-organic layers decreased with increasing temperature of heat treatment except for layer which was heat treated at 200 °C when the *rms*-roughness increased from 17.1 nm to 25.1 nm. The high standard deviation of *rms*-roughness of this layer confirmed that its surface was non-uniform and affected by the thermal decomposition of octyl groups on the surface.

Table 1: *Rms*-roughness of inorganic-organic layers

| Sol | Temperature [°C] | <i>Rms</i>-roughness [nm] |
|-----------------|-------------------------|----------------------------------|
| BA17010V | 140 | 28.4±2.5 |
| BA17011V | 160 | 25.6±1.8 |
| BA17012V | 180 | 17.1±1.9 |
| BA17013V | 200 | 25.1±11.0 |
| BA17014V | 220 | 14.5±2.7 |

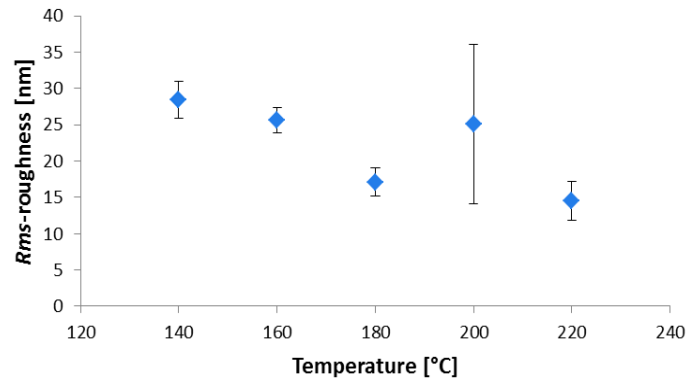


Fig. 2: The dependence of *rms*-roughness of inorganic-organic layers on the heat treatment

The Fig. 3 shows the dependence of contact angle of water on inorganic-organic layers on the heat treatment. The mean values of contact angle of water can be considered as a measure of the hydrophobicity. The results showed that prepared layers were hydrophobic up to a temperature of 180 °C. Above this temperature of heat treatment, the mean values of contact angle of water decreased and the layers became hydrophilic.

Table 2: Contact angles of water on inorganic-organic layers

| Sol | Temperature [°C] | θ of water [°] |
|----------|------------------|-----------------------|
| BA17010V | 140 | 96.3±1.8 |
| BA17011V | 160 | 95.9±5.2 |
| BA17012V | 180 | 98.5±0.8 |
| BA17013V | 200 | 82.3±4.0 |
| BA17014V | 220 | 87.8±1.9 |

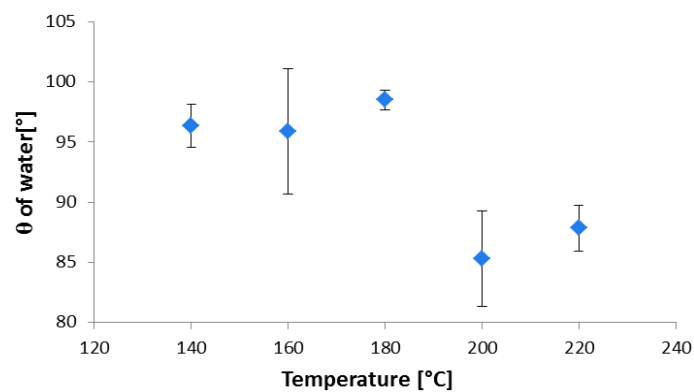


Fig. 3: The dependence of water contact angle of inorganic-organic layers on the heat treatment

The Fig. 4 shows the dependence of surface free energy and its dispersion and polar components of inorganic-organic layers on the heat treatment. The surface free energy of prepared inorganic-organic layers slightly increased with increasing temperature of heat treatment. The similar dependence was observed for dispersion as well as polar component of SFE. The results showed that the dispersion component of surface free energy prevailed over the polar component of surface free energy. The relation between the mean values of the polar component of SFE and the hydrophobicity of prepared inorganic-organic layers was observed. The higher the mean values of polar component of SFE were, the lower the hydrophobicity was. The highest value of polar component of SFE and the lowest hydrophobicity were observed for inorganic-organic heat treated layer at 200 °C.

Table 3: Surface free energy and its dispersion and polar components of inorganic-organic layers

| Sol | Temperature [°C] | γ_s [$\text{mJ}\cdot\text{m}^{-2}$] | γ_s^d [$\text{mJ}\cdot\text{m}^{-2}$] | γ_s^p [$\text{mJ}\cdot\text{m}^{-2}$] |
|----------|------------------|--|--|--|
| BA17010V | 140 | 28.1±0.6 | 26.8±0.6 | 1.3±0.2 |
| BA17011V | 160 | 27.2±1.1 | 25.5±1.0 | 1.6±0.8 |
| BA17012V | 180 | 28.1±0.3 | 27.3±0.4 | 0.9±0.1 |
| BA17013V | 200 | 32.4±1.0 | 28.2±0.6 | 4.2±0.9 |
| BA17014V | 220 | 32.5±0.4 | 29.5±0.3 | 3.0±0.4 |

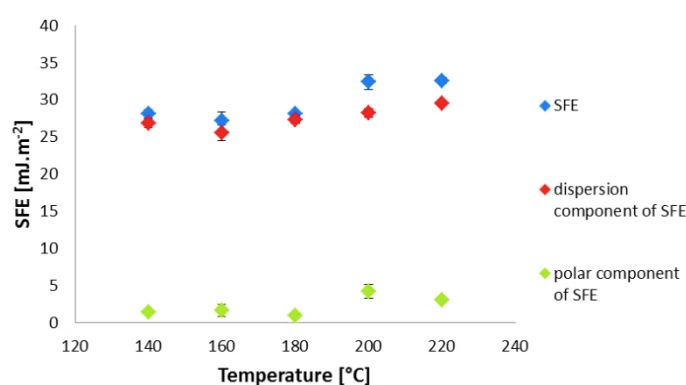


Fig. 4: The dependence of surface free energy and its dispersion and polar components of inorganic-organic layers on the heat treatment

CONCLUSION

The inorganic-organic layers were prepared by the sol-gel method and dip-coating technique on glassy substrates and heat treated at 140, 160, 180, 200 and 220 °C. The inorganic-organic layers

were non-uniformly and consisted mostly of spherical bumps and depressions of different size and shape. The layers were hydrophobic up to a temperature of 180 °C and above this temperature, the layers became hydrophilic. The *rms*-roughness of inorganic-organic layers decreased with increasing temperature of heat treatment except for layer which was heat treated at 200 °C. The surface free energy and its components of prepared inorganic-organic layers slightly increased with increasing temperature of heat treatment. Based on the results, we can conclude that the morphology, hydrophobicity, *rms*-roughness and polar component of surface free energy were significantly affected by the thermal decomposition of octyl groups on the surface of inorganic-organic heat treated layers at 200 and 220 °C. Therefore, the hydrophobic inorganic-organic layers prepared from given sol in “TEOS-OTES-H₂O-HNO₃-IPA” system should be heat treated maximal at 180 °C.

ACKNOWLEDGMENT

The work was supported by the „CEKSiM“ project, ITMS 262 201 200 56.

REFERENCES

- [1] Sanchez et al., Applications of hybrid organic-inorganic nanocomposites, *Journal of Materials Chemistry* 15 (2005) 3559-3592.
- [2] D.J. Kang et al., Fabrication and characterization of photocurable inorganic-organic hybrid materials using organically modified colloidal-silica nanoparticles and acryl resin, *Journal of Non-Crystalline Solids* 355 (2009) 397-402.
- [3] G. Kickelbick, Hybrid Materials – Past, Present and Future, *Hybrid Materials* 1 (2014) 39-51.
- [4] S.I. Huang, Y.J. Shen, H. Chen, Study on the hydrophobic surfaces prepared by two-step sol-gel process, *Applied Surface Science* 255 (2009) 7040-7046.
- [5] D. Kumar et al., Development of durable self-cleaning coatings using organic-inorganic hybrid sol-gel method, *Applied Surface Science* 344 (2015) 205-212.
- [6] K. Akamatsu et al., Water-repellent coating films on glass prepared from hydrolysis and polycondensation reactions of fluoroalkyltrialkoxysilane, *Thin Solid Films* 389 (2001) 138-145.

- [7] H.J. Jeong et al., Preparation of water-repellent glass by sol-gel process using perfluoroalkylsilane and tetraethoxysilane, *Journal of Colloid and Interface Science* 235 (2001) 130-134.
- [8] A.J. Kessman, D.R. Cairns, Template-assisted encapsulation of fluorinated silanes in silica films for sustained hydrophobic-oleophobic functionality, *Journal of Colloid and Interface Science* 360 (2011) 785-792.
- [9] M. Raposo, O. Ferreira, P.A. Ribeiro, A Guide for Atomic Force Microscopy Analysis of Soft-Condensed Matter, in: A. Méndez-Vilas, J. Díaz (Eds), *Modern Research and Educational Topics in Microscopy*, vol. 2, Formatex, 2007, 758-769.
- [10] M. Żenkiewicz, Methods for the calculation of surface free energy of solids, *Journal of Achievements in Materials and Manufacturing Engineering* 24 (2007) 137-145.
- [11] M. Żenkiewicz, Comparative study on the surface free energy of a solid calculated by different methods, *Polymer Testing* 26 (2007) 14-19.

**PRÍPRAVA A CHARAKTERIZÁCIA KERAMICKÝCH POVLAKOV
SO SKLENÝMI PLNIVAMI NA OCEĽOVÝCH SUBSTRÁTOCH**

**PREPARATION AND CHARACTERIZATION OF PRECURSOR DERIVED
CERAMIC COATINGS WITH GLASS FILLER PARTICLES ON STEEL
SUBSTRATE**

Ivana Petříková¹, Milan Parchovianský¹, Peter Švančárek¹, Gunter Motz², Dagmar Galusková¹, Dušan Galusek¹

¹Vitrum Laugaricio – Joint Glass Center of the IIC SAS, TnU AD, and FCHFT STU, Študentská 2, 911 50 Trenčín, Slovakia

²University of Bayreuth, Ceramic Materials Engineering, D-95440 Bayreuth, Germany

ABSTRACT

A novel environmental barrier coating system for steel consisting of a perhydropolysilazane (PHPS) bond coat and a polysilazane-based glass/ceramic composite top coat has been developed. The slurry preparation as well as processing route, filler systems and microstructure of the coating system were optimized. After stabilizing the coating slurries, double layers consisting of a bond coat applied by dip coating and a top coat deposited by spray coating were prepared on stainless steel (AISI 441) substrates. The thermal treatment was performed in air at temperatures up to 800 °C. The optimized composite top coatings were prepared from the ceramic matrix forming polysilazane HTT1800 precursor, filled with YSZ and a powder precursor ($\text{Al}_2\text{O}_3\text{-Y}_2\text{O}_3\text{-ZrO}_2$) as passive fillers, and the commercial glasses G018-311 and G018-385 as sealing agents. After thermal treatment in air at 750°C, uniform and crack-free composite coatings on stainless steel with a thickness up to 90µm were prepared.

Keywords: polymer-derived ceramics, environmental barrier coating, passive filler

INTRODUCTION

Due to the increasing costs for metals, there is currently a need to enhance the performance and lifetime of steel, for example, those employed in exhaust systems, waste incineration plants or for applications in the chemical industry [1]. Protective coatings are frequently the most cost-effective solution for several engineering problems like corrosion, oxidation and wear [2]. Recently polymer derived ceramics have gained attention as promising candidates for preparation of environmental barrier coatings. Preceramic polymers (precursors) possess certain polymeric characteristics, which provide many processing advantages that are not possible with traditional ceramics. Precursors can be produced in liquid form, which facilitates processing by slurry methods. This also allows control of the precursor viscosity, which can be useful in coating process [3]. The main drawback of the preceramic polymer technology is the unavoidable shrinkage, which occurs due to the large density change when the polymer precursor is converted to the ceramic product [4]. The shrinkage of the polymer leads to crack formation in coatings and, in extreme cases, to complete failure of the coating. To overcome these drawbacks, the coatings have to be filled with components that compensate shrinkage and close the pores. Filler particles can also increase the coating thickness [5]. A coating with a minimum of closed porosity is formed when glass particles fill the polymer derived ceramic network in the coating [1]. Service temperature and softening point of the glass filler particles should be matched to make the coating most efficient [6].

The aim of this work is the development of a relatively thick (about 100 μ m), protective and well adherent coating system on steel. Therefore, a double layer composition with a bond coat and top coat was investigated. Glass powders were added as filler materials in order to densify and seal the coatings at the temperatures of their application, to increase the coating thickness and to improve its adhesion to substrate. Parameters like the type of precursor, the filler and glass systems, the volume fraction of the components and pyrolysis conditions were varied to optimize the composite coating system.

EXPERIMENTAL

The composite coatings consist of two layers that were consecutively applied to 1 mm thick stainless steel (AISI 441) substrates. Before coating, the steel plates were cut into sheets, cleaned by ultrasonic treatment in acetone and dried. The pre-treated substrates were dip-coated

(Relamatic RDC 15, Switzerland) in the PHPS solution to obtain the bond-coat. The curing of the PHPS bond-coat was carried out in air at 500 °C for 1h with heating rate of 5°C/min (N41/H, Nabertherm, Germany). The subsequently applied top coat was prepared by mixing defined volume fractions of a liquid polysilazane HTT1800, ceramic filler particles (yttria-stabilized zirconia - YSZ) and commercial barium silicate (G018-311, G018-385, Schott AG) and borosilicate (G8470, Schott AG) filler glass particles, which have similar thermal expansion coefficients ($9-10 \times 10^{-6}/K$) to that of the steel substrates ($14.5 \times 10^{-6}/K$). The average particle size of the glass powders was between 3 and 10 μm . This mixture of glass filler particles was incorporated into the suspension using dispersing agents. In some cases, specially tailored glass particles in the form of microspheres ($\text{Al}_2\text{O}_3\text{-Y}_2\text{O}_3$, $\text{Al}_2\text{O}_3\text{-Y}_2\text{O}_3\text{-ZrO}_2$) or a polycrystalline powder precursor ($\text{Al}_2\text{O}_3\text{-Y}_2\text{O}_3$, $\text{Al}_2\text{O}_3\text{-Y}_2\text{O}_3\text{-ZrO}_2$) for the preparation of glass microspheres were added as further passive fillers to the coatings described above. All coated samples were heat treated in air at temperatures up to 800 °C for 1 h. Selected compositions of prepared composite coatings are shown in Tab. 1. The SEM/EDS examination of the coatings after pyrolysis was conducted with the use of a FEG SEM JEOL 7600f and was focused at evaluation of homogeneity, adhesion and possible failures of the coatings. X-ray powder diffraction analysis ($\text{CuK}\alpha$, 2θ range 10-80°, Empyrean DY1098, PANalytical B.V., Netherlands) was used to investigate the phase composition of the coatings.

Tab. 1: The compositions of the composite top coats

| COATING | COMPOSITION (vol. %) (after pyrolysis) | | | | | | | | CTE (10^{-6}-K^{-1}) |
|-----------|---|---|--|---|----------|----------|-------|---------|------------------------------------|
| | YSZ | $\text{Al}_2\text{O}_3\text{-Y}_2\text{O}_3$ precursor | $\text{Al}_2\text{O}_3\text{-Y}_2\text{O}_3\text{-ZrO}_2$ precursor | $\text{Al}_2\text{O}_3\text{-Y}_2\text{O}_3\text{-ZrO}_2$ Microspheres | G018-385 | G018-311 | G8470 | HTT1800 | |
| C1 | 33 | - | - | - | - | 20 | 31 | 16 | 9.3 |
| C2 | 36 | - | - | 10 | - | 17 | 17 | 20 | 8.9 |
| C3 | 25 | 12.5 | 12.5 | - | 15 | 15 | - | 20 | 8.3 |
| C4 | 30 | - | 21 | - | 16 | 14 | - | 19 | 8.5 |

RESULTS

In Fig. 1a, a SEM micrograph of a HTT1800/glass composite coating (composition C1) after pyrolysis in air at the temperature of 700°C is presented. Micrograph of the cross-section shows that the softening of glass additives leads to formation of a homogeneous glass/ceramic matrix with evenly distributed zirconia particles. However, the approximately 100 µm thick coating exhibited significant fraction of closed pores with a diameter up to 10 µm. The amount and size of pores increased up to 40 µm with increasing temperature of pyrolysis (Fig. 1b). The pores resulted from the release of gases (such as CH₄, NH₃, H₂) generated during the polymer-to-ceramic transformation. Since diameter of the pores lies in the range of the coating thickness, such coating do not possess environmental barrier properties.

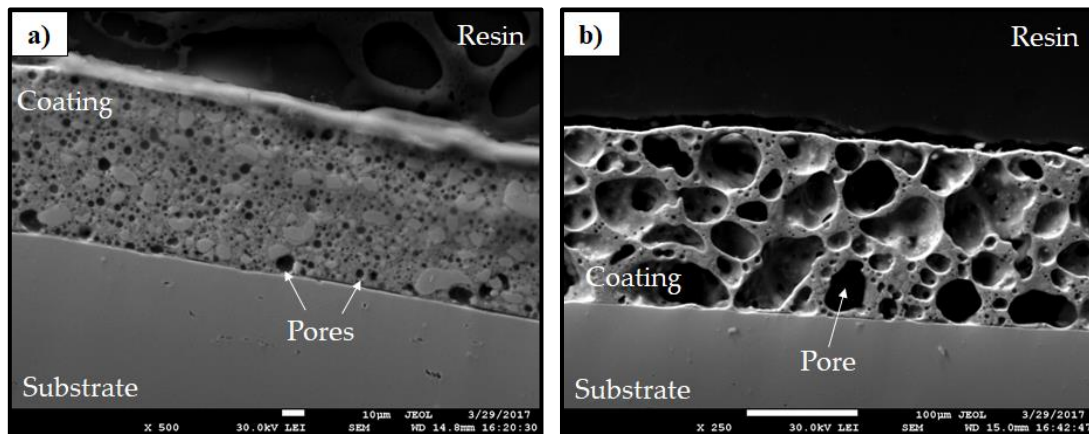


Fig. 1: SEM images of the coating C1 after pyrolysis at different temperatures: a) 700 °C, b) 750 °C

To reduce the porosity and the pore size of the coatings, polycrystalline powder precursor for preparation of glass microspheres (Al₂O₃-Y₂O₃-ZrO₂) or glass microspheres were used as additional passive fillers. These formed a rigid skeletal structure in the coating, thus facilitating escape of gases during pyrolytic conversion of the organosilicon precursor. In the case of the coating C2 (which includes glass microspheres), the pore size was reduced to 10 µm after pyrolysis in air at 750°C. However, the high volume shrinkage of the polysilazane precursor led to formation of severe cracks distributed across the whole surface (Fig. 2a). Moreover, as obvious from the cross section (Fig. 2b), the cracks penetrate through the coating to the metal surface and, in some cases, coating with a thickness of approximately 50 µm delaminates from the steel substrate.

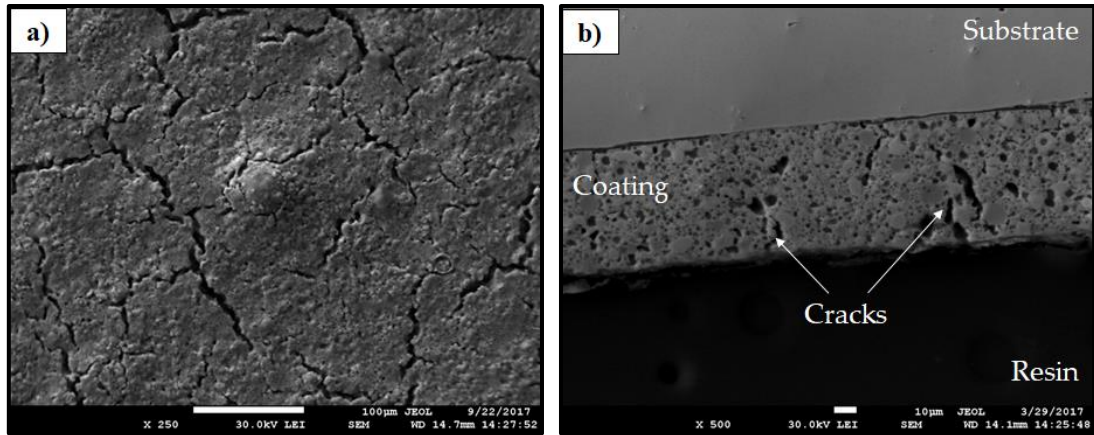


Fig. 2: SEM images of the coating C2 after pyrolysis at the temperature 750°C:

a) surface, b) cross-section

The best composite top coatings were prepared with YSZ, and powder precursors ($\text{Al}_2\text{O}_3\text{-Y}_2\text{O}_3\text{-ZrO}_2$) as passive filler and the glass systems G018-311 and G018-385 as sealing agents. On the basis of the analyzed surface and cross sectional micrographs (

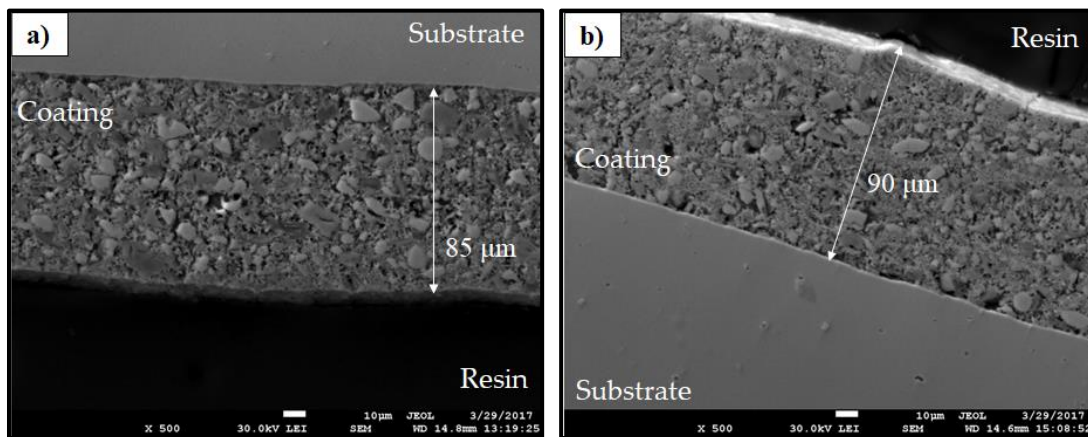


Fig. 3), it can be concluded that the addition of powder precursor was effective at preventing the formation of cracks and pores. Furthermore, a homogenous distribution of the fillers particles (YSZ, powder precursor) within the coating was observed. As confirmed by EDS analysis, the filler particles are surrounded by molten glass and embedded in a polymer derived ceramic matrix. The composite coating (composition C4) provides the most promising overall results. After a thermal treatment in air at 750 °C, uniform, well adherent and crack-free composite coatings on stainless steel were prepared.

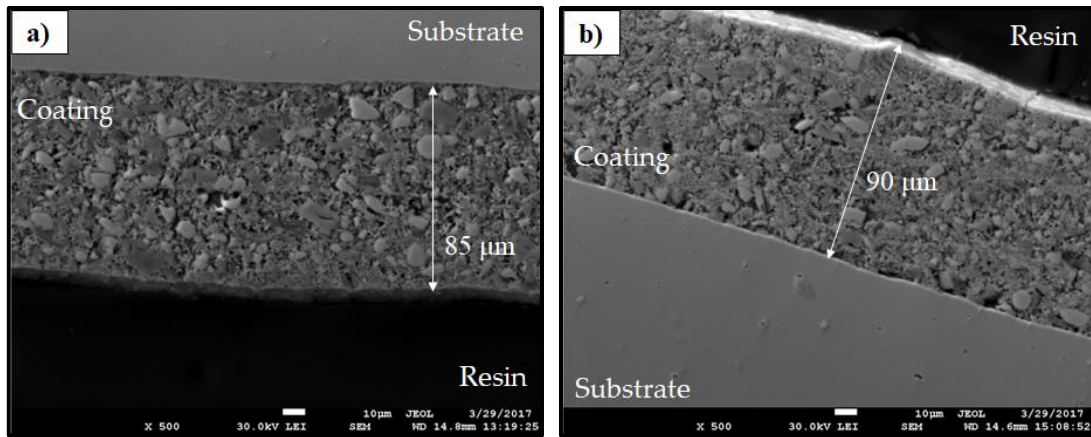


Fig. 3: Cross-sectional SEM images after pyrolysis in air at 750°C:

a) coating C3, b) coating C4

The phase composition of the coatings was investigated by X-ray diffraction (Fig. 4). For all the glass and YSZ filled coatings, the dominant phases are monoclinic and tetragonal zirconia. In the case of the coating C3, other crystalline phase was also detected, namely yttrium aluminium garnet, originating from the powder precursor ($\text{Al}_2\text{O}_3\text{-Y}_2\text{O}_3$). The results of the XRD measurements along with SEM analysis indicated that the coated stainless steel substrates were not oxidized at the applied temperature of pyrolysis and no reactions takes place between the polysilazane HTT1800 and the filler materials.

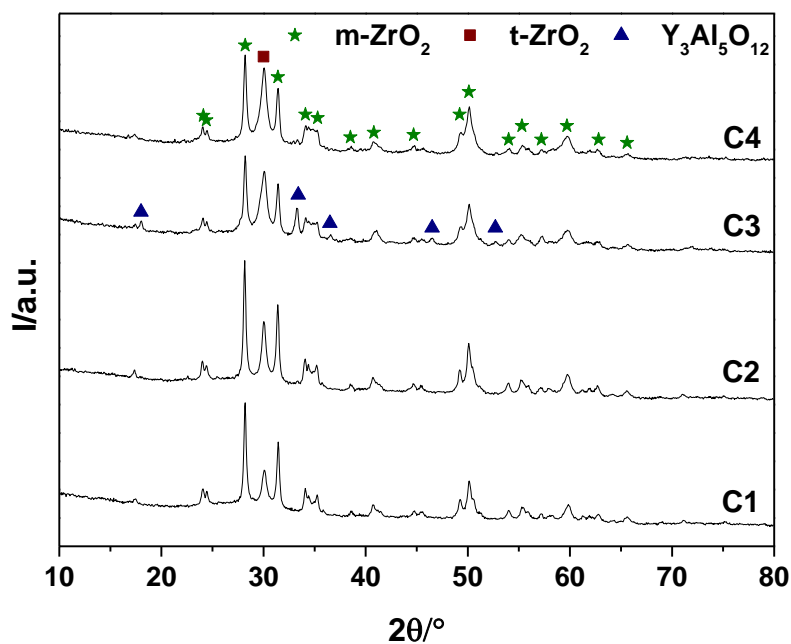


Fig. 4: X-Ray diffraction patterns of the composite coatings after pyrolysis in air at 750°C

CONCLUSION

A novel polymer-derived ceramic coating system as an environmental barrier coating for steel was developed, using a tailored combination of polymer pre-ceramic precursor with passive fillers and glass frits used as sealants. The resultant coating with the thickness up to 100µm, obtained by pyrolysis at 750°C in air, is almost fully dense, with no cracking or delamination, and it is expected to prevent the access of aggressive environment to the steel substrate at temperatures up to 900 °C. Oxidation and corrosion tests are in progress.

ACKNOWLEDGMENT

Financial support of this work by the grants VEGA 2/0026/17, VEGA 1/0145/17, APVV 0014-15 and by the Alexander von Humboldt Foundation in the frame of the institutional cooperation grant scheme is gratefully acknowledged. This publication was created in the frame of the project "Centre of excellence for ceramics, glass, and silicate materials" ITMS code 262 201 20056, based on the Operational Program Research and Development funded from the European Regional Development Fund.

REFERENCES

- [1] M. Günthner et. al, JECS, vol. 31, no. 15, pp. 3003–3010, 2011.
- [2] K. Tangermann-gerk et. al., JMADE, vol. 109, pp. 644–651, 2016.
- [3] M. D. Nguyen et. al., JECS., vol. 37, no. 5, pp. 2001–2010, 2017.
- [4] P. Greil, JACS, vol. 78, pp. 835-848, 1995.
- [5] P. Colombo, JACS, vol. 93, no. 3, p. 1805, 2010.
- [6] A. P. Zubekhin, GCEC, vol. 58, no. 9-10, p. 360, 2001.